Department of Precision and Microsystems Engineering

Development of novel manufacturing method for a contactless handling system using a variable outlet restriction

Kees Pijnenburg

Report no : 2022.011
Coach : Ir. J. Snieder
Professor : Dr. ir. R.A.J. van Ostayen
Specialisation : Mechatronic System Design
Type of report : Master thesis
Date : 19-04-2022

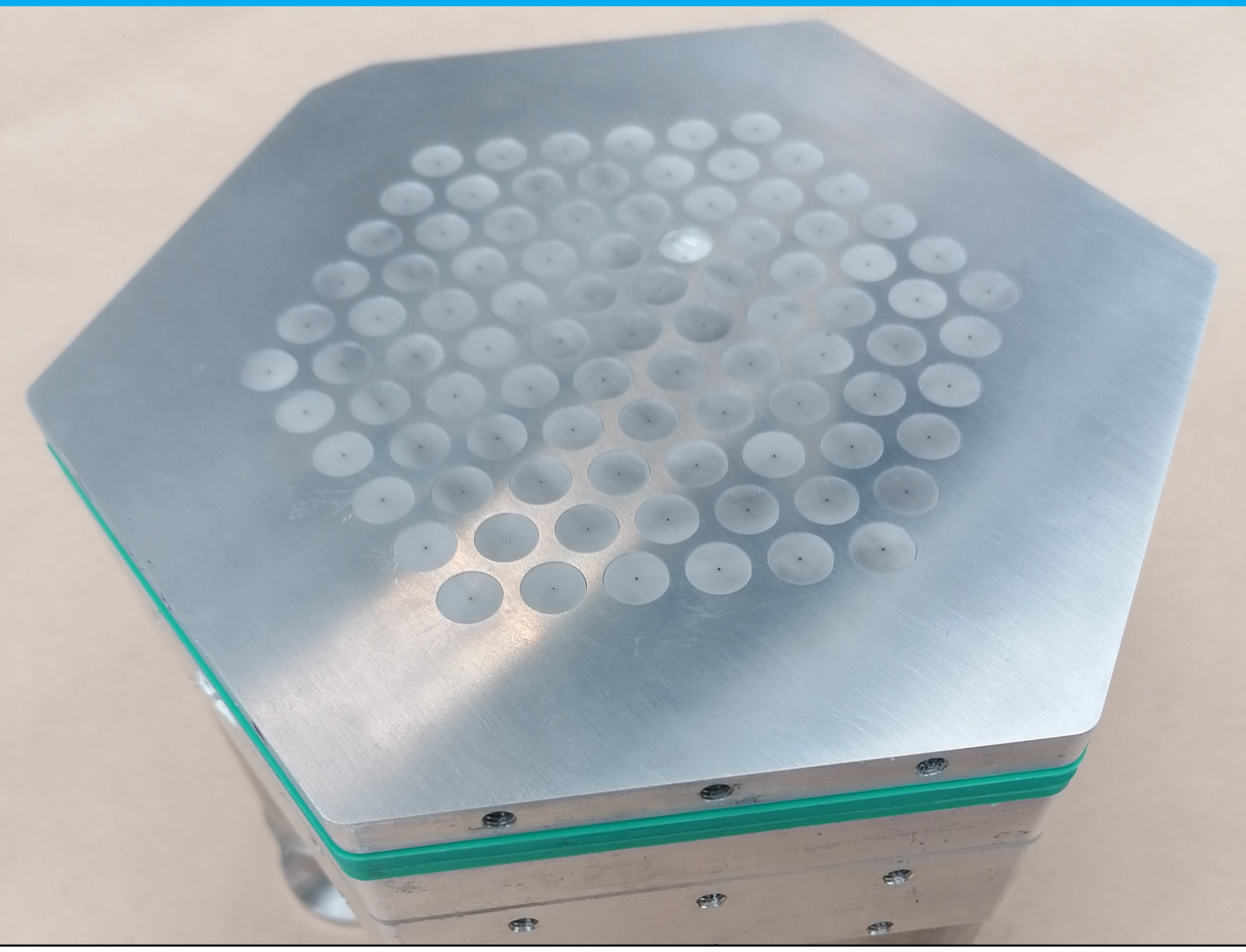

Development of a novel manufacturing method for a contactless handling system using a variable outlet restriction

by

K.H. Pijnenburg

to obtain the degree of Master of Science
at the Delft University of Technology,
to be defended publicly on Tuesday May 3rd, 2022 at 15:00.

Student number: 4311760

Thesis committee:	Dr. ir. R.A.J. van Ostayen,	TU Delft, supervisor
	Ir. J. Snieder,	TU Delft, daily supervisor
	Dr. ir. J.F.L. Goosen,	TU Delft, external member

TU Delft

Voor opa Piet

Contents

Chapter 1

Introduction

1.1 Background & motivation

Many products, such as solar cells, integrated circuits and flat panel displays are created from a flat base substrate. The manufacturing process of these products is comprised of multiple sub-processes. The substrates need to be transported between these sub-processes. In some cases, accurate positioning of the substrate within the sub-process is critical. For example when features are created that need to be aligned with previously created features.

Since these substrates are in general thin, fragile and costly, they need to be handled with great care. Any physical contact might lead to particle generation, which can contaminate the substrate. Physical contact might also induce high contact loads in the substrate which can damage the wafer. Three examples are presented below.

Solar cells

Since 1990, the thickness of solar cells has been decreasing, as shown in figure 1.1b. However, the thickness seems not to decrease below $\sim 180\,\mu$m. The reason for this is that wafers will break during the manufacturing process if they get too thin.

It was found by Lui et. al. that deceasing the thickness of solar cells to $50\,\mu$m could potentially reduce the cost of energy by 24% [1]. Many technical challenges have to be overcome in order to achieve this, one of which is improved wafer handling. In this research, a potential solution is proposed in the form of contactless handling using air bearing technology. This handling method could be used in the production of solar cells, but also in the production of flat panel display and integrated circuits.

(a) Manufacturing of solar cells.

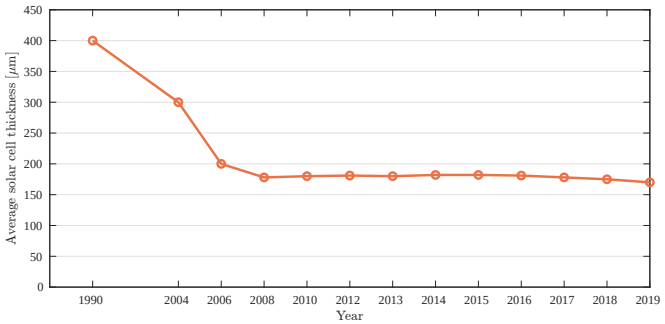

(b) Solar cell thickness over the years [2].

Figure 1.1: Solar cell manufacturing.

Integrated circuits

Silicon wafers are also used for the production of integrated circuits, tend to get larger and thinner [3], which increases risk of breakage. The features which are created on the wafer also tend to get smaller, thus more accurate positioning is required. Improved handling methods are required in order to satisfy these requirements.

Flat panel displays

Also for flat panel displays, the size increases, as can be seen in figure 1.2. Handling such large substrates can benefit from the distributed force that can be generated using contactless handling. This prevents stress concentrations from occurring within the material.

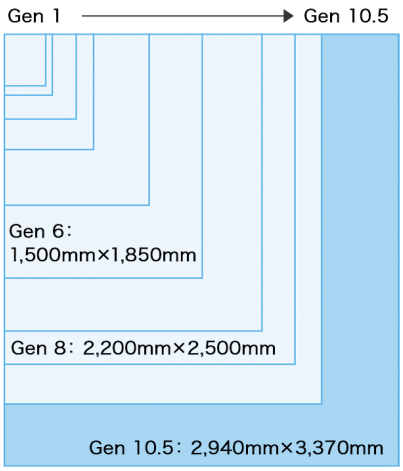

Figure 1.2: Size of several generations of glass panes used in the production of flat panel displays[1].

1.2 State of the art

Contactless handling can be achieved using various physical principles, such as electro-magnetic, electro-static, or acoustic. An overview of these systems is presented in [4, 5]. This research focusses on contactless handling using air bearing technology, hereafter referred to as contactless handling. Within Delft University of Technology, several concepts have been developed over the past, as shown in table 1.1. These concepts will be explained in more detail in the following subsections.

Table 1.1: Actuation principle used in existing demonstrators.

	Generation		
Actuation principle	*Generation 1*	*Generation 2*	*Generation 3*
Pressure control	[5]	-	-
Variable pocket restriction	-	[4]	-
Variable outlet restriction	-	-	[6]

1.2.1 Pressure control

Concept

An impression of the system developed by Wesselingh [5] is shown in figure 1.3a. A cross-section of the system is shown in figure 1.3b. As the name implies, the pressure is actively controlled, while the geometry of the unit cell is fixed. The supply pressure p_s is higher than the ambient pressure, while the vacuum pressure p_v is lower than ambient pressure. The average pressure below the substrate should equal the ambient pressure plus the distributed weight of the substrate in order to achieve levitation. Air will flow from the high pressure on the left towards the low pressure on the right. A small portion of the flow will be across the dam towards the neighbouring unit cell on the left. This parasitic flow decreases the net force. Since the geometry is fixed, the direction of this force cannot be controlled. The magnitude of the force can be controlled by controlling the supply and vacuum pressure. In order to create unilateral actuation, pairs of unit unit cells with alternating actuation directions should be used.

[1] Nikon FPD Lithography Systems

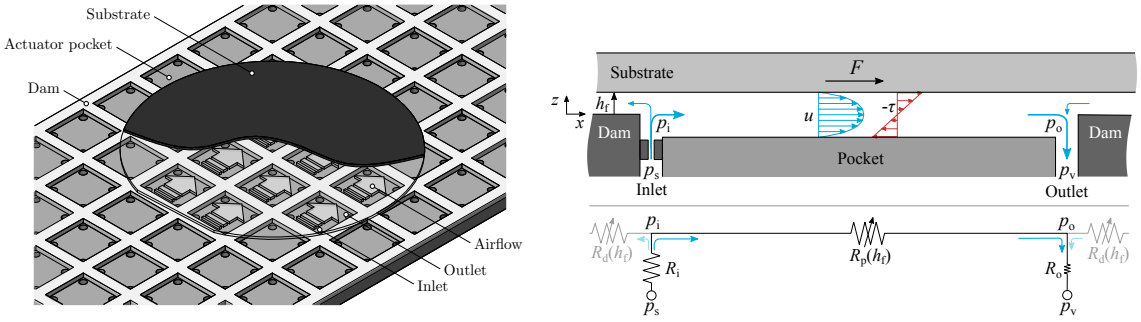

(a) Schematic representation of substrate on a contactless handling system. Adapted from [5].

(b) Cross section of unit cell.

Figure 1.3: Schematic representation of the Waferstage.

Demonstrator

A demonstrator was developed by Wesselingh, as shown in figure 1.4a. The shiny part in the centre of the figure is the effective bearing surface, which comprised of 6×6 unit cells. The dimensions of each unit cell is $10 \times 10\,\mathrm{mm}^2$. The orientation of the inlets and outlets is shown in figure 1.4b. It can be seen that four separate actuation directions exist. Lateral actuation in all planar Degreed Of Freedom (DOFs) can be achieved by controlling the magnitude of the force generated by each unit cell. Though, this will also introduce a parasitic torque.

The demonstrator has achieved a servo positioning accuracy of $6\,\mathrm{nm}(1\sigma)$ in all planar DOFs. A maximum acceleration of $600\,\mathrm{mm/s}^2$ has been measured, using a silicon substrate with a thickness of $525\,\mu\mathrm{m}$.

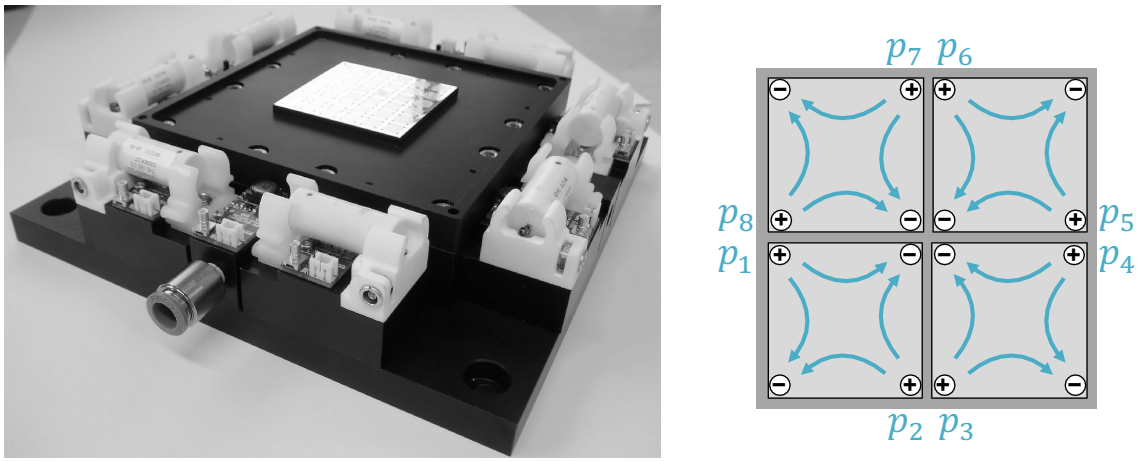

(a) Waferstage demonstrator. Adapted from [5].

(b) Arrangement of unit cells. Adapted from [7].

Figure 1.4: The Waferstage.

Issues

The manifold is a system of channels connecting each inlet and outlet at the bearing surface to its corresponding valve. The flow is controlled by the valves which are located relatively far from the bearing surface. The geometry of the manifold becomes complex rather quickly, which poses a challenge in terms of manufacturing. A delay is introduced since air is compressible and has to travel through the valves and through the manifold in order to reach the bearing surface. This is one of the reasons that the bandwidth of the system is limited to about 50 Hz.

For a larger system, the bandwidth would only decrease further. This is due to the fact that larger (i.e. heavier/slower) valves are required. Also, the channels in the manifold will become longer and more complex. This issue could be solved by controlling the air flow more locally, however, valves with the required characteristics do not exist.

1.2.2 Variable pocket restriction

Concept

The variable pocket restriction concept has been developed by Vuong [4]. The bearing surface consists of segments that can be tilted as shown in figure 1.5a. A cross section of the unit cell is shown in figure 1.5b. Instead of controlling the flow by directly controlling the pressure, the flow is controlled by tilting the segments.

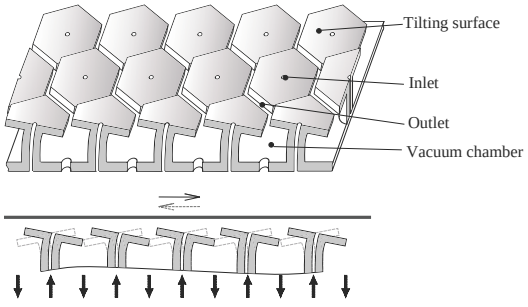

(a) Schematic representation of the bearing surface. Adapted from [4].

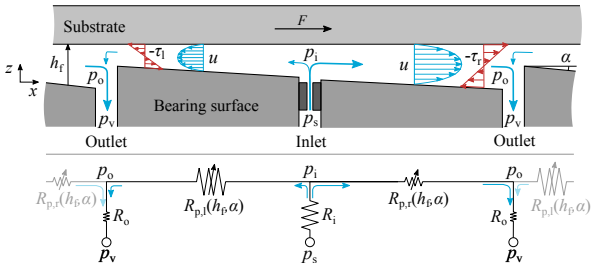

(b) Cross section of unit cell.

Figure 1.5: Schematic representation variable pocket restriction concept.

Demonstrator

A demonstrator, called the Flowerbed, was manufactured by Vuong [4]. This is shown in figure 1.6a. The demonstrator consists of 61 individual flowers, that each consist of several parts as shown in figure 1.6b. The segments are joined by flexible membranes, one at the top and one at the bottom. Since the membranes are each held between two thick plates, they allow for individual rotation about the x- and y- axis of each segment, while being relatively rigid overall. By moving the bottom thick plate with respect to the top thick plate, a tilt is introduced. The volume created between the actuator head and the top plate creates the vacuum chamber. Air is supplied through the stem of the flower, where a capillary flow restriction is located.

The mechanical system has been developed by Vuong. Using the actuators developed by Jansen [7] and the control system developed by Krijnen [8] an acceleration of 1170 mm/s^2 has been achieved using a silicon wafer with a thickness of 750 μm. A positioning accuracy of 104 nm(2σ) was achieved. Since the air flow is controlled at the bearing surface, the theoretical bandwidth is increased to 1000 Hz. A positioning bandwidth of 233 Hz was achieved by Jansen.

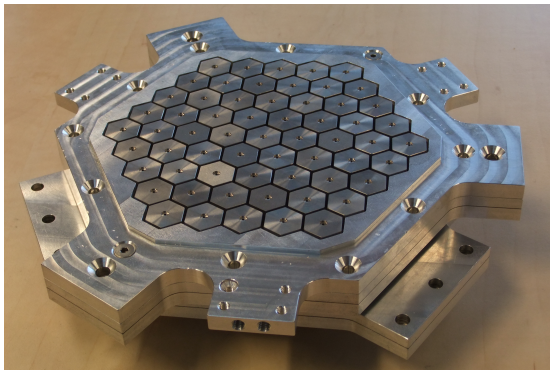

(a) Flowerbed demonstrator[2].

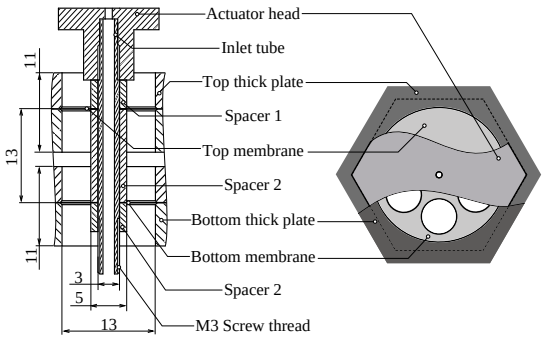

(b) Individual actuator components. Adapted from [4].

Figure 1.6: Schematic representation of the Flowerbed.

[2]Adapted from TU Delft - Tribotronics.

Issues

Since each segment is comprised of many parts, the assembly of the complete system is very complicated and cumbersome. Initially, the bearing surface was not flat, since all segments had a slightly different orientation. The bearing surface of the system was levelled using wire EDM. The performance of the system decreased over a longer period of time. Since the system is comprised of many separate parts, the orientation and position of parts shifts over time.

1.2.3 Variable outlet restriction

Concept

This concept has been developed by Verbruggen [6]. A schematic representation of the system is shown in figure B.1. A cross-section of a single unit cell is shown in figure 1.7b. As with the variable pocket restriction concept, the supply and vacuum pressure are fixed. The flow in the bearing film is controlled by controlling the eccentricity ε. The dam is moved in positive x-direction with respect to the pocket, which is assumed to be fixed. This narrows the outlet film on the left side of the inlet and widens the outlet film on the right side of the inlet. Therefore, the magnitude of the pressure gradient on the right side of the inlet will be larger than on the left side.

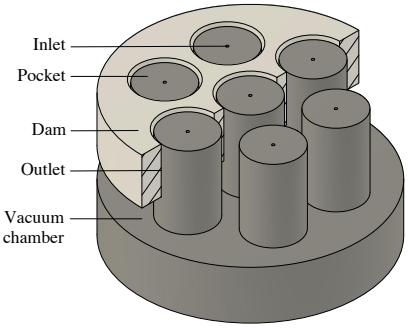

(a) Schematic representation of variable outlet restriction concept.

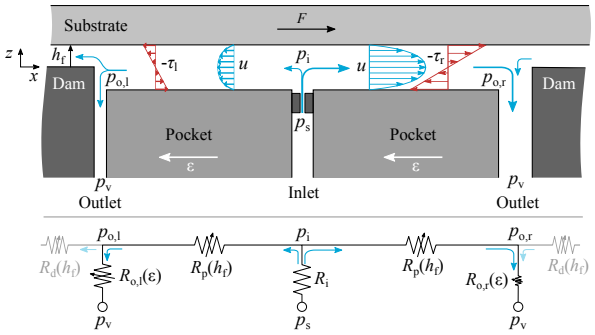

(b) Cross section of unit cell.

Figure 1.7: Variable outlet restriction concept.

Demonstrator

The demonstrator as developed by Verbruggen [6] is shown in figure 1.8. Figure 1.8a shows the in its assembled state, while figure 1.8b shows the system with the top plate removed. The three wire flexures on which the top plate is suspended can be seen. Air is supplied to a central supply chamber through the black pneumatic hose. Air then enters the bearing film through the centre of each pin. The air is evacuated through the blue pneumatic hose, which is connected to the cavity created between the two plates. This cavity effectively acts as a central vacuum chamber to which all outlet restrictions flow. The demonstrator was developed using conventional subtractive machining techniques.

During the research of Verbruggen, no control or actuator system has been developed. Therefore, no experimental data can be presented with regards to the positioning accuracy or the bandwidth. Using manual actuation (i.e. rotating the top plate by hand), an angular acceleration of $7.4\,\mathrm{rad/s^2}$ was measured. An angular deceleration of $14.7\,\mathrm{rad/s^2}$ was measured. This difference could be due to the Couette flow, which is the flow due to relative motion of the bodies.

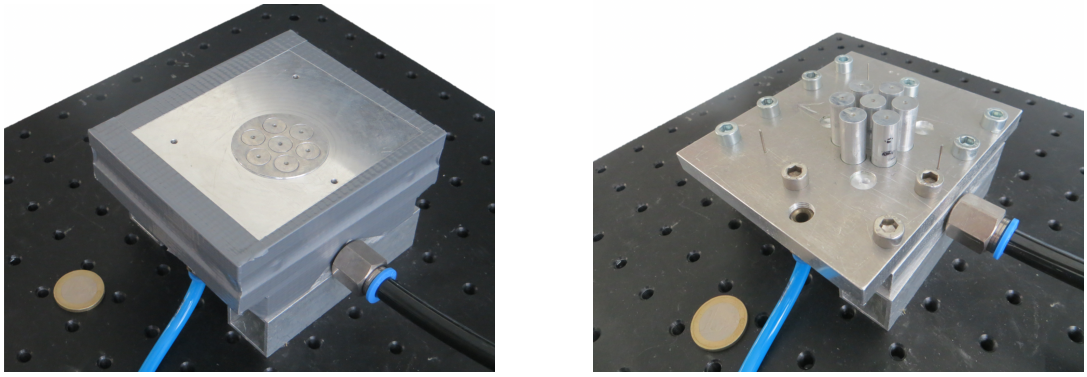

(a) Assembled. (b) Disassembled.

Figure 1.8: Demonstrator as developed by Verbruggen.

The demonstrator developed by Verbruggen consists of seven pins, i.e. seven unit cells. For an increasing number of pins, the system becomes increasingly more difficult to manufacture. This is due to the fact that the radial outlet film thickness is determined by the diameter of the pin, the diameter of the hole, the location of the pin with respect to the hole and the orientation of the pin with respect to the hole.

1.3 Problem statement

Air bearing systems are known for their tight manufacturing tolerances, and these contactless handling systems are no exception. Therefore, they are in general expensive and thus not applicable on a large scale.

The variable outlet restriction concept consists, in the essence, only of two mating parts. To a large extent, the behaviour of the system is defined by the clearance between these parts. Therefore, this clearance has to be very well defined, ideally with sub μm accuracy. Using the current manufacturing method developed by Verbruggen becomes infeasible for systems with more pins. Therefore, a new manufacturing method needs to be developed.

1.4 Research objective

- Designing a new manufacturing method in order to create a contactless handling system using a variable outlet restriction.
- Developing a (numerical) model that can be used to predict the behaviour of the contactless handling system.
- Manufacturing a demonstrator that verifies the feasibility of the developed manufacturing method and can be used to validate the theoretical performance.
- Verifying the performance of the demonstrator through physical experiments.

1.5 Reader's guide

The paper, presented in section 1.5 can be seen as an extended abstract, where a very condensed summary of the full research can be found. From the paper, references are made to various appendixes of the report. Here, more detailed and additional information is presented. The structure of the report is similar to that of the paper: the conceptual design is presented in appendix B. The theory that describes the behaviour of these systems is explained in appendix A, derivations are shown in appendix F. Dimensioning of the demonstrator is done using a numerical model, presented in appendix C. The actual manufacturing of the demonstrator is presented in appendix D. Finally, the conclusions and recommendations are presented in appendix E.

Development of a novel manufacturing method for a contactless handling system using a variable outlet restriction

Kees Pijnenburg, Ir. Jelle Snieder, Dr. ir. Ron van Ostayen

April 19th, 2022

Abstract

By using "improved handling methods", the manufacturing cost of solar cells and flat panel display could be decreased. A potential handling method would be to use a contactless handling system based on air bearing technology, where the substrate levitates on a thin film of air. The viscous shear force of the air flow is used to exert a lateral force on the substrate. There are several concepts that can be used to control the magnitude and direction of this lateral force.

In this research, the variable outlet restriction concept is used. The outlet restriction is created by the radial clearance ($\sim 50\,\mu$m) which is formed between a pin in a slightly oversized hole. A novel manufacturing method is developed, where resin casting. This ensures that the fit between the mating parts is guaranteed, regardless of the manufacturing process.

1 Introduction

Solar cells, flat panel displays and silicon wafers are all examples of parts that are thin, fragile and costly. By increasing the size and decreasing the thickness, their cost can be reduced [1, 2]. However, in order to ensure that the manufacturing yield does not decrease, improved handling methods are required [3].

A potential new handling method is contactless handling based on air bearing technology, hereafter referred to as contactless handling. As the name implies, this technology enables the *handling* (i.e. transportation and positioning) of a flat and thin substrate in a *contactless* manner. A thin layer of air ($\sim 10\,\mu$m) is used both to levitate the substrate, as well as to generate a lateral shear force acting on the surface of the substrate. Other physical principles could also be used to achieve contactless handling. An overview is presented in [4, 5].

Contactless handling has multiple advantages over conventional handling methods. First, since there is no physical contact, there is no wear, hence no particle generation. Second, the distributed load allows for the use of thinner substrates without decreasing the product yield. Third, as a result of the fact that the substrate can be carried directly by the air film, a carrier stage is not needed. This reduces the accelerated mass by several orders of magnitude, which in turn leads to lower actuation forces, lower distortion and thus a higher positioning accuracy. Contactless handling using a viscous air film is versatile because of the fact that it does not depend on (electromagnetic) properties of the substrate material.

1.1 State of the art

A schematic representation of a $\varnothing 100\,$mm substrate on a contactless handling system is shown in fig. 1. The substrate is levitating above the bearing surface surface through which a gas (e.g. air) is supplied and evacuated at multiple locations. Most often, a grid of identical unit cells can be identified, where each unit cell has its own supply and evacuation line, referred to as inlet and outlet. The vertical distance between the substrate and the bearing surface is smallest above the dam. The film thickness here is called the fly-height h_f and is typically in the order of $10\,\mu$m. The surface of the pocket is slightly recessed below that of the dam. This distance is referred to as the pocket height h_p, which is also typically in the order of $10\,\mu$m.

In many ways, such a contactless handling system is similar to a vacuum preloaded aerostatic bearing: if properly designed, a substrate will levitate above the bearing surface on a thin film of air, referred to as the *bearing film*. However, in contactless handling, the viscous shear force result-

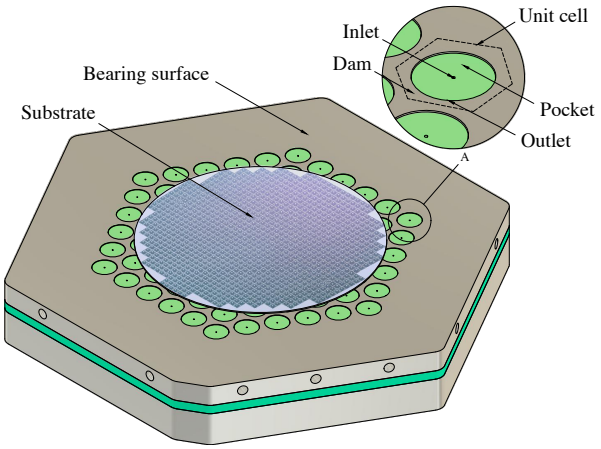

Figure 1: Schematic representation of a contactless handling system.

ing from the flow in the bearing film is used exert a lateral force on the substrate. The lateral forces that can be generated using this method are inherently low (10-100 $\mathrm{N/m^2}$). Though, since the substrates for which these systems are intended have a low distributed weight (20-50 $\mathrm{N/m^2}$), significant accelerations can still be achieved.

In order to control the position of the substrate, the direction and magnitude of the shear force, i.e. the flow, should be controlled over time. The behaviour of the flow is dictated by the geometry of the flow path and the supply and vacuum pressure. If the pressure distribution is symmetric within the unit cell, the shear force is equal and opposite, and thus no net shear force is generated. In general, this is the case in a regular aerostatic bearing, which explains why they are virtually frictionless. In order to generate a net force, an asymmetrical pressure distribution should be created within the unit cell.

We can state that the essence of contactless handling is to be able to control the pressure distribution in the bearing film over time. This can be achieved by either directly controlling the supply and vacuum pressure, or by controlling the geometry of the flow path. Both principles could also be used concurrently. Several demonstrators, using either of these principles, have been developed over the past [4, 5, 6]. These will be discussed in more detail below. First, the lumped restriction model is introduced because it can be used to gain intuitive insight into the qualitative behaviour of contactless handling systems.

1.1.1 Lumped restriction model

A flow restriction can be envisioned as an electrical resistance: like a voltage difference across a resistance will lead to a flow of electrons (i.e. current), a pressure difference across restriction will lead to a flow of air. A restriction in this case is a narrow channel or a thin film.

Using a lumped restriction model, a continuous geometry (i.e. the spatially distributed restriction) can be modelled as a discrete number of restrictions. In general, an inlet, pocket and outlet restriction can be identified.

Note on the figures

Figure 2, fig. 3 and fig. 4 each show a schematic cross-section of a single unit cell, which is part of an infinite grid of identical unit cells. The figures are not to scale: the typical width of a unit cell in x-direction is 10 mm, while the typical fly-height h_f is 10 μm. The the lumped restriction model is shown below the geometry in each figure.

Relevant symbols are indicated in table 1. In all figures, the negative shear stress profile (-τ) is shown, in order to make the figures more intuitive. Each figure shows a different method for generating shear force. In all cases, a net shear force in positive x-direction is exerted on the substrate.

Table 1: Nomenclature for concept comparison.

	Description		Description
R_i	Inlet restriction	p_s	Supply pressure
R_p	Pocket restriction	p_i	Inlet pressure
R_o	Outlet restriction	p_o	Outlet pressure
R_d	Dam restriction	p_v	Vacuum pressure
u	Velocity profile	τ	Shear stress

1.1.2 Pressure control

In this concept, developed by Wesselingh [4] the flow within the pocket is controlled by directly controlling the supply and vacuum pressure. The geometry of the unit cell is fixed, as shown in fig. 2. This means that the direction of the force F is fixed and only the magnitude can be controlled by varying the supply pressure p_s and or the vacuum pressure p_v. In order to achieve actuation in both directions, pairs of unit cells with alternating orientation should be used.

A demonstrator has been developed by Wesselingh, using square cells of $10 \times 10\,\mathrm{mm^2}$, arranged in a grid of 6 by 6. The servo error of this system was $6\,\mathrm{nm}\,(1\sigma)$ in all planar Degrees Of Freedom (DOFs). Acceleration of $600\,\mathrm{mm/s^2}$ has been achieved using a silicon wafer with a thickness of 525 μm. This gives an effective force density of $0.73\,\mathrm{N/m^2}$.

The downside of this concept is that the flow is controlled by valves, which are located far from the bearing surface. The air then has to travel to each inlet and outlet through a complex manifold. Since air is compressible, this introduces a delay in the system. Even for this relatively small demonstrator with an actuator area of $60 \times 60\,\mathrm{mm^2}$, the bandwidth of the system was limited to around 50 Hz. The performance and manufacturability will only decrease further if the size of the system is increased.

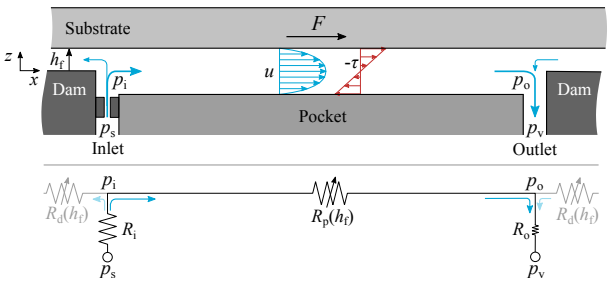

Figure 2: Schematic cross-section of a unit cell using pressure control concept.

1.1.3 Variable pocket restriction

In this concept, developed by Vuong [5], the bearing surface is comprised of separate segments. A net shear force can be generated by tilting the segments, which changes the magnitude of the pocket restriction $R_\mathrm{p}(\alpha)$ left and right.

The variable geometry is schematically shown in fig. 3, where the varying tilting angle is indicated by α.

The demonstrator developed by Vuong was comprised of 61 hexagonal segments that were joined by a leaf spring. The maximum tilt angle was 6 mrad. Using the actuators developed by Jansen [7] and the control system developed by Krijnen [8], an acceleration of $1170\,\mathrm{mm/s^2}$ was achieved using a silicon substrate with a thickness of $750\,\mu\mathrm{m}$. This gives an effective force density of $2.04\,\mathrm{N/m^2}$. The lowest achieved positioning error was $104\,\mathrm{nm}\,(2\sigma)$. For this concept, the bandwidth is no longer limited by the presence of the manifold. A change in tilt angle leads to an instant change of the shear force, at least up to theoretical bandwidth of 1000 Hz. A bandwidth of 300 Hz has been achieved in the experimental set-up [9].

Again, the downside of this concept is in the manufacturing. Each segment is comprised of many parts, which makes the assembly very cumbersome and expensive. Also, this causes the system to degrade over time.

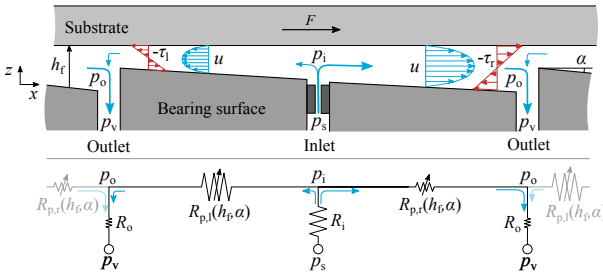

Figure 3: Schematic cross-section of a unit cell using the variable pocket restriction concept.

1.1.4 Variable outlet restriction

Lastly, the flow in the bearing film can be controlled by varying the film thickness in the outlet, i.e. the outlet restriction $R_\mathrm{o}(\varepsilon)$. The variable geometry is shown in fig. 4, where the normalised eccentricity is defined by ε. Since the film thickness is smaller on the left side, the outlet pressure on the left side $p_\mathrm{o,l}$ will be higher than the outlet pressure on the right side $p_\mathrm{o,r}$. The pressure in the bearing film can thus be controlled by controlling the eccentricity of the pocket.

A demonstrator with seven actuator pins was developed by Verbruggen [6], essentially as shown in fig. 7. Each outlet restriction was formed by the radial clearance between a pin ($\varnothing 10.000\,\mathrm{mm}$) and a hole ($\varnothing 10.100\,\mathrm{mm}$). The concentric outlet film thickness is influenced by the size of the pin, the size of the hole, and the relative position of each pin with respect to each hole. No measurements regarding the bandwidth or positioning accuracy were performed.

The demonstrator was manufactured using conventional subtractive manufacturing techniques, i.e. machining. For an increasing number of pins, it becomes increasingly difficult to meet the manufacturing tolerances using conventional subtractive techniques.

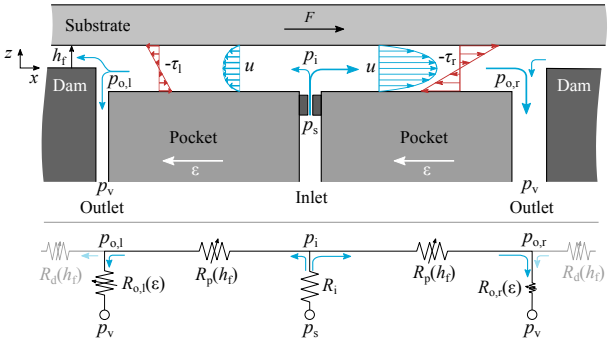

Figure 4: Schematic cross-section of a unit cell using the variable outlet restriction concept

1.2 Concept comparison

The theoretical performance of the different concept can be compared by evaluating their performance ratio P. This is a metric that has been introduced by Vuong, which is defined as [5]:

$$P = \frac{\bar{F}}{\bar{\dot{m}}} \qquad \left[\frac{\mathrm{N/m^2}}{(\mathrm{kg/s})/\mathrm{m^2}}\right] = \left[\frac{\mathrm{m}}{\mathrm{s}}\right] \tag{1}$$

By evaluating the performance ratio for a varying actuator length, the performance curves as shown in fig. 5 are generated. The procedure is described in appendix A.5. The actuator length L decreases along each curve in positive $\bar{\dot{m}}$ direction. The performance of the variable pocket restriction and the variable outlet restriction are virtually identical. Similar results were found by Verbruggen [6].

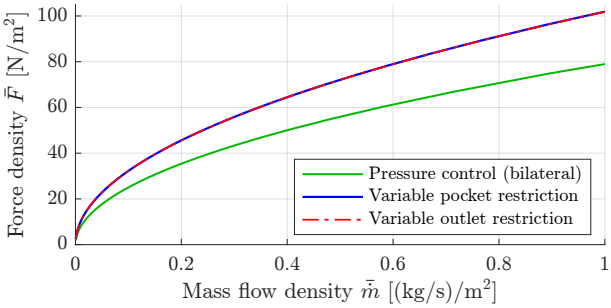

Figure 5: Performance comparison.

1.3 Problem statement

The existing contactless handling systems have shown promising results in the lab, thereby confirming the potential of this technology. The main reason that such systems are not used in the industry yet is the fact that manufacturing them is complicated and thus expensive. This is mainly due to very tight manufacturing tolerances.

1.4 Research objective

The aim of this research is to develop a contactless handling system that can be more easily manufactured than previously developed concepts. A redundancy for manufacturing errors should be created, such that very tight tolerances are no longer required.

The variable pocket restriction and variable outlet restriction have an identical theoretical performance, as shown in fig. 5. A potential improvement in terms of manufacturability is identified for the variable outlet restriction concept, since it essentially consists out of only two mating parts.

1.5 Reader's guide

This paper can be seen as an extended summary of the report. Throughout the paper, references will be made to the appendices, where additional and more extensive information is presented.

In this paper, the conceptual design and numerical model are presented in section 2. The manufacturing procedure is explained in section 3. The results are shown in section 4. Finally, the discussion and conclusion are shown in sections 5 and 6 respectively.

2 Design & modelling

The behaviour of any contactless handling system is to a large extent determined the geometry of the flow path. In general, an inlet, pocket and outlet restriction can be identified within this flow path. In case of the variable outlet restriction concept, the outlet restriction is formed by the clearance between a hole and a pin, as indicated in fig. 6b. The pocket restriction is formed by the thin film between the pocket surface and the substrate, which is not shown in this figure. The inlet restriction is created by a narrow channel in the centre of the pin.

Since the manufacturability of the system has a high priority, the conceptual manufacturing procedure is introduced first, in section 2.1. Here, an ideal case is presented where resin behaviour and manufacturing errors are not considered. However, these will be discussed in section 3.

2.1 Conceptual design

The proposed manufacturing method uses resin casting in order to create a system as shown in fig. 7. Casting methods have been used before to produce counter surfaces for aerostatic bearings [10, 11]. However, it has not been used in the proposed configuration, which requires extremely high dimensional accuracy and stability on the cast parts.

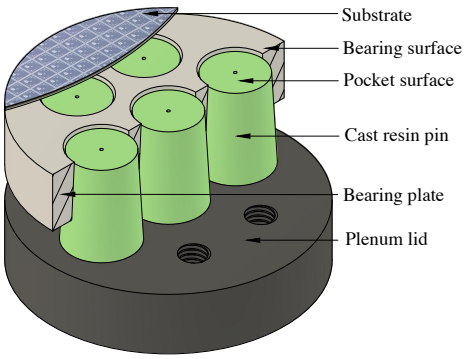

Figure 7: Schematic representation of proposed system.

The pins are created by means of resin casting in a two-part mould, formed by the plenum lid and bearing plate, as shown in fig. 6a. After curing, the two parts will be separated. The pins will be fixed to the plenum lid, as shown in fig. 6b. Since the geometry of the pin will be the exact negative the hole, the fit between the two parts is guaranteed. Next to that, the location of each pins on the plenum lid with respect to the bearing plate will only be determined by the geometry of the bearing plate itself. The tolerance on the position of the holes thus becomes obsolete.

There are two reasons why the holes are tapered. First, the taper helps to release the pins after curing. Second, by enforcing a distance t_v between the two plates after the resin has cured, a thin radial film is created as:

$$h_{o,c} = t_v \tan\delta \cos\delta \approx t_v \, \delta \tag{2}$$

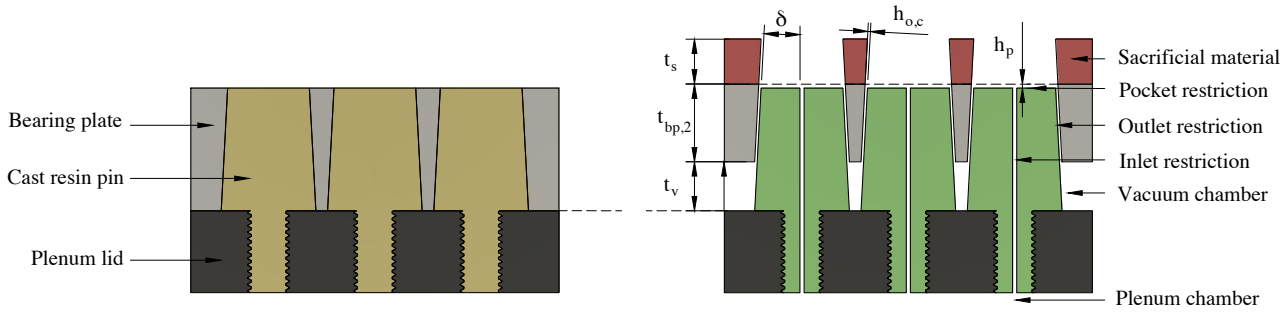

(a) System during casting

(b) System after curing and separating.

Figure 6: Cross section of the system shown in fig. 7.

The cavity that is created between the plates will serve as the vacuum chamber to which all outlet restrictions flow. High pressure air is supplied through the inlet restrictions, which are fed from a central plenum chamber, located below the pins.

In order to create the required pocket height h_p, the sacrificial material t_s is removed from the bearing plate after casting. The height of the pocket is defined as:

$$h_\mathrm{p} = t_\mathrm{v} - t_\mathrm{s} \tag{3}$$

This means that both the thickness of the sacrificial material, as well as the distance enforced between the two plates needs to be controlled with high accuracy.

2.2 Modelling

A numerical model was made in COMSOL, using the *General Form Boundary PDE* physics [12]. The model is used as a tool to find a suitable set of design parameters for the demonstrator. More information regarding the modelling method is presented in appendix C.

2.2.1 Governing equations

The behaviour of a fluid in a thin film is described by the simplified compressible Reynolds equation [13]:

$$\nabla \left(\frac{p h^3}{12 \eta R_\mathrm{s} T} \nabla p \right) = 0 \tag{4}$$

Where p is the pressure, h is the local film thickness, η is the dynamic viscosity of the fluid, R_s is the specific gas constant and T the temperature.

The Reynolds equation is used to model both the flow in the bearing film, as well as the flow in the radial outlet film. Only the flow due to a pressure gradient (i.e. Poiseuille flow) is considered. The flow due to relative motion of the substrate (i.e. Couette flow) is neglected. Since the film height is much smaller than the film length, the pressure is assumed constant across the film height (i.e. perpendicular to the surface). A no-slip condition is assumed at all interface surfaces.

2.2.2 Shear force

A net shear force can be generated by establishing an asymmetric pressure distribution in the bearing film. The force density in x-direction $\bar{F}_x$ is found by integrating the shear stress over the total area (eq. 5a). If the gas is assumed to be a Newtonian fluid, the shear stress is directly proportional to the velocity gradient (eq. 5b). The shear force is then found by evaluating the velocity profile at the surface of the substrate, i.e. $z = h$ (eq. 5c).

$$\bar{F}_x = \frac{1}{A} \int_A -\tau_x \, dA \tag{5a}$$

$$= \frac{1}{A} \int_A -\eta \frac{\partial u}{\partial z} \, dA \tag{5b}$$

$$= \frac{1}{A} \int_A -\frac{h}{2} \frac{\partial p}{\partial x} \, dA \tag{5c}$$

Note that the shear force is dependent on the film thickness and the pressure gradient, however these are not independent. An increase in film thickness will drastically decrease the pressure gradient. Minimising the film thickness (i.e. fly-height) is therefore desired.

2.2.3 Stiffness

When in operation, the substrate should levitate at a fixed fly-height. In order for the system to be stable, it should be able to restore this fly-height in case of a disturbance. Note that in a physical system, disturbances will always be present. Stiffness is achieved if the load capacity of the system is dependent on the fly-height.

The load capacity of a system is defined as the integral of all pressures over the area of the substrate A. For a system with a fixed geometry, the pressure distribution in the bearing film $p(x,y)$ is dependent on three operating conditions: the supply pressure p_s, vacuum pressure p_v, and the fly-height h_f. The load-capacity is thus defined as:

$$W = \int_A \Big(p(p_\mathrm{s}, p_\mathrm{v}, h_\mathrm{f}) - p_\mathrm{a} - p_\mathrm{sub} \Big) \, dA \tag{6}$$

Where p_a is the ambient pressure and p_sub is the distributed weight of the substrate. Assuming quasi-static behaviour, levitation is achieved if $W = 0$. This is referred to as the no-load condition.

If the load capacity increases upon a decreasing fly-height and vice versa, a positive stiffness is achieved. This can be written as:

$$k = -\frac{\partial W}{\partial h_\mathrm{f}} > 0 \tag{7}$$

A commonly used method to generate a positive stiffness in the bearing film is through the use of an inlet restriction. This could be a capillary tube, an orifice, or a porous restriction [14]. In this research, capillary tubes are used, since they can be easily integrated in the casting procedure. An inlet restriction introduces positive stiffness, while an outlet restriction introduces negative stiffness. This is explained in more detail in appendix A.3.3. For the system developed in this research, a variable outlet restriction is used to control the flow direction. As a result, the stiffness of the bearing is reduced.

Manual perturbation

From the stationary solution, a perturbation of the fly-height δh_f can be manually prescribed. Since the supply and vacuum pressure are fixed, perturbing the fly-height (i.e. altering the bearing film geometry) will lead to a different pressure distribution and thus a different load capacity. The stationary stiffness k_s (for low frequencies) can be approximated by:

$$k_\mathrm{s} = -\frac{\Delta W}{\Delta h_\mathrm{f}} = -\frac{W|_{h=h_{\mathrm{f},0}+\delta h_\mathrm{f}} - W|_{h=h_{\mathrm{f},0}-\delta h_\mathrm{f}}}{2\,\delta h_\mathrm{f}} \tag{8}$$

Where $W|_{h=h_{\mathrm{f},0}}$ is the load capacity at the fly-height for which the no-load condition is satisfied (i.e. $W=0$). The perturbation amplitude is defined as $\delta h_\mathrm{f} = 0.01 \cdot h_\mathrm{f}$.

Perturbed Reynolds equation

For the perturbation method, the stationary film thickness h_0 is replaced by a dynamic film thickness (eq. 9a). Solving the Reynolds equation for this dynamic fly-height will lead to a dynamic pressure distribution (eq. 9b).

$$h(t) = h_0 + \delta h(t), \qquad \delta h = \tilde{h} e^{i\omega t} \tag{9a}$$

$$p(t) = p_0 + \delta p(t), \qquad \delta p = \tilde{p} e^{i\omega t} \tag{9b}$$

Here, h_0 and p_0 represent the stationary solution, $\tilde{h}$ represent the amplitude of the fly-height perturbation and $\tilde{p}(x,y,z)$ represents the perturbed pressure distribution. Substituting eq. (9a) and (9b) in eq. (4) gives the perturbed Reynolds equation as [15]:

$$\begin{aligned}\nabla\left(p_0 h_0^3 \nabla\tilde{p} + 3p_0 h_0^2 \tilde{h}\nabla p_0 + \tilde{p} h_0^3 \nabla p_0\right) = \\ 12\eta i\omega\left(p_0\tilde{h} + \tilde{p}h_0\right)\end{aligned} \tag{10}$$

Where ω represents the perturbation frequency. In order to observe the influence of the perturbation only, the stationary solution (eq. 4) is subtracted. A derivation can be found in appendix F.4. The dynamic stiffness is then defined as:

$$\begin{aligned}k = -\frac{\partial W}{\partial h} \approx -\frac{W_0 - W(t)}{h_0 - h(t)} = -\frac{\int \delta p\, dA}{\delta h} \\ = -\frac{\int_A \mathrm{Re}(\tilde{p})\, dA}{\tilde{h}}\end{aligned} \tag{11}$$

And the damping is defined as:

$$\begin{aligned}c = -\frac{\partial W}{\partial \dot{h}} \approx -\frac{W_0 - W(t)}{\dot{h}_0 - \dot{h}(t)} = -\frac{\int \delta p\, dA}{\delta \dot{h}} \\ = -\frac{\int_A \mathrm{Im}(\tilde{p})\, dA}{\omega\tilde{h}}\end{aligned} \tag{12}$$

2.2.4 Geometry

The final prototype consists of 91 unit cells in hexagonal close packing, as shown in fig. 1. For simplicity, only one unit cell is modelled. The geometry of this unit cell is shown in fig. 8. The dashed line indicates the cross-section shown in fig. 9. The nominal values for the design parameters are shown in table 2. The taper angle δ is equal to $1/100$ rad. Note that the figure is not to scale, and the film thickness has been exaggerated for clarity.

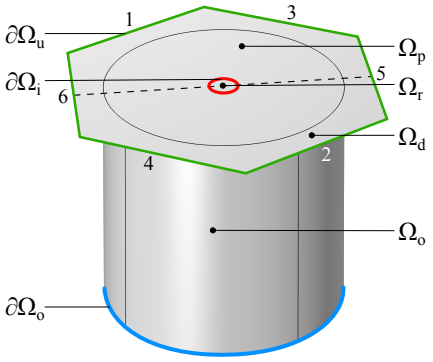

Figure 8: Unit cell geometry as used in COMSOL.

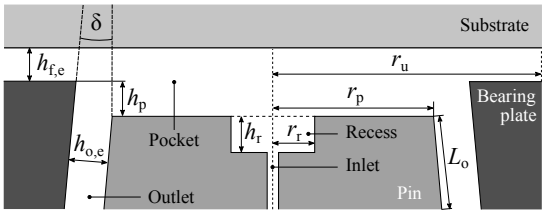

Figure 9: Schematic cross-section of unit cell for $\varepsilon = 0$.

The substrate is not modelled as a separate body, but is implemented through the definition of the film thickness of the top surfaces as shown in table 3. The eccentric outlet film thickness is defined as:

$$h_{\mathrm{o,e}}(\varepsilon) = h_{\mathrm{o,c}}\left(1 + \varepsilon\cos\varphi\right) \tag{13}$$

Where ε is the normalised eccentricity, which varies between -1 and 1. The concentric outlet film thickness $h_{\mathrm{o,c}}$ has a sinusoidal profile, where φ indicates the local angle in the x,y plane. By definition $h_{\mathrm{o,c}} = h_{\mathrm{o,e}}|_{(\varepsilon=0)}$.

Table 2: Nominal values for design parameters.

Symbol	Value [mm]	Symbol	Value [μm]
r_r	0.6	h_r	200
r_p	5	h_p	20
r_u	6.25	$h_{\mathrm{f,c}}$	15
L_o	10	$h_{\mathrm{o,c}}$	50

Table 3: Film thicknesses for stationary study.

Boundary	Section	Expression for h	Value [μm]
Ω_d	Dam	$h_\mathrm{f,e}$	15
Ω_p	Pocket	$h_\mathrm{f,e} + h_\mathrm{p}$	35
Ω_r	Recess	$h_\mathrm{f,e} + h_\mathrm{p} + h_\mathrm{r}$	235
Ω_o	Outlet	$h_\mathrm{o,e}$	50

2.3 Expected behaviour

The concentric fly-height $h_\mathrm{f,c}$ and the vacuum pressure p_v are prescribed by the user. The supply pressure p_s for which the no-load condition is satisfied is found using a *Global Equation* in the concentric state.

In the eccentric state, the outlet film thickness will vary locally, while the supply and vacuum pressure remain fixed. Therefore, it is expected that the no-load condition will be satisfied for a different fly-height. This will be referred to as the eccentric fly-height $h_\mathrm{f,e}$. By definition: $h_\mathrm{f,c} = h_\mathrm{f,e}|_{\varepsilon=0}$.

The total magnitude of the outlet restriction decreases in the eccentric state. Since an outlet restriction introduces negative stiffness, it is expected that the total stiffness will increase with the eccentricity.

2.3.1 Stationary boundary conditions

On the inlet edge a flux is defined as:

$$g = G_\mathrm{i}\,(p_\mathrm{s}^2 - p_\mathrm{i}^2)\,\frac{1}{2\pi r_\mathrm{r}} \qquad \text{on } \partial\Omega_\mathrm{i} \tag{14}$$

Where G_i is the inlet conductivity of the capillary restriction, which is assumed to be independent of the flow through the capillary. In reality, the inlet conductivity is dependent on the flow: the higher the flow through the restriction, the lower the conductivity.

This behaviour could be more accurately modelled, using a Fanno flow model [16], or by implementing the empirical data. In this model, the inlet conductivity was set to $1 \cdot 10^{-15}\,[\mathrm{m^2\,s^3/kg}]$, which is the restriction value that was experimentally found for a pressure drop of 1 bar across the restriction ($\Delta p = p_\mathrm{s} - p_\mathrm{i}$). This is explained in appendix D.2.1.

On the unit cell edge a periodic continuity is defined. Since the cell is assumed to be part of an infinite grid of unit cells, no net flux should pass the unit cell boundary. In other words, everything that leaves on one side should enter at the opposing side and vice versa. This can be written as:

$$\begin{array}{ccc} p_1 = p_2 & p_3 = p_4 & p_5 = p_6 \\ \nabla p_1 = -\nabla p_2 & \nabla p_4 = -\nabla p_3 & \nabla p_6 = -\nabla p_5 \end{array} \quad \text{on } \partial\Omega_\mathrm{u} \tag{15}$$

Where the subscripts refer to the sides of the hexagon, as indicated in fig. 8. In reality, the cells in the centre of the grid will have slightly different boundary condition compared to those on the outside.

On the outlet edge a pressure is prescribed using a Dirichlet boundary condition as:

$$p = p_\mathrm{v} \qquad \text{on } \partial\Omega_\mathrm{o} \tag{16}$$

The outlet restriction flows into the vacuum chamber, of which the flow restriction is negligible compared to that of the outlet restriction. Hence, a constant vacuum pressure can be assumed. The vacuum pressure p_v was set to 0.7 bar gauge, i.e. 0.3 bar below the ambient pressure p_a of 1 bar.

2.3.2 Perturbed boundary conditions

The perturbation of the fly-height only influences film thickness of the top boundaries. Expressions for the perturbed film thickness $\tilde{h}$ are shown in table 4.

Since the stationary solution is subtracted from the perturbed solution, the stationary boundary conditions are subtracted from the perturbed boundary conditions as well. The perturbed inlet flux can thus be defined as:

$$g = \left(-2\,G_\mathrm{i}\,p_0\tilde{p} - \frac{V_\mathrm{r}\tilde{p}i\omega}{R_\mathrm{s}T}\right)\frac{1}{2\pi r_\mathrm{r}} \qquad \text{on } \partial\Omega_\mathrm{i} \tag{17}$$

Where V_r represents the volume of the recess ($\pi r_\mathrm{r}^2 h_\mathrm{r}$). The derivation of this expression is shown in appendix C.3.3.

On the unit cell edge, the boundary condition is essentially identical, except now applied to the perturbed pressure $\tilde{p}$ as:

$$\begin{array}{ccc} \tilde{p}_1 = \tilde{p}_2 & \tilde{p}_3 = \tilde{p}_4 & \tilde{p}_5 = \tilde{p}_6 \\ \nabla\tilde{p}_1 = -\nabla\tilde{p}_2 & \nabla\tilde{p}_4 = -\nabla\tilde{p}_3 & \nabla\tilde{p}_6 = -\nabla\tilde{p}_5 \end{array} \quad \text{on } \partial\Omega_\mathrm{u} \tag{18}$$

For the outlet, the perturbed pressure on the outlet is defined as:

$$\tilde{p} = 0 \qquad \text{on } \partial\Omega_\mathrm{o} \tag{19}$$

Table 4: Film thicknesses for perturbation study.

Boundary	Section	Expression for $\tilde{h}$
Ω_d	Dam	$0.01 \cdot h_\mathrm{f,e}$
Ω_p	Pocket	$0.01 \cdot h_\mathrm{f,e}$
Ω_r	Recess	$0.01 \cdot h_\mathrm{f,e}$
Ω_o	Outlet	0

3 Manufacturing

3.1 Proposed manufacturing process

The manufacturing method used to manufacture the demonstrator is explained in this section. For more detailed information, the reader is referred to appendix D. Photos of the actual manufacturing process are shown in appendix G.4.

The finished system is shown in fig. 10. Air flows into the plenum chamber through the inlet. From there the air

flows through the dispensing needles into the pockets. The bearing surface would normally be covered by the substrate, which is not shown in the figure. The vacuum chamber is created by the cavity between the bearing plate and the plenum lid. The air is evacuated from the vacuum chamber through three outlets, spaced 120° apart. In order to allow for relative movement of the bearing plate with respect to the pins, the bearing plate is supported on 216 ball bearings placed in between the pins.

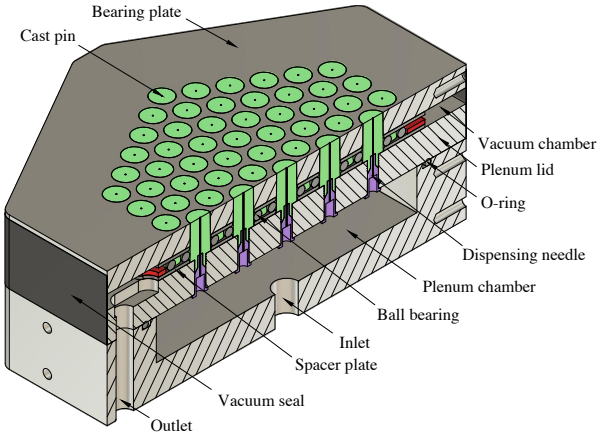

Figure 10: Cross section of the full system.

3.1.1 Machining

The manufacturing process starts by machining the bearing plate ($t_{bp,0} = 20\,\text{mm}$) and plenum lid ($t_{pl,0} = 15\,\text{mm}$). Both were machined from aluminium 7075-T6 on a DMG Mori Milltap 700. The tapered holes in the bearing plate were made using a machine pin reamer[1] with a conicity (i.e. included angle) of 1:50 (i.e. $\delta = 1/100\,\text{rad}$). In order to reduce the waviness of the surface, each hole was post-reamed using a hand pin reamer[2] with the same conicity.

3.1.2 Casting

A cross-section of the system in the casting set-up is shown in fig. 11. Before casting, both the plenum lid and the bearing plate are thoroughly cleaned using isopropyl alcohol. In order to ensure that the resin will only adhere to the plenum lid, the surface of the bearing plate is covered in a very thin layer of vaseline[3]. The needle hubs are pressed into the holes of the plenum lid, thereby sealing them from the bottom. By clamping the bearing plate and plenum lid together, a two-part mould is created. During casting and curing, temperature of the mould is maintained at $T_c = 38°\text{C}$.

[1] Dormer Pramet D9538.0
[2] Dormer Pramet D9038.0
[3] Kroon White Vaseline

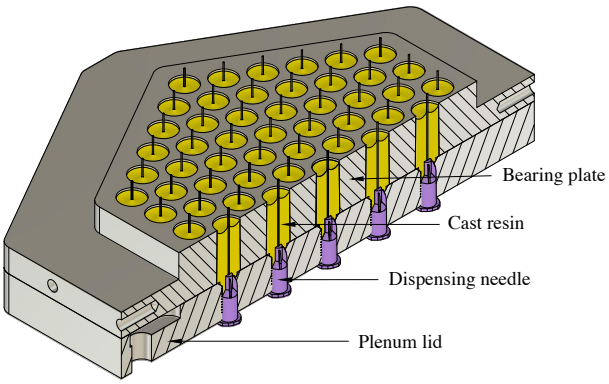

Figure 11: System during casting.

3.1.3 Post-processing

After curing, the first sacrificial layer ($t_{s,1} = 3.5\,\text{mm}$) is removed using a face mill. This is indicated in orange and red in fig. 12. After this step, the situation is essentially as shown fig. 6a.

The two parts can then be separated using a press brake and a 3D printed adapter. Since the pins have a higher Coefficient of Thermal Expansion (CTE) than the bearing plate, cooling the system will cause the pins to shrink more than the bearing plate. Therefore, the system is cooled to $-10°\text{C}$ before separating, in order to ease the separation step.

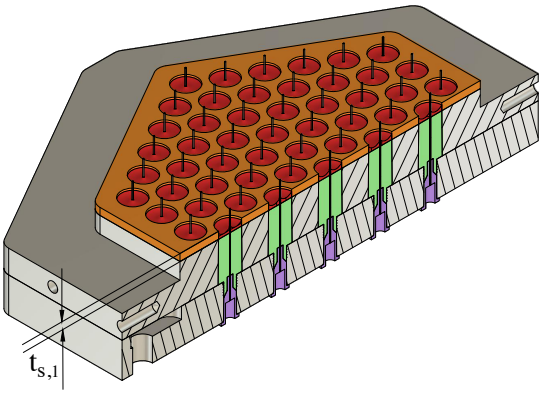

Figure 12: First sacrificial layer indicated.

After separating the parts, the bearing plate is machined to final size, by removing the second layer sacrificial material from the top of the bearing plate ($t_{s,2} = 7.3\,\text{mm}$). This is indicated in orange in fig. 13. The final thickness of the bearing plate $t_{bp,2}$ is 9.2 mm. This is effectively also the length L of the outlet restriction film.

$$t_{bp,2} = t_{bp,0} - t_{s,1} - t_{s,2} \tag{20}$$

In order to increase the nominal outlet film thickness and in order to improve the contact (steel on steel), two spacer plates (S235 steel, lasercut, $t_{sp} = 1.5\,\text{mm}$) have been placed

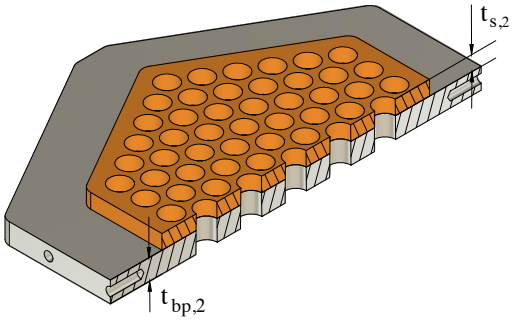

Figure 13: Bearing plate before second post-casting machining operation.

between the plates as shown in fig. 14. The final height of the vacuum chamber t_v can thus be defined as:

$$t_v = 2 \cdot t_{sp} + d_b \tag{21}$$

If the system is assembled using undersized balls ($d_{b-} = 3.974\,\text{mm}$), the pins are slightly protruding from the surface. The whole assembly is then abraded on a flat granite reference surface until the pin surfaces are flush with the top surface of the bearing plate. The system is then assembled using the slightly larger balls ($d_{b+} = 3.993\,\text{mm}$). The pocket height h_p will then be equal to the difference in ball diameter $\Delta d = 19\,\mu\text{m}$.

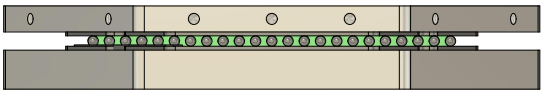

Figure 14: Side view of the system with spacer plates.

3.2 Inlet restriction

A capillary inlet restriction is created by using dispensing needles[4]. They are affordable, yet have a very well defined diameter and thus a predictable restriction value. Next to that, they are very suited to be implemented in the casting process, in contrast to orifice or porous restrictions.

The needles were aligned in the centre of the tapered holes using 3D printed adapters. The misalignment from the centre using this method was verified using a digital microscope[5] to be $73 \pm 30\,\mu\text{m}$. More information regarding the inlet restriction can be found in appendix D.2.

3.3 Outlet restriction

In this research, the main mechanism used to create a thin outlet film is conical spacing as shown in eq. (2). Despite the fact that the current manufacturing method should be relatively insensitive for manufacturing errors, there are still various factors that influence the final geometry of the system. The main factors are:

I. Mould geometry (appendix D.3)
   - ○ Deviation from perpendicularity
   - ○ Surface waviness
   - ○ Mould release agent layer thickness

II. Resin behaviour (appendix D.4)
   - ○ Thermal expansion
   - ○ Hygroscopic swelling
   - ○ Cure shrinkage
   - ○ Polymer creep

3.3.1 Mould geometry

The geometry of the mould will determine the geometry of the cast pins. Due to the design, the geometry of the mould is relatively insensitive for manufacturing errors. However, there are still three factors that will influence the final outlet film thickness.

Deviation from perpendicularity of the hole with respect the surface of the bearing plate, will cause the pins to also be non-perpendicular to that surface. The radial outlet film thickness then becomes asymmetric if the pin is concentric.

The theoretical stroke is defined as twice the concentric outlet film thickness. For a single pin, the stroke will become asymmetric for a misoriented hole, but it will not be reduced in total magnitude. However, for an increasing number of pins, the stroke of the full system in each direction will be bounded by most misoriented pin in that direction. No effective method to measure the misorientation of the holes has been found during this research.

Surface waviness of hole will be transferred to the surface of the cast pin. If the bearing plate is then shifted with respect to the casting arrangement, local variations in the outlet film thickness are created. The waviness of the pin surface was measured using a white light interferometer[6]. It is expected that the variations in film thickness due to the waviness are approximately $\pm 5\,\mu\text{m}$.

A mould release agent is used to ensure that the resin will not adhere to the bearing plate. This effectively changes the mould geometry. In this research, vaseline is used. Since the vaseline is removed from the mould surface after the resin has cured it will effectively increase the outlet film thickness. The thickness of the mould release agent has not been measured in this research.

3.3.2 Resin behaviour

The behaviour of the resin is to a large extent determined by the type of resin and the filler fraction. The resin used

[4] Miraject Luer 17/42
[5] Keyence VHX-6000
[6] Bruker Contour GT-K1

Table 5: First order approximation of influence on outlet filmthickness.

		Relevant parameters			
Mechanism	Expression for Δr	Symbol	Value	Unit	Expected effect on $h_{o,c}$ [μm]
Thermal expansion	$r\Delta\alpha\Delta T$	$\Delta\alpha$	58	ppm/K	+3
		ΔT	18	K	
Hygroscopic swelling	$r\beta_c\Delta RH$	β_c	1	%/(%RH)	-20 ± 5
		ΔRH	10	%	
Cure shrinkage	$r(\gamma_c/3)$	γ_c	3	%	+50

in this research is a bisphenol A/F type epoxy[7], in combination with an amine hardener[8]. In order to improve the mechanical properties of the resin, filler materials in the form of powders or fibres can be added. In this research, 10 wt% aluminium oxide powder[9] (Al_2O_3, D50 < 3.5 μm) is added.

The main mechanisms that influence the geometry of the cast pins are thermal expansion, hygroscopic swelling and cure shrinkage. The significance of these mechanisms decreases with an increasing filler ratio. This is due to the fact that the CTE of commonly used filler materials is much lower than that of the resin. Also, a filler material does not shrink during curing, nor does it absorb any moisture. A first order estimation of the influence of each mechanism on the radial outlet film thickness is shown in table 5.

Thermal expansion refers to the phenomena that a material will change its shape upon a change in temperature. The mould material (aluminium) has a lower CTE than the cast material (epoxy). This means that if the temperature during casting T_c differs from the temperature in operation T_o, the outlet film thickness will change.

The difference in radius Δr between the external radius of the pin and the internal radius of the hole can be written as:

$$\Delta r = r\Delta\alpha\Delta T \tag{22}$$

Where $\Delta\alpha$ represents the difference in CTE between the pin material and the mould material. ΔT represents the difference between the temperature during curing and in operation, i.e. $T_c - T_o$.

Hygroscopic swelling is the expansion of a material due to the absorption of moisture. The bearing plate is not susceptible to swelling, while the pins will expand due to swelling. This process will therefore decrease the radial outlet film thickness. Swelling is a reversible process, which means that the material can absorb and desorb moisture [17].

[7] Resion EP101
[8] Resion EP115
[9] Aluminium oxide powder

The difference in radius can then be written as [18]:

$$\Delta r = r\beta_c\Delta RH \tag{23}$$

Where β_c represents the linear Coefficient of Moisture Expansion (CME) of the composite material and ΔRH refers to the change in relative humidity.

Cure shrinkage refers to the phenomena that a thermosetting resin, such as an epoxy will undergo an increase in density and thus a decrease in volume during the polymerization reaction. This is due to the cross-links that are formed between the monomer chains. The linear cure induced shrinkage can be written as:

$$\Delta r = r\frac{\gamma_c}{3} \tag{24}$$

Where γ_c is the linear coefficient of cure shrinkage of the composite material. For unfilled epoxy, γ is typically 2-4%. The first 40-60% of the curing reaction occurs when the resin is still in the liquid state, and therefore does cause any shrinkage of the cast feature [18]. The epoxy used in this research cures very slowly, and thus stays in the liquid state longer. Therefore, the effective linear coefficient of cure shrinkage is taken as $\gamma_c/3$.

4 Results

The demonstrator did not perform as intended, due to a combination of reasons as presented in section 3.3. Hence, no experimental data can be presented to validate the numerical results. The results section therefore contains only results from the numerical analysis.

4.1 3D pressure distribution

The 3D pressure distribution is shown in fig. 15. Because of the asymmetric pressure distribution for $\varepsilon = 0.9$, a net shear force is generated in positive x-direction. Note that the pressure profiles on each of the opposing edges of the unit cell are identical.

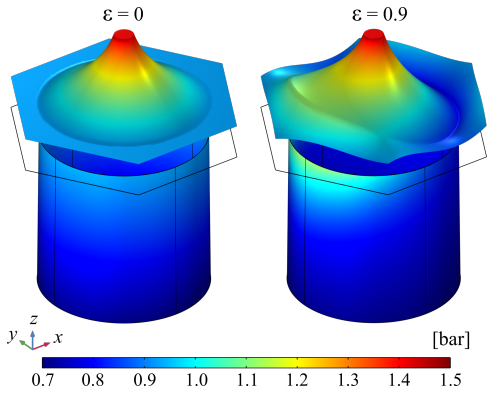

Figure 15: Three dimensional pressure distribution.

4.2 Dynamic behaviour

The dynamic behaviour of the system is shown in fig. 16. Since the magnitude of the outlet restriction decreases for the eccentric case, the stiffness $\bar{k}$ increases, while the damping $\bar{c}$ decreases. The cross-over point is around 10^4 Hz. The stiffness and damping are both positive for low frequencies, which means that the system is stable.

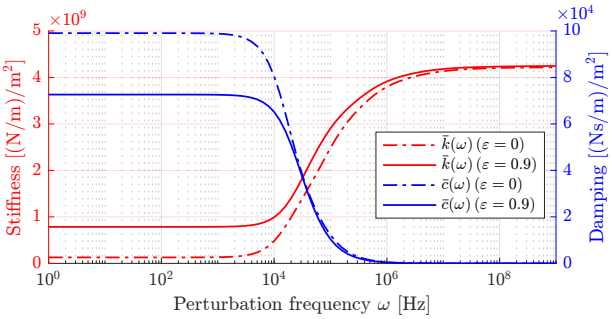

Figure 16: Dynamic behaviour of the system.

4.3 Performance

The force density for a varying mass flow density is shown in fig. 17. This plot was created by varying the vacuum pressure from $p_v = 1$ to 0.5 bar for $\varepsilon = 0.9$. The nominal operating point is indicated. The theoretical force density $\bar{F}$ is 19.5 N/m^2 for a vacuum pressure of 0.7 bar. For a silicon substrate (e.g. solar cell) with a thickness of 200 μm, the distributed weight is approximately 5 N/m^2. That means an acceleration of 4 m/s^2 could be achieved.

Table 6: Normalisation parameters.

Parameter	Value	Unit
$\bar{k}_{max}$	$78.5 \cdot 10^7$	(N/m)/m^2
$\bar{c}_{max}$	$99.1 \cdot 10^3$	(Ns/m)/m^2
P_{max}	66.0	m/s
$h_{f,c}$	15.0	μm

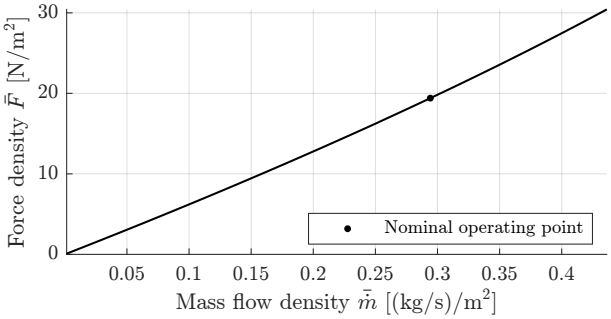

Figure 17: Force density as a function of the mass flow.

Relevant performance parameters for varying eccentricity are shown in fig. 18. They are normalised as:

$$\kappa = \frac{\bar{k}}{\bar{k}_{max}} \qquad \zeta = \frac{\bar{c}}{\bar{c}_{max}} \qquad \Pi = \frac{P}{P_{max}} \qquad H = \frac{h_{f,e}}{h_{f,c}}$$

Where the maximum value for each parameter can be found in table 6.

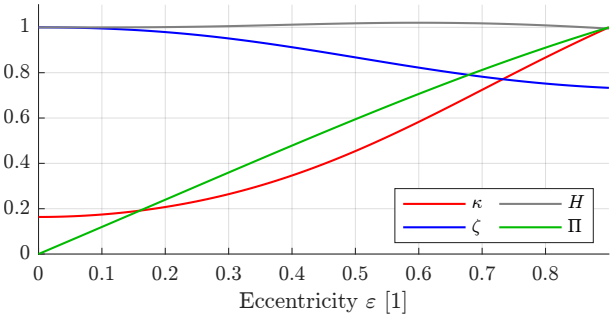

Figure 18: Relevant system parameters as a function of eccentricity.

4.4 Constant fly-height

From fig. 18, it can be seen that the normalised eccentric fly-height H is relatively constant. However, this is in general not the case. This is illustrated by analysing the system for three different values for the pocket height h_p as shown in fig. 19. Apart from a varying pocket height, the nominal design parameters as shown in table 2 are used.

For a pocket height of 17 μm, the fly-height increases with increasing eccentricity. This causes the magnitude of the pocket restriction to decrease and thus the mass flow increases. For a pocket height of 25 μm, the opposite behaviour is observed. The eccentric fly-height decreases and so does the mass flow. For a fly-height of 21 μm, the fly-height is relatively constant. Therefore, the mass flow is also relatively constant, which is desirable in an experimental set-up.

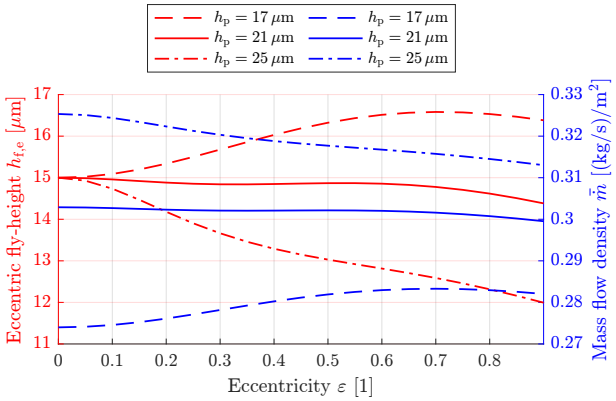

Figure 19: Eccentric fly-height and mass flow as a function of eccentricity.

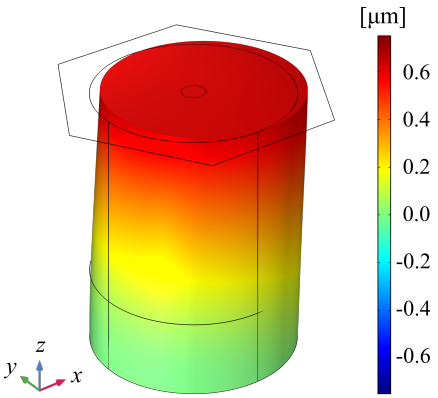

Figure 20: Pin deformation in x-direction.

4.5 Asymmetric pressure distribution

For the eccentric case, there exists an asymmetric pressure distribution in the outlet film, as shown in fig. 15. This means that in the quasi-static, frictionless case, an actuation force F_{act} of 0.67 N per unit cell is required to create an eccentricity of $\varepsilon = 0.9$. The friction of the bearing between plenum lid and bearing plate is not considered in this case.

The resulting deformation of the pin due to this pressure distribution is shown in fig. 20. This has little effect on the performance of the system as is shown in appendix C.7.

5 Discussion

5.1 Numerical model

The Reynolds equation is commonly used to describe the behaviour of aerostatic bearings and contactless handling systems. Therefore, it is assumed that the numerical model used in this research predicts the behaviour of the system with reasonable accuracy. Even though inlet and outlet effects and deformations of the geometry are not taken into account.

The following elementary conditions were satisfied:

1. Mass flow in equals mass flow out.
2. Net mass flow across unit cell edge equals zero.
3. Stiffness found using manual perturbation equals stiffness found using perturbed Reynolds for low frequencies

Currently, the discrepancy between the geometry used in the numerical model and the geometry of the demonstrator is too large. Therefore, the demonstrator cannot be used to verify the results found using the numerical model.

The first step towards achieving this is to create a demonstrator that forms a better resemblance of the geometry used in the numerical model. Where possible, manufacturing errors should be measured such that they can be implemented in a *true* numerical model. If possible, using non-destructive measurement techniques. The true numerical model should show results similar to those found in physical experiments.

5.1.1 Constant fly-height

Using the numerical model it was found that there exists a non-unique set of design parameters for which the eccentric fly-height remains relatively constant for a varying eccentricity (see fig. 19). Creating a system that maintains a constant fly-height while actuating can be very useful, for example during inspection of a substrate using a microscope.

In the numerical model, the supply and vacuum pressure are assumed to be constant, i.e. they are ideal pressure sources. In reality, for non-ideal pressure sources, the pressure will depend on the flow. If the fly-height remains relatively constant, the mass flow also remains relatively constant, which makes it easier to maintain a constant pressure. As an alternative of designing a system for a maximum performance ratio P, it could also be decided to design a system for a minimum variation in fly-height.

5.1.2 Pin deformation

As shown in fig. 20, the pin deforms due to the pressure gradient. Both the geometry of the outlet film as well as that of the pocket deform. The influence of this deformation on the performance of the system is minimal. and it is likely, the influence of deformation of the substrate is more significant. Wesselingh found that these deformations are in the order of 1 μm [4]. This will obviously depend on the type of substrate, operating conditions and unit cell dimensions.

5.2 Manufacturing

It has been difficult to manufacture a system with the required dimensional tolerances. Despite the redundancy inherent to the manufacturing method and all the care that has been taken.

The final geometry of the flow path is determined by the geometry of the mould and the geometry of the cast pin. The latter is to a large extent determined by the behaviour of the resin. The influence of the resin behaviour needs to be minimised, in order to obtain a higher dimensional accuracy and stability of the pins. To improve the manufacturing method, the mould geometry needs to be better defined.

5.2.1 Mould geometry

Any misorientation (i.e. deviation from perpendicularity) of the hole leads to an asymmetrical outlet film and thus also an uneven stroke. The stroke of the system has been measured, as is described in appendix D.4.8. However, this does not provide any information regarding the geometry of each individual outlet film. It does provide some information regarding the combined influence of both the mould geometry and resin behaviour combined.

Ideally, the influence of each mechanism can be measured separately. Obviously, the goal should always be to minimise the influence of these mechanisms. That way, the outlet film thickness will approach the theoretical outlet film thickness defined in eq. (2).

Any waviness present in the mould surface will be transferred to the surface of the cast pin. This causes the outlet film thickness to be uneven along the flow path and therefore not well defined. The waviness could be further reduced by additional manufacturing steps, e.g. burnishing or grinding. The waviness has been measured, however only using a destructive measurement technique.

The mould release agent is added in order to ensure that the resin does not adhere to the mould (i.e. the bearing plate). In this research, vaseline is used. After curing, it is removed, and thus it effectively increases the size of the outlet film thickness. The thickness of this layer has not been measured and thus its influence is unknown. If the thickness is consistent and can be well predicted, this can be taken into account during the manufacturing process. Alternatively, a solid release agent coating, e.g. parylene C, could be used [19]. In that case, this will not influence the outlet film thickness.

5.2.2 Resin behaviour

The behaviour of the resin determines the dimensions of the pin to a large extent in the current demonstrator. Thermal contraction and cure shrinkage will both decrease the size of the pin with respect to the bearing plate, thereby increasing the radial outlet film thickness. Hygroscopic swelling will cause the pins to expand, while the bearing plate is not susceptible to swelling, and thus decreases the radial outlet film thickness.

Exactly predicting the influence of these phenomena is complicated and would be a research on its own. Ideally, an extensive technical data sheet should be provided by the manufacturer. Alternatively, information regarding a certain type of resin could be found in the literature.

The dimensional stability will also increase by decreasing the volume of resin that is required. This could be achieved by machining a plenum lid that has solid cylinders in the centre of each pin, as shown in fig. 21. The resin will then only be used to fill in the gap, rather than to form the complete pin. By using a resin with a higher filler fraction, the dimensional stability will be further increased.

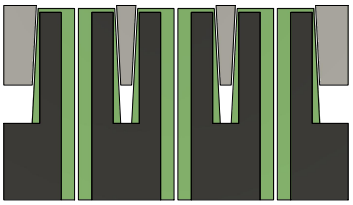

Figure 21: Plenum lid with solid core cylinders.

5.2.3 Inlet restriction

Using the dispensing needles as capillary flow restrictions worked well. The inlet conductivity was consistent and predictable. During the research of Hoogeboom [20] and Verbruggen [6], capillary flow restrictions were also used. They experienced difficulty minimising the recess volume, which increased the chance of pneumatic hammer. Due to the casting process, there is effectively no recess. An additional manufacturing step is required to create a recess.

5.2.4 Pocket restriction

As explained, the pocket restriction is created between the substrate and the surface of each pin. The pocket height is defined by the height of the pin, the thickness of the bearing plate and the distance enforced between the two plates. Alternatively it can thus be stated that the pocket height is equal to (see fig. 6):

$$h_\mathrm{p} = t_\mathrm{bp,2} + t_\mathrm{v} - h_\mathrm{pin} \tag{25}$$

The pins are levelled with respect to the bearing surface when the system is assembled using undersized ball bearings. This effectively ensures that the exact dimensions are not relevant and that the pocket height is only determined by the difference in ball diameter (i.e. $h_\mathrm{p} = \Delta t_\mathrm{v} = \Delta d_\mathrm{b}$).

Ball bearings were used since their diameter is well defined, and they allowed for local support of the bearing plate. This is required, since otherwise, the deformation due to the pressure gradient across the plate would be too high. In theory, the stiffness achieved using ball bearings should be equal to the Hertzian stiffness. This would result in a deformation in z-direction of $< 1\,\mu$m.

In reality however, the deformation due to the vacuum pressure was 10-20 μm. This is a very significant deformation compared to the nominal pocket height of 19 μm. The

reason is most likely due to the disk spring action of the spacer plates and the non-flatness of both plates in general.

For a future demonstrator, pocket height needs to be more accurately defined. This means that the vertical stiffness needs to be higher and the deformation needs to be minimised. Performing the final manufacturing step on the system in its assembled state is also cumbersome and could therefore be improved.

Reduced stroke

The system was initially designed for an outlet film thickness of $40\,\mu m$, for a distance between the two plates of 4 mm. By adding the spacer plates, this distance was increased to 7 mm. In theory, the outlet film thickness should then be equal to $70\,\mu m$, and thus the total stroke should be equal to $140\,\mu$m. However, the total stroke was only $29\,\mu$m before glueing the spacer plates. After glueing the spacer plates, the stroke essentially reduced to 0. This could be due to glue that seeped into the outlet restriction during curing, however, no sign of this was found upon inspection. Alternatively, it could be due to hygroscopic swelling of the pins.

6 Conclusion

Contactless handling based on air bearing technology is a technology that can be used to handle substrates in a fully contactless manner. Promising results have been shown in a lab environment, however, manufacturing such systems is in general complicated and expensive, due to very tight tolerances.

A system using the variable outlet restriction concept was developed. It was shown that this system has a performance ratio identical to that of the variable pocket restriction concept. The variable outlet restriction concept was selected for further development since the manufacturing process could potentially be simplified.

A novel manufacturing method has been developed. In theory, the system developed using method should be less sensitive for manufacturing errors than previously developed concepts. In practice however, the required manufacturing tolerances have not been met. This is partly due to geometrical errors present in the mould and partly due to insufficient dimensional stability of the cast pins.

The system has been modelled using COMSOL. It was discovered that there exists a set of design parameters for which the fly-height, and therefore the mass flow, remain relatively constant. However, this claim still needs to be confirmed by experimental data.

Additional research into the manufacturing method is required. By using non-destructive measurement techniques, relevant dimensions should be measured and implemented into a numerical model that forms a better resemblance of the geometry of the demonstrator.

References

[1] B. Hoefflinger, *Chips 2020: A Guide To the Future of Nanoelectronics*. 2012.

[2] G. M. Wilson, M. Al-Jassim, W. K. Metzger, S. W. Glunz, P. Verlinden, G. Xiong, L. M. Mansfield, B. J. Stanbery, K. Zhu, Y. Yan, J. J. Berry, A. J. Ptak, F. Dimroth, B. M. Kayes, A. C. Tamboli, R. Peibst, K. Catchpole, M. O. Reese, C. S. Klinga, P. Denholm, M. Morjaria, M. G. Deceglie, J. M. Freeman, M. A. Mikofski, D. C. Jordan, G. Tamizhmani, and D. B. Sulas-Kern, "The 2020 photovoltaic technologies roadmap," *Journal of Physics D: Applied Physics*, vol. 53, no. 49, 2020.

[3] Z. Liu, S. E. Sofia, H. S. Laine, M. Woodhouse, S. Wieghold, I. M. Peters, and T. Buonassisi, "Revisiting thin silicon for photovoltaics: A technoeconomic perspective," *Energy and Environmental Science*, vol. 13, no. 1, pp. 12–23, 2020.

[4] J. Wesselingh, *Contactless positioning using an active air film*. Phd thesis, Delft University of Technology, 2011.

[5] V. Hong Phuc, *Air-based contactless actuation system for thin substrates*. Phd thesis, Delft University of Technology, 2016.

[6] N. Verbruggen, *Air-Based Contactless Positioning of Thin Substrates*. Master thesis, Delft University of Technology, 2017.

[7] R. Jansen, *Actuator System for the Flowerbed*. Master thesis, Delft University of Technology, 2018.

[8] M. E. Krijnen, *Control System Design for a Contactless Actuation System*. Master thesis, Delft University of Technology, 2016.

[9] R. Hooijschuur, N. Saikumar, S. H. Hosseinnia, and R. A. van Ostayen, "Air-based contactless wafer precision positioning system," *Applied Sciences (Switzerland)*, vol. 11, no. 16, 2021.

[10] R. Snoeys and F. Al-Bender, "Development of improved externally pressurized gas bearings," *KSME Journal*, vol. 1, no. 1, pp. 81–88, 1987.

[11] C. Hahm, R. Theska, A. Flohr, and O. Hartmann, "Concrete – future material for high precision machines," no. September, pp. 8–12, 2014.

[12] COMSOL Inc., "COMSOL Multiphysics Version 5.6," 2021.

[13] B. J. Hamrock and S. R. Schmid, *Fundamental of Fluid Film Lubrication*. 1991.

[14] W. Brian Rowe, *Hydrostatic, Aerostatic and Hybrid Bearing Design*. Elsevier, first ed., 2012.

[15] F. Al-Bender, *Air Bearings: Theory, Design and Applications*. Tribology in Practice Series, Wiley, 2021.

[16] E. Urata, "A flow rate equation for subsonic Fanno flow," *Proceedings of the Institution of Mechanical Engineers, Part C: Journal of Mechanical Engineering Science*, vol. 227, no. 12, pp. 2724–2729, 2013.

[17] Y. He, "Moisture absorption and hygroscopic swelling behavior of an underfill material," *Thermochimica Acta*, vol. 546, pp. 143–152, 2012.

[18] J. de Vreugd, *The Effect of Aging on Moulding Compound Properties*. Phd thesis, Delft University of Technology, 2011.

[19] P. Sethu and C. H. Mastrangelo, "Cast epoxy-based microfluidic systems and their application in biotechnology," *Sensors and Actuators, B: Chemical*, vol. 98, no. 2-3, pp. 337–346, 2004.

[20] R.P. Hoogeboom, *Design and experimental validation of low stiffness aerostatic thrust bearings*. Master thesis, Delft University of Technology, 2016.

Appendix A

Theory

In this chapter, the physics which are relevant to the working of a contactless handling system are explained in an intuitive way. Also, the theoretical performance of the concepts presented in the state-of-the-art will be compared.

A.1 Reynolds equation

The flow within a thin film as shown in figure A.1 is described by the Reynolds equation. The full Reynolds equation in x-direction is defined as [9]:

$$\underbrace{\frac{\partial}{\partial x}\left(\frac{\rho h^3}{12\eta}\frac{\partial p}{\partial x}\right)}_{\text{Poiseuille}} = \underbrace{\frac{\partial}{\partial x}\left(\frac{\rho h\left(u_a+u_b\right)}{2}\right)}_{\text{Couette}} + \underbrace{\frac{\partial}{\partial t}\left(\rho h\right)}_{\text{Dynamic}} \tag{A.1}$$

Which consists of three terms: a Poiseuille term, a Couette term and a dynamic term. The Couette term describes the flow due to relative motion of the bodies. In this research, the influence of this flow is assumed to be negligible. The dynamic term is also neglected for the stationary part of the study. An interpretation of the these terms can be found in appendix F.1. Throughout this chapter, only the x-direction will be discussed. However, all expressions are identical in y-direction.

When the Couette term and the dynamic term are neglected, the simplified Reynolds equation can be defined as:

$$\frac{\partial}{\partial x}\left(\frac{\rho h^3}{12\eta}\frac{\partial p}{\partial x}\right) = \frac{\partial}{\partial x}\left(\frac{p h^3}{12\eta\,\mathrm{R_s}T}\frac{\partial p}{\partial x}\right) = 0 \tag{A.2}$$

Where p represents the pressure, h represents the film thickness and η represents the dynamic viscosity of the fluid. Using the ideal gas law, the density ρ can be expressed in terms of the pressure p, the specific gas constant of the fluid R_s and the temperature T.

The pressure driven flow is shown in figure A.1. The pressure on the left side p_1 is higher than the pressure on the right p_2, i.e. $\partial p/\partial x < 0$. The velocity profile is indicated by u and the shear stress profile by τ. In this research a typical length for L is 10 mm and a typical length for h is 10 μm.

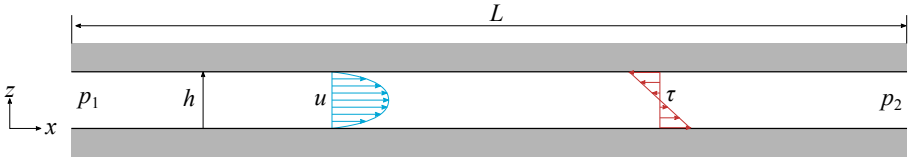

Figure A.1: Poiseuille flow.

General assumptions that are made when using the Reynolds equation are [10]:

- The influence of body forces acting on the fluid are assumed to be negligible. An example of a body force would be gravity.
- The pressure is assumed to be constant in the direction perpendicular to the surface (i.e. the film thickness direction).
- A no-slip condition is assumed at the interfaces between the fluid and a solid object.
- The flow is assumed to be laminar and isothermal.

A.2 Shear force

The shear force that is generated by the flow in the pockets acts on the substrate, as well as on the bearing surface. Because the substrate is floating on this viscous film of air, the shear force will cause an acceleration of the substrate. The shear force in x-direction can be defined as:

$$F_x = \int_A -\tau_x \, dA \quad = \int_A -\eta \frac{\partial u}{\partial z} \, dA \tag{A.3}$$

If it is assumed that the gas behaves as a Newtonian fluid, the shear stress τ is proportional to the velocity gradient $\partial u/\partial z$. The velocity profile in x-direction u for a pressure driven (Poiseuille) flow is given as:

$$u(z) = \frac{1}{2\eta} \frac{\partial p}{\partial x} \left(z^2 - hz \right) \tag{A.4}$$

The derivation is shown in appendix F.2. Differentiating this velocity profile with respect to z gives:

$$\frac{\partial u}{\partial z} = \frac{1}{2\eta} \frac{\partial p}{\partial x} \left(2z - h \right) \tag{A.5}$$

Evaluating this expression at the substrate surface gives:

$$\left. \frac{\partial u}{\partial z} \right|_{z=h} = \frac{h}{2\eta} \frac{\partial p}{\partial x} \tag{A.6}$$

The shear force in x-direction acting on the substrate ($z = h$) can thus be defined as:

$$F_x = \int_A -\eta \frac{\partial u}{\partial z} \, dA = \int_A -\frac{h}{2} \frac{\partial p}{\partial x} \, dA \tag{A.7}$$

A.2.1 Mass flow

The volumetric flow is found by integrating the velocity profile over the film thickness as:

$$\dot{q}_x = \int_0^h u(z) \, dz \tag{A.8}$$

Substituting equation (A.4) gives:

$$\begin{gathered} \dot{q}_x = \int_0^h \frac{1}{2\eta} \frac{\partial p}{\partial x} \left(z^2 - hz \right) \, dz = \frac{1}{2\eta} \frac{\partial p}{\partial x} \left(\frac{2z^3}{3} - \frac{hz^2}{2} \right) \Bigg|_{z=0}^{z=h} \\ \dot{q}_x = -\frac{h^3}{12\eta} \frac{\partial p}{\partial x} \end{gathered} \tag{A.9}$$

The mass flow can then be found by multiplying the volumetric flow rate with the density:

$$\dot{m}_x = \rho \dot{q} = -\frac{\rho \, h^3}{12\eta} \frac{\partial p}{\partial x} \tag{A.10}$$

A.3 Bearing stiffness

The stiffness of the bearing film is defined as the change in load capacity, upon a change in fly-height. Where the load capacity is defined as the sum of the vertical forces. In order for the system to be stable, the load capacity should decrease when the fly-height increases and vice versa. This ensures that the nominal fly-height is restored after a perturbation.

Bearing stiffness is introduced in the section below using and electrical analogy of Ohm's law and a lumped restriction model. Afterwards, the influence of various restrictions on the bearing film stiffness is discussed conceptually.

A.3.1 Electrical analogy

The lumped restriction model can be used to gain insight into the qualitative behaviour of aerostatic bearing systems. The continuous geometry essentially forms one spatially distributed flow restriction. This single, continuous, flow restriction can be modelled as a discrete number of restrictions. An electrical analogy of Ohm's law is used to model the volumetric flow and flow restrictions.

The electrical resistance created by a long wire (A.2a) can be represented by a lumped electrical resistance, defined as:

$$R_\mathrm{e} = \frac{\rho L}{A} \tag{A.11}$$

Where ρ is the electrical resistivity, L is the length of the wire and A is the cross-sectional area. The flow of electrons (i.e. current) can then be expressed using Ohm's law as:

$$I = \frac{\Delta U}{R_\mathrm{e}} \tag{A.12}$$

Where ΔU represents the voltage difference (i.e. potential difference) between point 1 and 2.

Ohm's law can also be used to analyse the volumetric flow of fluid $\dot{q}$ through a flow restriction R_f as a consequence of the pressure difference (i.e. potential difference) across the restriction:

$$\dot{q} = \frac{\Delta p}{R_\mathrm{f}} \tag{A.13}$$

Using equation (A.13) and the expression for the volumetric flow rate found in equation (A.9), an expression for the flow restriction can be found as:

$$R_\mathrm{f} = \frac{\Delta p}{\dot{q}} = \frac{\Delta p}{\frac{h^3}{12\,\eta}\frac{\Delta p}{L}} = \frac{12\eta L}{h^3} \qquad [\mathrm{Pa}/(\mathrm{m}^2/\mathrm{s})] \tag{A.14}$$

Where η represents the dynamic viscosity of the fluid, L represents the length of the flow path and h the film thickness. Note that expression holds for a 2D geometry as shown in figure A.1, hence the units. For a rectangular channel with a certain width w, the magnitude of the restriction becomes:

$$R_\mathrm{f} = \frac{12\,\eta L}{w\,h^3} \qquad [\mathrm{Pa}/(\mathrm{m}^3/\mathrm{s})] \tag{A.15}$$

(a) Lumped electrical resistance.

(b) Lumped flow restriction.

Figure A.2

A.3.2 Load capacity

The load capacity of a contactless handling system can be seen as the sum of the forces in the direction perpendicular to the bearing surface. As the name implies, it defines how much load the system can carry. The load capacity is a function of the pressure distribution below the substrate $p(x, y)$ and the ambient pressure p_a as:

$$W = \int_A \Big(p(x,y) - p_\mathrm{a} - p_\mathrm{sub}\Big)\, dA \approx \int_A \Big(p(x,y) - p_\mathrm{a}\Big)\, dA \tag{A.16}$$

In this research, the distributed weight of the substrate p_sub is typically 20-50 Pa, which is negligible compared to ambient pressure $1 \cdot 10^5$ Pa. Levitation is achieved if $W = 0$ for a given fly-height > 0.

If there is a relation between the load capacity W and the bearing film thickness h, this is referred to as stiffness of the bearing film. Stiffness in an air film might can be envisioned as many distributed helical springs on which the substrate is suspended. For a helical spring, the stiffness in z-direction defined as:

$$k = -\frac{\partial F_z}{\partial z} \tag{A.17}$$

Where a displacement in positive z-direction, will generate a restoring force F_z in the spring in negative z-direction. The higher the displacement, the higher the restoring force. In a similar fashion, the stiffness of a contactless handling system is defined as:

$$k = -\frac{\partial W}{\partial h} \tag{A.18}$$

A positive stiffness in the bearing film is thus achieved if the load capacity decreases upon an increase in fly-height and vice versa. The stiffness in the bearing film can also be negative, much like the behaviour observed with two opposing-pole permanent magnets. In this case, decreasing the distance between the two will cause the attraction force to increase, thereby again decreasing the distance.

A.3.3 Influence of restrictions

The influence of the three restrictions in the system will now be explained using the lumped restriction model. An ideal supply and vacuum source are assumed, this means that the flow will be independent of the pressure gradient. The supply and vacuum pressure are assumed to be fixed. The fluid is assumed to be incompressible, in order for the figures to be clearer. A perturbation of the fly-height in positive z-direction is discussed as an example. The opposite behaviour will be observed for a decreasing fly-height.

Bearing film restriction

The situation without an inlet or outlet restriction is schematically shown in figure A.3. Where figure A.3a shows the situation for the nominal fly-height ($h_\mathrm{f} = h_0$) and figure A.3b shows the situation for an increased fly-height($h_\mathrm{f} > h_0$). The geometry is shown in the middle of each figure. The incompressible pressure distribution in the bearing film is shown in the graph above the geometry. For simplicity, only the pressure between the dashed lines is shown. Below the geometry, the equivalent restriction scheme is shown. This the same for figures A.4 and A.5

If the inlet and outlet restriction are negligible compared to the bearing film restriction, the pressure will drop only across the bearing film. This means that $p_\mathrm{i} = p_\mathrm{s}$ and $p_\mathrm{o} = p_\mathrm{v}$. The pressure decreases linearly from the supply pressure p_s to the vacuum pressure p_v as shown in the graph.

If the fly-height increases, the magnitude of the film restriction decreases. This means that the flow will increase, since the supply and vacuum pressure are fixed. However, the load capacity W does not change, since it is only dependent on the pressure profile, and not on the flow. A system where there is only a restriction in the bearing film therefore has no stiffness:

$$k = -\frac{\partial W}{\partial h_\mathrm{f}} = 0 \tag{A.19}$$

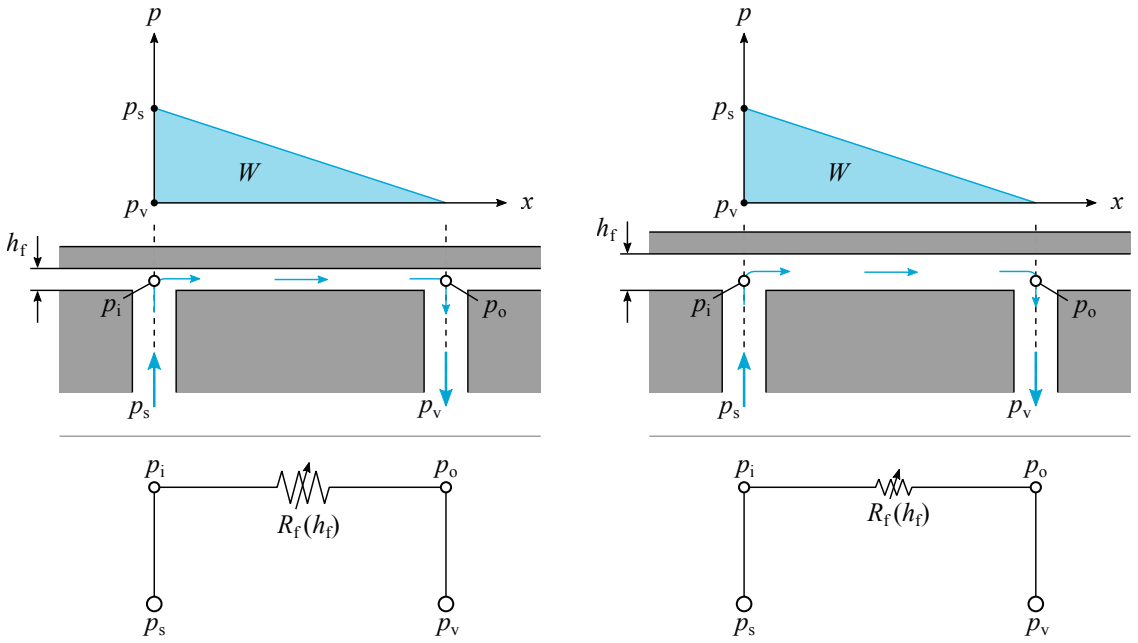

(a) Load capacity for $h_f = h_0$.

(b) Load capacity for $h_f > h_0$.

Figure A.3: Load capacity for system without inlet or outlet restriction.

Inlet restriction

Shown in figure A.4a is the system with an inlet restriction and a bearing film restriction. The fly-height is equal to the nominal fly-height. Since there are now two restrictions present, the supply pressure is no longer equal to the inlet pressure ($p_s \neq p_i$). As a result, a higher supply pressure is required to generate the same load capacity.

When the fly-height is increases, as shown in figure A.4b, the magnitude of the film restriction decreases, hence the relative pressure drop across the film restriction decreases. Since the supply and vacuum pressure are fixed, the pressure drop across the inlet restriction will increase, thereby effectively decreasing the inlet pressure at the bearing surface p_i. This decreases the load capacity W and thus restores the nominal fly-height. An inlet restriction thus generates a positive stiffness in the bearing film:

$$k = -\frac{\partial p_i}{\partial h_f} \propto -\frac{\partial W}{\partial h_f} > 0 \tag{A.20}$$

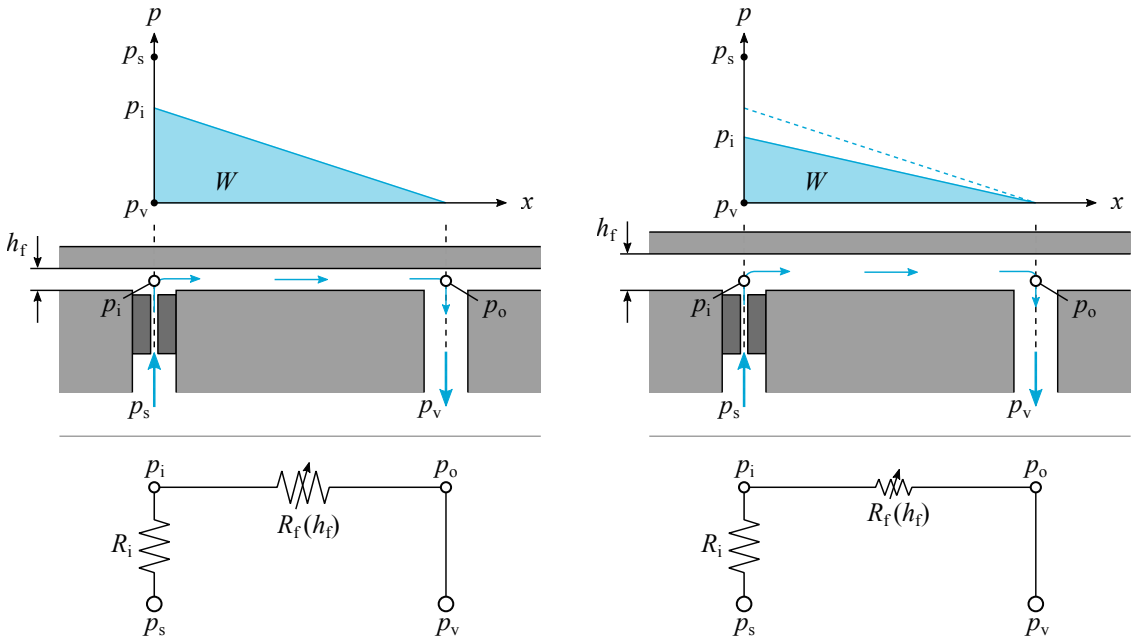

(a) Load capacity for $h = h_0$.

(b) Load capacity for $h > h_0$.

Figure A.4: Load capacity for system with inlet restriction.

Outlet restriction

Shown in figure A.5a is the system with a film restriction and an outlet restriction for the nominal fly-height. Due to the presence of the outlet restriction, the outlet pressure is no longer equal to the vacuum pressure ($p_o \neq p_v$). If the fly-height now increases, as shown in figure A.5b, the magnitude of the film restriction decreases, thereby decreasing the pressure drop across it. The pressure difference across the outlet restriction will therefore increase. This effectively increases the outlet pressure and thus the load capacity increases. Thus, upon an increase in fly-height the load capacity increases, thereby increasing the fly-height even further. The system is therefore unstable, which corresponds to a negative stiffness:

$$k = -\frac{\partial p_o}{\partial h_f} \propto -\frac{\partial W}{\partial h_f} < 0 \tag{A.21}$$

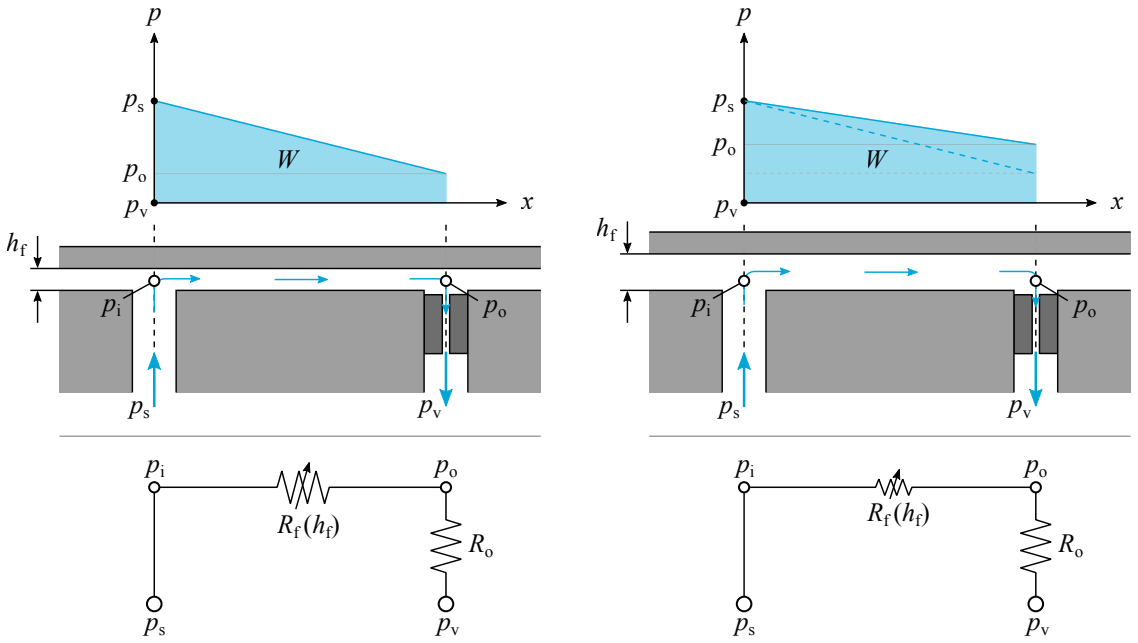

(a) Load capacity for $h = h_0$.

(b) Load capacity for $h > h_0$.

Figure A.5: Load capacity for system with outlet restriction.

Damping

Because the bearing film is compressible, energy can be stored (as in a helical spring). When this stored energy is released *in phase* with the oscillations this will increase the amplitude of the oscillations, which will in turn again increase the compression. This is referred to as pneumatic hammer and causes the system to be unstable [11].

A.4 Generating bearing stiffness

In order to obtain stiffness in the bearing film, the load capacity needs to be dependent on the fly-height, as has been shown above. This could be achieved by actively controlling the supply and vacuum pressure, for example using valves [12]. However, by making use of an inlet restriction a system can be created that is passively stable. There are three main types of flow restrictions that can be used, which will be discussed below.

A.4.1 Inlet restrictions

Capillary flow restriction

A capillary tube is a cylindrical tube with a high ratio of length L over diameter d. The flow restriction created by a capillary tune can be described by the Hagen-Poiseuille law as [13]:

$$R_c = \frac{128\eta L}{\pi d^4} \tag{A.22}$$

This holds for laminar flow of incompressible, Newtonian fluids. Therefore, it is only valid for a low pressure difference across the restriction. This will be discussed in more detail in appendix D.2.

Orifice flow restriction

A simple orifice is a hole with a very low ratio of the length L over the ratio d, as shown in figure A.6a. The smallest cross-sectional area A is defined as $\pi\, d^2/4$. An annular orifice, shown in figure A.6b is created when the smallest cross-sectional area A is equal to $\pi\, d\, h$.

(a) Simple orifice.

(b) Annular orifice.

Figure A.6: Orifice comparison.

The flow through an orifice is a polytropic process, which means that the process obeys [14]:

$$p\,V^{\kappa} = \text{constant} \tag{A.23}$$

In this case, the value for κ is the ratio of the heat capacity at constant pressure over the heat capacity at constant volume. This means that the process is assumed to be isentropic (i.e. constant entropy). There is no transfer of mass or heat, and the process is reversible.

$$\dot{m} = \begin{cases} C_{\mathrm{d}}\,\pi r_{\mathrm{o}}^2\,p_{\mathrm{s}}\sqrt{\frac{\kappa}{\kappa-1}\left[\left(\frac{p}{p_{\mathrm{s}}}\right)^{2/\kappa} - \left(\frac{p}{p_{\mathrm{s}}}\right)^{(\kappa+1)/\kappa}\right]\frac{2}{R_{\mathrm{s}}T}}, & \text{if } \frac{p}{p_{\mathrm{s}}} \geq \left(\frac{2}{\kappa+1}\right)^{\frac{\kappa}{\kappa-1}} \\ & \text{unchocked} \\ C_{\mathrm{d}}\,\pi r_{\mathrm{o}}^2\,p_{\mathrm{s}}\sqrt{\left(\frac{2}{\kappa+1}\right)^{2/(\kappa-1)}\left(\frac{\kappa}{\kappa+1}\right)\frac{2}{R_{\mathrm{s}}T}}, & \text{if} \frac{p}{p_{\mathrm{s}}} < \left(\frac{2}{\kappa+1}\right)^{\frac{\kappa}{\kappa-1}} \\ & \text{chocked} \end{cases} \tag{A.24}$$

Where C_{d} represents the discharge coefficient. The value of C_{d} varies with the Mach number and ratio of pressures across the restriction. For a pressure ratio of less than 0.7, the value for C_{d} is typically in the range of 0.7-0.96 [12]. Simple orifice restrictions were used by Snieder [15]. For more information, the reader is referred here. Also, the practical implications of creating small holes is discussed in more detail.

Porous flow restriction

A porous flow restriction is created by a material with a porous structure, that creates a network of many small channels. Porous flow restrictions are commonly used in aerostatic bearings. The flow restriction created by a porous restrictor can be defined using Darcy's law as:

$$R_{\mathrm{p}} = \frac{\eta t}{\kappa A} \tag{A.25}$$

Where κ is the permeability of the material, η represents the dynamic viscosity of the fluid, t is the thickness of the restriction and A is the cross-sectional area.

Porous flow restrictions can for example be made of graphite or porous sintered metal [16]. A company known for their aerostatic bearings with porous restrictions is New Way Air Bearings. An image of one of their vacuum pre-loaded air bearings is shown in figure A.7.

Figure A.7: Vacuum pre-loaded aerostatic bearing using a porous restriction[1].

[1]New Way Air Bearings

A.5 Analytical performance

In this section, the performance of the variable outlet restriction concept is compared to the pressure control concept and the variable pocket restriction concept. The working principle of these concepts is explained in section 1.2. The symbolic toolbox in MATLAB [17] is used to perform the analytical derivation. The evaluation of the performance is performed in COMSOL [18]. More detailed derivations of the results presented in this section can be found in appendix F.3.

The metric used to compare the performance is the performance ratio, which was introduced by Vuong [4] as:

$$P = \frac{\bar{F}}{\bar{\dot{m}}} \qquad \left[\frac{\mathrm{N/m^2}}{\mathrm{(kg/s)/m^2}}\right] = \left[\frac{\mathrm{m}}{\mathrm{s}}\right] \tag{A.26}$$

Where $\bar{F}$ represents the force density, i.e. unit shear force per unit area and $\bar{\dot{m}}$ represents the mass flow density, i.e. unit mass flow per unit time per unit area.

A.5.1 Variable outlet restriction geometry

A single unit cell of the variable outlet restriction geometry is shown in figure A.8. The unit cell is assumed to be part of an infinite grid of identical unit cells. This is represented by the light grey sections on either side. The analysis is performed in 2D, which means that the length in y-direction is assumed to be infinite. Below the geometry, the electrical analogous circuit is shown. The limit case is considered, where the outlet restriction is fully closed for $x = x_2$ and fully open for $x = x_1$ and $x = x_4$. Therefore, the outlet restriction at $x = x_2$ is assumed to be infinite (i.e. open circuit), while for $x = x_1$ and x_4, the outlet restriction is assumed to be negligible (i.e. $p_o = p_v$). Also, the width of the inlet and outlet are assumed to be negligible compared to the full length L of the system.

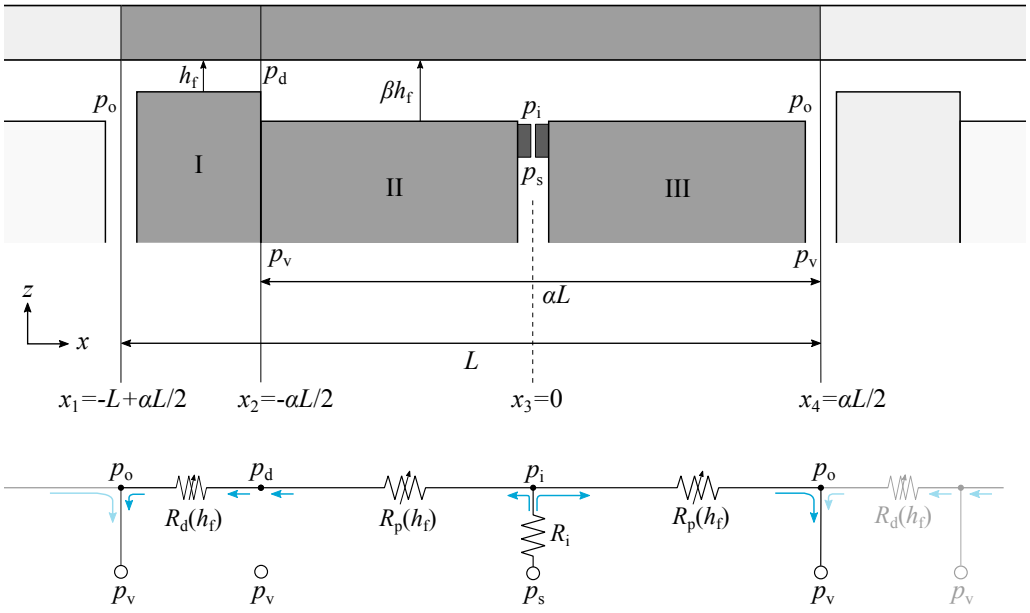

Figure A.8: Variable outlet restriction unit cell geometry and lumped restriction circuit.

The parameter α describes the ratio of the length of the dam relative to the length of the pocket and varies between 0 (i.e. no pocket) and 1 (i.e. no dam). The parameter β describes the film thickness in the pocket as a factor of the film thickness above the dam. The value for β varies between 1 (i.e. no pocket) and ∞ (i.e. infinitely deep pocket).

A.5.2 Incompressible case

The governing equation for the incompressible case is the simplified Reynolds equation:

$$\frac{\partial}{\partial x}\left(p\frac{\partial p}{\partial x}\right) = 0 \tag{A.27}$$

The constant terms are removed. This governing equation can be solved on each of the sections of the geometry. The three resulting pressure profiles are globally defined as:

$$p(x, \alpha, L, p_\mathrm{i}, p_\mathrm{d}, p_\mathrm{o}) = Ax + B \tag{A.28}$$

Where the values for A and B can be found by applying the boundary conditions on each section. The incompressible pressure profile for various values of β is shown in figure A.9.

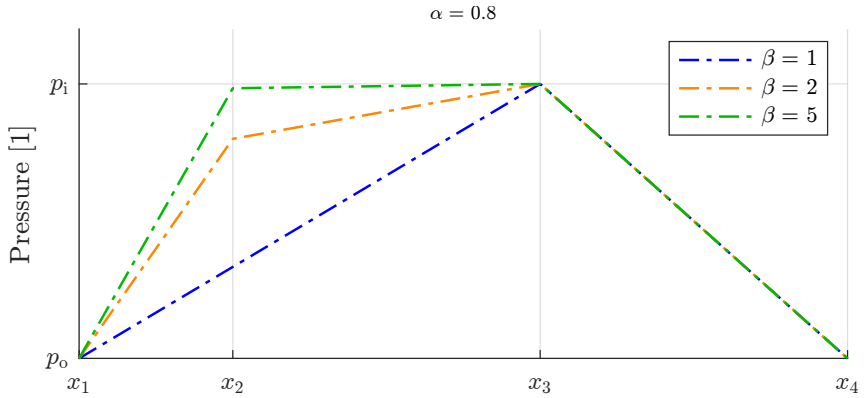

Figure A.9: Incompressible pressure profiles for variable outlet restriction.

Force density

Using the pressure profiles shown in equation (A.28), the force density can be expressed as:

$$\begin{aligned} \bar{F} &= \frac{1}{L}\int_L \left(-\frac{h(x)}{2}\frac{\partial p(x)}{\partial x}\right) dx \\ \bar{F}(p_\mathrm{d}, p_\mathrm{o}, \beta, h_\mathrm{f}, L) &= \frac{1}{L}\underbrace{\frac{h_\mathrm{f}\,(\beta-1)}{2}}_{1}\underbrace{(p_\mathrm{d}-p_\mathrm{o})}_{2} \end{aligned} \tag{A.29}$$

Where the first term represents the influence of the geometry and the second term represents the pressure difference across the dam.

Mass flow density

The mass flow density through the pocket can be determined as:

$$\bar{\dot{m}} = \frac{1}{L}\rho\,\dot{q} = \frac{1}{L}\rho\frac{\Delta p}{R_\mathrm{e}} \tag{A.30}$$

Where R_e is the effective restriction value defined as:

$$R_\mathrm{e}(\alpha, \beta, h_\mathrm{f}, L, \eta) = \left(\frac{1}{R_\mathrm{d}(h_\mathrm{f}) + R_\mathrm{p}(h_\mathrm{f})} + \frac{1}{R_\mathrm{p}(h_\mathrm{f})}\right)^{-1} \tag{A.31}$$

The total mass flow density can then be written as:

$$\bar{\dot{m}}(p_\mathrm{i}, p_\mathrm{o}, \alpha, \beta, h_\mathrm{f}, L, \eta, \mathrm{R_s}, T) = \underbrace{\frac{(p_\mathrm{i}+p_\mathrm{o})}{2\,\mathrm{R_s}\,T}}_{1}\underbrace{\frac{\beta^3\,h_\mathrm{f}^3}{6\,\eta\,L^2}\left(\frac{1}{\alpha}-\frac{1}{\alpha\,(2\,\beta^3-1)-2\,\beta^3}\right)}_{2}\underbrace{(p_\mathrm{i}-p_\mathrm{o})}_{3} \tag{A.32}$$

Where the first term represents the average density across the bearing film, the second term represents the restriction as a function of the geometrical parameters. The third term represents the pressure difference across the bearing film.

Performance ratio

The load capacity is defined as:

$$W = \frac{1}{L}\int_L (p(x) - p_\mathrm{a})\,dx = \frac{p_\mathrm{d} + p_\mathrm{o}}{2} - \alpha\left(\frac{p_\mathrm{d} + p_\mathrm{o} - 2\,p_\mathrm{i}}{4}\right) - p_\mathrm{a} \tag{A.33}$$

The inlet pressure for which the load capacity is equal to 0 can thus be defined as:

$$p_{\mathrm{i},0} = \frac{p_\mathrm{d} + p_\mathrm{v}}{2} - \frac{p_\mathrm{d} + p_\mathrm{v} - 2\,p_\mathrm{a}}{\alpha} \tag{A.34}$$

The dam pressure can be expressed in terms of the geometrical parameters α and β and the inlet pressure p_i as:

$$p_\mathrm{d} = \frac{\alpha p_\mathrm{o} + 2\,\beta^3 p_\mathrm{i}\,(1-\alpha)}{\alpha + 2\,\beta^3\,(1-\alpha)} \tag{A.35}$$

Since the outlet restriction for $x = x_1$ and $x = x_4$ is assumed to be negligible we can state that:

$$p_\mathrm{o} = p_\mathrm{v} \tag{A.36}$$

The expressions for the no-load inlet pressure (A.34), dam pressure (A.35) and the outlet pressure (A.36) are substituted in the expressions found for the force density (A.29) and the mass flow density (A.32). Gives an expression for the performance ratio:

$$P = \frac{\bar{F}}{\bar{\dot{m}}} = f(p_\mathrm{a}, p_\mathrm{v}, \alpha, \beta, h_\mathrm{f}, L, \eta, \mathrm{R_s}, T) \tag{A.37}$$

Where f is an analytical function of the parameters indicated between the brackets.

A.5.3 Compressible case

The procedure for the compressible case is in many ways similar to the procedure presented above. However, the governing equation is now defined as:

$$\frac{\partial}{\partial x}\left(p\frac{\partial p}{\partial x}\right) = 0 \tag{A.38}$$

Therefore, the pressure profiles on section I, II and III are now defined globally as:

$$p(x, \alpha, L, p_\mathrm{i}, p_\mathrm{d}, p_\mathrm{o}) = \sqrt{Ax + B} \tag{A.39}$$

The qualitative pressure profiles for various values of β are shown in figure A.10.

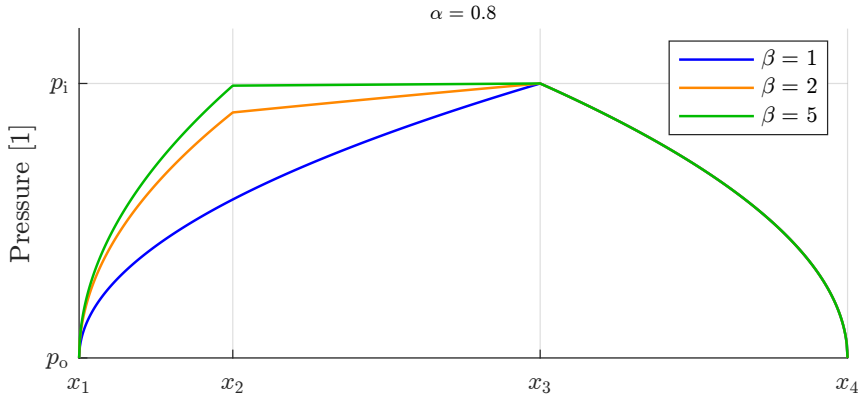

Figure A.10: Compressible pressure profiles for variable outlet restriction.

The expressions for the mass flow density and force density are identical to the ones presented in equations (A.29) and (A.32) respectively. However, the expression for the dam pressure p_d and the expression for the no-load inlet pressure are different. The pressure at the dam is now defined as:

$$p_\mathrm{d} = \sqrt{\frac{\alpha\,p_\mathrm{o}^2 + \beta^3\,p_\mathrm{i}^2(1-\alpha)}{\alpha + 2\beta^3\,(1-\alpha)}} \tag{A.40}$$

For the no-load inlet pressure, no analytical expression could be found. Therefore, this is solved numerically.

A.5.4 Optimised geometry

In this section, the theoretical performance of the three different concepts will be compared. First, the values for the relative dam length α and the relative pocket height β for which the performance ratio is maximised are found. Then, using those values for α and β, the force density and mass flow density are evaluated for a varying actuator length length L.

These analyses were performed using COMSOL, using the *General Form PDE* physics on a line geometry. The simplified Reynolds equation (A.2) should hold on the full domain. The supply pressure p_s is found using a *Global Equation*, such that the load capacity W (A.16) is equal to 0.

Variable outlet restriction

The geometry for the variable outlet restriction unit cell was shown in figure A.8. Shown in figure A.11 is the performance ratio P for varying values of α and β. The values for which the performance ratio is maximised are $\alpha = 0.748$ and $\beta = 1.864$.

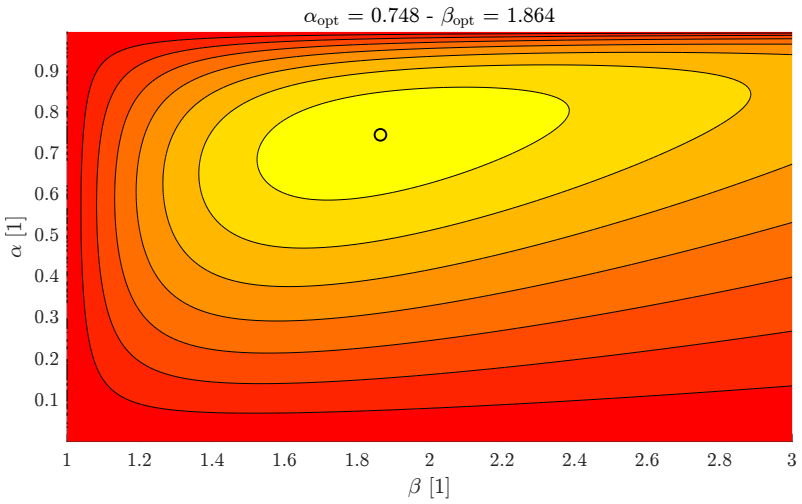

Figure A.11: Performance ratio contour plot for variable outlet restriction concept.

Pressure control

The geometry used for the analysis of the pressure control concept is schematically shown in figure A.12. Similar to as seen with the variable outlet restriction concept, the parameter α is related to the relative dam length, while the parameter β is related to the relative pocket height.

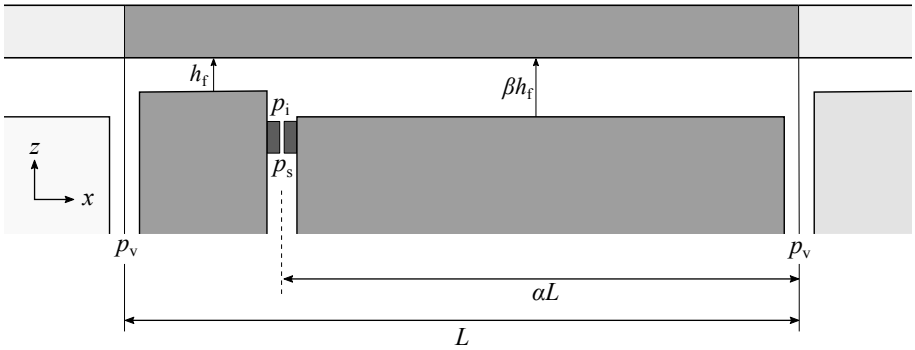

Figure A.12: Geometry for pressure control unit cell.

The results for the parameter sweep are shown in figure A.13. The values for which the performance ratio is maximised are $\alpha = 0.718$ and $\beta = 1.864$.

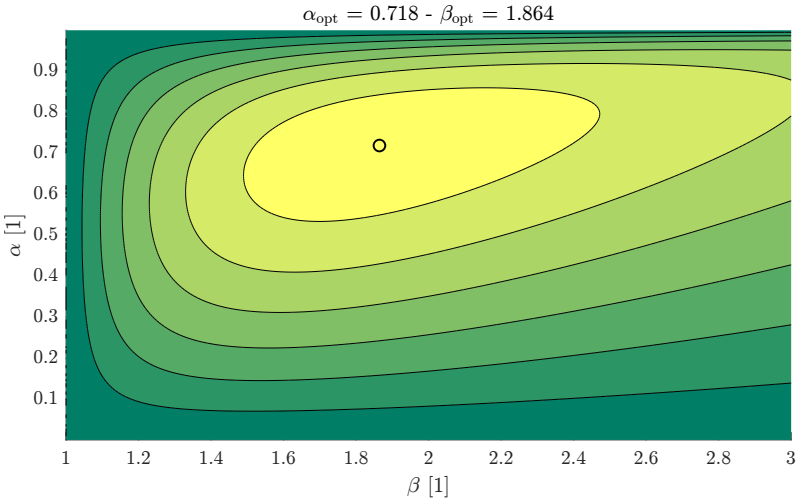

Figure A.13: Performance ratio contour plot for pressure control concept.

Variable pocket restriction

The geometry for the variable pocket restriction unit cell is shown in figure A.14. The inlet is located in the centre of the unit cell. The fly-height h_f is defined as the minimum film thickness. Varying values of Δh are then prescribed and evaluated for varying values of the actuator length L. The result for this analysis is shown in figure A.15a.

It becomes clear from figure A.15a that no local optimum exists. Instead, the optimum tilt angle is dependent on the actuator length. This is illustrated in figure A.15b. When comparing this concept to the other concepts, the value of Δh was set to $10\,\mu$m. This corresponds to the optimum tilt angle for an actuator length of $L = 10\,$mm.

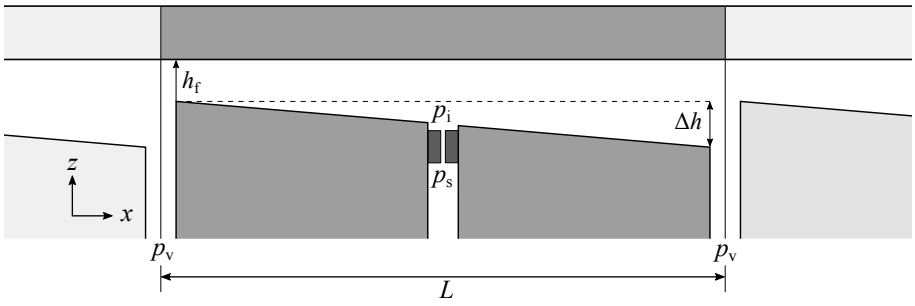

Figure A.14: Geometry for variable pocket restriction unit cell.

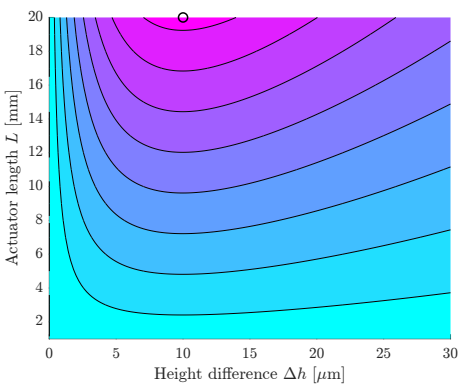

(a) Performance ratio for the variable pocket restriction concept.

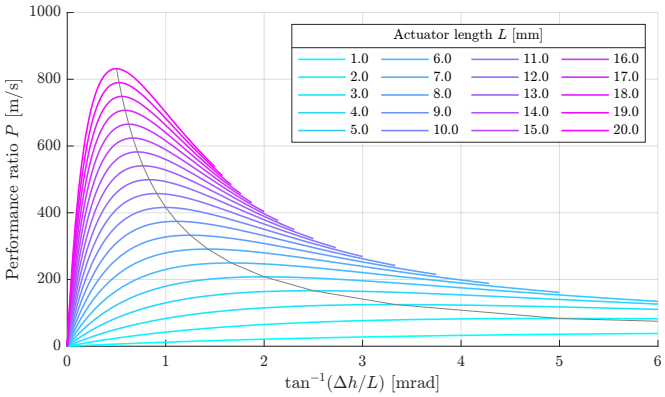

(b) Performance ratio as a function of the tilt angle.

Figure A.15

A.5.5 Performance comparison

The performance of the concepts is then evaluated for varying values of the actuator length. The values for used for α, β and Δh are summarised in table A.1. The values used for the physical parameters are shown in table A.2.

The resulting performance curves are shown in figure A.16. The dashed green line corresponds to the actuator geometry as shown in figure A.12. This geometry is only able to generate a shear force towards the right (i.e. unilateral), while the other two concepts can generate an equal force in both directions (i.e. bilateral). Therefore, in order to form a fair comparison, pairs of unit cells with opposing actuation direction should be placed are required. This effectively makes the required area twice as large. This is indicated by the solid green line. The theoretical performance of the variable pocket restriction and the variable outlet restriction concept are identical. Similar results were found by Verbruggen [6].

Table A.1: Optimal values found for α and β.

Concept	α	β	Δh [μm]
Stepped surface	0.718	1.864	-
Variable outlet restriction	0.748	1.864	-
Variable pocket restriction	-	-	10

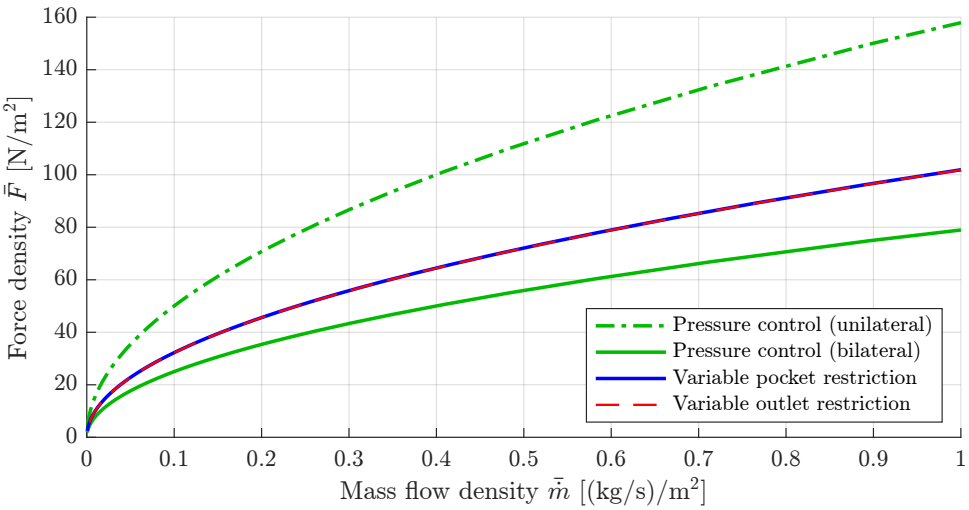

Figure A.16: Performance curves.

Table A.2: Variables used in performance analysis.

Description	Symbol	Value	Unit
Fly-height	h_f	10	μm
Ambient pressure	p_a	$100 \cdot 10^3$	Pa
Vacuum pressure	p_v	$50 \cdot 10^3$	Pa
Dynamic viscosity (air)	η	$18 \cdot 10^{-6}$	Pa $\cdot$ s
Specific gas constant (air)	$\mathrm{R_s}$	287	J/kg/K
Temperature	T	293	K

A.6 Conclusions

- The behaviour of the system is described using the simplified Reynolds equation, where only the Poiseuille flow is taken into account.
- The electrical analogy, in combination with the lumped restriction model can be used to gain insight into the behaviour of air bearing systems.
- Stiffness is obtained if the load capacity W is dependent on the film thickness h. Positive stiffness is required in order for the system to be stable.
- A commonly used method to create stiffness is to implement an inlet restriction. This could be a capillary tube, an orifice or a porous flow restrictor.
- The performance metric used in this research is the performance ratio P, defined as the unit force per unit area over the unit mass flow per unit area.
- For the pressure control concept and the variable outlet restriction concept, a local optimum can be found for the (2D) geometric parameters α and β, such that the performance ratio is maximised.
- For the variable pocket restriction concept, the tilt angle for which the performance ratio is optimised is dependent on the actuator length L.
- The performance curve of the variable outlet restriction concept identical to that of the variable pocket restriction concept. Both have a higher theoretical performance than the bilateral pressure control concept. Note that this is an approximation, valid for limit cases in a 2D geometry.

Appendix B

Conceptual design

In this chapter, the proposed manufacturing method is presented in a conceptual way. It can be seen as a simplified approach, where the resulting system is only determined by the laws of trigonometry. Practical implications, such as manufacturing imperfections and resin behaviour will not be considered here. These will be discussed in appendix D.

B.1 Motivation

As explained in section 1.2, there are three methods that can be used to generate a net shear force: the pressure control concept, the variable pocket restriction concept and the variable outlet restriction concept. In appendix A.5.4, it was shown that the performance of the variable outlet restriction concept is as good as that of the variable pocket restriction concept.

The variable pocket restriction concept consists essentially out of only two mating parts. This is identified as a potential benefit in terms of manufacturability. However, the dimensional tolerances on these two parts are extremely tight. This makes manufacturing them very challenging, especially using traditional, subtractive manufacturing methods. Therefore, the design of the system was slightly altered, such that a novel manufacturing method could be used. Through this method, the tolerances become obsolete, as the accuracy is inherent to the manufacturing process. The method will be described below. Alternative designs and manufacturing methods will be briefly discussed at the end of this chapter.

B.2 Conceptual requirements

The demonstrator developed by Verbruggen [6] was produced using subtractive manufacturing techniques. Seven pins were machined separately and then fixed onto a plate with 7 holes. It would become increasingly hard to meet the required manufacturing tolerances for an increasing number of pins using this method. Tight tolerances in general lead to an expensive manufacturing process. The aim is to redesign the system such that it becomes less sensitive for manufacturing errors. If this can be achieved, the manufacturing cost of the system can be reduced.

Casting is a manufacturing technique that has been around for many centuries. However, it is not often that the dimensional tolerances of the final product are as tight as required in this application. Therefore, not much information regarding this type of high precision casting of macro sized features can be found in the literature. This study can therefore be seen as an exploration to investigate what is possible using the developed manufacturing method. The conceptual requirements are presented below:

- The system should have an active area which is larger than the demonstrator developed previously by Verbruggen [6].
    - The active area should be comprised of several identical unit cells.
    - A hexagonal close packing should be used in order to maximise the amount of unit cells per area.
- An inlet restriction should be manufactured.

- The inlet conductivity should be well defined and repeatable between unit cells.
- Ideally the amount of (post-)processing steps should be minimised, e.g. no drilling small holes.

- An outlet restriction with a well defined geometry needs to be manufactured.
  - The concentric outlet film thickness should have a thickness tens of micrometres, with a tolerance of 1 μm.
  - The outlet film length should have a length of several millimetres, with a tolerance of 0.1 mm.
  - Each pin needs to be concentric with its mating hole.
  - The outlet film thickness should be radially symmetrical in the concentric case.

- A pocket restriction needs to be manufactured.
  - A discrete step should be created between the top surface of the bearing plate and the top surface of each pin. The height difference should be 10-20 μm, with a tolerance of 1 μm.
  - The waviness of the bearing surface should be minimised in order to allow for a low fly-height and decrease the deformation of the substrate.

- Air should be supplied to each pin from a single plenum chamber, rather than through a manifold. The same goes for the vacuum chamber.

B.3 Proposed manufacturing method

The proposed manufacturing method is to cast resin in a two-part mould, to create a system as shown in figure B.1. Casting resin has been used by Snoeys et.al. to produce the counter surface for an aerostatic bearing [19]. In a similar way, concrete casting has been used by Hahm et. al. to produce aerostatic guideways [20]. Though, to the knowledge of the author, it has not been used as presented below, where high dimensional accuracy and stability are required.

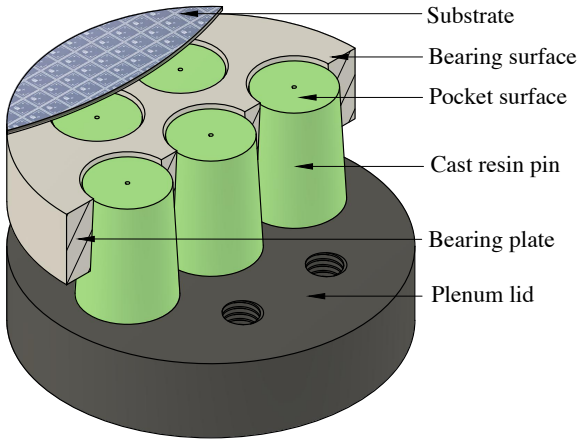

Figure B.1: Schematic representation of the proposed system.

B.3.1 Conceptual procedure

The pins are created by casting resin in a mould, as shown in figure B.2a. The mould is comprised of the bearing plate and the plenum lid, which are clamped together during casting. The holes in the plenum lid are sealed from the bottom, which is not shown in the figure for simplicity.

After curing, the mould is separated and the pins should be fixed onto the plenum lid, as indicated by the ragged edges. Since the holes are tapered δ, a narrow radial outlet film h_o is created by enforcing a certain fixed distance t_v between the two plates. This is shown in figure B.2b.

The geometry of each pin is the exact negative of its mating hole. This ensures that each pin is aligned with each hole. Any difference between the location of the hole in the bearing plate and the location of the hole in the plenum lid will not be transferred to the final location of the pin. The outlet film thickness is therefore also radially symmetric. The sacrificial material (indicated in red) is then removed in order to create the pocket restriction.

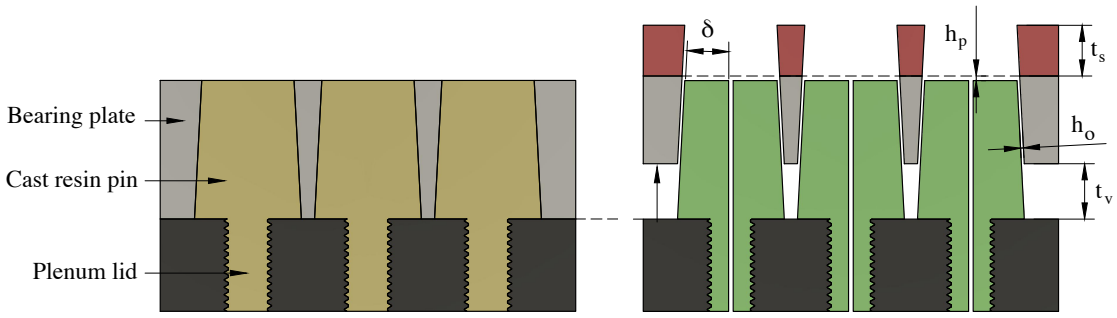

(a) System during casting. (b) System after separating mould.

Figure B.2: Cross section of system shown in figure B.1.

B.3.2 Outlet film thickness resolution

It is desired that the outlet film thickness can be controlled with a high resolution. Ideally, potential manufacturing errors should not influence the outlet film thickness. Since the holes in the bearing plate are tapered, a radial outlet film can be created by enforcing a certain distance t_v between the bearing plate and the plenum lid after curing. This was shown in figure B.2b. The cavity that is created due to this translation serves as the vacuum chamber, to which all outlet restrictions flow. Using trigonometry, the outlet film thickness can be written as:

$$h_\mathrm{o} = t_\mathrm{v} \, \tan\delta \cos\delta \tag{B.1}$$

Where t_v represents the thickness (i.e. height) of the vacuum chamber and δ represents the taper angle. If the taper angle is chosen small (e.g. $\delta = 1/100\,\mathrm{rad}$), the outlet film thickness can be written as:

$$h_\mathrm{o} \approx t_\mathrm{v}\,\delta = \frac{t_\mathrm{v}}{100} \tag{B.2}$$

This means that for every 1 mm distance that is enforced between the plates creates, the radial outlet film thickness increases by $10\,\mu$m. Also, the outlet film thickness is independent of the diameter of the hole in the bearing plate. This means that any deviation from the required hole size will not influence the outlet film thickness.

B.3.3 Pocket restriction

In order to create the pocket restriction, there needs to be a well defined height difference between the bearing surface and the top surface of the pins. This is achieved by removing the sacrificial material (indicated in red in figure B.2b) from the bearing plate after curing. After this step, the system looks as shown in figure B.3. The height of the pocket is defined as:

$$h_\mathrm{p} = t_\mathrm{v} - t_\mathrm{s} \tag{B.3}$$

This means that both the thickness of the sacrificial material t_s as well as the height of the vacuum chamber t_v influence the final pocket height. This poses a challenge, since the pocket height should ideally be controlled with $1\,\mu$m accuracy.

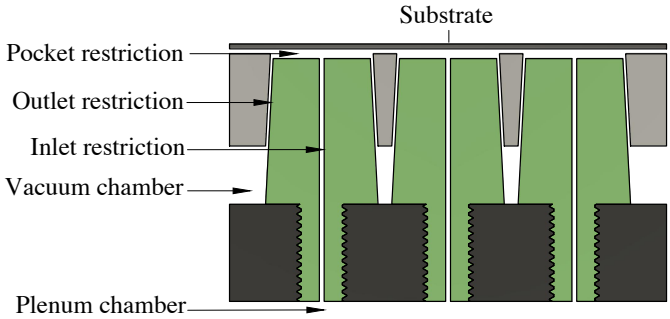

Figure B.3: Cross section of the final system.

B.4 Alternative designs

B.4.1 Deformable restriction

In an aim to lower the manufacturing tolerances, it was considered to place a deformable, porous material in the outlet restriction. This could for example be a spongelike, open cell foam, as shown in green in figure B.4. This way, the outlet restriction would no longer be highly dependent on the clearance between the two mating parts, and thereby allowing for less stringent manufacturing tolerances. However, if the system would consist of several unit cells, the discrepancy between the hole and pin locations could still become an issue.

The flow of viscous fluids through a deformable matrix has been researched by L.W. Morland [21]. The possibility of using compacted-cementitious composites as a porous restrictor for aerostatic bearings is investigated by Z.M.V. Missagia et al. [22]. This research is mainly aimed at manufacturing porous restrictions which can be used as inlet restrictions. Research into the properties of sintered metal porous media is presented in W. Zhong [16]. However, the stiffness of sintered porous metal is most likely too high.

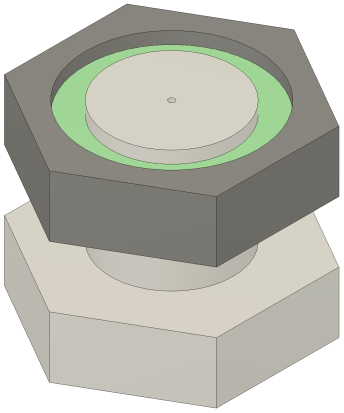

Figure B.4: Deformable outlet restriction (shown in green).

B.4.2 Compliant design

Alternatively, a compliant version of the system could be made from a single piece of material as shown in figure B.5. The tolerance on locations of each pin with respect to each hole would removed. The pins in the system could be produced using a milling operation. Afterwards, the slits could be created using another manufacturing technique. Manufacturing thin slits with a high aspect ratio poses a challenge in terms of manufacturing. It could potentially be done with water jet laser cutting [23]. Using this technique, slits as narrow as 50 μm have been produced, with an aspect ratio of 1:400.

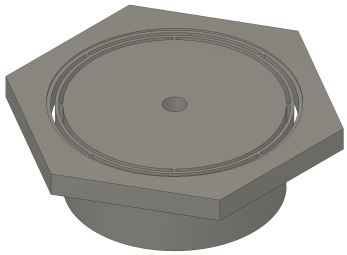

Figure B.5: Compliant monolithic bearing surface.

B.5 Alternative manufacturing techniques

Some alternative manufacturing methods to create exactly mating components are presented below. The pins should be the exact negative of the hole, or vice versa.

B.5.1 Electrical Discharge Machining

In order to produce an exact negative of a certain shape, sinker Electrical Discharge Machining (EDM) can be used. A very high potential difference is created between the tool-electrode (most often made of copper or graphite) and the workpiece-electrode (electrically conductive), which are both submerged in a dielectric liquid. The tool and workpiece are brought in very close proximity, while the potential difference is increased. At some point, dielectric breakdown occurs in the liquid and an electric arc is created. This essentially melts or evaporates the material (mostly of the workpiece), and creates significant heat. The removed material is flushed away by the dielectric liquid. This cycle is then repeated until the desired shape is created.

The clearance that occurs between the electrode and the workpiece can be controlled by controlling the current density. In theory, this process should produce an exact negative of the electrode in the workpiece. Unfortunately, the electrode is also eroded in the process [24], which makes it harder to predict the final film geometry. Also, a new electrode would have to be produced each time, which is a very costly process. EDM in general is an expensive manufacturing method and is therefore deemed not suitable for this research.

B.5.2 Electrochemical machining

Electrochemical machining (ECM), is a process where material is removed by dissolving it using electric current [25]. A DC current is passed from the workpiece (anode) to the tool (cathode) through an electrolyte. The tool is commonly made of copper or graphite. The gap between the tool and the workpiece is typically between 80 and 800 μm. The rate at which the machining takes place depends on the rate at which the workpiece dissolves. Contrary to EDM, there is no tool-wear in ECM. Also, no thermal or mechanical stress is induced in the workpiece. However, ECM requires high capital investment and is an expensive process, due to the high power consumption. Therefore it was decided that this manufacturing method is not suitable for this research.

B.5.3 CNC machining

More traditional manufacturing methods such as milling could in theory be used to produce the two mating parts. Using a state of the art CNC milling machine, tolerances of $\pm 1\,\mu$m can be achieved [26]. Even though it might be possible to create a system using this technique, it will be an expensive operation and creating the inlet restrictions will be challenging. Next to that, this manufacturing method is not very novel. It has therefore been decided to use this manufacturing method in this research. Though, a working demonstrator could potentially be produced using this method.

B.6 Conclusions

- The geometry of the film thickness is defined by the geometry of the mating parts. Due to the nature of the physics involved, the tolerances very tight. Typically $< 1\,\mu$m on a feature size of 10 mm.
- A novel manufacturing method is presented which makes the final geometry relatively insensitive for manufacturing errors.
    - By making use of a two-part mould, any discrepancy between the hole locations in the two plates will not influence the position of each pin with respect to each hole.
    - An oversized hole in the bearing plate will also produce an oversized pin. Hence, any deviation in hole diameter will not influence the outlet film thickness.
    - By making the holes tapered, a radial outlet film can be created by enforcing a distance between the two parts of the mould after casting.
    - By making this taper very small, the outlet film thickness can be controlled with a high resolution. In other words: the outlet film thickness is insensitive for variations in the distance enforced between the plates.
- The redundancy which is present for the radial outlet film thickness is not present for the pocket height.
    - For the pocket restriction, the thickness of sacrificial material as well as the distance between the plates need to be defined with high accuracy.
- In order to generate a force on the substrate, the bearing plate needs to be able to move with respect to the pins in x- and y- direction and rotate about the z-axis.

Appendix C

Modelling

In this chapter, the numerical model which is used to describe and predict the behaviour of the system is explained. The model is eventually used to select a set of suitable design parameters for the demonstrator. These are presented in appendix D.1.

The model is created using COMSOL Multiphysics 5.6 [18]. Words that refer to specific terms used in COMSOL are written in *italic* font. First, the expected behaviour is described qualitatively, based on intuitive understanding of the theory presented in appendix A. The set-up of the model is explained in appendix C.1. Both a stationary and a dynamic analysis is performed. These are explained in more detail in appendices C.2 and C.3 respectively. The results of the numerical analysis are presented in appendix C.4. In all simulations, an net shear force in positive x-direction is generated. Similar results can be obtained for actuation in y-direction, or x, y-direction.

Up to this point, the geometry is assumed to perfectly defined and the bodies are assumed to be rigid. In appendix C.6, the influence of manufacturing imperfections is investigated. The influence of deformation of the bodies (i.e. the film geometry) due to the pressure gradient is studied in appendix C.7.

C.1 Nominal model

C.1.1 Metric and definitions

Performance ratio

The perfomance ratio P introduced in appendix A.5 will be used to quantify the performance of the system. The aim is to generate a high force density $\bar{F}$ for a low mass flow density $\bar{\dot{m}}$, i.e. maximise P.

Concentric and eccentric fly-height

The concentric fly-height $h_{\mathrm{f,c}}$ is prescribed by the user. By definition this is equal to the eccentric fly-height for $\varepsilon = 0$, as shown in equation (C.1a). The eccentric fly-height $h_{\mathrm{f,e}}$ is a result of the numerical analysis. It is defined as the fly-height for which the no-load condition is satisfied, given a certain supply and vacuum pressure. This is in general not equal to the concentric fly-height (C.1b).

$$h_{\mathrm{f,c}} = h_{\mathrm{f,e}}(\varepsilon = 0) \tag{C.1a}$$

$$h_{\mathrm{f,c}} \neq h_{\mathrm{f,e}}(\varepsilon \neq 0) \tag{C.1b}$$

Concentric and eccentric film thickness

Similar to the fly-height, the concentric radial outlet film thickness is defined by the user. This is also referred to as the nominal outlet film thickness. The outlet film thickness can be changed by moving the bearing plate in x, y-direction with respect to the pin, which is assumed to be fixed in space. This is referred to as actuation (of the bearing plate). The amount of actuation is defined by the dimensionless eccentricity ratio ε, which varies between 0 (concentric) and ± 1 (fully eccentric).

The eccentric outlet film thickness is then defined as:

$$h_{o,e}(\varepsilon, \varphi) = h_{o,c}\,(1 + \varepsilon\,\cos\varphi) \tag{C.2}$$

Where the local angle in the x, y plane with regards to the positive x-axis φ is defined as:

$$\varphi = \tan^{-1}(y/x) \tag{C.3}$$

The eccentric outlet film thickness for varying values of ε is shown in figure C.1. Since actuation in positive x-direction is modelled, the outlet film thickness will be narrowest at $\varphi = \pi$ rad, as shown in figure C.1b. This corresponds to the orange line shown in figure C.1a.

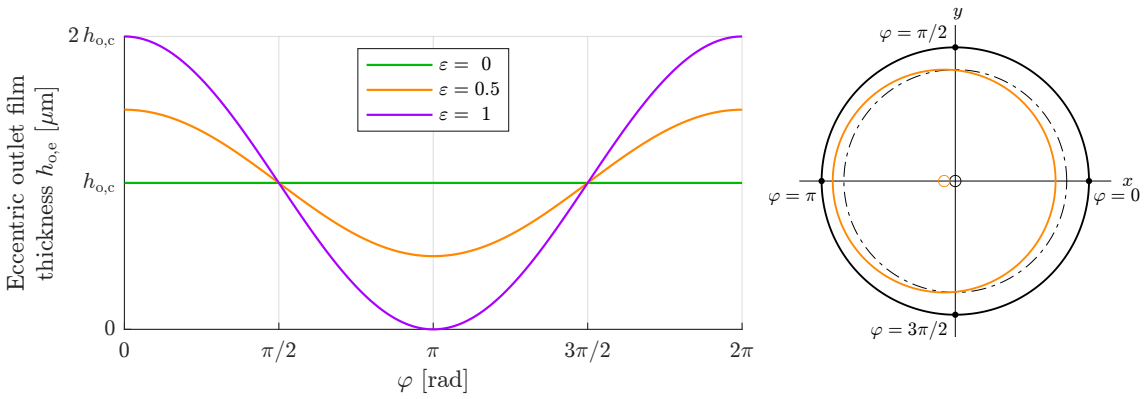

(a) Outlet film thickness for varying values of ε.

(b) Schematic representation for $\varepsilon = 0.5$.

Figure C.1: Schematic representation of the outlet film thickness.

Similar to the eccentric fly-height. The concentric outlet film thickness is by definition equal to the eccentric outlet film thickness for $\varepsilon = 0$, as shown inequation (C.4a). In general the eccentric outlet film thickness will not be equal to the concentric outlet film thickness, as shown inequation (C.4b). Except for $\varphi = \pi/2$ and $\varphi = 3\pi/2$, as can be seen in figure C.1a.

$$h_{o,c} = h_{o,e}(\varepsilon = 0) \tag{C.4a}$$

$$h_{o,c} \neq h_{o,e}(\varepsilon \neq 0) \tag{C.4b}$$

C.1.2 Expected behaviour

Concentric case

For the concentric case, the eccentricity ratio ε is equal to 0. This means that the pin is located concentrically in the hole. The outlet film thickness is equal everywhere and therefore the pressure distribution in the pocket is symmetric. Air will flow from the inlet, radially towards the outlet. The shear force is equal in all directions, hence no net shear force will be generated. The system is essentially a regular vacuum pre-loaded aerostatic bearing, with an outlet restriction. The substrate will levitate at the concentric fly-height $h_{f,c}$, defined by the user. When imagining the lumped restriction model, a certain ratio of restriction magnitudes exists ($R_i : R_p(h_f) : R_o$). This ratio of restriction magnitudes will change for the eccentric case.

Eccentric case

In order to generate a net shear force, the pin is moved eccentric with respect to the hole, i.e. $\varepsilon \neq 0$. As a result, the film thickness in the outlet varies locally and therefore an asymmetric pressure distribution is created in the outlet restriction. This will cause the pressure distribution on the bearing surface to become asymmetric as well.

Moving the pin eccentric with respect to the hole will decrease the magnitude of the outlet restriction R_o. Since the supply and vacuum pressure are fixed, the ratio of pressure drops across each restriction will change in order to restore equilibrium. Since the magnitude of the inlet restriction R_i is assumed to be fixed, changing the outlet restriction will cause a change of the

pocket restriction. A change in the magnitude of the pocket restriction in reality means a change in fly-height h_f. The fly-height will change from the concentric fly-height $h_\mathrm{f,c}$ to the eccentric fly-height $h_\mathrm{f,e}$. Since the magnitude of the outlet restriction decreases, an increase in stiffness can be expected upon actuation.

C.1.3 Model structure

One unit cell of the system is modelled using the *General Form Boundary PDE* physics module in COMSOL. Using this package, a partial differential equation can be solved on the boundary (i.e. surface) of a geometry. The partial differential equation used to model the behaviour of the air flow in the thin film is the simplified Reynolds equation equation (A.2).

The levitating substrate is modelled by defining the fly-height h_f as a variable, in combination with the no-load condition. The latter is implemented through a *Global Equation* in the *Global ODEs and DAEs* physics. The no-load condition states that the instantaneous load capacity should equal 0. This can be written as:

$$W = \int_A \Big(p\left(p_\mathrm{s}, p_\mathrm{v}, h_\mathrm{f}\right) - p_\mathrm{a} - p_\mathrm{sub} \Big)\, dA = 0 \tag{C.5}$$

Where the pressure distribution below the substrate p is dependent on the boundary conditions (i.e. supply and vacuum pressure p_s and p_v) and the film geometry (i.e. the fly-height h_f). The average pressure below the substrate should equal the sum of the ambient pressure p_a and the distributed weight of the substrate p_sub. This is assuming quasi static behaviour of the system.

Step 1 - Concentric case

First, the supply pressure p_s for which the substrate will levitate at the prescribed concentric fly-height $h_\mathrm{f,c}$ needs to be found. Therefore, the following system of equations is solved:

- Simplified Reynolds equation
- No-load condition that finds suitable supply pressure p_s
    - Given the prescribed vacuum pressure p_v and prescribed concentric fly-height $h_\mathrm{f,c}$

Two of the three variables (p_s, p_v, $h_\mathrm{f,c}$) need to be prescribed in order to solve the system of equations. It was decided to prescribe the vacuum pressure and the fly-height. Prescribing the vacuum pressure ensures that the vacuum pump used in the demonstrator will be able to generate the required vacuum pressure, at the required flow rate. Prescribing the fly-height enables the user to directly find the correct supply pressure to reach the desired fly-height, rather than through an iterative process. The model is then solved such that both the simplified Reynolds equation and the no-load condition hold. The result is a pressure profile $p(x, y, z)$ and a supply pressure p_s.

Step 2 - Eccentric case

A net shear force is generated by varying the film thickness in the outlet, i.e. introducing eccentricity. As explained, this will lead to a new pressure distribution, hence a new fly-height $h_\mathrm{f,e}$. This means that the fly-height is not prescribed, but in fact is calculated by solving the no-load condition. The system of equations is solved:

- Simplified Reynolds equation
- No-load condition that finds the new eccentric fly-height $h_\mathrm{f,e}$
    - Given the supply pressure and vacuum pressure adapted from step 1

The generated shear force can then be calculated by evaluating the integral of the pressure gradient over the surface. The shear force density is defined as:

$$\bar{F}_x = \frac{1}{A}\int_A -\tau_x \, dA \tag{C.6a}$$

$$= \frac{1}{A}\int_A -\eta\frac{\partial u}{\partial z} \, dA \tag{C.6b}$$

$$= \frac{1}{A}\int_A -\frac{h}{2}\frac{\partial p}{\partial x} \, dA \tag{C.6c}$$

The stationary study is explained in more detail in appendix C.2.

Step 3 - Stationary stiffness

In order to determine the stiffness of the system, the change in load capacity for a change in fly-height needs to be calculated. At this point, the no-load condition no longer holds, since this would make it impossible to observe a change in load capacity. Therefore, only the Reynolds equation is solved, while the perturbed fly-height is prescribed. The system of equations that is solved is defined as:

- Simplified Reynolds equation
  - Supply and vacuum pressure adapted from step 1
  - Manual perturbation of the eccentric fly-height $h_{\mathrm{f,c}}$ found in step 2.

Step 3 - Dynamic stiffness

Alternatively, the dynamic stiffness can be determined by solving the perturbed Reynolds equation, which is implemented in a separate *General Form Boundary PDE*. The results from the stationary study are used. The procedure then looks as follows:

- Repeat step 1 - find supply pressure p_{s}
- Repeat step 2 - find eccentric fly-height $h_{\mathrm{f,e}}$
- Perturbed Reynolds equation
  - Prescribed perturbation of the eccentric fly-height found in step 2.

This method is shown in detail in appendix C.3.

C.1.4 Geometry

The global geometry of the unit cell is shown in figure C.2. Air flows from the recess Ω_{r} through the pocket film Ω_{p} into the outlet film Ω_{o}. Neighbouring unit cells are separated by a dam Ω_{d} which is in reality created by the bearing plate. The dashed line indicates the cross section, as shown in figure C.3. The total areal of the bearing face is defined as:

$$A = \Omega_{\mathrm{r}} + \Omega_{\mathrm{p}} + \Omega_{\mathrm{d}} \tag{C.7}$$

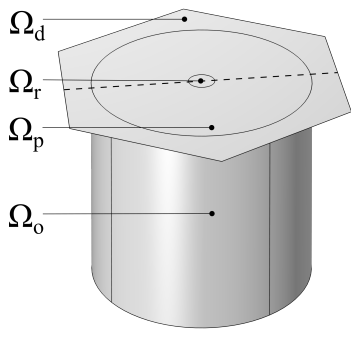

Figure C.2: Geometry with boundaries indicated.

The values used in the nominal model are shown in table C.1. Film thicknesses are defined on each boundary as specified in table C.2. This is implemented through the use of four different *Variables* groups, each defined on the respective boundary.

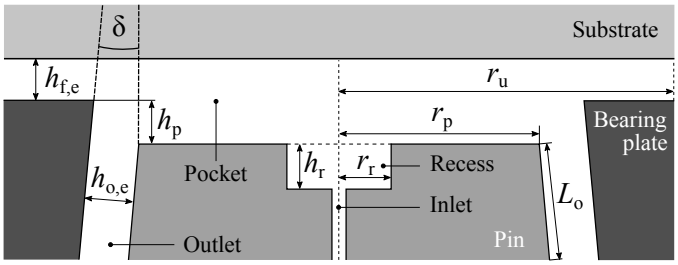

Figure C.3: Schematic cross section of unit cell.

Table C.1: Relevant dimensions of the geometry shown in figure C.3.

Symbol	Value [mm]	Symbol	Value [μm]
r_r	0.6	h_r	200
r_p	5	h_p	20
r_u	6.25	$h_{f,c}$	15
L_o	10	$h_{o,c}$	50

Table C.2: Film thicknesses for stationary study.

Boundary	Section	Expression for h	Value [μm]
Ω_d	Dam	$h_{f,e}$	15
Ω_p	Pocket	$h_{f,e} + h_p$	35
Ω_r	Recess	$h_{f,e} + h_p + h_r$	235
Ω_o	Outlet	$h_{o,e}$	50

C.1.5 Geometry ratios

Pin ratio

The pin ratio is defined as:

$$\varrho = \frac{r_p}{r_u} \tag{C.8}$$

Where r_p is the pocket radius and r_u is the radius of the inscribed circle of the hexagonal unit cell. This is essentially the 3D equivalent of the parameter α that was used in appendix A.5.

Pocket ratio

The pocket ratio is defined as:

$$\beta = \frac{h_p + h_{f,c}}{h_{f,c}} \tag{C.9}$$

Where h_p is the pocket height and $h_{f,c}$ is the concentric fly-height. This is in fact the same as the parameter β that was used in appendix A.5. As in the 2D analysis, the fly-height is assumed to be fixed. In other words, the pocket ratio is calculated with respect to the concentric fly-height. Note that the force density and mass flow density however are calculated using the eccentric fly-height $h_{f,e}$.

C.1.6 Assumptions

Within this numerical model, several assumptions are made. These are additional to the general assumptions made when using Reynolds equation. The assumptions made in the numerical model are:

- The flow is assumed to be viscous throughout the full film. This means that the entrance section is ignored, as well as inertial effects occurring on the transition between the pocket and the outlet.
- It is assumed that linearisation of the governing equation by using a small perturbation from the steady state equilibrium provides sufficient accuracy. At least for small oscillation amplitudes [11].
- It is assumed that there is no relative motion between the bearing surface and the substrate, i.e. Couette flow is assumed to be negligible. This means that the substrate will not move laterally, even though a lateral force will be generated.
- The supply and vacuum pressure are assumed to be independent of the flow, i.e. they behave as an ideal supply and vacuum source.
- The inlet conductivity G_i is assumed to be constant and independent of the flow through the restriction.
- Any dynamic behaviour within the inlet restriction assumed to be negligible.
- The unit cell geometry is assumed to be part of an infinite grid of unit cells.
- The geometry is assumed to be rigid. The influence of elastic deformation is studied in appendix C.7.

C.1.7 Mesh and solver settings

A *Free Triangular* mesh is used on the recess, pocket and dam boundary (Ω_r, Ω_p, Ω_d). The mesh was calibrated for general physics, using a predefined *Finer* element size. On the pocket edge $\partial\Omega_\mathrm{p}$, the mesh is refined using the *Distribution* command.

No changes have been made to the solver settings. This means that a suitable numerical solver was selected by COMSOL.

C.2 Stationary analysis

In this study, the performance of the system is determined. Also, the stationary stiffness can be calculated, by manually perturbing the fly-height.

C.2.1 Governing equations

The simplified Reynolds equation is used to describe the behaviour of the system in the stationary study. Using the *General Form Boundary PDE* physics, the equation can be solved on the boundary of a certain geometry. The *General Form PDE equation* is defined within COMSOL as:

$$e_\mathrm{a}\frac{\partial^2 p}{\partial t^2} + d_\mathrm{a}\frac{\partial p}{\partial t} + \nabla\cdot\Gamma = f \tag{C.10}$$

The source term f defines how much mass is accumulating or disappearing over time. Since we assume that the system is stationary, this term is set to 0 $\mathrm{kg}/(\mathrm{m}^2\cdot\mathrm{s})$. The damping coefficient d_a and mass coefficient e_a are set to 0. The simplified Reynolds equation is implemented by defining the conservative flux as:

$$\Gamma = \frac{ph^3}{12\eta R_\mathrm{s} T}\nabla p \tag{C.11}$$

The dynamic viscosity η and ambient temperature T are assumed to be constant, as shown in table C.3.

Table C.3: Physical variables.

Parameter	Symbol	Value	Unit
Dynamic viscosity of air	η	$18 \cdot 10^{-6}$	$\mathrm{Pa \cdot s}$
Specific gas constant of air	R_s	287	J/kg/K
Ambient temperature	T	293	K

C.2.2 Boundary conditions

The three relevant edges of the unit cell are the inlet, unit cell and outlet edge. They are indicated in figure C.4. The boundary conditions defined on these edges will be explained below.

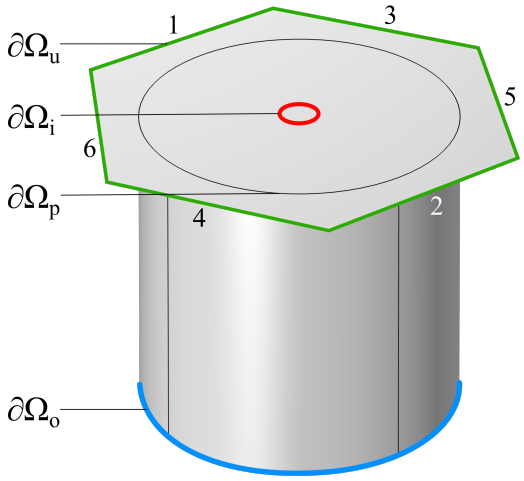

Figure C.4: Unit cell geometry with edges indicated.

Inlet

In general, the volumetric flow through a restriction is defined as:

$$\dot{q}_\mathrm{i} = \frac{\Delta p_\mathrm{i}}{R_\mathrm{c}} \tag{C.12}$$

Where Δp_i is the pressure difference across the inlet restriction $(p_\mathrm{s} - p_\mathrm{i})$ and R_i represents the magnitude of the inlet restriction. The flow restriction of a capillary is defined by its length L_c and inner diameter d_c as:

$$R_\mathrm{i} = \frac{128\,\eta L_\mathrm{c}}{\pi d_\mathrm{c}^4} \tag{C.13}$$

Substituting this expression for the flow restriction in equation (C.12) gives:

$$\dot{q}_\mathrm{i} = \frac{\Delta p_\mathrm{i}}{R_\mathrm{f,i}} = \frac{\pi d_\mathrm{c}^4}{128\,\eta L_\mathrm{c}}(p_\mathrm{s} - p_\mathrm{i}) \tag{C.14}$$

Where p_s is the supply pressure (i.e. upstream the capillary) and p_i is the inlet pressure at the film (i.e. downstream the capillary). In order to find the mass flow rate, the volumetric flow rate is multiplied by the density.

$$\dot{m}_\mathrm{i} = \dot{q}_\mathrm{i}\rho \tag{C.15}$$

For the density ρ, the average density $\bar{\rho}$ is used. This is calculated using the ideal gas law as:

$$\bar{\rho}_\mathrm{i} = \frac{p_\mathrm{s} + p_\mathrm{i}}{2}\frac{1}{R_\mathrm{s}T} \tag{C.16}$$

The mass flow therefore becomes:

$$\dot{m}_\mathrm{i} = \dot{q}_\mathrm{i}\bar{\rho}_\mathrm{i} = \frac{\pi d_\mathrm{c}^4}{128\eta L_\mathrm{c}}(p_\mathrm{s} - p_\mathrm{i})\,\frac{p_\mathrm{s} + p_\mathrm{i}}{2}\frac{1}{R_\mathrm{s}T} = \frac{\pi d_\mathrm{c}^4}{256\,\eta R_\mathrm{s} T L_\mathrm{c}}(p_\mathrm{s}^2 - p_\mathrm{i}^2) \tag{C.17}$$

The mass flow through a capillary is proportional with the difference of the squared pressures. The constant of proportionality will be referred to as the inlet conductivity G_i, which is the reciprocal of the inlet restriction R_i.

$$G_\mathrm{i} = \frac{\pi d_\mathrm{i}^4}{256\,\eta R_\mathrm{s} T L_\mathrm{i}} \tag{C.18}$$

In reality, the conductivity is dependent on the pressure difference across the restriction. A higher pressure difference causes a higher flow rate and therefore a lower conductivity. In this research, the inlet conductivity has been determined experimentally, as shown in appendix D.2.1. The magnitude of the inlet conductivity in the model is taken as a constant from the empirical data, for the expected pressure drop (i.e. a zeroth order approximation). The mass flow can then be simply written as:

$$\dot{m}_\mathrm{i} = G_\mathrm{i}\,(p_\mathrm{s}^2 - p_\mathrm{i}^2) \tag{C.19}$$

This is implemented through a *Flux/Source* boundary condition defined as:

$$g = \frac{G_\mathrm{i}}{2\,\pi r_\mathrm{r}}\,(p_\mathrm{s}^2 - p^2) \qquad \text{on } \partial\Omega_\mathrm{i} \tag{C.20}$$

In reality there will be a very small pressure drop from the outlet of the capillary to the edge of the recess. However, the restriction created by the recess is negligible compared to other restrictions present in the system.

Unit cell edge

The unit cell is assumed to be surrounded by an infinite grid of identical unit cells. Therefore, any air that flows across a boundary has to enter at the opposing boundary and vice versa. This means that the pressures have to be equal on opposing edge. The pressure gradient needs to be continuous, which means that the derivative needs to be equal and opposite on opposing edges. This can be written as:

$$p_1 = p_2 \qquad p_3 = p_4 \qquad p_5 = p_6 \tag{C.21a}$$

$$\nabla p_2 = -\nabla p_1 \qquad \nabla p_4 = -\nabla p_3 \qquad \nabla p_6 = -\nabla p_5 \tag{C.21b}$$

Where the subscripts refer to the edges as indicated in figure C.4.

This is implemented by defining six *Linear Extrusion* coupling operators: one on each unit cell edge. On the edges 1, 3 and 5, a *Dirichlet Boundary Condition* is defined, where the solution should be equal to the solution on the opposing edge. Thereby ensuring that equation (C.21a) is satisfied. On the edges 2, 4 and 6, a *Flux/Source* boundary condition is used, where the flux is defined as the inverse of the flux on the opposing edge. This ensures that equation (C.21b) holds.

Outlet

The air flows through the outlet restriction, across the outlet edge $\partial\Omega_\mathrm{o}$ into a vacuum chamber. The restriction posed by this vacuum chamber is assumed to be negligible compared to the outlet restriction. Therefore, the pressure at the outlet edge Ω_o is assumed to be constant and equal to the vacuum pressure. The vacuum pressure is assumed to be independent of the flow and therefore constant. This is implemented in the model using a Dirichlet boundary condition, defined as:

$$p = p_\mathrm{v} \qquad \text{on } \partial\Omega_\mathrm{o} \tag{C.22}$$

C.2.3 Initial conditions

The system is not sensitive for the initial condition and converges in almost all cases. Except when the initial pressure is chosen to be equal to 0 Pa, since this would mean that the density is equal to 0 $\mathrm{kg/m^3}$. In this model, the initial pressure is defined as:

$$p = p_\mathrm{a} \qquad \text{on } \Omega_\mathrm{r},\ \Omega_\mathrm{p},\ \Omega_\mathrm{d}, \text{ and } \Omega_\mathrm{o} \tag{C.23}$$

C.2.4 Evaluated variables

The main parameters of interest in are the performance and stiffness of the system.

Performance

The shear force density is determined by integrating pressure gradient (both x and y) over the full surface of the unit cell, as indicated in equation (C.7).

$$\bar{F}_x = \frac{1}{A}\int_A -\frac{h}{2}\frac{\partial p}{\partial x}\, dA \tag{C.24}$$

The mass flow is determined by taking the integral of the defined inlet flux, which is simply equal to the mass flow:

$$\dot{m}_\mathrm{i} = \int_{\partial\Omega_\mathrm{r}} \frac{G_\mathrm{i}}{2\pi r_\mathrm{r}} \left(p_\mathrm{s}^2 - p_\mathrm{i}^2\right) dL = G_\mathrm{i}\left(p_\mathrm{s}^2 - p_\mathrm{i}^2\right) \tag{C.25}$$

As a verification step it is verified that the mass flow in equals the mass flow out. Also, the sum of the mass flow across the unit cell edge should be 0.

Stationary stiffness

The stiffness is evaluated by evaluating the load capacity for a perturbed fly-height, as described in appendix C.1.3. The stationary stiffness can thus be evaluated as:

$$k_\mathrm{s} = -\frac{\Delta W}{\Delta h_\mathrm{f}} = -\frac{W|_{h_\mathrm{f}=h_\mathrm{f,e}+\delta h_\mathrm{f}} - W|_{h_\mathrm{f}=h_\mathrm{f,e}-\delta h_\mathrm{f}}}{2\,\delta h_\mathrm{f}} \tag{C.26}$$

Where $h_\mathrm{f,e}$ represents the eccentric fly-height for which the no-load condition is satisfied. The manual perturbation of the fly-height δh_f should not be taken too small, in order to reduce the influence of numerical noise. If the manual perturbation is taken too large, the linearisation approximation is not valid anymore. The perturbed film thicknesses are defined as shown in table C.4.

Table C.4: Film thicknesses for manual perturbation study.

Boundary	Section	Expression for h
Ω_d	Dam	$(1 \pm 0.01)\, h_\mathrm{f,e}$
Ω_p	Pocket	$(1 \pm 0.01)\, h_\mathrm{f,e} + h_\mathrm{p}$
Ω_r	Recess	$(1 \pm 0.01)\, h_\mathrm{f,e} + h_\mathrm{p} + h_\mathrm{r}$
Ω_o	Outlet	$h_\mathrm{o,e}$

C.3 Dynamic analysis

In order to gain more insight into the dynamic behaviour of the system, a perturbation method is used. The set-up of the model is to a large extend identical to that of the stationary study. However, the governing equations and boundary conditions differ. These are explained below.

C.3.1 Perturbation technique

Perturbation techniques is a class of methods to determine an approximate solution of an equation for which an exact solution cannot be obtained [27, 28]. The use of the perturbation method specifically applied to Reynolds equation is described by Al-Bender [11]. In this case, the stationary fly-height h_0 is perturbed by a complex valued perturbation signal $\delta h(t)$. A dynamic fly-height is thus defined as:

$$h(t) = h_0 + \delta h(t), \qquad \delta h = \tilde{h} e^{i\omega t} \tag{C.27}$$

This dynamic fly-height leads to a dynamic pressure distribution, which is defined as:

$$p(t) = p_0 + \delta p(t), \qquad \delta p = \tilde{p} e^{i\omega t} \tag{C.28}$$

Where $\tilde{h}$ represents the amplitude of the fly-height perturbation, as defined in table C.5. The perturbed pressure distribution is represented by $\tilde{p}(x, y, z)$. Substituting equations (C.27) and (C.28) in the Reynolds equation gives the perturbed Reynolds equation [10]:

$$\frac{1}{12\eta R_\mathrm{s} T} \nabla \cdot \left(p_0 h_0^3 \nabla \tilde{p} + 3 p_0 h_0^2 \tilde{h} \nabla p_0 + \tilde{p} h_0^3 \nabla p_0 \right) = \frac{1}{R_\mathrm{s} T} i\omega \left(p_0 \tilde{h} + \tilde{p} h_0 \right) \tag{C.29}$$

Note that the calculations are performed using a *Stationary* study. The dynamic effects are essentially integrated into the governing equation, rather than performing a *Time Dependent* study. The aim is to find a solution for the perturbed pressure distribution $\tilde{p}$, which is complex valued. A perturbation around 0 is observed by subtracting the stationary solution from the perturbed solution. Also, in order to get rid of the $e^{i\omega t}$, the governing equation is multiplied by $e^{-i\omega t}$. For all boundary conditions, the stationary boundary conditions are subtracted and they are also multiplied by $e^{-i\omega t}$.

Table C.5: Film thicknesses for dynamic perturbation study.

Boundary	Section	Expression for $\tilde{h}$
Ω_d	Dam	$0.01 \cdot h_\mathrm{f,e}$
Ω_p	Pocket	$0.01 \cdot h_\mathrm{f,e}$
Ω_r	Recess	$0.01 \cdot h_\mathrm{f,e}$
Ω_o	Outlet	0

C.3.2 Governing equations

A second *General Form Boundary PDE* physics is used to implement the perturbed Reynolds equation. The conservative flux specified in the *General Form PDE Equation* is defined as:

$$\Gamma = \frac{1}{12\eta R_\mathrm{s} T} \nabla \cdot \left(p_0 h_0^3 \nabla \tilde{p} + 3 p_0 h_0^2 \tilde{h} \nabla p_0 + \tilde{p} h_0^3 \nabla p_0 \right) \tag{C.30}$$

The source term is no longer equal to 0 and is defined as:

$$f = \frac{1}{R_\mathrm{s} T} i\omega \left(p_0 \tilde{h} + \tilde{p} h_0 \right) \tag{C.31}$$

The damping and mass coefficient are both set to 0.

C.3.3 Boundary conditions

Boundary conditions are again applied to the boundaries indicated in figure C.4.

Inlet

Since the dynamic behaviour of the system is now analysed, the compressibility of the fluid in the recess volume also needs to be taken into account. Because of this compressibility, there will be a time delay between a perturbation of the fly-height and a change in pressure in the recess [29]. Normally, if the fly-height decreases, the pressure in the recess will increase in order to restore the fly-height. If this however happens too slowly, overcompensation will occur. The pressure in

the recess will increase excessively, which leads to an excessive increase in fly-height. This will subsequently lead to a decrease of the recess pressure, which causes the fly-height to decrease again, repeating this cycle. This phenomena is called pneumatic hammer and can occur if the *dead volume* in the system is too large. Dead volume is defined as a volume where there is no pressure drop. As a rule of thumb, it can be stated that the dead volume should be less than 1/20th of the *live volume* [29].

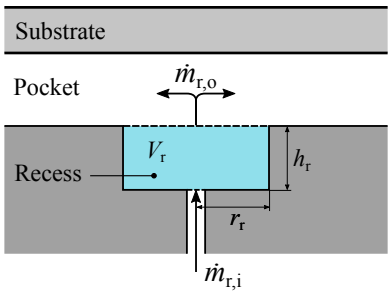

Figure C.5: Compressible recess volume.

The recess volume (not to scale) is schematically shown in figure C.5. The mass balance over the recess volume is given as:

$$V_r \frac{\partial \rho}{\partial t} = \dot{m}_{r,i} - \dot{m}_{r,o} \tag{C.32}$$

Where $\dot{m}_{r,i}$ represents the mass flow entering the recess volume from the capillary restriction, and $\dot{m}_{r,o}$ represents the mass flow leaving the recess volume, flowing into the pocket film. By using the ideal gas law this can be written as:

$$V_r \frac{\partial}{\partial t}\left(\frac{p}{R_s T}\right) = \frac{V_r}{R_s T}\frac{\partial p}{\partial t} = \dot{m}_{r,i} - \dot{m}_{r,o} \tag{C.33}$$

The mass flow entering the pocket film can thus be written explicitly as:

$$\dot{m}_{r,o} = \dot{m}_{r,i} - \frac{V_r}{R_s T}\frac{\partial p}{\partial t} \tag{C.34}$$

Recalling the definition for the dynamic pressure defined in equation (C.28), the derivative with respect to time can be defined as:

$$\frac{\partial p}{\partial t} = \frac{\partial}{\partial t}\left(p_0 + \tilde{p}e^{i\omega t}\right) = i\omega\tilde{p}\, e^{i\omega t} \tag{C.35}$$

The pressure downstream the restriction will also be perturbed, and is therefore defined as:

$$p(t) = p_0 + \tilde{p}e^{i\omega t} \qquad \text{on } \partial\Omega_i \tag{C.36}$$

Substituting equation (C.36) in the equation for the mass flow through the capillary defined in equation (C.20) gives:

$$\begin{aligned} \dot{m}_i &= G_i\left(p_s^2 - (p_0 + \tilde{p}e^{i\omega t})^2\right) \\ &= G_i\left(p_s^2 - p_0^2 + -2\,p_0\tilde{p}e^{i\omega t} - \tilde{p}^2 e^{2i\omega t}\right) \end{aligned} \tag{C.37}$$

Subtracting the stationary solution (equation (C.20)) and neglecting higher order terms $\tilde{p}^2$ the perturbed mass flow through the capillary is defined as:

$$\dot{m}_{r,i} = -2\,G_i\; p_0\tilde{p}e^{i\omega t} \tag{C.38}$$

Equation (C.38) is substituted in equation (C.34) and all terms are multiplied by $e^{-i\omega t}$. This is expression is implemented in the model by using a *Flux/Source* boundary condition, defined as:

$$g = \Big(-2\,G_i\,p_0\tilde{p} - \frac{V_r\tilde{p}i\omega}{R_s T}\Big)\frac{1}{2\pi r_r} \qquad \text{on } \partial\Omega_i \tag{C.39}$$

Unit cell edge

The boundary conditions defined on the edges of the unit cell for the perturbation study are very similar to those defined in the stationary study. However, the boundary conditions should now hold for the perturbed pressure $\tilde{p}$ and the gradient of the perturbed pressure $\nabla\tilde{p}$ as:

$$\tilde{p}_1 = \tilde{p}_2 \qquad \tilde{p}_3 = \tilde{p}_4 \qquad \tilde{p}_5 = \tilde{p}_6 \tag{C.40a}$$

$$\nabla\tilde{p}_2 = -\nabla\tilde{p}_1 \qquad \nabla\tilde{p}_4 = -\nabla\tilde{p}_3 \qquad \nabla\tilde{p}_6 = -\nabla\tilde{p}_5 \tag{C.40b}$$

This is applied to the unit cell edges $\partial\Omega_\mathrm{u}$, indicted in figure C.4.

Outlet

The stationary boundary conditions are subtracted from the perturbed boundary conditions. The Dirichlet boundary condition on the outlet edge is thus defined as:

$$\tilde{p} = 0 \qquad \text{on } \partial\Omega_\mathrm{o} \tag{C.41}$$

C.3.4 Initial conditions

As the initial condition, the pressure is defined as:

$$\tilde{p} = 0 \qquad \text{on } \Omega_\mathrm{r},\ \Omega_\mathrm{p},\ \Omega_\mathrm{d}, \text{ and } \Omega_\mathrm{o} \tag{C.42}$$

C.3.5 Evaluated variables

The parameters of interest for the dynamic analysis are the dynamic stiffness and the damping.

Dynamic stiffness

The bearing film can be characterised as a non-linear, frequency dependent spring damper element where the dynamic stiffness K is defined as [30]:

$$K = k(\omega) + i\omega c(\omega) \tag{C.43}$$

Due to the stiffness, a force will be generated that opposes a change in fly-height. Substituting the expressions presented in equations (C.27) and (C.28) for the dynamic fly-height and pressure in the expression for the stiffness gives:

$$k = -\frac{\partial W}{\partial h} \approx -\frac{W_0 - W(t)}{h_0 - h(t)} = -\frac{\int p_0\, dA - \int (p_0 + \delta p)\, dA}{h_0 - (h_0 + \delta h)} = -\frac{\int \delta p\, dA}{\delta h} \tag{C.44}$$

Substituting the expressions for δp and δh gives:

$$k = -\frac{e^{i\omega t}\int \tilde{p}\, dA}{\tilde{h} e^{i\omega t}} = -\frac{\int \tilde{p}\, dA}{\tilde{h}} \tag{C.45}$$

Since the stiffness is concerned with the real part of the perturbed pressure amplitude $\tilde{p}$, it can be evaluated as:

$$k = \mathrm{Re}\left(-\frac{\int \tilde{p}\, dA}{\tilde{h}}\right) \tag{C.46}$$

Due to the damping, a force will be generated that is proportional to the vertical velocity w, which is defined as:

$$w = \frac{dh}{dt} = \dot{h} \tag{C.47}$$

The damping can thus be written as:

$$c = -\frac{\partial W}{\partial \dot{h}} \approx -\frac{W_0 - W(t)}{\dot{h}_0 - \dot{h}(t)} = -\frac{\int p_0\, dA - \int (p_0 + \delta p)\, dA}{\dot{h}_0 - (\dot{h}_0 + \delta \dot{h})} = -\frac{\int \delta p\, dA}{\delta \dot{h}} \tag{C.48}$$

Substituting the expressions for δp and $\delta \dot{h}$ gives:

$$c = -\frac{\int \tilde{p} e^{i\omega t}\, dA}{i\omega\, \tilde{h} e^{i\omega t}} = -\frac{\int \tilde{p}\, dA}{i\omega\, \tilde{h}} \tag{C.49}$$

The damping is associated with the complex part of the perturbed pressure

$$c = \mathrm{Im}\left(-\frac{\int \tilde{p}\, dA}{i\omega\, \tilde{h}}\right) \tag{C.50}$$

Expected behaviour

The following qualitative behaviour can be expected using the proposed modelling method [30]:

- If properly designed, the stiffness $k(\omega)$ will be positive across the full frequency spectrum.
- The static damping $c(\omega = 0)$ could be either positive or negative.
  - If the static damping is positive $c(\omega = 0) > 0$, the stiffness will increase and the damping will decrease for an increasing perturbation frequency.
  - If the static damping is negative $c(\omega = 0) < 0$, the stiffness will decrease and the damping will increase for an increasing perturbation frequency.
  - In both cases, the damping will go to 0 for $\omega \to \infty$.

C.4 Results

In this section, the results of the numerical studies is presented. The values for the parameters used can be found in tables C.1 to C.3 and C.6. In the next section, the influence of design parameters on the performance investigated by performing several parameter sweeps. The relevant system parameters will be normalised with as:

$$\kappa = \frac{\bar{k}}{\bar{k}_{\max}} \qquad \zeta = \frac{\bar{c}}{\bar{c}_{\max}} \qquad \Pi = \frac{P}{P_{\max}} \qquad H = \frac{h_{\mathrm{f,e}}}{h_{\mathrm{f,c}}} \tag{C.51}$$

The stiffness $\bar{k}$ and damping $\bar{c}$ will be evaluated using the perturbed Reynolds equation for a perturbation frequency of $\omega = 1\,\mathrm{rad/s}$. The values for $\bar{k}_{\max}$, $\bar{c}_{\max}$ and $P_{\max}$ will vary per study, while the value of $h_{\mathrm{f,c}}$ is equal to $15\,\mu\mathrm{m}$ for all studies.

Table C.6: Nominal values used in the simulation.

Description	Symbol	Value	Unit
Ambient pressure	p_{a}	$100 \cdot 10^3$	Pa
Vacuum pressure	p_{v}	$70 \cdot 10^3$	Pa
Distributed weight substrate	p_{sub}	50	Pa
Eccentricy	ε	0.9	1
Conicity	δ	1/100	rad

C.4.1 Pressure distribution

Stationary

Shown in figure C.6a is the pressure distribution for $\varepsilon = 0$. As expected, the pressure distribution is radially symmetric with respect to the inlet. This means that the pressure gradient is equal in all directions and thus no net shear force is generated.

In order to generate a net shear force, the outlet film thickness is decreased on the left side ($\varphi = \pi$). As can be seen in figure C.6b, the pressure distribution is no longer radially symmetric. The outlet pressure at the bearing surface on the left side is increased, which means that the magnitude of the pressure gradient towards the left ($\partial p/\partial x$) is smaller than the one towards the right. This means that a net force in positive x-direction is generated.

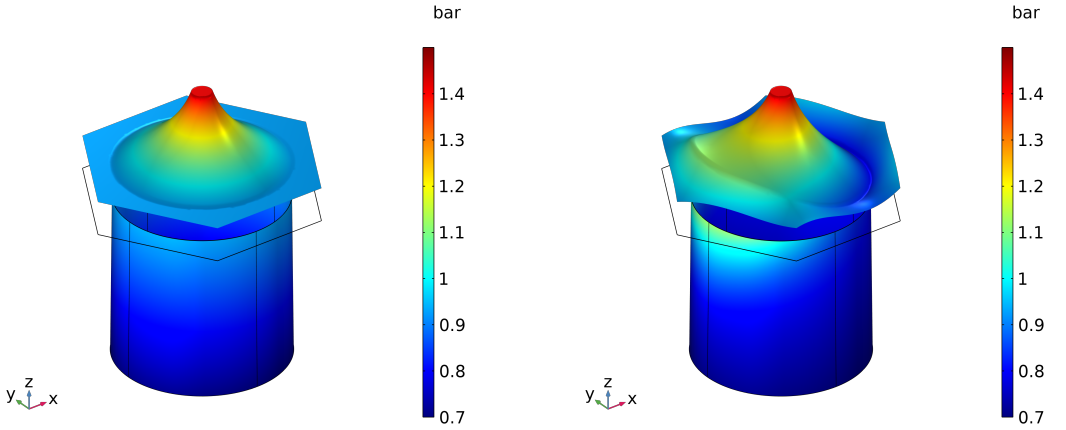

(a) Stationary pressure distribution p_0 for $\varepsilon = 0$. (b) Stationary pressure distribution p_0 for $\varepsilon = 0.9$.

Figure C.6: Stationary pressure distribution.

Perturbed

Shown in figure C.7 is the dynamic pressure distribution for the concentric case and a low perturbation frequency. The real part of the perturbed pressure profile is shown in figure C.7a. The fly-height is perturbed in positive z-direction, which explains why the pressure distribution in the pocket becomes negative. The complex part of the perturbed pressure profile is shown in figure C.7b. This can be interpreted as a phase shift of the pressure distribution with respect to the perturbation in fly-height. Additional graphs of the perturbed pressure distribution can be found in appendix G.1.

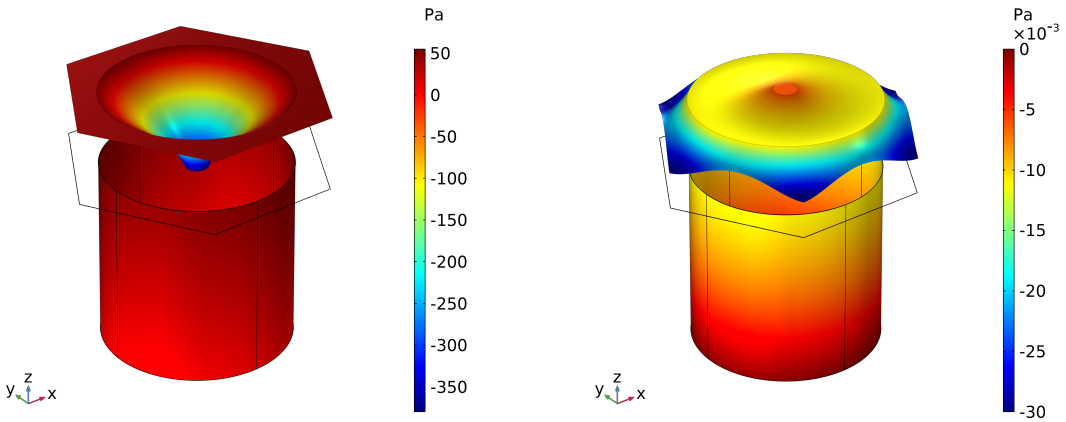

(a) Re($\tilde{p}$) for $\omega = 1\,\mathrm{rad/s}$, $\varepsilon = 0$. (b) Im($\tilde{p}$) for $\omega = 1\,\mathrm{rad/s}$, $\varepsilon = 0$.

Figure C.7: Perturbed pressure distribution.

C.4.2 Performance curve

The performance curve of the system is shown in figure C.8. The same parameters are shown on the x- and y- axis as for the figure shown in figure A.16. However, in this study the vacuum pressure is varied (1-0.5 bar), while in the other study, the actuator length L is varied.

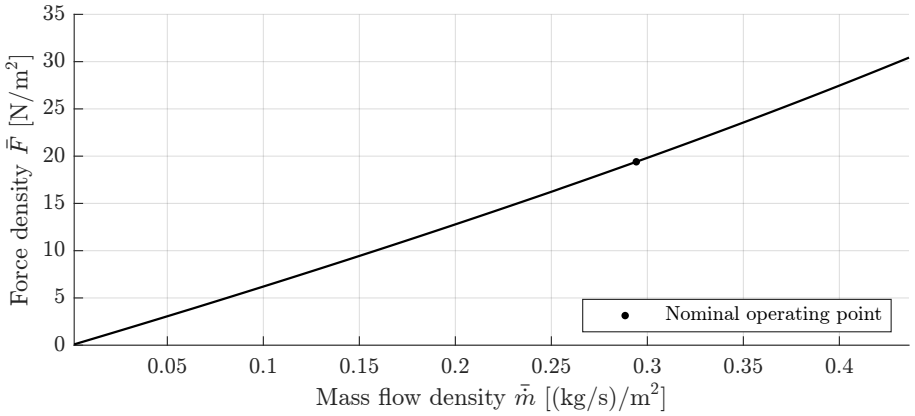

Figure C.8: Performance curve for varying vacuum pressure for $\varepsilon = 0.9$.

C.4.3 Dynamic behaviour

The dynamic behaviour of the system is shown in figure C.9. The stationary stiffness is indicated with $\bar{k}_{\mathrm{m}}(\omega)$, while dynamic stiffness is indicated with $\bar{k}(\omega)$. These are calculated using different methods. The stationary stiffness is calculated by prescribing a manual perturbation (see appendix C.2.4). The dynamic stiffness is calculated by solving the perturbed Reynolds equation (see appendix C.3.1). For low frequencies, the value found for the stiffness should be approximately identical for both methods. This is in fact true, as can be seen in figure C.9. The corresponding values are shown in table C.7.

The system behaves in accordance with the expected behaviour presented in appendix C.3.5. Also, since the total magnitude of the outlet restriction reduces for the eccentric case, the stiffness will increase and the damping decreases.

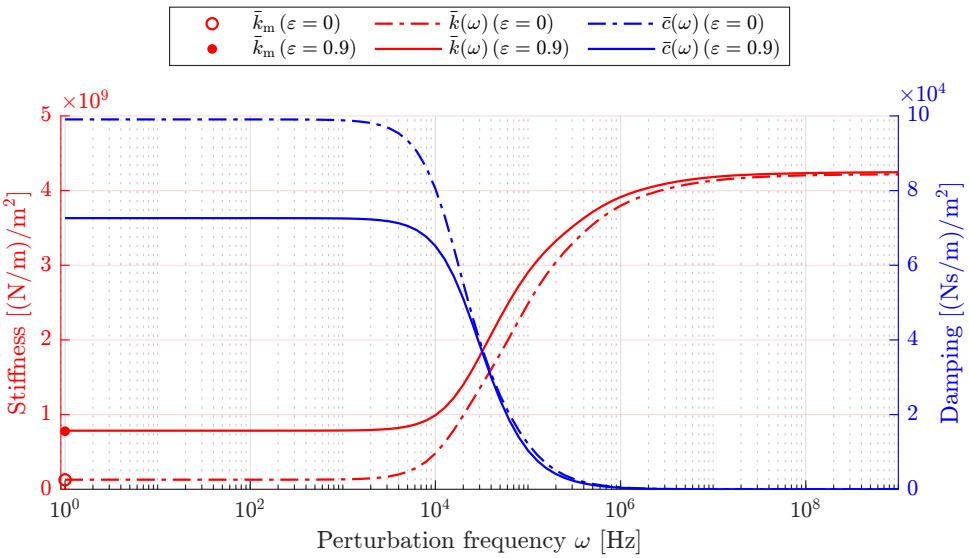

Figure C.9: Dynamic behaviour of the nominal model.

Table C.7: Stiffness value comparison.

Eccentricity ε [1]	Manual perturbation $\bar{k}_{\mathrm{m}}$ [(N/m)/m^2]	Perturbed Reynolds $\bar{k}(\omega)$ [(N/m)/m^2]
0	$1.2707 \cdot 10^8$	$1.2831 \cdot 10^8$
0.9	$7.7721 \cdot 10^8$	$7.8496 \cdot 10^8$

C.4.4 Varying eccentricity

As shown in figure C.10, the force density is approximately proportional to the eccentricity. This is beneficial if a control system were to be designed. The normalised mass flow density M is shown on the same axis as the normalised eccentric fly-height H. It then becomes clear that the mass flow density reaches its maximum if the eccentric fly-height also reaches its maximum. The normalised mass flow density is in this case defined as:

$$M = \frac{\bar{\dot{m}}}{\bar{\dot{m}}_{\max}} \tag{C.52}$$

For the set of nominal design parameters, this occurs for $\varepsilon = 0.60$, where $\bar{\dot{m}}_{\max} = 0.30$ (kg/s)/m^2.

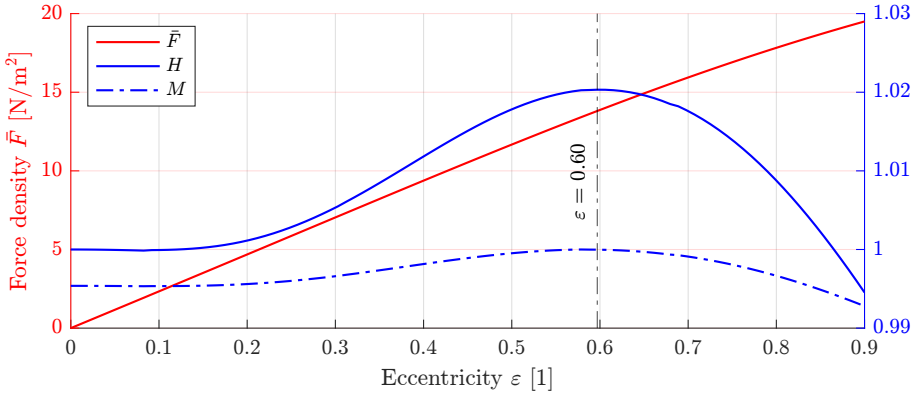

Figure C.10: Force density as a function of the eccentricity.

Other relevant system parameters, as introduced in equation (C.51) are shown in figure C.11. The stiffness increases with eccentricity, while the damping decreases with eccentricity. The eccentric fly-height is relatively stable. The performance ratio is approximately proportional to the eccentricity.

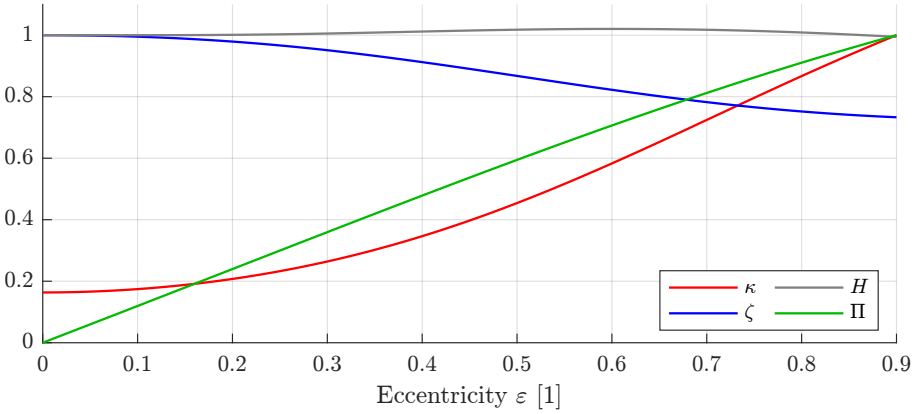

Figure C.11: Normalised system parameters as a function of the eccentricity.

C.5 Parameter influence

The relevant system parameters are investigated by performing parameter sweeps of selected design parameters. One parameter is varied at a time. The values for the other parameters are as shown in tables C.1, C.3 and C.6

In some cases, the studies for the pin ratio ϱ and the pocket ratio β lead to unrealistic geometries, which cause the system to become unstable. Therefore, these studies are performed using a low eccentricity of $\varepsilon = 0.05$.

In further studies, the relevant system parameters are investigated by varying the other design parameters about their nominal value. These studies are performed with an eccentricity of $\varepsilon = 0.9$ and should give a more realistic impression of the sensitivity for variations of these parameters.

C.5.1 Pin ratio

As can be seen in figure C.12, there exists a value for the pin ratio ($r_\mathrm{p}/r_\mathrm{u}$) where the performance ratio is maximised ($\varrho_\mathrm{opt} = 0.93$). This can be explained intuitively by performing a thought experiment. Imagine the limit case where $\varrho \to 1$. The dams would effectively disappear. Therefore, the parasitic flow towards neighbouring unit cells would increase and thus the performance decreases. On the other hand, if $\varrho \to 0$, the dam will make up almost the entire area of the unit cell. This means that the shear force generated per unit area of the system decreases. Since the no-load condition still has to be satisfied, this will also cause the supply pressure to increase to unrealistically high values. The normalisation parameters are show in table C.8. The low performance ratio is due to the low eccentricity, while the extreme values for the stiffness and damping are due to the unrealistic unit cell geometries.

For values of the pin ratio below 0.68, the stiffness is negative. This is due to the fact that the majority of the load capacity is determined by the pressure above the dam. The negative stiffness causes the fly-height to decrease upon actuation. At $\varrho = 0.68$, the stiffness changes from negative to positive, which explains the spike in both the normalised performance ratio Π and the normalised eccentric fly-height H.

Manufacturing this system becomes difficult for pin ratios close to 1, due to the fact that very little solid material will remain to form an actual bearing *plate*. This effect is amplified by the fact that the holes taper outwards towards the vacuum side. As a compromise between performance and manufacturability it was decided to design the demonstrator using a pin ratio of 0.8.

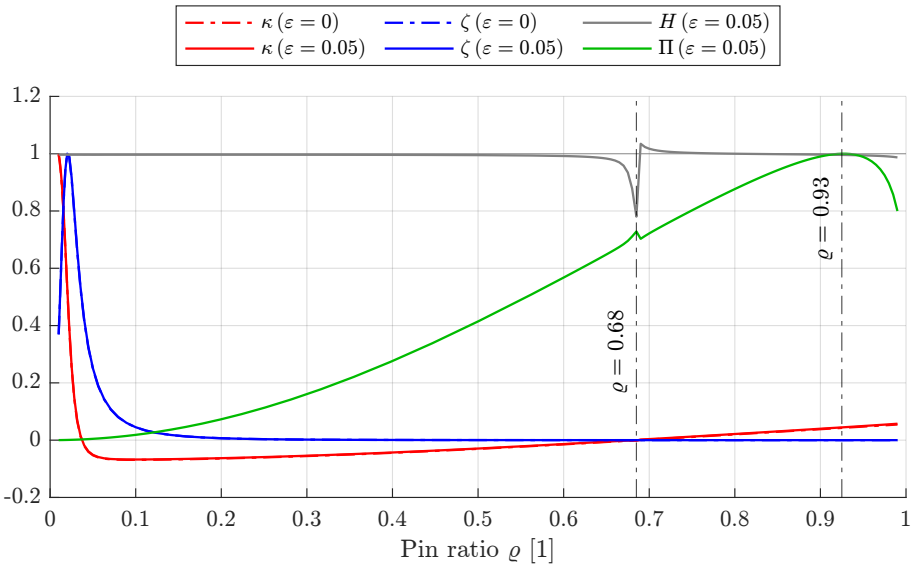

Figure C.12: Normalised system parameters as a function of the pin ratio ϱ.

Table C.8: Normalisation parameters for pin ratio sweep.

Parameter	Value	Unit
$\bar{k}_\mathrm{max}$	$63.8 \cdot 10^8$	$(\mathrm{N/m})/\mathrm{m}^2$
$\bar{c}_\mathrm{max}$	$35.0 \cdot 10^8$	$(\mathrm{Ns/m})/\mathrm{m}^2$
P_max	6.8	m/s

C.5.2 Pocket ratio

The normalised system parameters are shown in figure C.13, where the normalisation values are shown in table C.9. Again, in order for the system to remain stable, this analysis was performed using a low eccentricity. The performance ratio is maximised for a pocket ratio of $\beta = 3.33$. This value is much higher the one found in the 2D analysis. This may be explained by the fact that the

eccentric fly-height decreases, thereby effectively decreasing the mass flow density. The stiffness is maximised for $\beta = 1.73$.

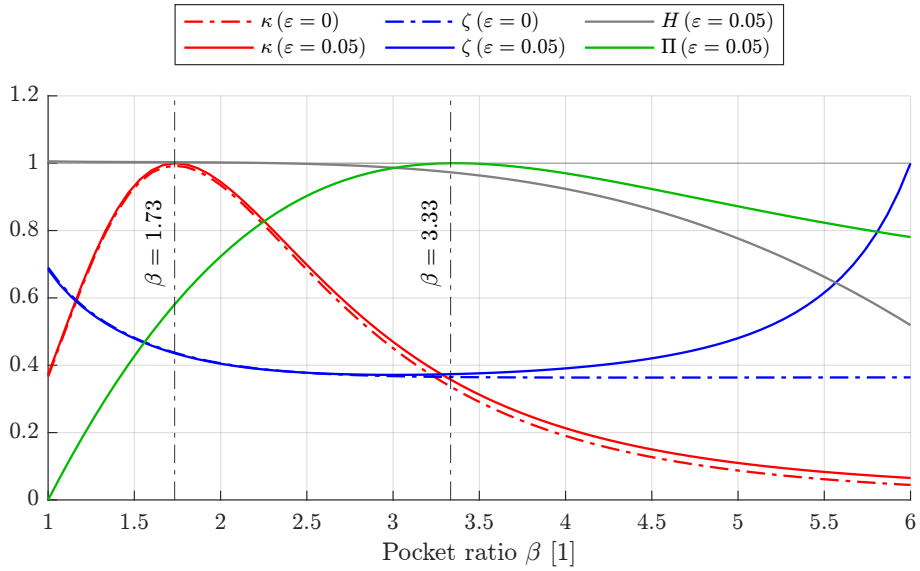

Figure C.13: Normalised system parameters as a function of the pocket ratio β.

Table C.9: Normalisation parameters for pocket ratio sweep.

Parameter	Value	Unit
$\bar{k}_{\max}$	$16.6 \cdot 10^7$	$(\mathrm{N/m})/\mathrm{m}^2$
$\bar{c}_{\max}$	$25.8 \cdot 10^4$	$(\mathrm{Ns/m})/\mathrm{m}^2$
$P_{\max}$	4.6	m/s

C.5.3 Constant fly-height

As shown in figure C.10, the eccentric fly-height is dependent on the eccentricity. It was observed that, depending on the design parameters, the eccentric fly-height would either increase or decrease throughout the actuation stroke.

This is demonstrated using three different values for the pocket height h_p. The resulting eccentric fly-height and mass flow are shown in figure C.14. For a pocket height of $h_\mathrm{p} = 17\,\mu\mathrm{m}$, the eccentric fly-height increases for increasing eccentricity. This decreases the magnitude of the pocket restriction and thus increases the mass flow density. The opposite behaviour is observed for $h_\mathrm{p} = 25\,\mu\mathrm{m}$.

For a pocket height of $h_\mathrm{p} = 21\,\mu\mathrm{m}$, the eccentric fly-height changes very little compared to the concentric fly-height. This is beneficial if the contactless handling system would be used in a process where the fly-height should change as little as possible. For example, an inspection step where a microscope is used. A constant fly-height allows for the use of a constant focal length. Another benefit is that for this set of design parameters, the mass flow density is approximately constant across the eccentricity range. This is beneficial for a real system, where the supply and vacuum pressure will be dependent on the flow rate. In other words, having a constant flow rate makes it easier to maintain constant a supply and vacuum pressure.

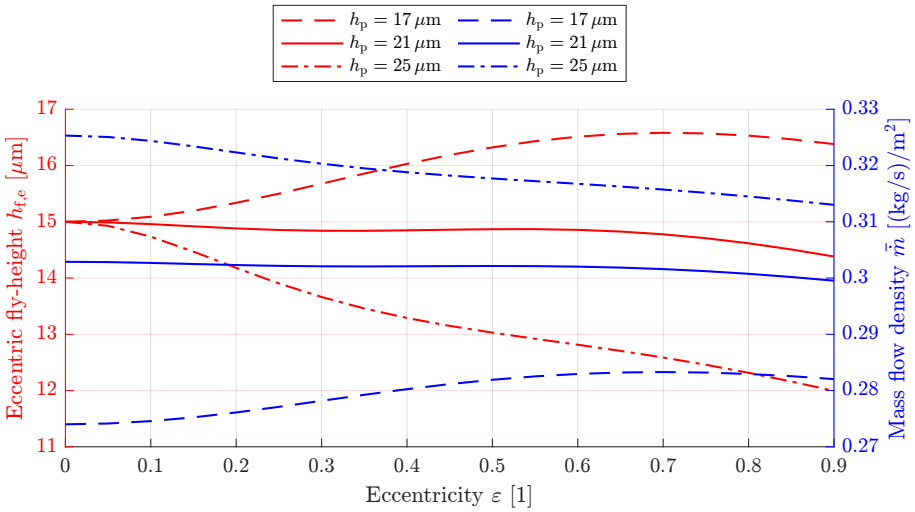

Figure C.14: Eccentric fly-height as a function of eccentricity for various pocket heights.

C.5.4 Pocket height

Shown in figure C.15 are the relevant system parameters for a varying pocket height. The normalisation parameters are shown in table C.10. Both the concentric and eccentric stiffness decreases with increasing pocket height, while the eccentric damping increases with increasing pocket height. This can be explained by the fact that the air in the pocket is compressible. The performance increases with the pocket depth. However, the eccentric fly-height will decrease further and further upon actuation, as shown in figure C.14. Using this set of design parameters, a constant fly-height is reached for $h_p = 19.81\ \mu$m.

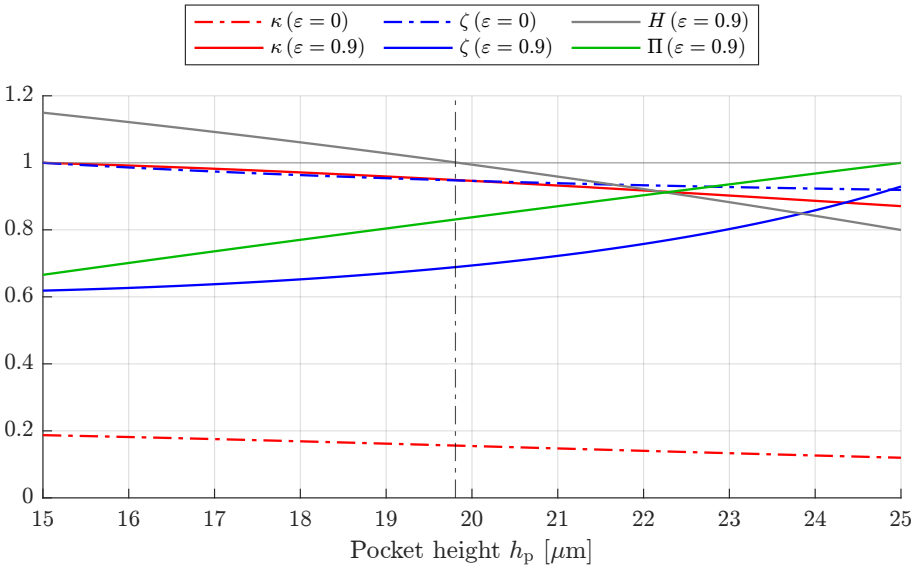

Figure C.15: Normalised system parameters as a function of the pocket height.

Table C.10: Normalisation parameters for pocket height sweep.

Parameter	Value	Unit
$\bar{k}_{max}$	$83.0 \cdot 10^7$	(N/m)/m^2
$\bar{c}_{max}$	$10.5 \cdot 10^4$	(Ns/m)/m^2
P_{max}	78.8	m/s

C.5.5 Inlet conductivity

The relevant system parameters for a varying inlet conductivity are shown in figure C.16. The normalisation parameters are shown in table C.11. Since the no-load condition always has to be satisfied, and the vacuum pressure is fixed, the inlet pressure will not change. This means that only the supply pressure will change. A higher inlet conductivity will decrease the stiffness, as expected. The inlet conductivity is assumed to be independent of the pressure difference across the inlet restriction. This is discussed in more detail in appendix D.2.1.

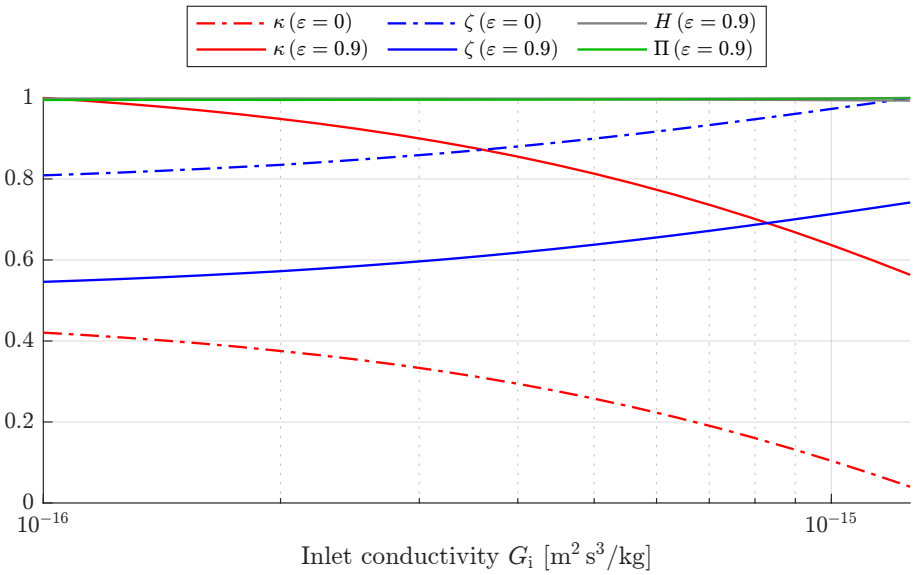

Figure C.16: Normalised system parameters as a function of the inlet conductivity.

Table C.11: Normalisation parameters for inlet conductivity sweep.

Parameter	Value	Unit
$\bar{k}_{\max}$	$12.3 \cdot 10^8$	(N/m)/m^2
$\bar{c}_{\max}$	$10.2 \cdot 10^4$	(Ns/m)/m^2
$P_{\max}$	66.1	m/s

C.5.6 Concentric outlet film thickness

The relevant system parameters as a function of the concentric outlet film thickness are shown in figure C.17. The normalisation parameters are shown in table C.12. The stiffness decreases for a decreasing outlet film thickness, since the magnitude of the total outlet restriction increases. If the concentric outlet film thickness becomes too small, the system will become unstable. As expected, the damping decreases for an increasing concentric outlet film thickness.

Using this set of design parameters, a constant fly-height is achieved for $h_{\mathrm{o,c}} = 50.12$ μm. For values below this value, the eccentric fly-height will decrease across the eccentricity range. For values above this value, the opposite is true. The eccentric fly-height will change the mass flow density and thereby the performance ratio. Therefore, the performance increases with a smaller film thickness. The same behaviour is observed when varying the outlet film length L_o. However, since restriction magnitude scales with L_o^1 versus $h_{\mathrm{o,c}}^{-3}$, the effect is less pronounced.

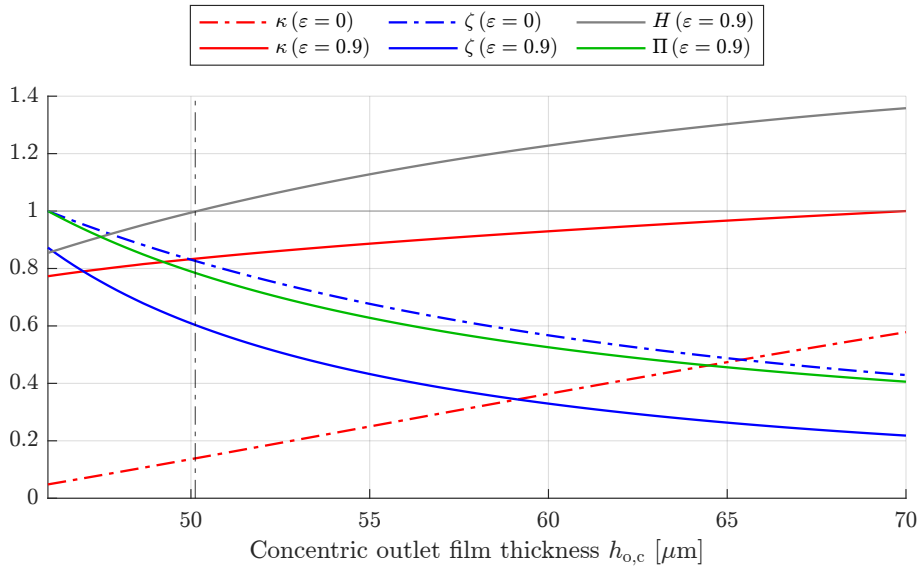

Figure C.17: Normalised system parameters as a function of the concentric outlet film thickness.

Table C.12: Normalisation parameters for concentric outlet film thickness sweep.

Parameter	Value	Unit
$\bar{k}_{\max}$	$94.3 \cdot 10^7$	$(\mathrm{N/m})/\mathrm{m}^2$
$\bar{c}_{\max}$	$11.9 \cdot 10^4$	$(\mathrm{Ns/m})/\mathrm{m}^2$
$P_{\max}$	83.6	m/s

C.5.7 Concentric fly-height

The relevant system parameters as a function of the concentric fly-height are shown in figure C.18. The normalisation parameters are shown in table C.13. The eccentric fly-height is now normalised with respect to each evaluation of the concentric fly-height:

$$H = \frac{h_{\mathrm{f,e}}}{h_{\mathrm{f,c}}} \tag{C.53}$$

Where, $h_{\mathrm{f,c}}$ is now varying instead of being equal to $15\,\mu$m. The behaviour is similar to the behaviour seen for a varying the pocket depth. This makes sense, as both these parameters influence the bearing film thickness. Using this set of design parameters, the stable fly-height is reached for $h_{\mathrm{f,c}} = 14.86$ μm.

A lower concentric fly-height is beneficial in terms of performance, stiffness and damping. In reality, the achievable fly-height is mostly determined by manufacturing tolerances. A bearing surface with a lower waviness will allow for a lower fly-height. If the waviness of the bearing surface too high, physical contact might occur between the substrate and the bearing surface. The substrate is partly deformed to the shape of the bearing surface. This means that any waviness of the bearing surface will introduce additional stress in the substrate, which is undesirable.

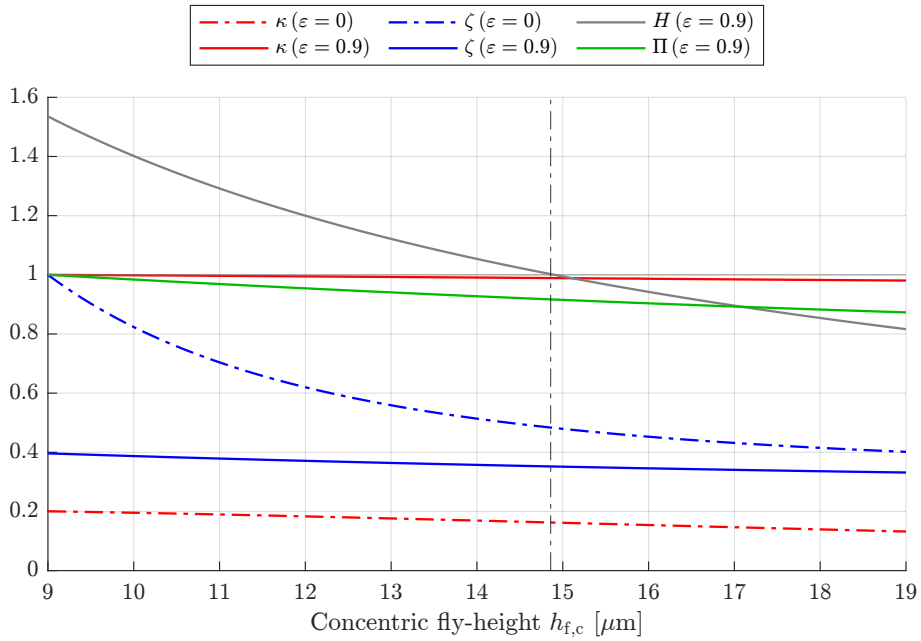

Figure C.18: Normalised system parameters as a function of the concentric fly-height.

Table C.13: Normalisation parameters for concentric fly-height sweep.

Parameter	Value	Unit
$\bar{k}_{\max}$	$79.4 \cdot 10^7$	$(\mathrm{N/m})/\mathrm{m}^2$
$\bar{c}_{\max}$	$20.7 \cdot 10^4$	$(\mathrm{Ns/m})/\mathrm{m}^2$
$P_{\max}$	72.1	m/s

C.5.8 Vacuum pressure

The relevant system parameters as a function of the vacuum pressure are shown in figure C.19. The normalisation parameters are shown in table C.14. Using this set of design parameters, the stable fly-height is reached for $p_{\mathrm{v}} = 0.78$ bar. If the vacuum pressure is approaching ambient pressure, there is virtually no pressure drop across the pocket restriction. This explains why the stiffness κ reduces to 0.

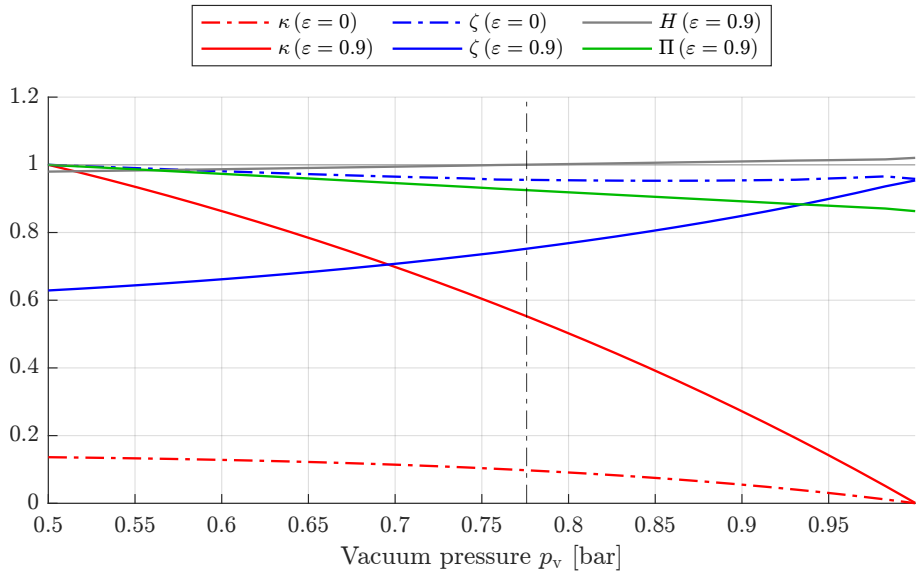

Figure C.19: Normalised performance parameters as a function of the vacuum pressure.

Table C.14: Normalisation parameters for vacuum pressure sweep.

Parameter	Value	Unit
$\bar{k}_{\max}$	$11.2 \cdot 10^8$	$(\mathrm{N/m})/\mathrm{m}^2$
$\bar{c}_{\max}$	$10.3 \cdot 10^4$	$(\mathrm{Ns/m})/\mathrm{m}^2$
$P_{\max}$	69.7	m/s

Pressure values

The absolute pressures are shown in figure C.20. The nominal operating point, is indicated by the black dashed line. The absolute pressures corresponding to this operating point are show in table C.15.

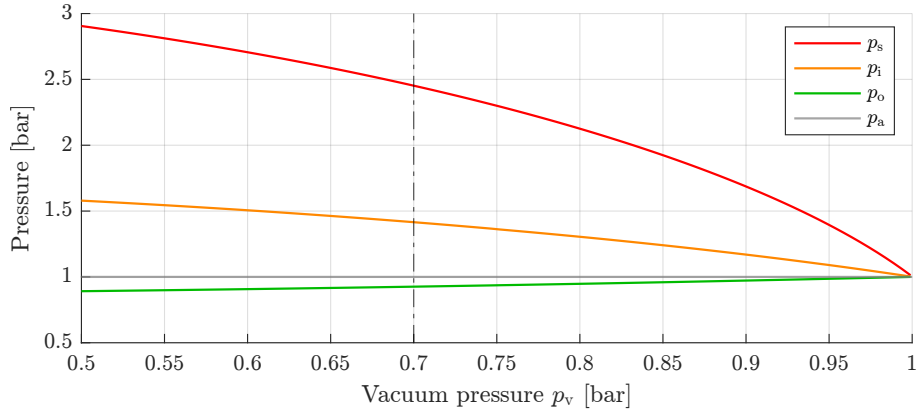

Figure C.20: Pressure values as a function of the vacuum pressure ($\varepsilon = 0$).

Table C.15: Pressures for $p_\mathrm{v} = 0.7\,\mathrm{bar}$.

Parameter	Symbol	Pressure [bar]
Supply pressure	p_s	2.45
Inlet pressure	p_i	1.41
Outlet pressure	p_o	0.93

C.6 Modelling manufacturing imperfections

Due to manufacturing imperfections, the unit cell geometry of the demonstrator will differ from the one in the numerical model. These manufacturing imperfections are discussed in more detail in appendix D.2.2 and appendix D.3.1. In this section, a starting point is presented in how to model these manufacturing imperfections.

Since manufacturing imperfections were not taken into account up to this point, any actuation in x-direction resulted in an actuation force only in x-direction. In other words, $\bar{F}_\mathrm{t} = \bar{F}_x$. However, due to the parasitic force as a result of these imperfections, the generated force will not necessarily be only in x-direction. Therefore, the performance parameter for the following two analyses is defined as:

$$P_x = \frac{\bar{F}_x}{\bar{\dot{m}}_\mathrm{i}} \tag{C.54}$$

In general it is hard to predict the influence of these manufacturing imperfections on the full system by only modelling a single unit cell. Most likely, a net force will be created when this is not desired. It different unit cells create a force in different directions, a parasitic torque will be generated. This will also depend on the nature of the manufacturing error. It could be systematic, randomly distributed or normally distributed.

C.6.1 Inlet misalignment

The influence of the misalignment of the inlet is shown in figures C.21 and C.22. A misalignment in x-direction will change the magnitude of the force density in x-direction, $\bar{F}_x$. The force density however is still proportional to the eccentricity, as shown in figure C.21a. The parasitic force density in y-direction is negligible, as shown in figure C.21b.

A misalignment in y-direction does not affect the force density in x-direction as can be seen in figure C.22a. A misalignment in y-direction will generate a parasitic force that is independent of the eccentricity, as shown in figure C.22b.

In reality, misalignment will occur in x- and y-direction and will vary per unit cell. This will introduce a parasitic torque acting on the substrate. From measurements of the sample pieces, the misalignment is expected to have a magnitude of $73 \pm 30\,\mu\mathrm{m}$, with a randomly distributed angle φ. In order gain insight into the influence of the misalignment on the full system, multiple unit cells should be modelled.

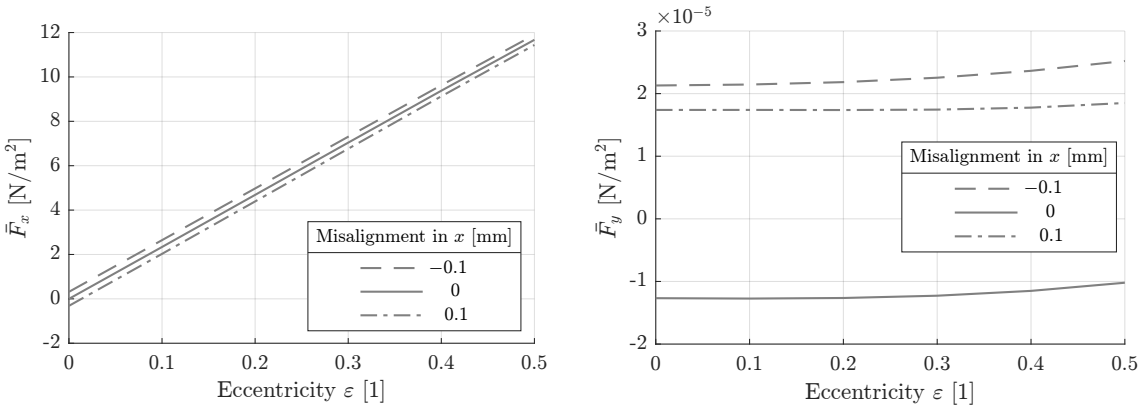

(a) Force density in x-direction.

(b) Force density in y-direction.

Figure C.21: Influence of inlet misalignment in x-direction.

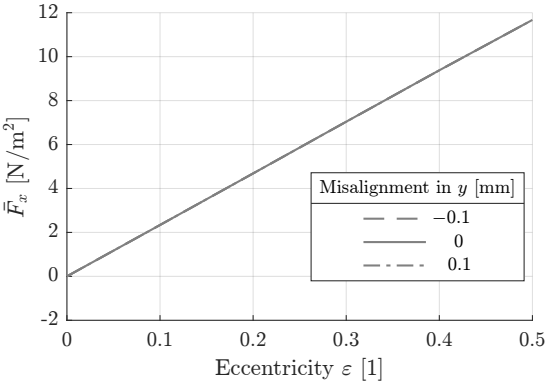

(a) Force density in x-direction.

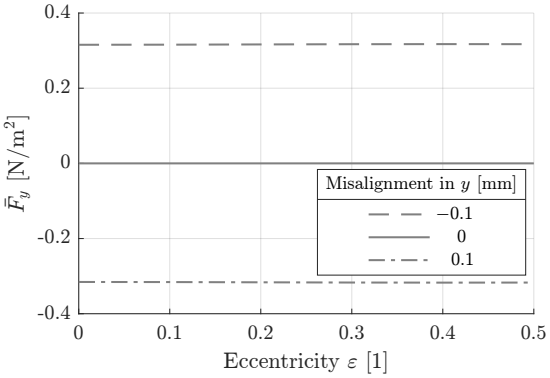

(b) Force density in y-direction.

Figure C.22: Influence of inlet misalignment in y-direction.

C.6.2 Outlet misorientation

If the hole is not perpendicular to the bearing surface, the outlet film thickness will be effected. More information regarding this can be found in appendix D.3.1. The deviation from perpendicularity will be called misorientation. In order to simulate the misorientation of the outlet restriction, the eccentric outlet film thickness is defined as:

$$h_{\mathrm{o,e}} = h_{\mathrm{o,c}} \left(1 + \varepsilon \cos\varphi - \frac{\alpha}{\delta} \cos\varphi - \frac{\beta}{\delta} \sin\varphi\right) \tag{C.55}$$

Where δ represents the theoretical conicity and α and β represent the angular deviation from perpendicularity about the x- and y- axis respectively. The influence of a deviation from perpendicularity about the x-axis is shown in figure C.23. As expected, for an eccentricity of $\varepsilon = 0$, a force is generated in negative x-direction for $\alpha = 1\,\mathrm{mrad}$, and vice versa for $\alpha = -1\,\mathrm{mrad}$. The influence of deviation from perpendicularity about the y-axis is shown in figure C.24. Again, multiple unit cells need to be modelled to gain insight into the influence on the full system.

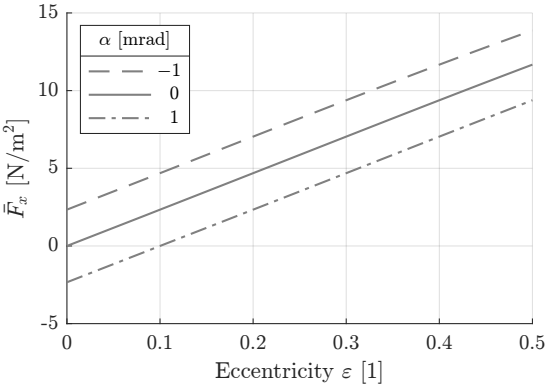

(a) $\bar{F}_x$ for $\beta = 0$.

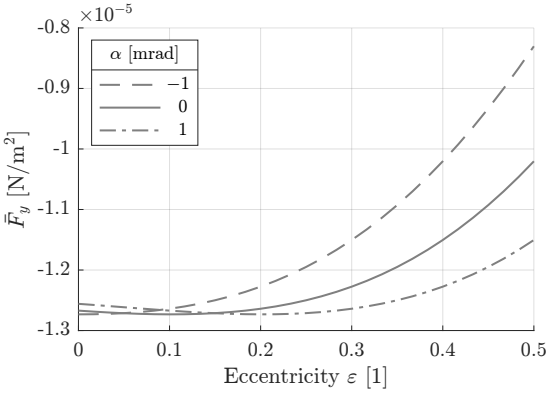

(b) $\bar{F}_y$ for $\beta = 0$.

Figure C.23: Influence of the deviation from perpendicularity about the x-axis.

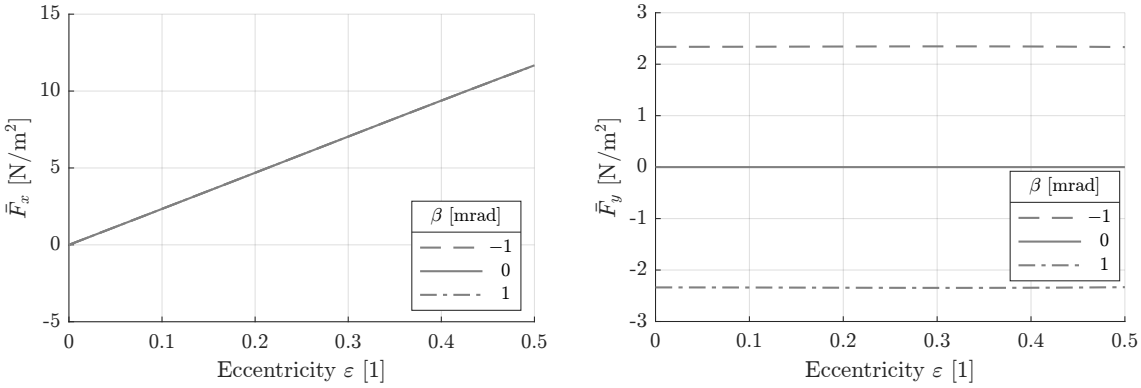

(a) $\bar{F}_x$ for $\alpha = 0$.

(b) $\bar{F}_y$ for $\alpha = 0$.

Figure C.24: Influence of the deviation from perpendicularity about the y-axis.

During this analysis, it is assumed that the surfaces of both the hole and the pin are parallel and perfectly flat, i.e. no waviness is present. In reality, there will be a certain waviness present in the surface of the hole and the pins. This will cause local variations in the outlet film thickness. The waviness most likely introduces local variations with an amplitude of $\pm 5\,\mu$m (see appendix D.3.2). This could in theory also be implemented in the numerical model.

C.7 Pin deformation

Up to this point, the geometry was assumed to be rigid. In reality, the pin will deform as a result of the (asymmetric) pressure distribution in the outlet. This is schematically shown in figure C.25, where a top view of the unit cell is shown. Moving the bearing plate (shown in grey) in positive x-direction will decrease the outlet film thickness on the left side of the pin (shown in green), thereby increasing the pressure on the left side. This results in a net force F_r acting on the pin in positive x-direction. This causes the outlet film to increase again on the left side. In the close-up, the decrease in film thickness on the right side is shown.

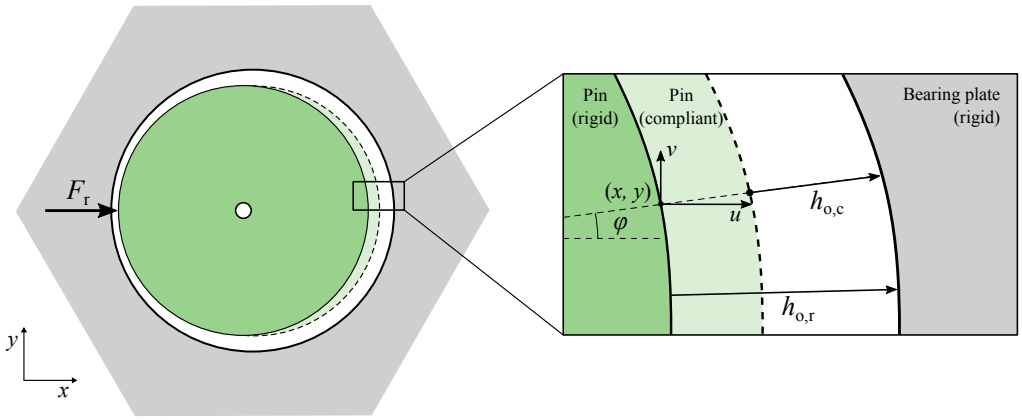

Figure C.25: Schematic representation of elastic deformation due to pressure gradient.

C.7.1 Model

The numerical model is in the basis identical to the one presented in appendix C.1. However, now the definition of the film thicknesses changes. Three different cases are considered:

0. Rigid pin - deformation not considered
1. Compliant pin - deformation of the outlet film thickness considered.
2. Compliant pin - deformation of the outlet film thickness and pocket film thickness considered.

The case 0 is identical to the nominal model. For case 1 and 2, the deformation of the pin is modelled by applying the pressure profile as a *Boundary Load* in the *Solid Mechanics* physics. The resulting deformation of the pin is then implemented through the definition of the film thicknesses in the *Variables* section. The model is then solved for both the *General Form Boundary PDE* (i.e. Reynolds equation) and the *Solid Mechanics* simultaneously, using the new definition of the outlet film thickness.

C.7.2 Geometry

The geometry used to model the deformation of the pin study is shown in figure C.26. The pin geometry consists of two domains. The first domain, the top part of the pin, forms the outlet restriction (together with the bearing plate). The second domain, the pin base, is the domain that connects the outlet restriction domain to the plenum lid in the demonstrator. These two domains form a single isotropic, solid body.

The Reynolds equation is only solved on the outlet restriction domain, identical to appendix C.1.4. The values used for the material parameters are shown in table C.16. How these values were determined is explained in detail in appendix D.4.9.

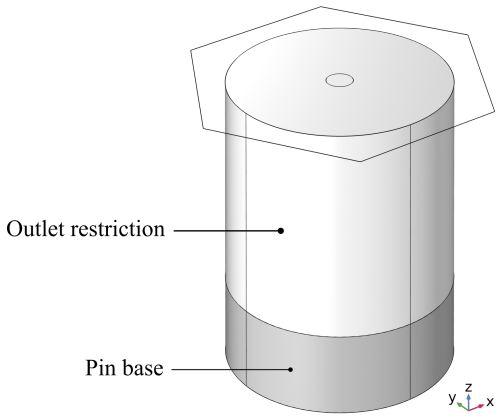

Figure C.26: Solid pin geometry.

Table C.16: Material parameters.

Parameter	Symbol	Value	Unit
Young's modulus	E	$1.66 \cdot 10^9$	Pa
Density	ρ	$1.44 \cdot 10^3$	kg/m^3
Poisson's ratio	ν	0.39	1

C.7.3 Boundary conditions

Since the pins were created under ambient pressure p_a, any pressure below ambient pressure will be perceived as a negative pressure. Hence, the ambient pressure is subtracted from the loads which are applied to the boundaries. The pressure distribution that is found by solving the Reynolds equation is applied to the outlet restriction domain as:

$$p = p_0(x, y, z) - p_\mathrm{a} \tag{C.56}$$

The vacuum pressure is applied to the pin base as:

$$p = p_\mathrm{v} - p_\mathrm{a} \tag{C.57}$$

Since the pin is glued onto the plenum lid (not shown in the figure), a *Rigid Constraint* is applied to the bottom boundary of the pin base. The applied load is shown graphically in figure C.27.

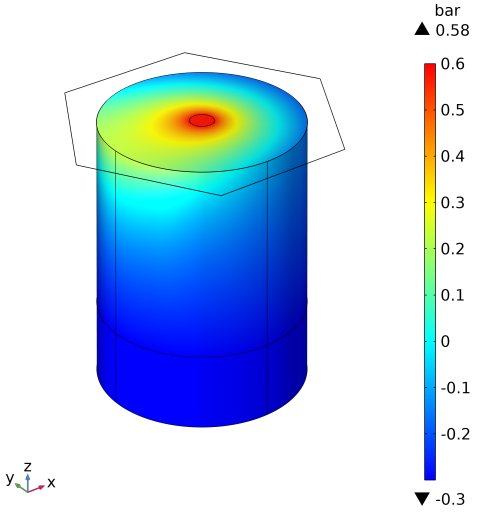

Figure C.27: Applied load for pin deformation study.

C.7.4 Film thickness

For case 0, the eccentric outlet film thickness is defined as:

$$h_{\mathrm{o,e}\,0} = h_{\mathrm{o,c}}\,(1 + \varepsilon\,\cos\varphi) \tag{C.58}$$

Where ε is the normalised eccentricity and φ indicates the local angle in the x, y plane. The asymmetric pressure distribution in the outlet film will lead to a deformation of the pin in x-, y- and z-direction, referred to as u, v and w respectively. The eccentric outlet film thickness for case 1 is thus defined as:

$$h_{\mathrm{o,e}\,1} = h_{\mathrm{o,c}}\,(1 + \varepsilon\,\cos\varphi) - u\cos\varphi - v\sin\varphi \tag{C.59}$$

The film thickness in the pocket in the pocket will also vary due to deformation of the pin. The deformation in z-direction can be implemented in the model by subtracting it from the film thickness as defined in the initial study. The film thickness in the pocket is for case 2 is therefore defined as:

$$h_{\mathrm{p},2} = h_{\mathrm{p}} + h_{\mathrm{f,e}} - w \tag{C.60}$$

For case 2, the eccentric outlet film thickness is still defined using equation (C.59).

C.7.5 Results

Deformation

The resulting deformation (i.e. displacement) for the pressure distribution is shown in figure C.28. As predicted, the deformation due to the pressure gradient causes an increase of the film thickness on the narrow side. The maximum deformation in x-direction is $0.63\,\mu$m, which is significant compared to the narrowest film thickness of $5\,\mu$m.

The maximum deformation of the pin in z-direction is $-0.37\,\mu$m, as shown in figure C.28c. The pocket film thicknesses for case 0,1 and 2 are shown in figure C.29. Including the deformation of the pocket surface changes the value of the film thickness by $< 1\%$.

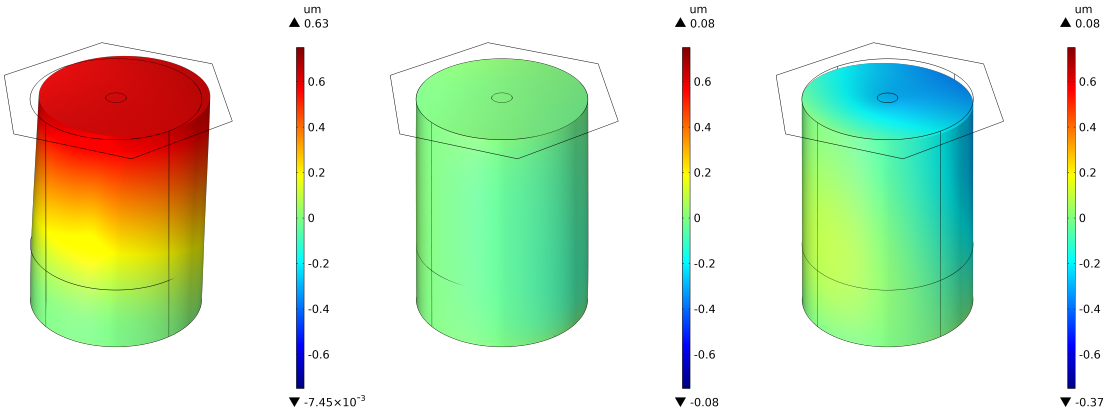

(a) Displacement in x-direction. (b) Displacement in y-direction. (c) Displacement in z-direction.

Figure C.28: Deformation due to pressure gradient for $\varepsilon = 0.9$.

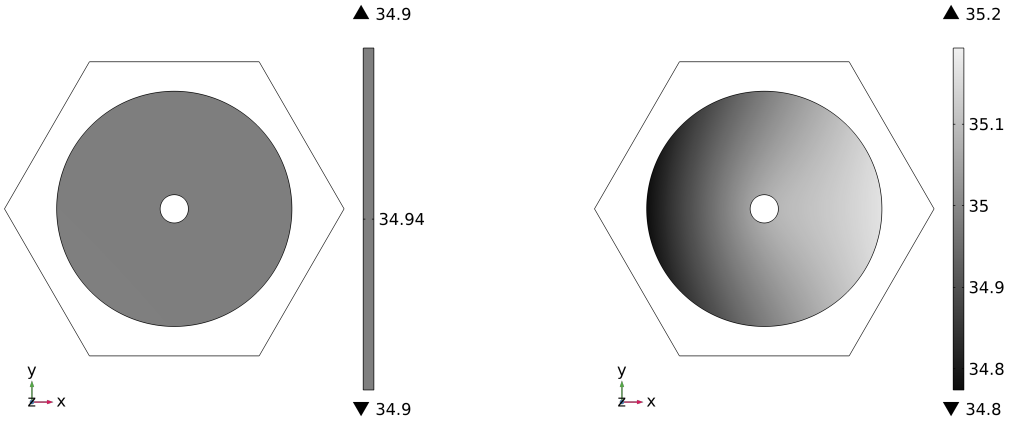

(a) For case 0 and 1. (b) For case 2.

Figure C.29: Pocket film thickness ($h_\mathrm{p} + h_\mathrm{f,e}$) for $\varepsilon = 0.9$.

The pressure distribution in the bearing film will lead to a deformation of the substrate as well. This is not considered in this model. However, it was found by Wesselingh [5] that these deformations are typically in the order of 1 μm. This will of course depend on the size of the unit cells, the operating conditions and the properties of the substrate. Though, it is likely that the deformations of the substrate are more significant than the variation of the film thickness in the pocket due to the tilt of the pin surface.

Surface tilt

In order to calculate the tilt, the angle of the surface is calculated with respect to the centre. The height profile is normalised with respect to t in z-direction of the centre of the pin, as shown in figure C.30a. The local tilt about the y-axis is then calculated as:

$$\theta = \tan^{-1}\left(\frac{w - \bar{w}_0}{x}\right) \tag{C.61}$$

This means that the solution is undefined for $x = 0$. By using the `dtang()` operator, the tangential derivative is calculated.

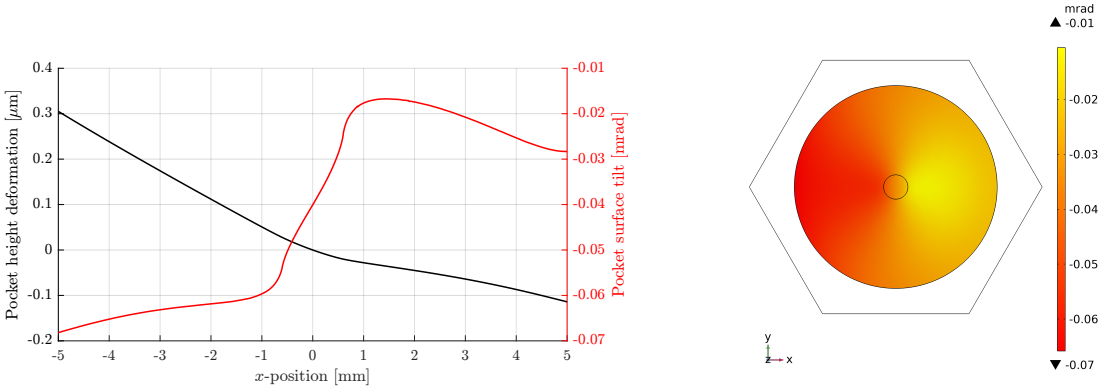

(a) Normalised height profile of top surface.

(b) Tilt of the top surface.

Figure C.30: Surface tilt due to pin deformation.

Film thickness comparison

The outlet film thickness around $\varphi = 0$ is shown in figure C.31. This corresponds to the situation as shown in figure C.25. If there is no coupling, the pin is essentially a rigid body and thus the outlet film thickness for $\varepsilon = 0.9$ is equal to $95\,\mu$m at $\varphi = 0$. When the deformation of the outlet restriction is taken into account (case 1), the thickness will decrease at $\varphi = 0$. If the deformation of the pocket is also taken into account, the pressure distribution in the pocket will also change. This leads essentially to a moment that slightly increases the film thickness again at $\varphi = 0$ (case 2). The values for the maximum outlet film thickness are shown in table C.17. The maximum performance ratio is achieved for the rigid pin. From this analysis, it can be concluded that the stiffness of the pin should be maximised, in order to maximise the performance ratio.

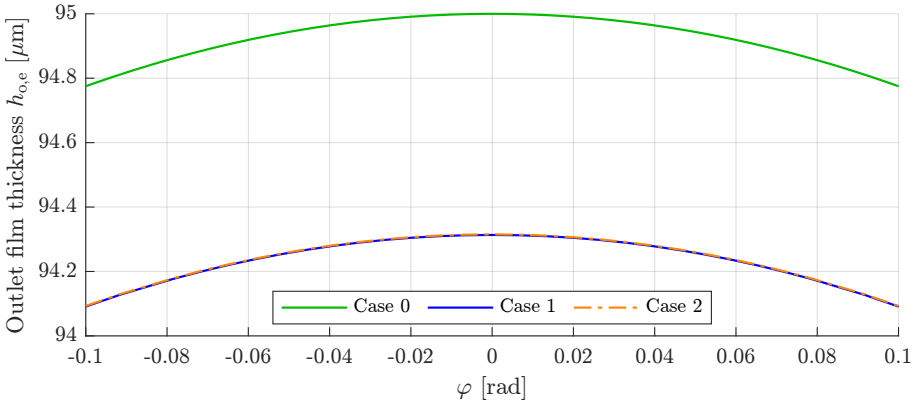

Figure C.31: Outlet film thickness for $\varepsilon = 0.9$ around $\varphi = 0$.

Table C.17: Maximum outlet film thickness at $\varphi = 0$ and performance ratio for $\varepsilon = 0.9$.

Coupling	$h_{o,e\,max}$ [μm]	P [m/s]
Case 0	95.0000	46.013
Case 1	94.3134	45.665
Case 2	94.3153	45.003

C.8 Conclusions

- The concentric fly-height is prescribed by the user. The eccentric fly-height is the fly-height for which the no-load condition is satisfied given a certain eccentricity ε. By definition $h_{\mathrm{f,c}} = h_{\mathrm{f,e}}|_{\varepsilon=0}$. The eccentric fly-height is in general not equal to the concentric fly-height.
- There exists a set of design parameters for which the eccentric fly-height remains approximately equal to the concentric fly-height upon actuation ($\varepsilon < 0.65$). In this case, the mass flow is also approximately constant.
- There exists a value for the pin ratio ($\varrho_{\mathrm{opt}} \approx 0.95$) for which the performance ratio is maximised. Due to practical implications, a pin ratio of 0.8 is selected for the prototype.
- There exists a value for the pocket ratio ($\beta_{\mathrm{opt}} \approx 2.40$) for which the performance ratio is maximised. However, a large pocket depth causes the system to become unstable for higher values of eccentricity.
- Given the nominal design parameters, the generated shear force is approximately proportional to the eccentricity. At least for values of $\varepsilon < 0.5$.
- The performance of the system is not influenced by varying the inlet conductivity. The stiffness will decrease, and the damping will increase upon increasing the inlet conductivity.
- The performance of the system will increase with increasing pocket height, while the stiffness and damping will decrease.
- The performance of the system will increase for a smaller outlet film thickness. Since this increases the magnitude of the outlet restriction, the stiffness will decrease, while the damping will increase. The system will become unstable if the outlet film thickness becomes too small.
- Misalignment of the inlet restriction and misorientation of the hole in the bearing plate will generate a parasitic force. For multiple unit cells combined, this could lead to a parasitic torque acting on the substrate.
- Elastic deformation of the pin due to the pressure gradient has a minimal effect on the system. These effects can be taken into account, however, the variations in film thickness due to manufacturing errors are most likely more significant than the variations due to the elastic deformations of the pin.

Appendix D

Manufacturing

In this appendix, the manufacturing process is described in detail. The practical implications of the conceptual design discussed in appendix B are discussed. The complete manufacturing process as proposed is presented in appendix D.1. Inspection of the system, measurements and something is presented in the remaining sections. Pictures of the actual manufacturing process are presented in appendix G.4.

D.1 Final manufacturing method

D.1.1 Dimensions & requirements

The relevant design parameters of the system were determined using the numerical model presented in appendix C. The values used in the nominal model are shown in table D.1 in the column indicated with *Model*. This set of design parameters forms a good compromise between maximising the performance ratio and minimising variations in fly-height, while avoiding an un-manufacturable geometry. The theoretical values for which the performance ratio is maximised are shown in *Optimum* as a comparison. However, a system that uses these optimum values will not be stable for a wide range of eccentricity, as was shown in appendix C.5.

The set of design parameters for which the demonstrator has been created is shown in the column indicated with *Demonstrator*. The values mentioned for pocket height and concentric outlet film thickness are the theoretical values, but have not been realised. No values are mentioned for the concentric fly-height and pocket ratio, since no stable fly-height has been realised in the experimental set-up. The definition of the pin ratio and pocket ratio is repeated here for clarity:

$$\varrho = \frac{r_\mathrm{p}}{r_\mathrm{u}} \qquad\qquad \beta = \frac{h_\mathrm{f,c} + h_\mathrm{p}}{h_\mathrm{f,c}} \tag{D.1}$$

Note that not all design parameters are independent, e.g. β and $h_\mathrm{f,c}$, however they are mentioned for completeness.

In general, the system properties of these contactless handling systems improve when scaling down the size of the unit cell and increasing the operating pressure difference [5]. A pin diameter of 10 mm was selected as a compromise between performance and manufacturability. A system with a pin ratio of 0.93 is hard to manufacture, simply because there would be very little material left to form an actual bearing plate. Especially with the holes tapering outwards. In addition, there would be very little space in between the pins to realise local support of the bearing plate. Therefore, the system was designed for a pin ratio of 0.8. Due to the additional manual reaming operation, the pin radius slightly increased.

Table D.1: Design parameters for numerical model and demonstrator.

Parameter	Symbol	Value *Optimum*	Value *Model*	Value *Demonstrator*	Unit
Pin ratio	ϱ	0.93	0.8	0.84	1
Pocket ratio	β	3.33	2.26	-	1
Concentric fly-height	$h_{\mathrm{f,c}}$	-	15	-	μm
Pocket height	h_{p}	-	21	19*	μm
Concentric outlet film thickness	$h_{\mathrm{o,c}}$	-	50	70*	μm
Vacuum height	t_{v}	-	5	7	mm
Outlet film length	L_{o}	-	10	9.2	mm
Pin radius	r_{p}	-	5.00	5.28	mm
Inscribed radius hexagonal unit cell	r_{u}	-	6.25	6.25	mm
Conicity	δ	-	1/100	1/100	rad

An isometric cross-section of the final system is shown in figure D.1. A uniform, radial clearance should be formed between each pin and the corresponding hole, as this will form the outlet restriction. The top surface of the bearing plate is slightly higher than the top surface of the pins. The pocket restriction will then be created between the substrate and the top surface of the pin.

Air is supplied to the plenum chamber through a single inlet port. From the plenum chamber, air flows through the inlet restrictions, located in the centre of each pin, into the pocket. From the pocket, the air flows through the outlet restriction to the vacuum chamber. The vacuum chamber is created in the space between the bearing plate and the plenum lid, which is sealed using duct tape. The air is evacuated through three vacuum ports, spaced 120° apart.

Both the plenum body and the bearing plate have tapped holes (M5) on all six sides. These were machined in order to be able to mount sensors and actuators to the demonstrator. However, since the demonstrator performed unsatisfactory, these have not been used. The top left corner of the system has been faceted. This was done such that the the orientation of the different parts cannot be mixed up during the manufacturing process.

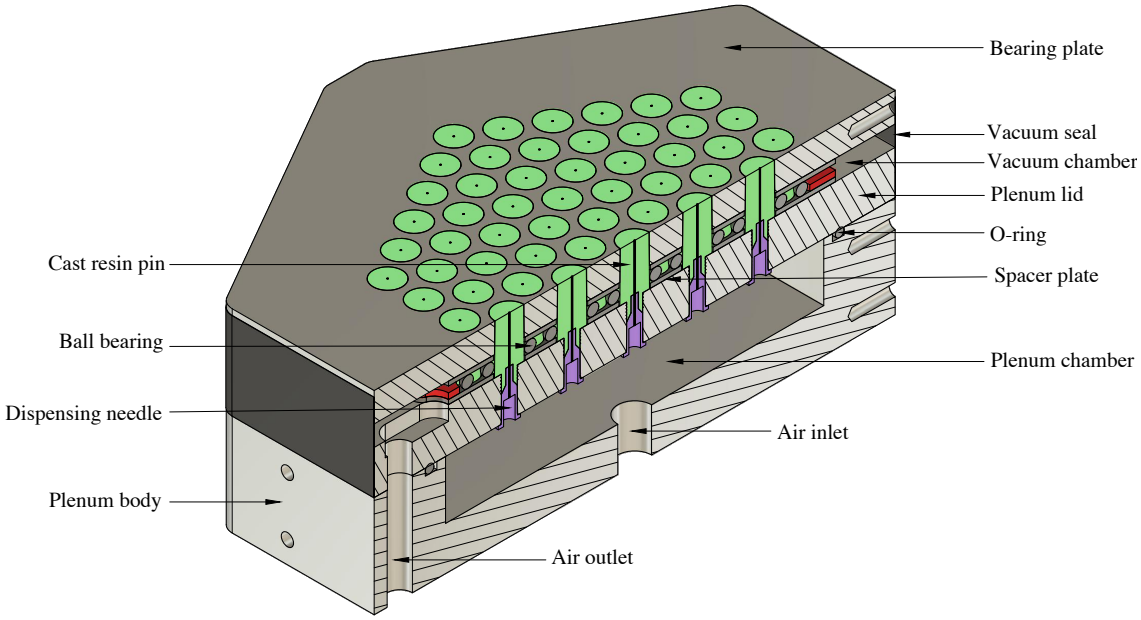

Figure D.1: Isometric cross section of the final demonstrator.

D.1.2 Pre-cast machining

The first step of the manufacturing process is to manufacture bearing plate and the plenum lid. These two components together make up the two-part mould. The bearing plate and plenum lid were both machined on a DMG Mori Milltap 700 from aluminium 7075-T6, purchased from Salomon's Metalen.

Bearing plate

An isometric view of the bearing plate is shown in figure D.3. Relevant dimensions are indicated in figure D.7. The 91 holes have a nominal diameter of 10 mm and are places in a close-packed hexagonal grid, spaced 12.5 mm apart. The conicity of the holes is 1:50 (included angle), or 1:100 measured to the centreline. The tapered holes were created using a spiral flute machine pin reamer[1] on the CNC machine. In order to reduce the surface waviness of the holes the holes, they were manually reamed using a hand pin reamer[2] with straight flutes. This is discussed in detail in appendix D.3.2.

The holes in the side of the bearing plate are tapped (M5) and can later be used to attach sensors and actuators. This also explains why the thickness of the bearing plate is reduced on the sides. This was done, such that the holes on the side could be machined in a single clamping set-up.

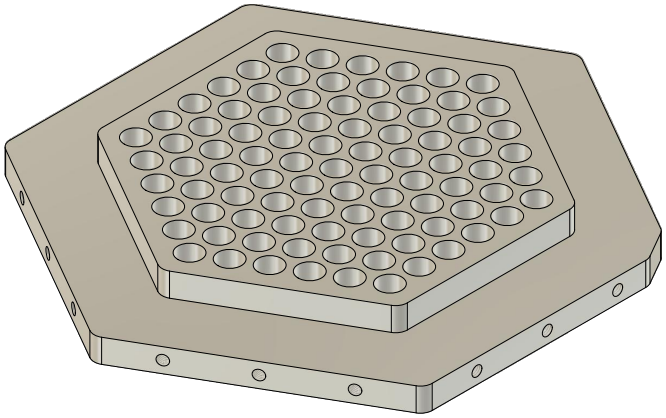

Figure D.2: Isometric view of the bearing plate after initial machining.

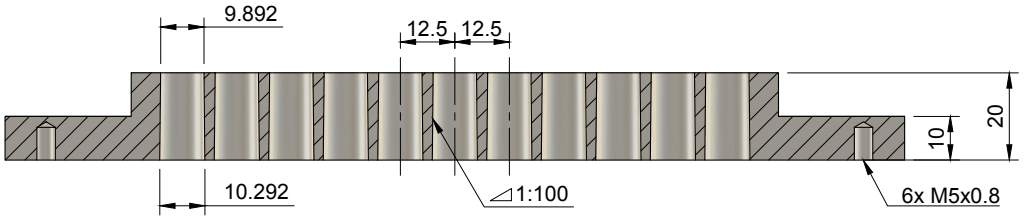

Figure D.3: Cross-section of the bearing plate with relevant dimensions indicated.

Plenum lid

An isometric view of the plenum lid is shown in figure D.4. Relevant dimensions are indicated in the cross-section shown in figure D.5. The hole pattern in the plenum lid matches the hole pattern in the bearing plate. A tight tolerance on the hole locations is not required, since the alignment of the pins with respect to the holes will be determined in the casting procedure. The locational accuracy of the CNC machine was specified as $\pm 25\,\mu$m, which is more than sufficient for this manufacturing method.

[1] Dormer Pramet machine pin reamer (1:50) - B9538.0
[2] Dormer Pramet hand pin reamer (1:50) - B9038.0

Since the resin should adhere to the surface during casting, a high quality surface finish is not required, or even desired. The holes are threaded (M6) in order to create a mechanical lock for the resin. The top side of each hole was chamfered in order to prevent stress concentrations in the cast resin. The diameter of the hole ($\varnothing 5.5\,\text{mm}$) is chosen such that a press fit is achieved with the hubs of the dispensing needles. A small chamfer on the bottom side of each hole was added in order to prevent any sharp edges from damaging the hub of the dispensing needle.

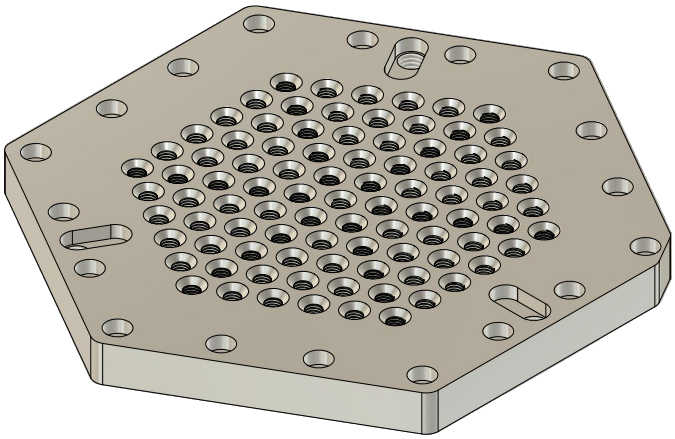

Figure D.4: Isometric view of the plenum lid.

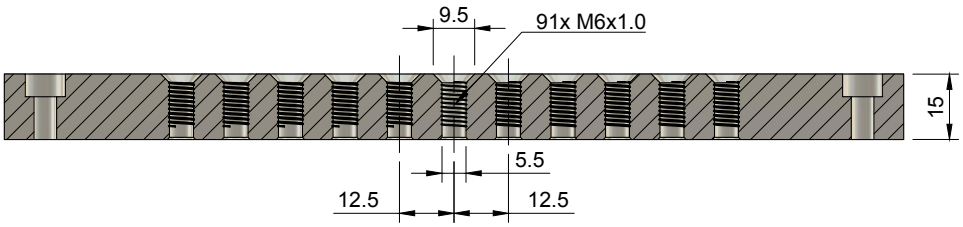

Figure D.5: Cross-section of the plenum lid after CNC machining and post-processing.

D.1.3 Casting

Part preparation

As mentioned, the resin should adhere to the plenum lid and should not adhere to the bearing plate. Such that the pins are fixed to the plenum lid after curing. In order to achieve this, each part is prepared differently for the casting step. The bearing plate is cleaned after machining, to remove any chips, dust and oil from the surface. This is done using a paper towel and isopropyl alcohol. After the part is thoroughly cleaned, all surfaces are prepared with a very thin layer of vaseline[3]. After applying a very thin coat of vaseline to all surfaces, they are wiped with a clean paper towel in order to remove as much vaseline as possible. This creates a greasy surface that prevents adhesion of the resin.

The plenum lid is also cleaned in order to remove any chips and dust that remained from the machining process. Each hole is then thoroughly cleaned using cotton swabs and isopropyl alcohol twice. Since the resin should adhere to these surfaces it is important that they are thoroughly cleaned. After the holes are cleaned, the needles are inserted from the bottom side of the plenum lid using a bench press. The PTFE coating that is present on the dispensing needles is removed using sandpaper. This ensures that the resin will also adhere properly to the needles. The hubs of the needles seal the bottom of the holes. After this step, the bearing plate is clamped on top of the plenum lid, thereby creating a mould with open cavities, as shown in figure D.6.

[3]Kroon White Vaseline

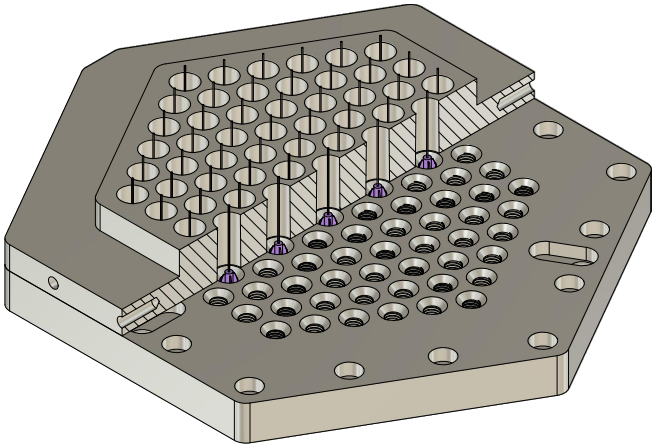

Figure D.6: Assembly at the start of the casting procedure.

Resin preparation

For the demonstrator, a total of 300 g of resin was used. The resin is a bisphenol A/F type epoxy[4], in combination with an amine hardener[5]. In order to improve the mechanical properties of the resin 10 wt% aluminium oxide powder[6] (Al_2O_3, D50 $< 3.5\,\mu$m) is added. The resin was mixed in two separate batches of 150 g. Because the curing reaction is exothermic, the heat generated during this process will further accelerate the curing. A larger batch generates more heat, which will not dissipate as easily, thereby decreasing the pot life. The resin was mixed for 5 minutes, then degassed for 15 minutes. This leaves 20 minutes of working time per batch.

Casting

After mixing an degassing the resin, it is now cast into the cavities of the mould using a syringe. Each hole is filled to the top. The system then looks as shown in figure D.7. The needle aligners are then slid down in order to ensure that the each needle is aligned in the centre of its hole. For clarity, these are not shown in the figure. However, this is explained in appendix D.2.2.

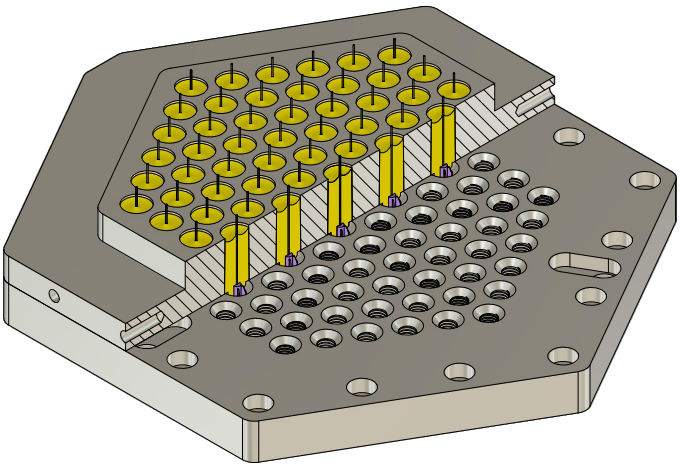

Figure D.7: Cross section of the system when the casting procedure is finished.

A cross-section of the system is shown in figure D.8. The effective height of the pins after the resin has cured is equal to the thickness of the bearing plate $t_{\mathrm{bp},0}$ minus the size of the meniscus

[4]Resion EP101
[5]Resion EP115
[6]Aluminium oxide powder

that is created during the curing t_m. This meniscus occurs due to the curing shrinkage of the resin and air escaping from the resin. This meniscus is approximately 3 mm deep.

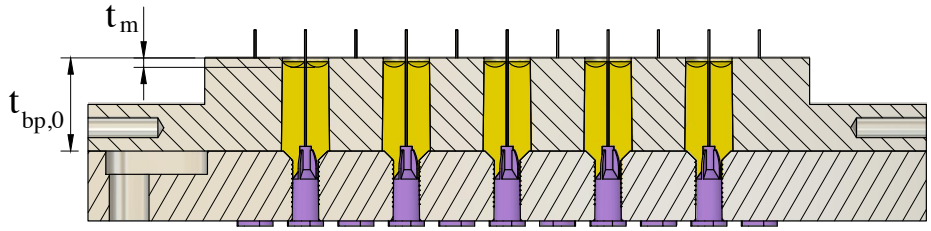

Figure D.8: Cross sectional view of the set-up during casting.

D.1.4 Separation

Before the two parts of the mould can be separated, the initial sacrificial layer needs to be removed. This layer is indicated in orange and red in figure D.9. A total of $t_{s,1} = 3.5$ mm is removed from the bearing plate and the pins using a shell mill on a manual lathe. The result is shown in figure D.10.

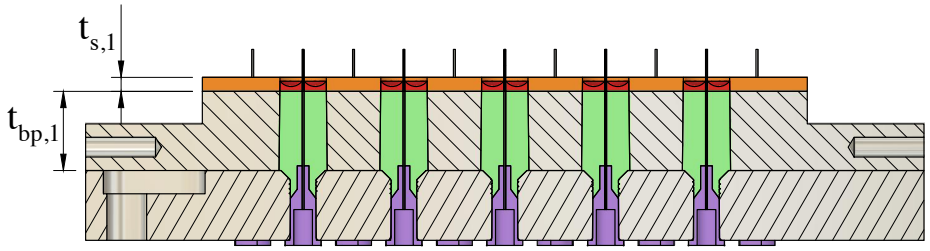

Figure D.9: Cross-section of the set-up after casting.

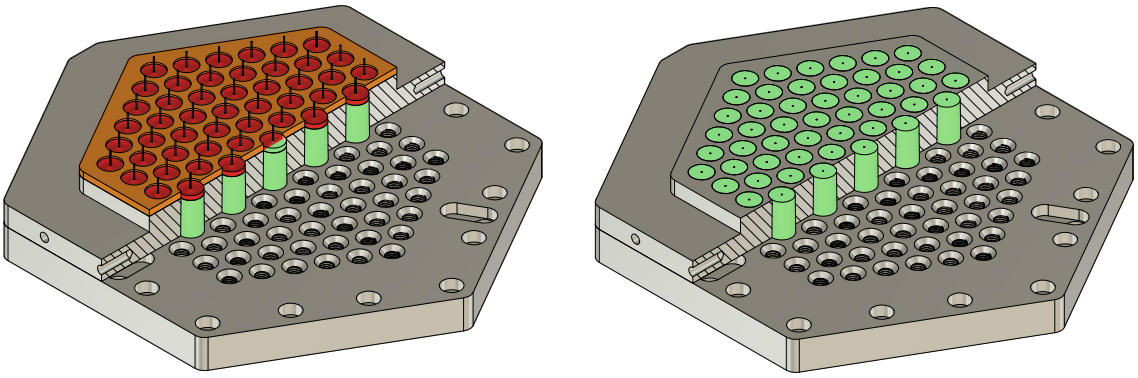

(a) Before machining operation.

(b) After machining operation.

Figure D.10: First machining operation.

After this machining operation, the two parts are separated, thereby creating a plate with pins (D.11a) and a plate with holes (D.11b). The assembly is supported by socket head cap screws that are inserted in the tapped holes of the bearing plate. Using a 3D printed adapter a force is exerted on the top of each pin. Thereby separating the two parts. This is explained in more detail in appendix D.4.8.

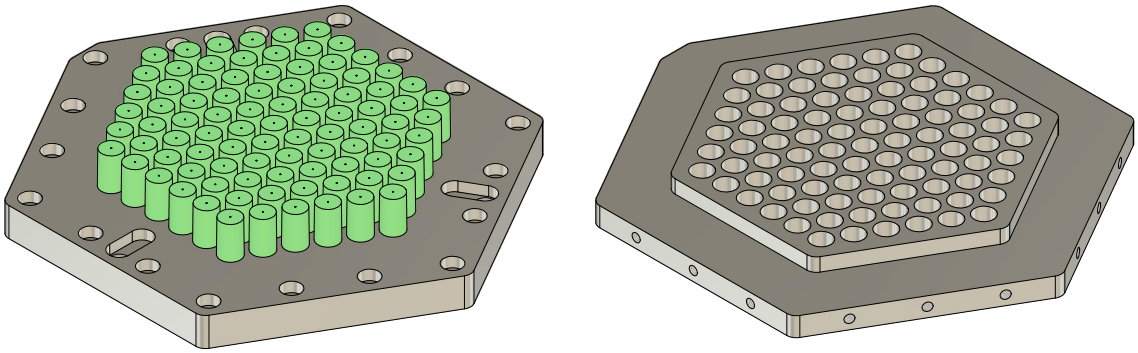

(a) Plenum lid with pins.

(b) Bearing plate after machining operation 1.

Figure D.11: Separated system.

D.1.5 Post-cast machining

After the initial layer of sacrificial material has been removed, the height of the pins is equal to that of the thickness bearing plate as:

$$t_{\mathrm{bp},1} = t_{\mathrm{bp},0} - t_{\mathrm{s},1} \tag{D.2}$$

In order to create pockets with the correct pocket height, more material needs to be removed from the bearing plate. In theory, the amount of material that should be removed during the second machining operation should be equal to the distance enforced between the two plates after curing t_{v}, minus the height of the pocket:

$$t_{\mathrm{s},2} = t_{\mathrm{v}} - h_{\mathrm{p}} \tag{D.3}$$

Though, it is very difficult in practice to reach such accuracy ($< 1\,\mu\mathrm{m}$) using a manual lathe. It could potentially be achieved using a surface grinder, but such a machine was not available in the workshop. Therefore, the secondary layer is also removed using a manual lathe, as shown in figure D.12. A cross-section is shown in figure D.13. The amount of material is chosen such that the pins are slightly protruding if the system is assembled. Protruding pins are achieved if:

$$t_{\mathrm{s},2} > t_{\mathrm{v}} \tag{D.4}$$

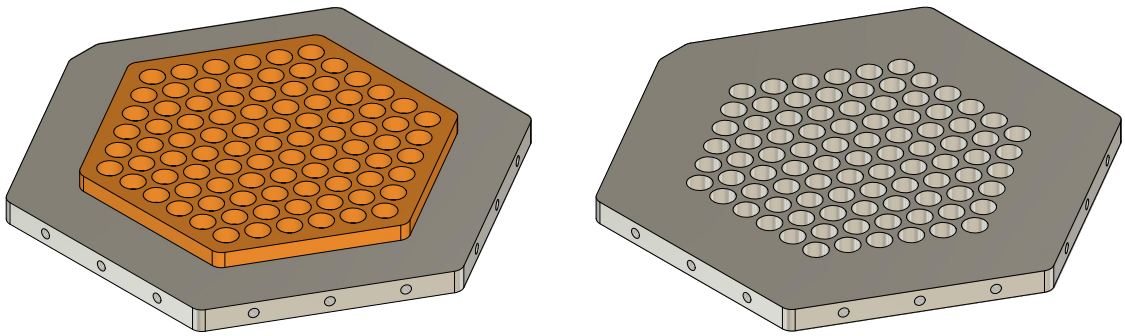

(a) Bearing plate before machining operation 2.

(b) Bearing plate after machining operation 2.

Figure D.12: Second machining operation.

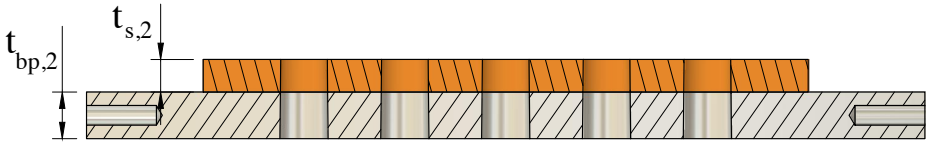

Figure D.13: Cross-section of the bearing plate.

D.1.6 Spacer plates

In order to increase the outlet film thickness, two spacer as shown in figure D.14 were added. A side vied of the system is shown in figure D.15. The spacer plates are laser cut from a sheet of steel S235. The nominal thickness is 1.5 mm. In combination with the ⌀4 mm ball bearings, a total vacuum height t_v of 7 mm is created.

During the manufacturing of the spacer plates, a lot of material is being removed and a lot of heat is introduced due to the laser cutting. This causes the spacer plates to warp slightly, essentially creating two disc springs. This reduces the vertical stiffness of the bearing plate with respect to the plenum lid. In order to minimise this effect, the spacer plates were glued to the bearing plate and plenum lid. This was done using the same epoxy resin as was used for the casting of the pins. The system was assembled, including all 216 ball bearings. It was then cured under vacuum pressure.

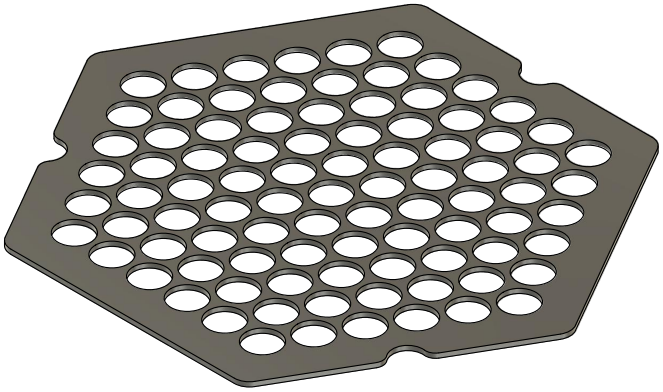

Figure D.14: Spacer plate.

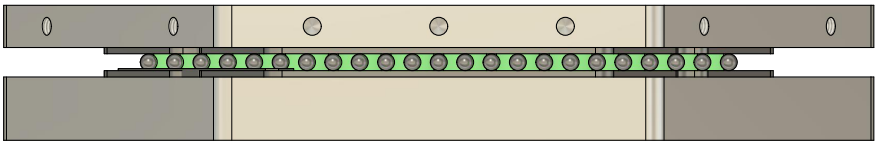

Figure D.15: Side view of the system, with the spacer plates inserted.

After this operation, the system is assembled using undersized ball bearings. With the pins slightly protruding, the assembled system is sanded on a flat granite surface plate. The top surface of the pins is brought into one plane with the top surface of the bearing plate. Next to that, this also *opens* the needles, by removing the burrs that might have been caused by the machining operation. The system is then disassembled and re-assembled using nominal sized balls. The pocket depth is then equal to the difference in ball diameters.

Note on the spacer plates

The spacer plates were added after the system had been designed and machined. The system was initially designed for a vacuum height t_v of 4 mm, which would result in a concentric outlet film thickness of 40 μm. However, the numerical model was not completely finished at this time. When the numerical model was finished, it turned out that an outlet film thickness of 40 μm could cause the system to become unstable with higher values of eccentricity.

Because of the conicity, the outlet film thickness could be increased by increasing the height of the vacuum chamber. However, the largest nominal size balls that fit in between the pins is ⌀4 mm. In order to increase the distance between the bearing plate and plenum lid, it was decided to add the spacer plates.

A potential advantage of using spacer plates is improved contact mechanics: steel on steel instead of steel on aluminium. This is discussed in more detail in appendix D.5.4.

D.1.7 Thickness simplified

As the manufacturing process can be somewhat confusing, the thickness of the bearing plate and the height of the pins throughout the process are shown here. The situation before, and after each machining operation is shown for a single pin only. The values are shown in table D.2.

Table D.2: Dimensions throughout the manufacturing process.

		Bearing plate thickness	Pin height	Ball diameter	Figure
Step 1	Before	$t_{\mathrm{bp},0}$	$t_{\mathrm{p},0}$	-	D.16a
	Material removed	$t_{\mathrm{s},1}$	$t_{\mathrm{s},1}$	-	D.16b
	After	$t_{\mathrm{bp},1}$	$t_{\mathrm{p},1}$	-	D.16c
Step 2	Before	$t_{\mathrm{bp},1}$	$t_{\mathrm{p},1}$	-	D.17a
	Material removed	$t_{\mathrm{s},2}$	-	-	D.17b
	After	$t_{\mathrm{bp},2}$	$t_{\mathrm{p},1}$	-	D.17c
Step 3	Before	$t_{\mathrm{bp},2}$	$t_{\mathrm{p},1}$	$d_{\mathrm{b}-}$	D.18a
	Material removed	-	$t_{\mathrm{s},3}$	$d_{\mathrm{b}-}$	D.18b
	After	$t_{\mathrm{bp},2}$	$t_{\mathrm{p},2}$	$d_{\mathrm{b}-}$	D.18c
	Final result	$t_{\mathrm{bp},2}$	$t_{\mathrm{p},2}$	$d_{\mathrm{b}+}$	D.19

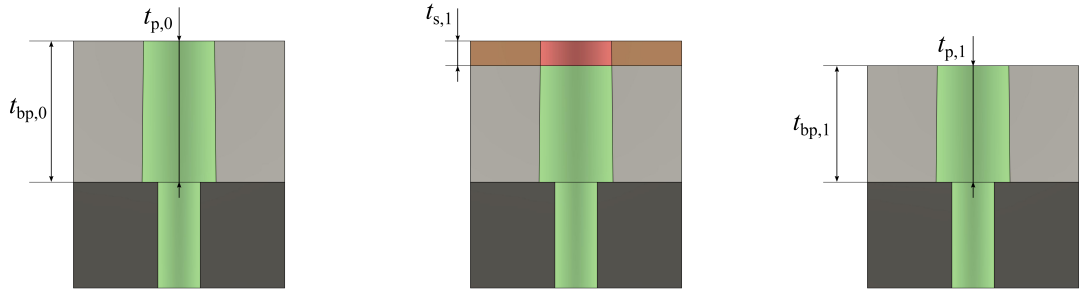

(a) Before. (b) Sacrificial layer 1. (c) After.

Figure D.16: Machining step 1.

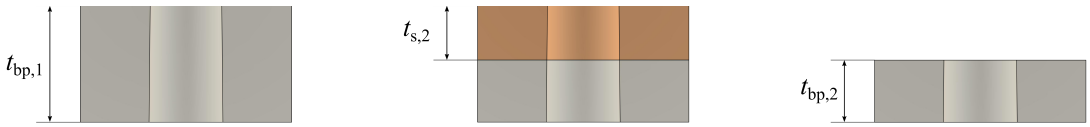

(a) Before. (b) Sacrificial layer 2. (c) After.

Figure D.17: Machining step 2.

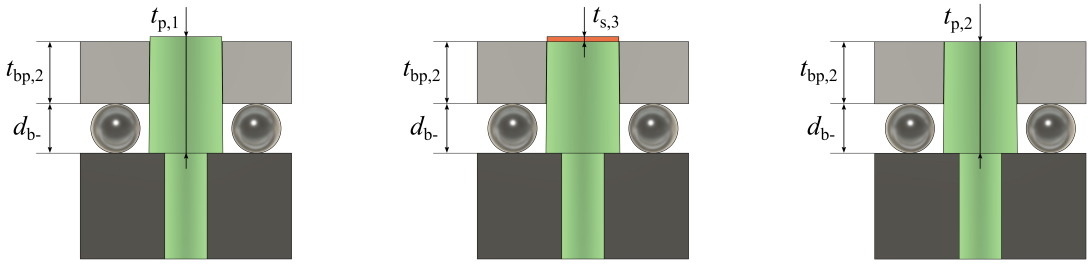

(a) Before. (b) Sacrificial layer 3. (c) After.

Figure D.18: Machining step 3 using undersized balls $d_{\mathrm{b}-}$.

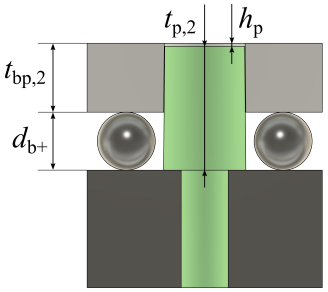

Figure D.19: Final result using oversized balls d_{b+}.

D.2 Inlet restriction

Dispensing needles are used to create capillary inlet restrictions. These dispensing needles were used since they can easily be integrated into the proposed manufacturing procedure. The measurement of the inlet restriction value is explained in appendix D.2.1. Practical notes on the use of the needles are shown in appendix D.2.2. Alternative methods that could be used to manufacture an inlet restriction are presented in appendix D.2.3.

D.2.1 Restriction measurement

Measurement set-up

The measurement set-up is shown in figure D.20. High pressure air is supplied from the wall outlet ($\sim 6-7\,\text{bar}$). A tank[7] with a volume of 2 L is filled. The measurement is started as soon as the valve is closed. Due to the restriction of the capillary tube, sufficient pressure can be build up downstream from the tank without the need for an additional valve. The high pressure air that is present in the tank will flow through the restriction to ambient pressure. This essentially creates a pressure sweep. The pressure drop across the pneumatic tubing from the tank to the restriction is assumed to be negligible with respect to the restriction of the capillary tube.

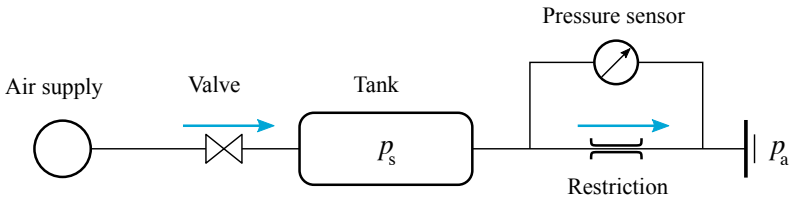

Figure D.20: Schematic representation of measurement set-up.

The mass of air that is present in the tank can be written as:

$$m = \rho V \tag{D.5}$$

Where the volume V is the volume of the tank, plus the volume of the pneumatic tubing ($\approx 0.02L$). The density ρ can be determined by using the ideal gas law. Thus the mass can be written as:

$$m = \frac{pV}{R_s T} \tag{D.6}$$

The mass flow can then be determined by taking the derivative of the mass with respect to time:

$$\dot{m} = -\frac{\partial p}{\partial t}\frac{V}{R_s T} \tag{D.7}$$

The pressure gradient over time can easily be measured by sampling the pressure and time. Using MATLAB, a polynomial fit is used to fit over the pressure versus time data. This ensures that the

[7] Festo CRVZS-2

derivative ($\partial p/\partial t$) is smooth and not distorted by measurement noise. The mass flow through the capillary was defined as:

$$\dot{m}_\mathrm{i} = G_\mathrm{i}(p_\mathrm{s}^2 - p_\mathrm{i}^2) \tag{D.8}$$

The inlet conductivity can therefore be written as:

$$G_\mathrm{i} = \frac{\dot{m}_\mathrm{i}}{p_\mathrm{s}^2 - p_\mathrm{i}^2} \tag{D.9}$$

Where the supply pressure p_s is sampled by the pressure sensor and the pressure downstream from the restriction p_i is in this case the ambient pressure p_a.

Sample preparation

Needles of three different gauges were used: G25[8], G27[9] and G30[10]. In an initial test it was found that the result of the test is very repeatable (see figure D.23). Therefore, only one of each specific length/gauge combination is tested.

The needles were embedded in a block of aluminium as shown in figure D.21a. The top part of the cast assembly (indicated in red) is removed using a face mill. The resulting part is shown in figure D.21b. The numbers correspond to a specific length/gauge combination. The dimensions in mm can be found in figure D.22. They were chosen such that they replicate a system with a system with a pin height of 13, 14 or 15 mm. The effective length of the needles is shown on the right.

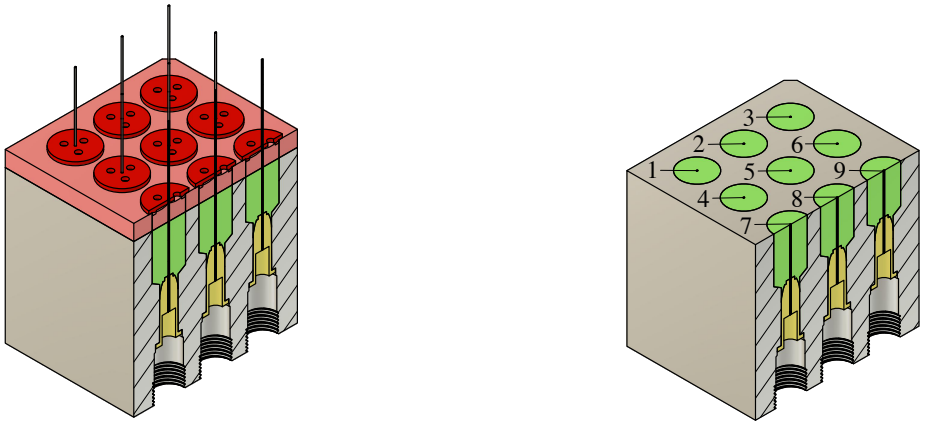

(a) Partial cross section of restriction block, before machining.

(b) Partial cross section of restriction block, after machining.

Figure D.21

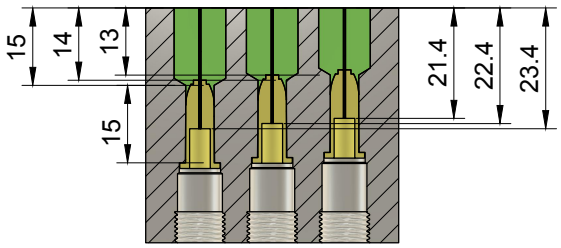

Figure D.22: Final dimensions of the restriction test block.

[8]Miraject Luer 17/42 , 25 Gauge
[9]Miraject Luer 30/42, 27 Gauge
[10]Miraject Endo Luer, 30 Gauge

Results - first test

Initially, a sample piece was made using G30 dispensing needles[11], since they were already available in the lab. A sample piece was prepared similar to the method as shown in figure D.21. The effective length of the needles (also taking into account the needle length inside the hub) is 18 mm. A total of 9 tests was performed: 3 restrictions were tested, and each restriction was tested three times. The results for all tests are nearly identical, as can be seen in figure D.23.

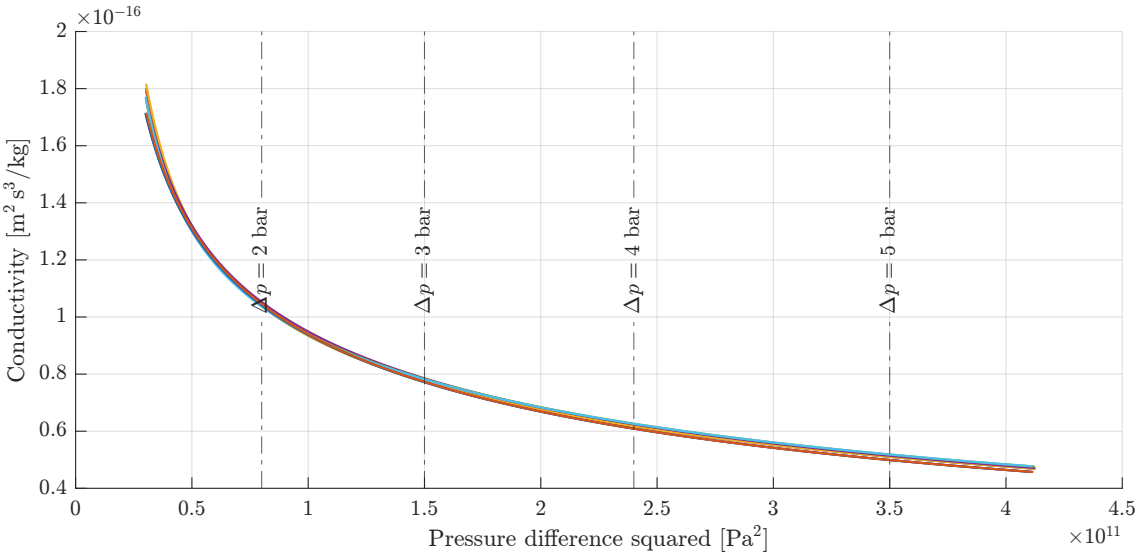

Figure D.23: Inlet conductivity as a function of the pressure difference for the first restriction test. The needles have a length of $L = 18\,\text{mm}$ and a diameter of $d = 160\,\mu\text{m}$.

Results - second test

For the second test, the restriction test block as described in appendix D.2.1 is used. The mass flow over time is shown in figure D.24. It can be seen that for each needle gauge, the needle with the smallest length takes the least time to discharge, as is expected.

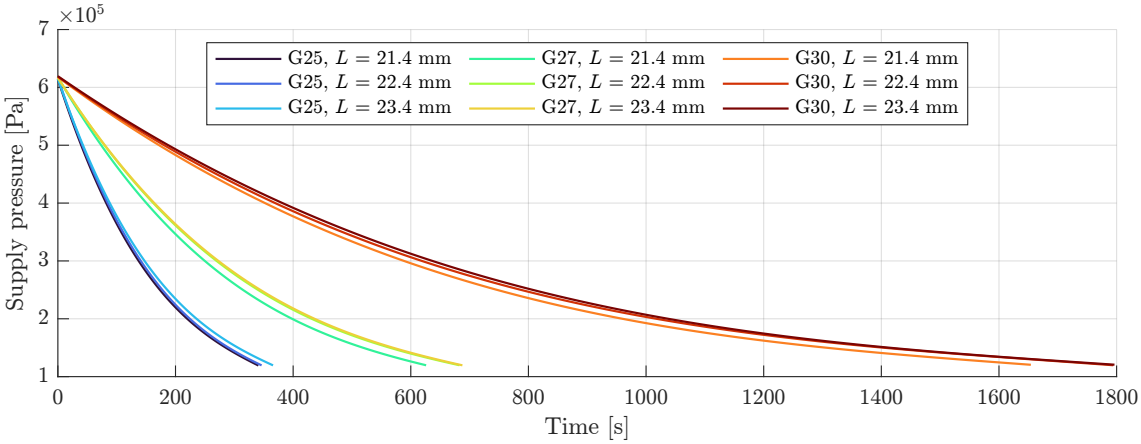

Figure D.24: Mass flow over time of various needles. The pressure downstream the restriction is equal to the ambient pressure, which is assumed to be $p_\text{a} = 1 \cdot 10^5$ Pa.

COMSOL inlet conductivity

In the numerical model, the inlet conductivity is assumed to be constant, i.e. independent of the flow through the restriction. independent of the flow through the restriction. Shown in figure D.25

[11] Jensen Global G30 NT Premium series

is the resulting pressure drop for a given (fixed) inled conductivity. The axis on the left shows the pressure drop across the inlet restriction, i.e. $p_s - p_i$.

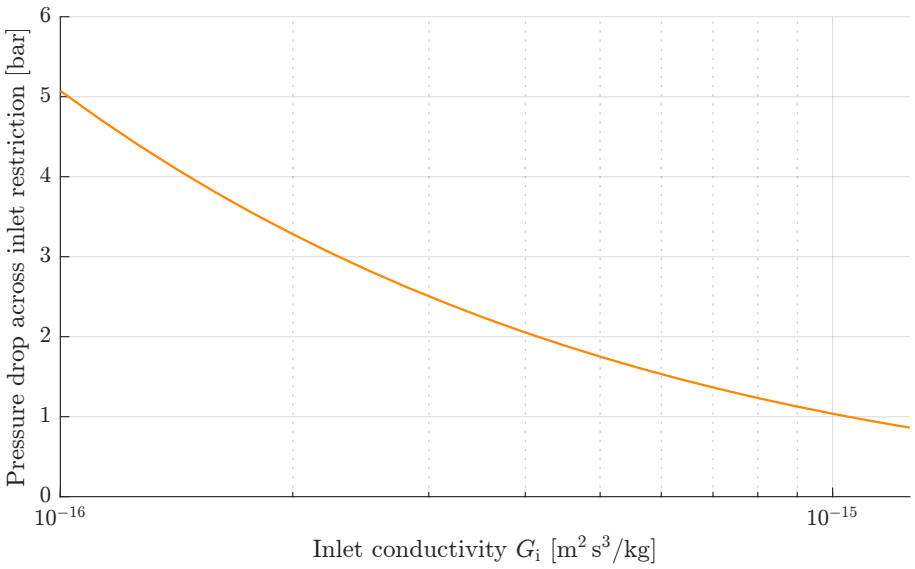

Figure D.25: Pressure drop across the inlet restriction as a function of the inlet conductivity.

In appendix D.2.1, this data is added to the experimental data. The experimental data should be interpreted as the inlet restriction for a given pressure difference. The numerical data should be interpreted as the resulting pressure drop, given a fixed value for the inlet restriction. Where the line indicated with COMSOL intersects the lines of the experimental data is where the value used in the model is correct. In the numerical model, a value of $G_i = 1 \cdot 10^{-15}\,m^2\,s^3/kg$ is used. The real conductivity lower. A better value could be found by iteratively changing the value in the COMSOL model. An even more accurate solution would be to implement the empirical data into the model.

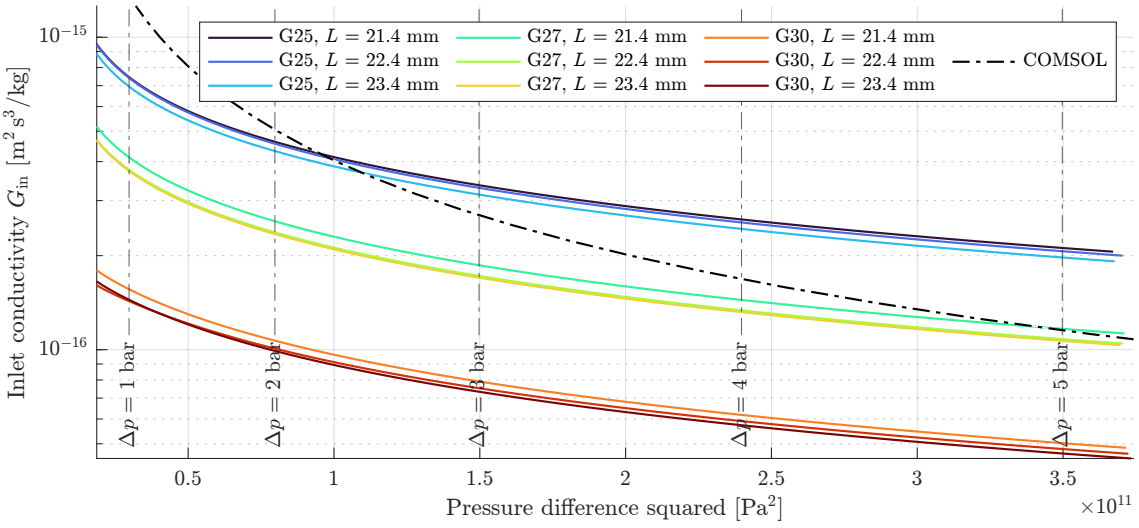

Figure D.26: Inlet conductivity for varying pressure.

Theoretical inlet restriction value

The diameter of the needles was measured using a digital microscope. An example of each size is shown in figure D.27. Per gauge, six needles were measured. The average diameters are shown in table D.3.

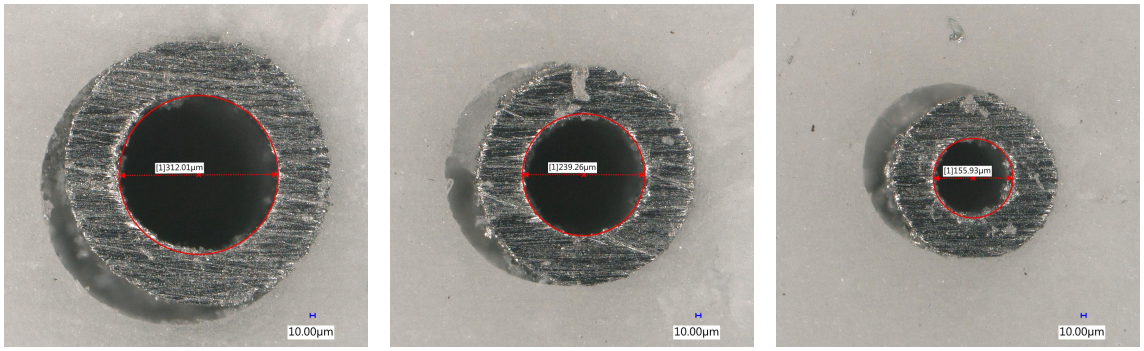

(a) G25 needle. (b) G27 needle. (c) G30 needle.

Figure D.27: Needle diameter measurement.

Table D.3: Needle diameter, averaged over 6 measurements

Needle gauge	Diameter $\mu \pm \sigma$ [μm]
G25	312.7 ± 1.5
G27	239.3 ± 1.7
G30	157.4 ± 1.5

The theoretical conductivity of a capillary tube is given as:

$$G_{\mathrm{i}} = \frac{\pi d^4}{256\,\eta R_{\mathrm{s}} T L} \tag{D.10}$$

This equation was evaluated using the respective values as used in the test sample block. The results are shown in table D.4.

Table D.4: Theoretical inlet conductivity for given length and diameter.

ID	Gauge	Length L [mm]	Diameter d [μm]	Ratio L/d [1]	$G_{\mathrm{i,t}} \cdot 10^{15}$ [$\mathrm{m^2\,s^3/kg}$]
1	G25	21.4	313	68	3.62
2	G25	22.4	313	72	3.46
3	G25	23.4	313	75	3.31
4	G27	21.4	239	89	1.24
5	G27	22.4	239	94	1.19
6	G27	23.4	239	98	1.14
7	G30	21.4	157	136	0.23
8	G30	22.4	157	142	0.22
9	G30	23.4	157	149	0.21

D.2.2 Practical notes

Needle edge post processing

Depending on the tool that is used to remove the sacrificial material, the needles will be clogged due to smearing. This is solved relatively easy by sanding the pins on a surface plate. The difference is show in figure D.28.

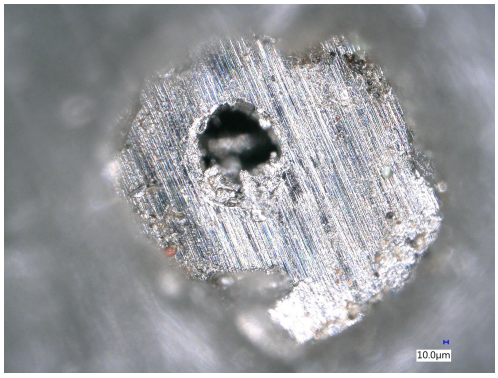

(a) Needle after machining.

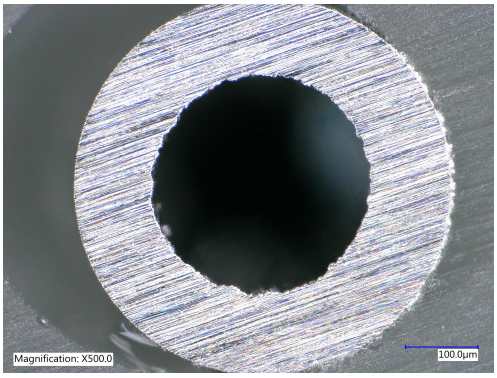

(b) Needle after sanding.

Figure D.28: Comparison of the needle before sanding (a) and after sanding (b).

Needle centring

The aligning is done using a 3D printed adapter piece as shown in figure D.29. The dimensions are determined by the needle and hole diameter. It takes some iterations before the correct fit is achieved on both the needle and in the hole. The manufacturing procedure is then as shown in figure D.30.

The alignment of the needles with respect to the hole was measured using a digital microscope[12]. The results are shown in figure D.31. After the first iteration, the design was slightly altered to improve "printability". The average misalignment error was then measured to be $e = 77 \pm 30\,\mu$m and the maximum misalignment was $125\,\mu$m.

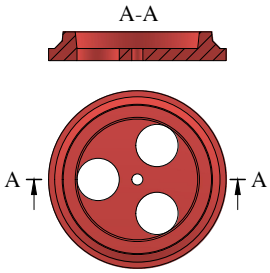

(a) Cross section of needle aligner.

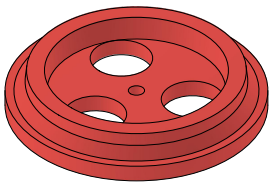

(b) Isometric view of needle aligner.

Figure D.29

(a) Step 1: Insert needles from the bottom.

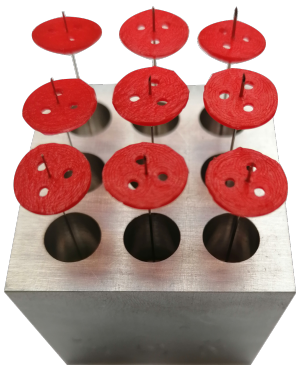

(b) Step 2: Slide needle aligners over the top of the needle.

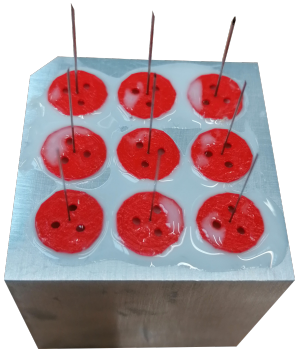

(c) Step 3: Fill cavity with resin. Afterwards, press needle aligners into the hole.

Figure D.30

[12]Keyence VHX-6000

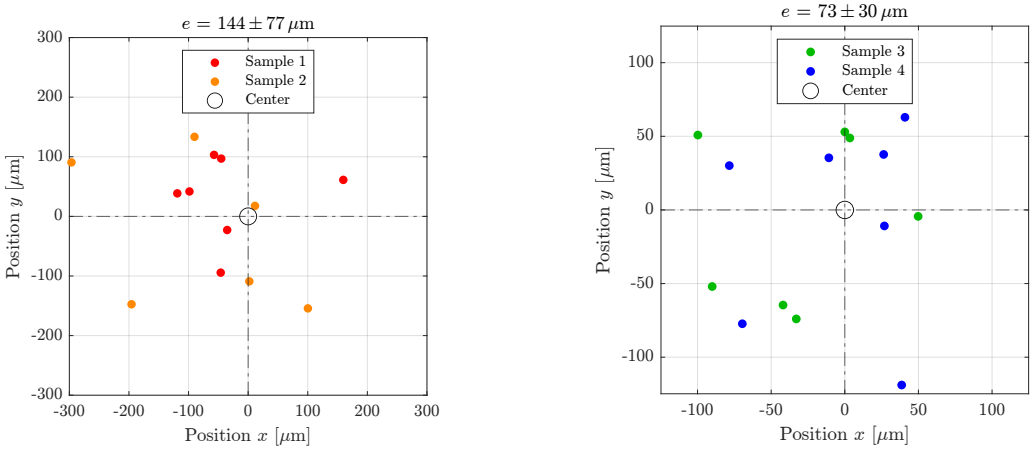

(a) Sample pieces 1 and 2.

(b) Sample pieces 3 and 4.

Figure D.31: Needle alignment measurement

Recess manufacturing

The recess is machined using a diamond tipped cone burr tool ($d = 1\,$mm) and a manual milling machine. The diamond tool should be used at a high rotational speed. The maximum RPM of the machine 4500 rpm. The aim was to manufacture a recess with a depth of 200 μm and a diameter of 1 mm.

The surface was inspected using a digital microscope, the results are shown in figures D.33 and D.34. Both the diameter and the depth of the recess are larger than the desired value. Probably, this is due to particles that remain in the recess during the operation and essentially increase the size of the tool. This could easily be solved by selecting a tool with a smaller diameter and reducing the tool depth. The diameter of the needle seems to have been slightly increased ($d_1 = 158.2\,\mu$m, $d_2 = 169.2\,\mu$m). Part of this could be due to the backlash in the microscope lens.

Note that this test has been performed using a G30 needle. For the final prototype, G25 needles have been used. This might alter the outcome of this manufacturing step. However, in general it was found that the lower gauge needles (i.e. larger diameter) are easier to work with.

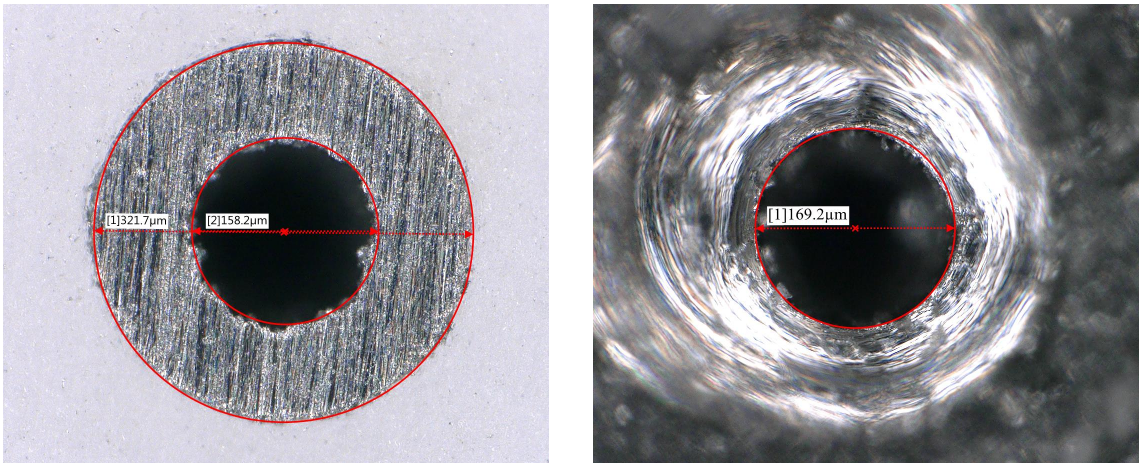

(a) G30 needle before recess manufacturing.

(b) G30 needle after recess manufacturing.

Figure D.32

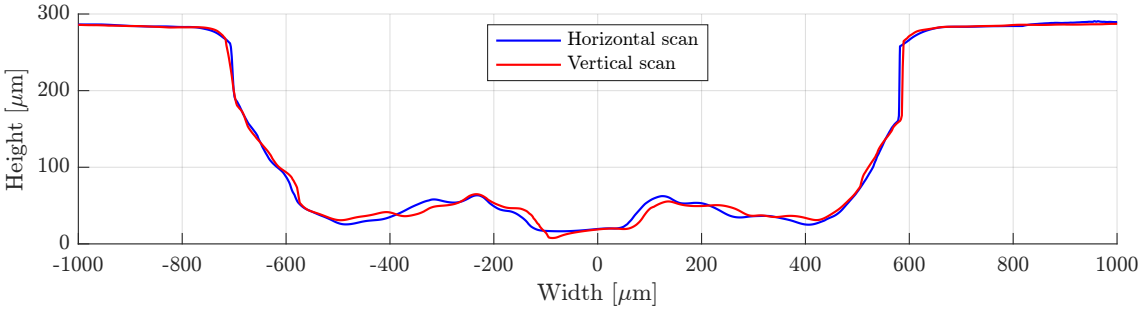

Figure D.33: Depth scan of the surface as indicated in figure D.34.

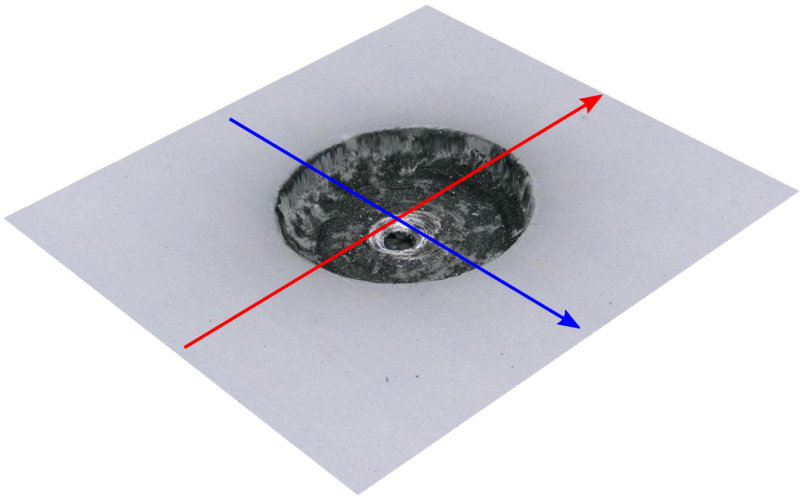

Figure D.34: 3D representation of the pin surface with the manufactured recess.

D.2.3 Alternative methods

Metal wire removal

Song et. al. use a low temperature soldering wire in combination with PDMS resin to produce a circular channel [31]. The PDMS is able to withstand temperatures of up to 200 °C. The wire is 60% tin and 40% lead and has a eutectic point of approximately 190 °C. Soldering wires that have an ever lower melting point are also available (e.g. SMDIN52SN48[13] has a melting point of 118 °C). After the PDMS has cured, the wire is removed by heating the workpiece to approximately 190 °C under vacuum (max 0.2 bar absolute pressure).

Such methods could in theory be applied within the current manufacturing method. However, the melting point of the soldering wire needs to remain below the glass transition temperature of the polymer.

Polymer wire removal (ABS)

Saggiomo and Velders have created microfluidic devices by casting a 3D printed (ABS) scaffold in PDMS [32]. After curing, the scaffold is removed by dissolving it in acetone. Channels with a diameter as small as 90 μm have been created using this method. Also a complex air manifold-like structure has been created, where the channels have a diameter of 2 mm. Potentially, this method could be used to created a manifold as was required in the pressure control concept [5].

For this research, this method has not been used, since epoxy does not handle exposition to acetone very well. In most cases, it will not fully dissolve, however the epoxy becomes gummy and brittle. Instead, a similar method has been tried, where water soluble PVA is used.

[13] Digi-Key: digikey.nl

Polymer wire removal (PVA)

PolyVinyl Alcohol (PVA) is a material that can be used in a 3D printer and is soluble in water. As an experiment, it was tried whether similar results as shown by Saggiomo could be replicated using epoxy resin and PVA filament. Strands of PVA were created by printing a small disk on the print bed. This disk is used to ensure that the part adheres to the print bed and can later be used for aligning the part. From the centre of the disk, the extruder is then moved straight up, without extruding any material. This creates a thin strand of PVA attached to a disk as shown in figure D.35.

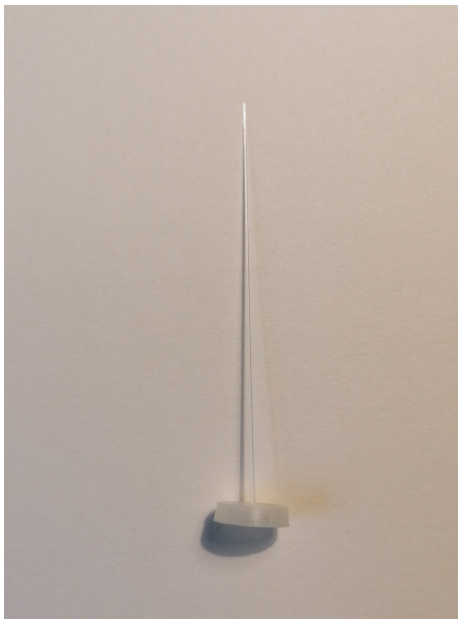

Figure D.35: PVA strand attached to disk.

This disk was then cast in epoxy resin in a 3D printed mould. After curing, the PVA was removed by dissolving it in water. Due to the narrow channel, this took approximately 2 days. The resulting capillary channel is shown in figure D.36a. The hole diameter was measured to be $d = 313\,\mu\text{m}$, as shown in figure D.36b. The length of the channel was approximately $L = 15\,\text{mm}$, which gives a ratio of $L/d = 50$. The restriction value of the channel has not been measured. It is believed that channels with a higher L/d ratio can be created, though this will increase the time it takes to dissolve the filament. This will also cause the pins to swell, which is undesired. It has therefore been decided not to use this method in the final demonstrator.

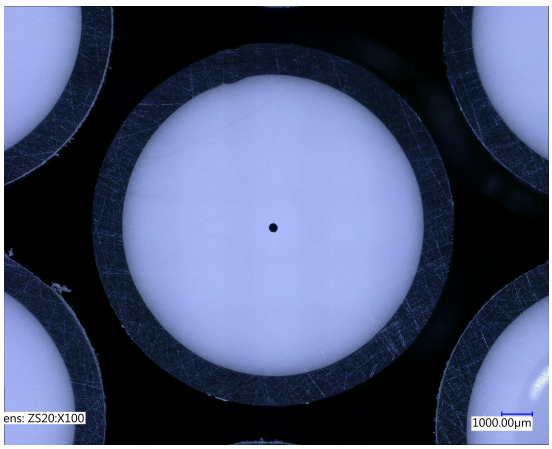

(a) Magnification 100×.

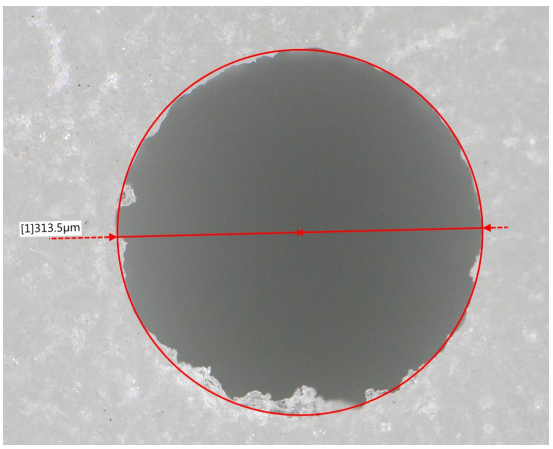

(b) Magnification 500×.

Figure D.36: Restriction created using PVA wire.

D.3 Mould geometry

In this section, various phenomena and processes are introduced that influence the final dimension of the outlet restriction. In general, the geometry of the radial outlet restriction is determined by two factors:

1. Mould geometry
    - Deviation from perpendicularity
    - Surface waviness
    - Release agent layer thickness
2. Resin behaviour

This section focusses on the influence of the mould geometry on the outlet film thickness. The term resin behaviour is used to describe the processes occurring within the resin during and after curing. This is discussed in appendix D.4. The main manufacturing errors that affect the stroke $\bar{S}$ and the concentric outlet film thickness $h_{\mathrm{o,c}}$ are shown in table D.5.

Table D.5: Influence of manufacturing errors on the stroke and concentric outlet film thickness.

Imperfection	Influence on $\bar{S}$	Influence on $h_{\mathrm{o,c}}$
Deviation from perpendicularity	Decreases	Varies radially
Surface waviness	Decreases	Varies radially and vertically
Mould release agent	Increases	Increases radially and vertically

D.3.1 Deviation from perpendicularity

The perpendicularity of the hole with respect to the surface influences the local outlet film thickness and the maximum travel. Shown in figure D.37a is the situation where the hole is perfectly perpendicular to the surface of the bearing plate (shown in green). This produces an outlet film thickness that is equal on both sides as well as a symmetric stroke. If the hole is out of square, the cast pin that originates from that hole will also be out of square, as shown in figure D.37b. This leads to an increase of concentric outlet film thickness on one side and a decrease of the concentric outlet film thickness on the other side, as shown in figure D.37. Also, the stroke becomes asymmetrical.

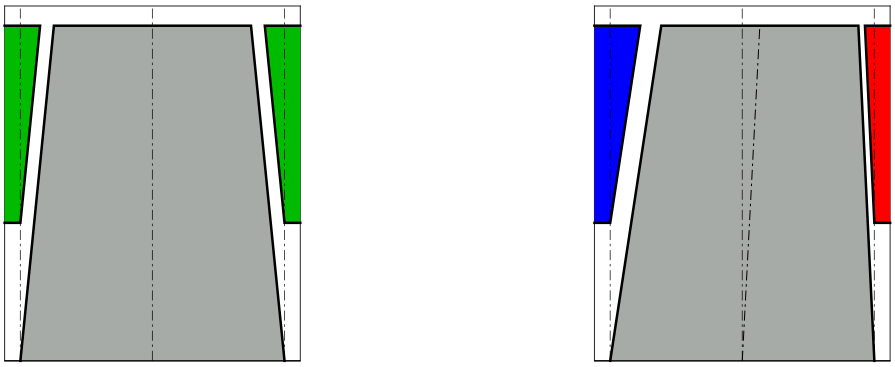

(a) Perpendicular pin.

(b) Misoriented pin.

Figure D.37

The concentric outlet film thickness for a perpendicular hole is defined as:

$$h_{\mathrm{o,c}} = h_{\mathrm{v}} \tan\delta \cos\delta \approx h_{\mathrm{v}}\,\delta \tag{D.11}$$

For a hole that is perfectly perpendicular to the surface, the stroke S (total travel) is independent of the direction of travel and can be defined as:

$$S = 2\,h_{\mathrm{o,c}} \tag{D.12}$$

However, if there is a deviation from perpendicularity to the surface of the bearing plate this is no longer true. In that case, the conicity effectively becomes dependent on the radial location. There will be a major and minor conicity, defined as:

$$\begin{aligned} \delta^+ &= \delta + \alpha \\ \delta^- &= \delta - \alpha \end{aligned} \tag{D.13}$$

Where α is the angle of misorientation. The major and minor concentric outlet film thickness then can be written as:

$$\begin{aligned} h_{\mathrm{o,c\,max}} &= h_\mathrm{v} \tan\delta^+ \cos\delta^+ \approx h_\mathrm{v} \tan\delta^+ \\ h_{\mathrm{o,c\,min}} &= h_\mathrm{v} \tan\delta^- \cos\delta^- \approx h_\mathrm{v} \tan\delta^- \end{aligned} \tag{D.14}$$

This is shown graphically in figure D.38 for a nominal conicity of $\delta = 1/100$ rad and a vacuum height of $t_\mathrm{v} = 5\,\mathrm{mm}$.

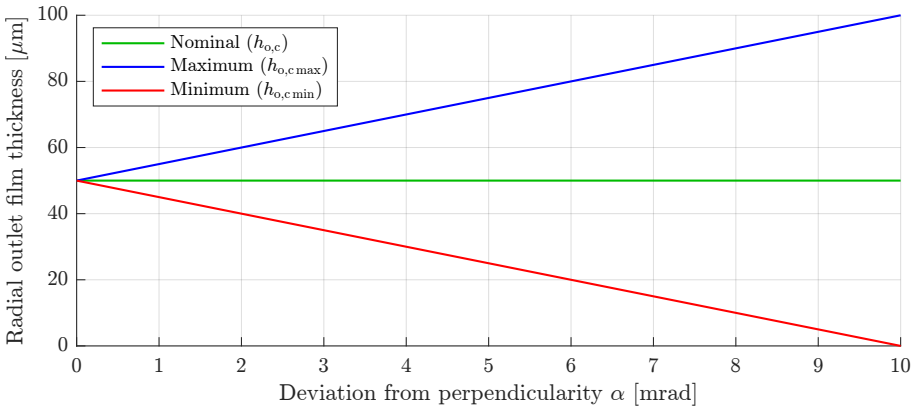

Figure D.38: The film thickness as a function deviation from perpendicularity.

For a single misoriented pin, the magnitude of the total stroke S remains identical to the stroke of the perpendicular pin, regardless of the deviation from perpendicularity.

$$|S| = h_{\mathrm{o,\,max}} + h_{\mathrm{o,\,min}} = 2\,h_{\mathrm{o,\,nom}} \tag{D.15}$$

However, the stroke does become dependent on the direction of travel, since it is asymmetrical. In a system with multiple pins, the orientation of each hole might be different. If this is the case, the total stroke of the system will be reduced.

Misorientation inspection

It was attempted to measure the misorientation of the holes in the bearing plate using a digital microscope[14]. The result is shown in figure D.39. The centre of each hole was found using the edge recognition function of the accompanying software. This data was then exported and processed using MATLAB.

[14] Keyence VHX 6000

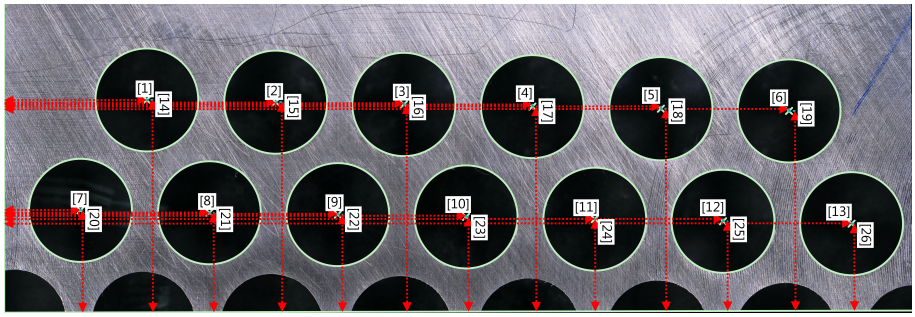

(a) Bearing side.

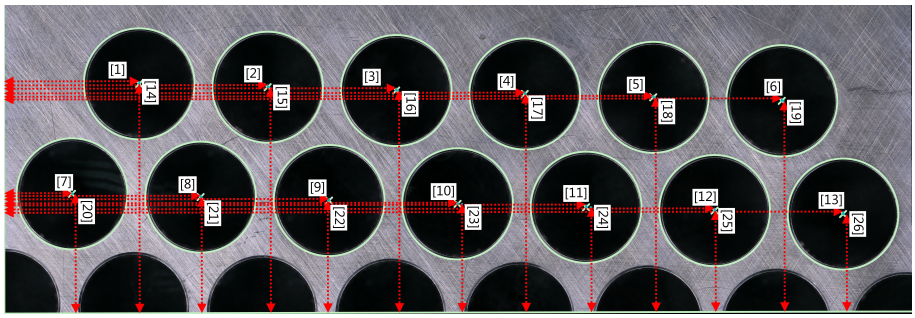

(b) Vacuum side.

Figure D.39: Inspection of hole misorientation.

Since the position data corresponds to opposing sides, the x-positions of the vacuum side was inverted. The grid on the bearing side was then translated and rotated with respect to the grid on the vacuum side, such that the total squared length of the vectors between corresponding holes was minimised.

$$r_{\mathrm{e}} = \sqrt{(x_{\mathrm{v}} - x_{\mathrm{b}})^2 + (y_{\mathrm{v}} - y_{\mathrm{b}})^2} \tag{D.16}$$

The result is shown in figure D.40. The numbers refer to the hole IDs as shown in figure G.3. The average length of the vectors between corresponding holes was 191 μm. This would translate to an average misorientation of 19.1 mrad, which is an unrealistically high value. This measurement method is therefore deemed unsuited for this application.

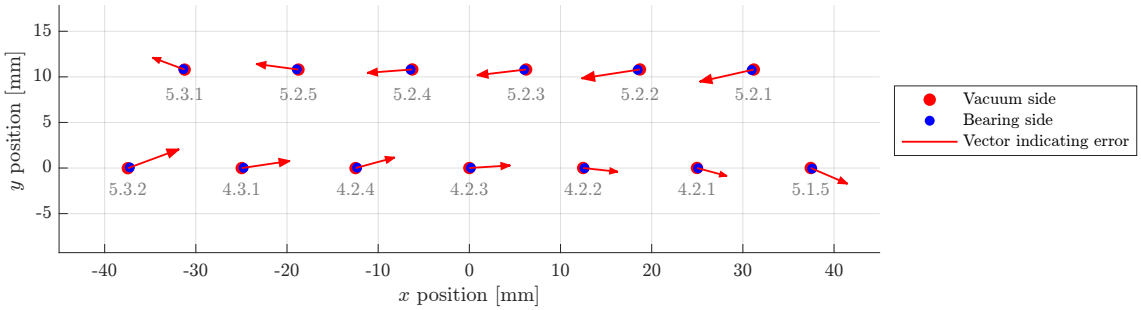

Figure D.40: Hole alignment overlay.

D.3.2 Surface waviness

Definition

A schematic representation of a surface profile is shown in figure D.41. This is an exaggerated, close up view of a surface, where relevant definitions are indicated. The total surface profile is determined by a low frequency component, which is called the waviness profile and a high frequency component, called the roughness profile. According to ASME standards [33], measurements of the surface profile should be performed in the direction which gives the maximum reading. In general, this will be perpendicular to the direction of the lay, which is the direction of the dominant pattern.

In general, any waviness in the surface is caused by deformation of the workpiece during the manufacturing operation. This may also include influences of deformation of the machine itself. Any vibrations or chatter might also cause waviness. Roughness usually results from the inherent action of the production process, and is dependent on the workpiece material.

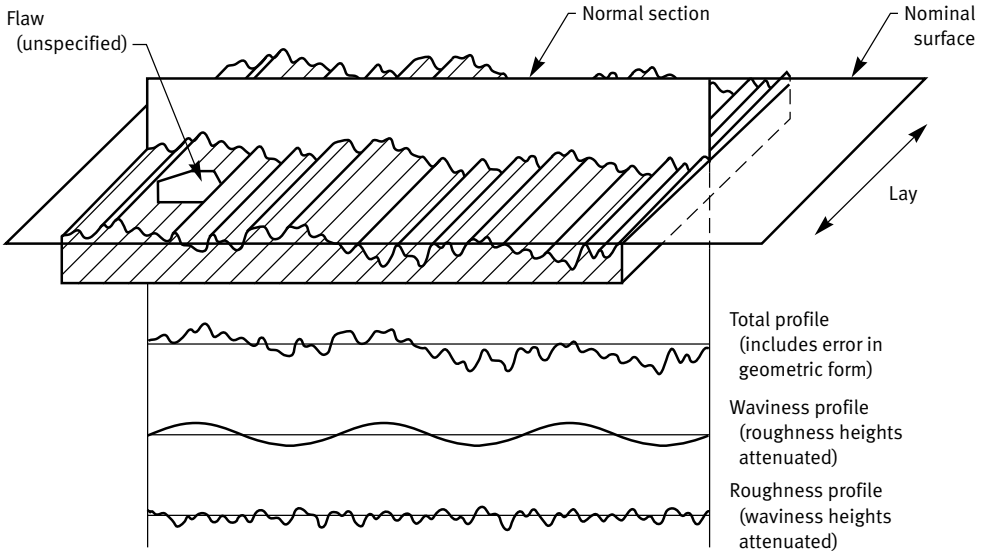

Figure D.41: Surface texture[15].

Global influence

The influence of the waviness on the cast geometry is shown graphically in figures D.42 and D.43. This shows the interface of the bearing plate and the cast pin, essentially turned on its side. In other words, the positive x-direction normally corresponds to what is normally the positive z-direction. The outlet restriction is created by enforcing a distance t_v between the bearing plate and the plenum lid after curing. The plenum lid is not shown in these figures, but is located on the left side, essentially fixed to the pin.

If the mould surface (i.e. bearing plate) is perfectly flat, the cast pin that originates from that surface is also perfectly flat. This is valid if resin behaviour is not taken into account. This situation is shown in figure D.42. The outlet film thickness is consistent and therefore predictable. However, if the mould surface has a certain waviness, the created pin will have the same waviness. This is shown in figure D.42a. After releasing the cast from the mould, the outlet film thickness will be inconsistent and thus unpredictable. This is shown in figure D.42b. Also, the stroke could be reduced or become asymmetrical.

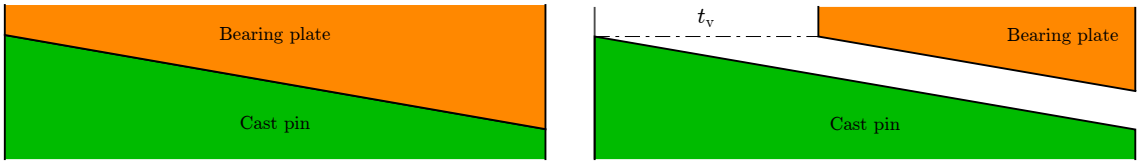

(a) Bearing plate in casting set-up.

(b) Bearing plate after curing.

Figure D.42: Ideal surface.

[15]Figure adapted from ASME B46.

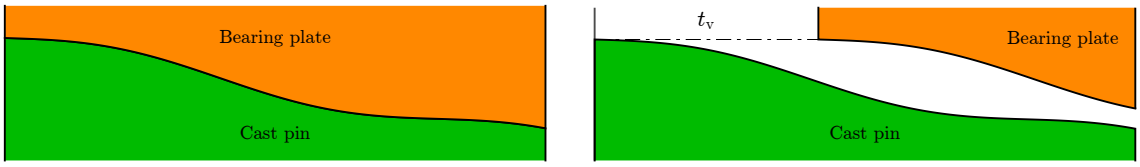

(a) Bearing plate in casting set-up.

(b) Bearing plate after curing.

Figure D.43: Surface waviness.

Initial reaming procedure

In order to investigate the surface profile, a sample piece has been manufactured as shown in figure D.44a. This was done using a manufacturing procedure, and design parameters similar to those used in the final demonstrator. However, the holes were only reamed with the tapered machine pin reamer[16]. In order to be able to inspect the surface with a white light interferometer, the sample piece was then cut into pieces using a band saw. The result is shown in figure D.44b.

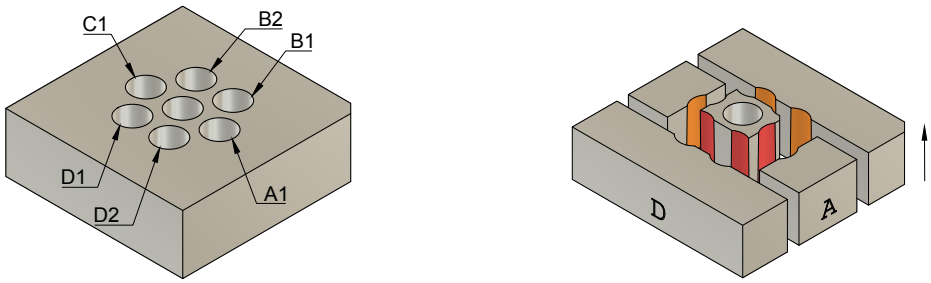

(a) Sample piece after initial machining steps.

(b) Sample piece after test preparation.

Figure D.44: Surface profile inspection sample.

Measurement results

The surface of each hole of the sample piece shown in figure D.44b was scanned. Both on the inside (indicated with red) and on the outside (indicated in orange). A selection of the results is shown in figure D.45. Additional results are shown in appendix G.5.1. The green line represents the surface of the cast pin that originates from that specific hole.

From both figures D.45a and D.45b, it seems that the surface profile is radially symmetric. As shown in figure D.45a, the waviness is extremely high. With a peak to peak distance of almost $100\,\mu$m. For figure D.45b, the waviness is not as high, however it can be seen that the profile of the pin does not coincide very well with the profile of the mould. Since the waviness will create a poorly defined outlet film geometry it needs to be reduced as much as possible.

[16]Dormer Pramet machine pin reamer (1:50) - B9538.0

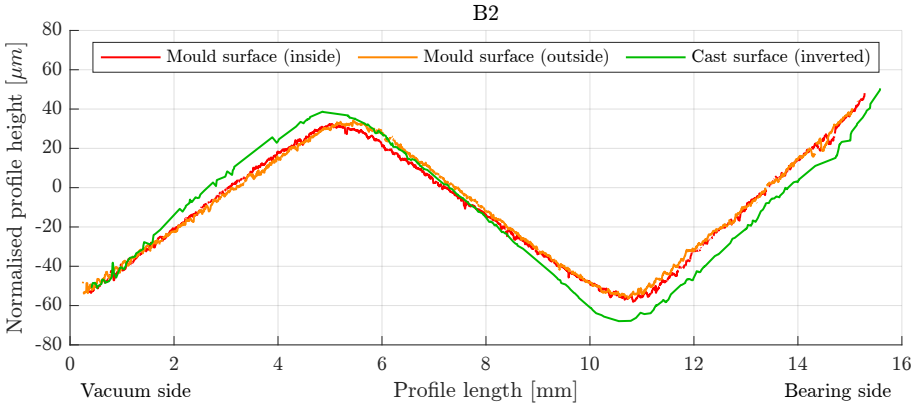

(a) Surface profile of feature B2.

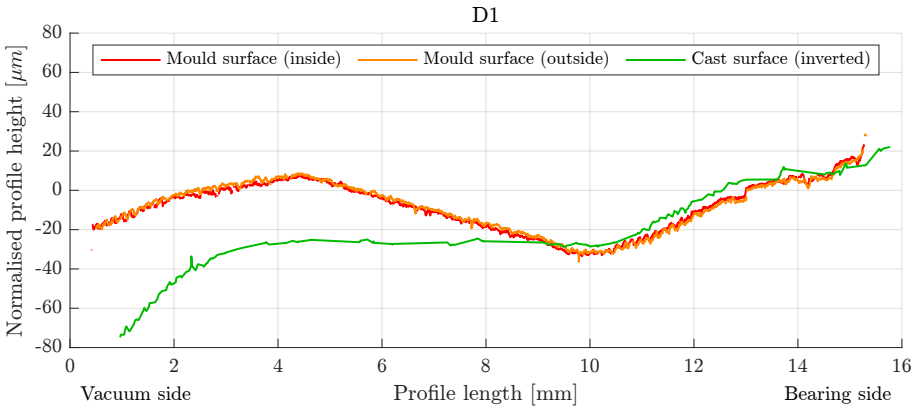

(b) Surface profile of feature D1.

Figure D.45: Surface inspection.

Sample preparation

Two test pieces were manufactured, as shown in figure D.46a. Each block had a thickness of 20 mm, and each hole was reamed to a nominal size of ⌀10 mm. The exact diameter is not critical. First, the holes were drilled using a regular ⌀9.7 mm spiral drill bit. The holes were then reamed on the lathe machine using a machine pin reamer as shown in figure D.47a. The first sample piece was only reamed using this spiral flute reamer. For the second sample piece, a secondary reaming operation was performed by hand using a hand pin reamer as shown in figure D.47b.

The workpiece was clamped in a bench vice. The clamping force is kept to a minimum, in order to distort the workpiece as little as possible. The reamer was cleaned using a paper towel, to remove any chips. Cutting oil was then applied to the surface and the holes were reamed using 10 half turns while applying light pressure. While still rotating the reamer, the reamer was retracted from the hole. Care was taken not to scratch the surface. This procedure was then repeated for each hole.

The hole diameter was measured before hand reaming. The results are shown in figure G.4. The hole diameter after hand reaming is show in figure G.5. The difference (i.e. amount of removed material) is shown in figure G.6. This operation will most likely not benefit the perpendicularity of the hole with respect to the surface.

The sample pieces were then cut in half on the band saw as shown in figure D.46c. The colors green and red indicate to the opposing sides of the hole.

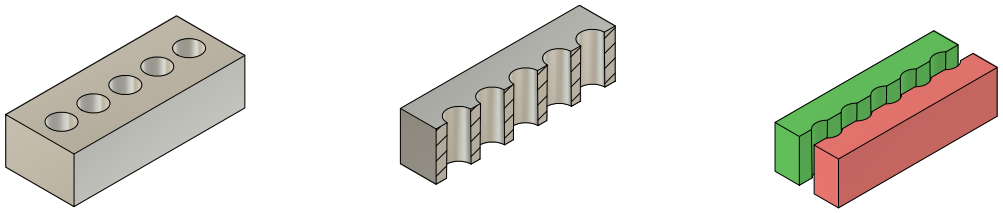

(a) Isometric view of reamer test piece.

(b) Isometric cross-section of reamer sample pieces.

(c) Isometric cross-section of reamer sample pieces.

Figure D.46: Reamer comparison sample piece.

(a) Tapered pin reamer[1] (1:50) with left-handed spiral flutes, to be used in a machine.

(b) Tapered pin reamer[2] (1:50) with straight flutes, to be used by hand.

Figure D.47: Pin reamer comparison.

The surface was then scanned again using a white light interferometer[17]. A selection of the results is shown below. The remaining data can be found in appendix G.5.2. Shown in figure D.48, is the surface profile of the sample where only the machine pin reamer was used. In contrast to what was seen in figure D.45, the surface profile is not radially symmetric. The surface profile after the hand reaming procedure is shown in figure D.49. From figure D.48 it can be seen that the surface waviness is significantly reduced, from about $\pm 20\,\mu$m to $\pm 6\,\mu$m. A close-up of the surface is shown in figure D.49a.

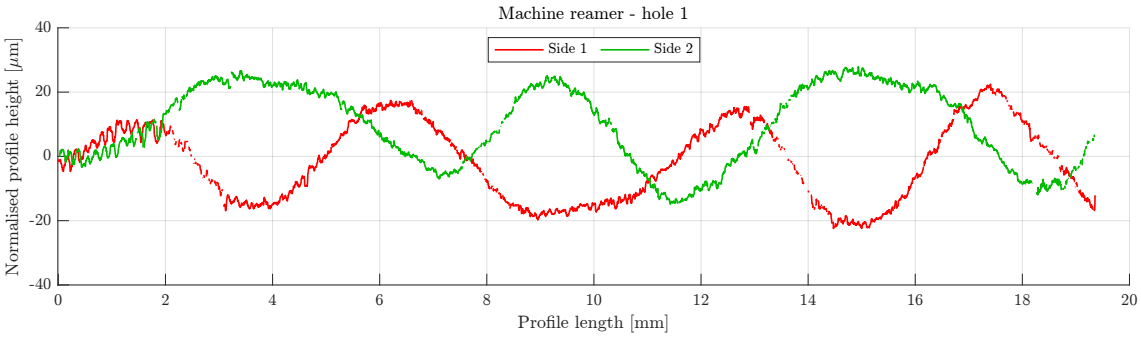

Figure D.48: Surface profile for machine reamed surface.

[1]Dormer Pramet machine pin reamer (1:50) - B9538.0
[2]Dormer Pramet hand pin reamer (1:50) - B9038.0
[17]Bruker Contour GT-K1

(a) Surface profile for machine reamed surface, using same axis limits as in figure D.48.

(b) Surface profile for hand reamed surface (close-up).

Figure D.49: Surface profile hole 1.

Influence on the outlet film thickness

The surface profile of hole 1 (side 1) is shown in figure D.50. This is essentially the inverse of the profile shown in figure D.49b. The black line indicates the waviness profile, where the high frequency component removed. The system during the casting process is shown in figure D.51. The x-direction normally corresponds to the z-direction. For now it is assumed that the cast pin will form the exact negative of the bearing plate.

After curing, the bearing plate is separated from the cast pin and shifted. This is shown in figure D.52. For simplicity, the profile is level and the conicity is implemented in the shift, as indicated by the dashed black lines. The outlet restriction is created between the bearing plate and the cast pin, as indicated in blue.

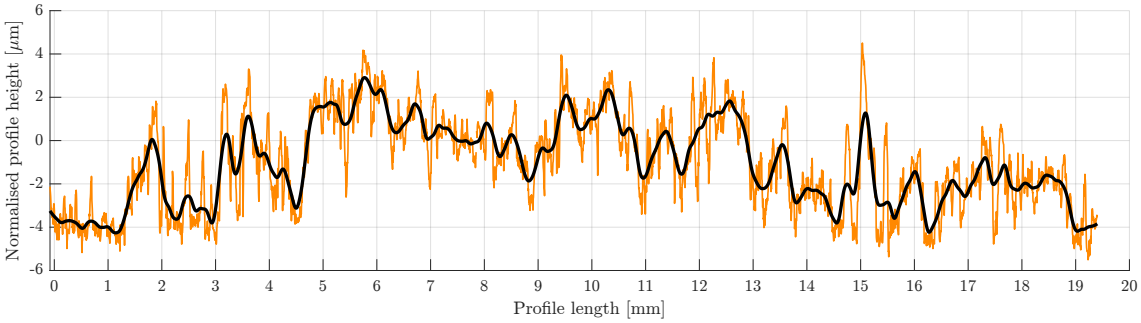

Figure D.50: Surface profile hole 1 - side 1 (inverted).

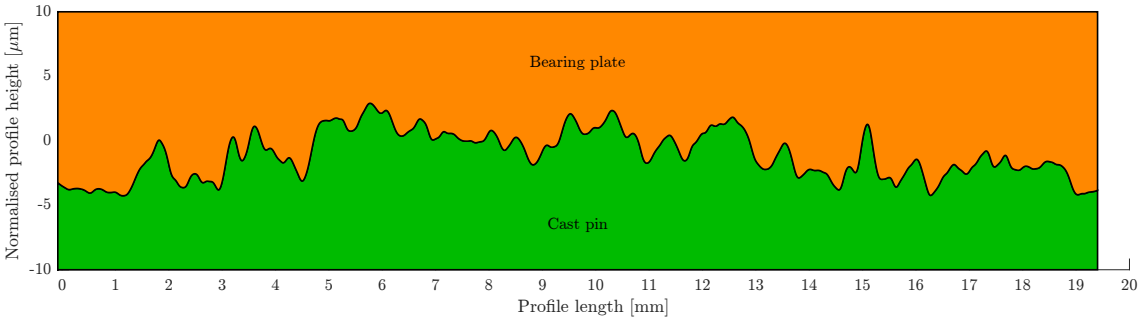

Figure D.51: System during casting set-up.

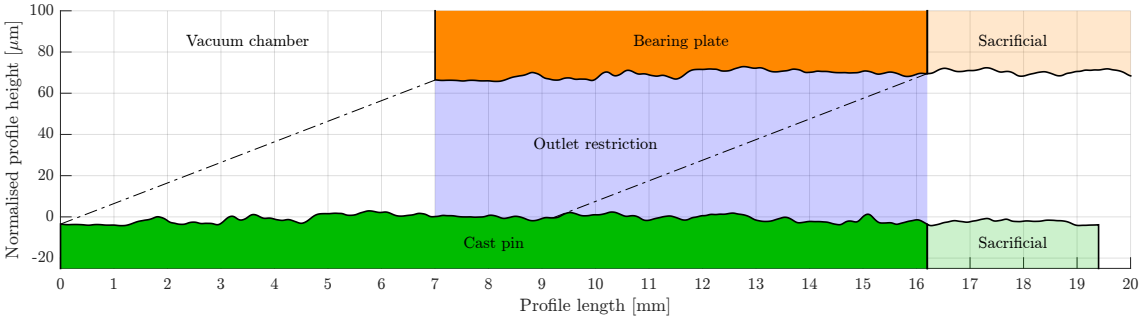

Figure D.52: System after curing and separating.

Given a conicity of $\delta = 1/100$ rad and distance between the plates of 7 mm, the nominal outlet film thickness should be 70 μm. However, due to the surface waviness, the outlet film thickness varies along the outlet length. This varying outlet film thickness is shown in figure D.53. The deviation from the theoretical film thickness due to the surface waviness is approximately $\pm 5\,\mu$m.

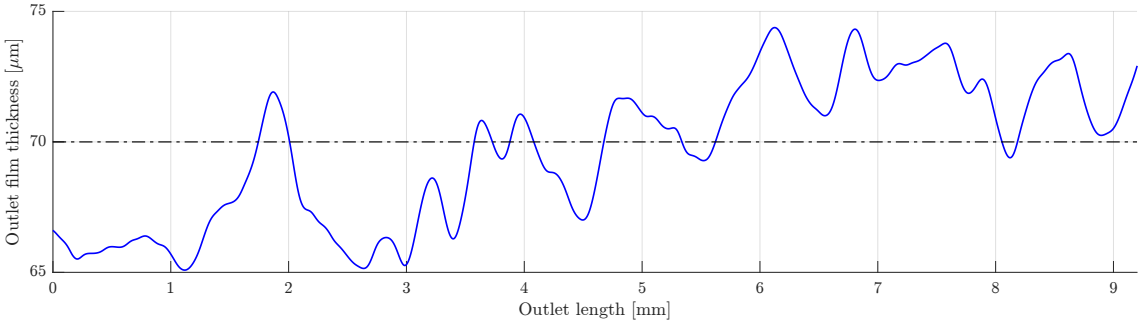

Figure D.53: Effective outlet film thickness along outlet length.

Burnishing

In order to further reduce the surface waviness and surface roughness, burnishing could be used. Burnishing is a process where one or multiple hardened balls or rollers are pressed against the surface of the workpiece [34]. This smears out the roughness peaks, essentially cold forming the material. Therefore, the hardness of the surface can be increased. Using a burnishing tool the surface roughness can be reduced even well below 0.1 μm Ra [35]. An example of an internal burnishing tool is shown in figure D.54. If the process parameters are chosen correctly, burnishing could both decrease the waviness and the surface roughness. An advantage of burnishing over grinding is that it is generally cheaper, since it can be performed on the same (CNC) lathe.

Figure D.54: Internal burnishing tool[18].

D.3.3 Mould release agent

Since epoxy is such an excellent adhesive, a mould release agent is required in order to ensure that the epoxy only adheres to the parts where adhesion is desired. In this research, vaseline[19] was used as a release agent. Vaseline is non-hazardous and relatively chemically inert, thus it will not react with the epoxy. In order to ensure that the vaseline remains on the surface, the temperature needs to remain below the dropping point. For temperatures above the dropping point, the grease will transform from a semi-solid to a liquid. For the vaseline used in this research, this is specified as 42-60°C.

A very thin layer was rubbed on all surfaces of the bearing plate. The thickness of this layer was not measured. One should not think of a visible layer of vaseline, but rather a very lightly greasy surface. An impression of the difference can be seen by the behaviour of a drop of water on an aluminium surface as is shown in figure D.55. After curing and separating the two parts, the vaseline is removed by cleaning the surface with isopropyl alcohol. Therefore, the radial outlet film thickness effectively increases.

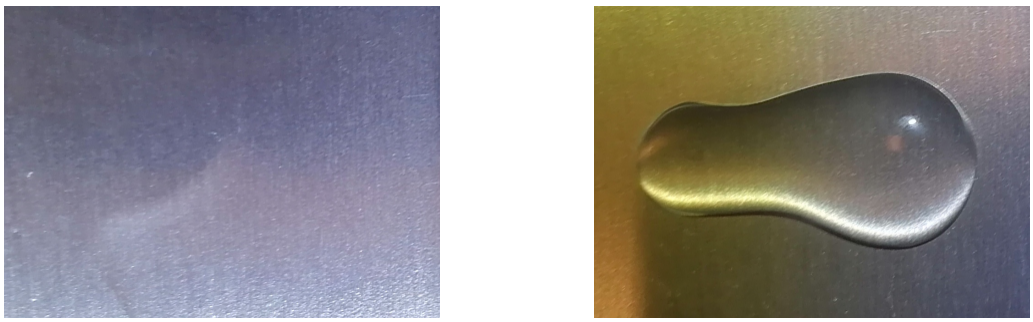

(a) Surface cleaned with isopropyl alcohol.

(b) Surface prepared with vaseline.

Figure D.55: Water drop on aluminium surface after different surface treatment.

Alternative mould release agents

Alternative liquid release agents do exists, such as PolyVinyl Alcohol, silicone spray or PTFE spray. In some cases it is specified that the release agent will leave *swirls* in the surface, which is undesirable.

As an alternative to a liquid mould release agent, a solid coating could be used, such as Parylene C. This is a is polymer with properties similar to PTFE. It is chemically inert, has a very low coefficient of friction and a very low surface energy of 19.6 mN/m [36]. This means its suitable to be used as a mould release agent. It can be applied to a substrate by means of chemical vapour deposition. The layer thickness can be controlled with sub micrometer accuracy. In Sethu et.al. [37], a 0.2 μm thick layer of Parylene C is applied to a silicon mould. A microfluidic device is then created by casting epoxy.

[18]Figure adapted from Cogsdill.
[19]Kroon White Vaseline 03010

Low surface energy plastics

It has also been investigated whether it would be possible to use a low surface energy type of plastic, such as High Density Polyethylene (HDPE) or PTFE (i.e. Teflon). Due to their very low surface energy, they are inherently very difficult to adhere to, so a mould release agent would not be required.

The properties of the materials are shown in table D.6. Where α indicates the coefficient of linear thermal expansion, E is the Young's modulus and ρ is the density. The critical surface tension is represented by γ_c, which can be seen as a measure of how well an adhesive can adhere to the surface (the higher γ, the better the adhesion).

Table D.6: Data adapted from [38, 39]

Material	α [ppm/K]	γ_c [mN/m]	E [GPa]	ρ [kg/m^3]
PTFE	112-125	18.5	0.5	2200
HDPE	125-180	31	0.9-1.55	940
Aluminium 7075	23.6	800	72	2800

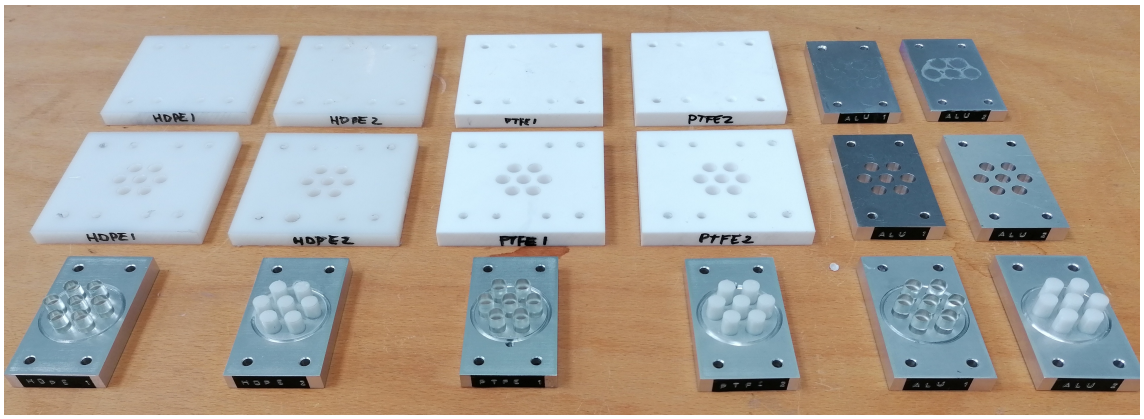

Figure D.56: Initial cast test samples.

D.4 Resin behaviour

Resin behaviour is a term that is used to describe several processes occurring during and after curing. The resin behaviour consists of different processes that all influence the final outlet film thickness. The general, qualitative effect for each process is shown in table D.7. The extent to which these processes affect the radial gap thickness will depend on many factors, such as: resin type, filler type, filler fraction, curing temperature, operating temperature, relative humidity and load.

To accurately describe the behaviour of these materials during and after the curing process is highly complicated and would be a study on its own. In this section, we will present an introduction to resin casting for mechanical engineers. The main influences will be discussed and analysed separately. In reality, the different processes are not independent. For more in-depth information, the reader is referred to [40, 41, 42].

Table D.7: Qualitative effect of different processes on the radial film thickness

Process	Radial film thickness
Differential thermal expansion	Increases
Cure shrinkage	Increases
Swelling	Decreases
Creep	Unknown

Thermosetting polymer

A thermosetting polymer is a polymer that is obtained by irreversible hardening (i.e. curing) of a viscous liquid prepolymer (i.e. resin) [40]. The curing is induced by heat. This heat can be applied externally, as with thermal curing resins. Alternatively, this heat is generated by the curing reaction itself. If a curing agent is added to the resin, the exothermic polymerization reaction generates sufficient heat. This is the case with two component resins. During the curing reaction, crosslinks will form between the monomer chains of the resin, essentially creating a three dimensional structure. The amount of reactive groups will determine the degree of crosslinking, and thus the properties of the polymer product.

D.4.1 Resin type

Not all material types can be used in all manufacturing method. A non-definitive list is presented in table D.8 [41]. In casting, a liquid material is poured into an open cavity (i.e. the mould), where it is allowed to solidify. Epoxy is used in this research because of the following reasons [40]:

- Excellent adhesion to surfaces and good bonding to fillers.
- Dimensional stability in the cured product.
- Relatively low cure shrinkage.
- Cure by an addition reaction prevents the emission of volatile condensation molecules.
- High Young's modulus compared to other resins suitable for casting.

Table D.8: Suitable materials for different manufacturing methods.

Manufacturing method	Suitable materials
Casting	Epoxies Polyurethanes Polyester Silicones
Transfer moulding	Epoxies Silicones Phenolics Polyimides
Injection moulding	Polyethelyne Polypropylene Polyphenylene suphide Polycarbonate Polyetherimide ABS

Epoxy is type of resin with low molecular weight pre-polymers that form a three dimensional (cross-linked) structure after curing. They all contain epoxide groups (also called epoxy groups) as shown in figure D.57. This is a strained, three membered ring structure. Strained, in this context refers to the phenomena that the molecule has an elevated internal energy due to internal stresses present in the molecule. This is much like the potential energy that is present in a compressed spring. Due to this elevated internal energy it is highly reactive, which makes it suitable to be used as a moulding compound. While all epoxy resins share this epoxide group, they can have highly varying physical and chemical properties, depending on the type of resin, hardener and filler.

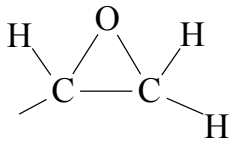

Figure D.57: Epoxide group

Curing is the process in which the epoxy resin, combined with a curing agent, forms a three dimensionally cross-linked polymer. During curing, the epoxide groups react. This explains why they are no longer present after curing. Only a few, unreacted groups will remain. The curing agent is also commonly called a hardener or co-reactant and can work in two different ways:

Heteropolymerisation is when the hardener causes the resin to undergo an addition reaction. In general, this is a type of reaction where two or more molecules are combined to form one larger molecule. In the case of epoxy, the hardener molecule serves as a bridge for cross-linking several resin molecules.

Homopolymerisation is when the hardener acts as a catalyst to stimulate self-polymerisation of the resin. Since the polymerisation reaction is exothermic, heat will be generated during the reaction, which in turn aids the reaction. It could also be that external energy is required to initiate the reaction, for example by heat or UV.

The liquid epoxy resin and hardener are relatively non-hazardous when handled correctly. Gloves, long sleeves and safety glasses should be worn when working with epoxy, since it may cause irritation when in direct contact with the eyes or skin. Cured epoxy is in general classified as a non-hazardous material, since it is are in general non-reactive and relatively chemically inert.

D.4.2 Filler materials

If a filler is introduced to a resin, the resulting material will be referred to as a composite. A composite consists of a matrix material (e.g. epoxy), that binds the filler material (e.g. powder or fibres). By adding filler materials, the properties of the composite can be tuned and or enhanced. Typical filler materials are silicon dioxide (SiO_2), aluminium oxide (Al_2O_3) and titanium dioxide (TiO_2). In general, they come in powder form, with a particle size between 10-100 μm. More recently, nano-filler materials are also used, with particle sizes of 10-40 nm [39]. Using nano-fillers can help to increase the volume fraction of filler material in the composite. The general trend of various properties as a function of the filler fraction is shown in table D.9.

Table D.9: General trend for an increasing filler fraction on various material properties.

Trend for increasing filler fraction	Property of composite
Increases	Young's modulus Thermal conductivity Weight Viscosity Abrasion resistance
Decreases	Coefficient of thermal expansion Cure shrinkage Hygroscopic swelling Creep Material cost

In this research, aluminium oxide[20] was used as a filler material. The aluminium oxide has a grain size of D50 <3.5 μm. This means that 50% of the particles is smaller than 3.5 μm. A maximum of 5% of the particles is larger than 20 μm. The volume fraction ϕ_f and mass fraction w_f of the filler material will be defined with respect to the total material as:

$$\phi_\mathrm{f} = \frac{V_\mathrm{f}}{V_\mathrm{m} + V_\mathrm{f}} \qquad\qquad w_\mathrm{f} = \frac{m_\mathrm{f}}{m_\mathrm{m} + m_\mathrm{f}} \tag{D.17a}$$

The density of the composite material is thus defined as:

$$\rho_\mathrm{c} = \phi_\mathrm{f}\,\rho_\mathrm{f} + (1 - \phi_\mathrm{f})\,\rho_\mathrm{m} \tag{D.18}$$

The volume fraction can then be written as a function of the mass fraction as:

$$\phi_\mathrm{f} = \frac{\rho_\mathrm{m}}{\rho_\mathrm{m} + \rho_\mathrm{f}\,(1/w_\mathrm{f} - 1)} \tag{D.19}$$

The mass fraction can be written as a function of the volume fraction as:

$$w_\mathrm{f} = \frac{\rho_\mathrm{f}}{\rho_\mathrm{f} + \rho_\mathrm{m}\,(1/\phi_\mathrm{f} - 1)} \tag{D.20}$$

D.4.3 Differential coefficient of thermal expansion

The increase of a linear dimension of a solid due to a rise in temperature is referred to as thermal expansion. The change in radius Δr of an object with nominal length r due to a change in temperature ΔT can be written as:

$$\Delta r = r\,\Delta\alpha\,\Delta T \tag{D.21}$$

Where the $\Delta\alpha$ represents the difference of Coefficient of Linear Thermal Expansion (CLTE) between the resin material and the mould material. If there is a difference between the CLTE of the resin and the CLTE of the mould material, this is referred to as a differential CLTE. If the temperature of the system in operation is different from the temperature during casting, the CLTE will influence the outlet film thickness.

[20] Aluminium oxide powder

The CLTE of the composite resin dependent on the type of resin, type of filler material and volume fraction of filler material. It can be defined as:

$$\alpha_c = \phi_f \, \alpha_f + (1 - \phi_f) \, \alpha_m \tag{D.22}$$

Where ϕ_f represent the volume of filler material, α_m represents the CLTE of the matrix material (epoxy) and α_f represents the CLTE of the filler material (aluminium oxide). The CLTEs of the filler is in general much lower than that of the matrix material differ. Therefore, the CLTE of the composite can be decreased by adding more filler material. This is shown graphically in figure D.58.

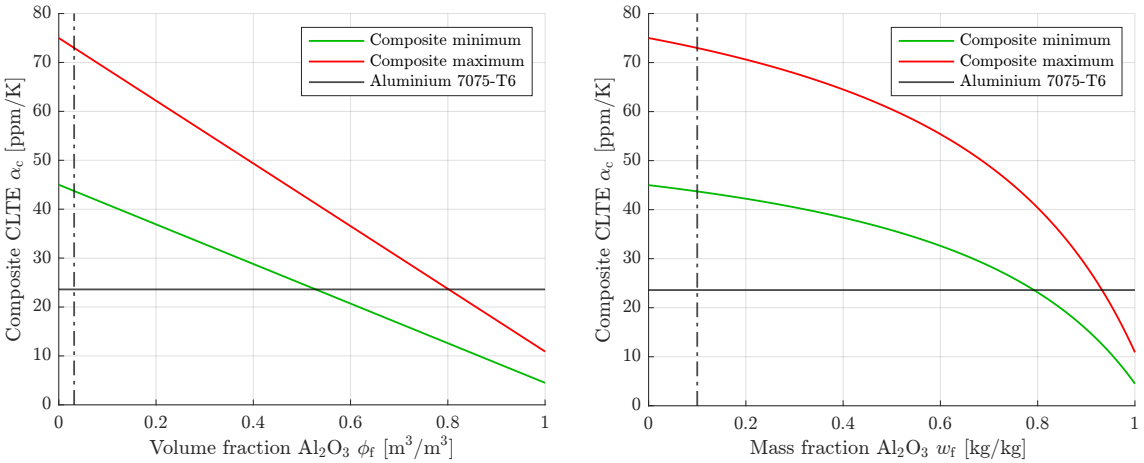

(a) As a function of the volume fraction Al_2O_3.

(b) As a function of the mass fraction Al_2O_3.

Figure D.58: Composite CLTE as a function of the filler fraction.

Change in radial outlet film thickness

By making use of the differential CLTE and the difference between the temperature during casting and in operation, the outlet film thickness can be controlled. Shown in figure D.59 is the change in size for a feature with a radius of 5 mm for a varying temperature range. The temperature difference refers to the difference between the temperature during curing and the temperature in operation. The relative change in size, i.e. increase in concentric outlet film thickness as a function of temperature is indicated by the orange line. The design point used in this research is indicated and refers to a temperature difference of $\Delta T = 18°C$ (curing temperature of 38°C and an operating temperature of 20°C). This would in theory result in an increase of the radial film thickness of 3.1 μm.

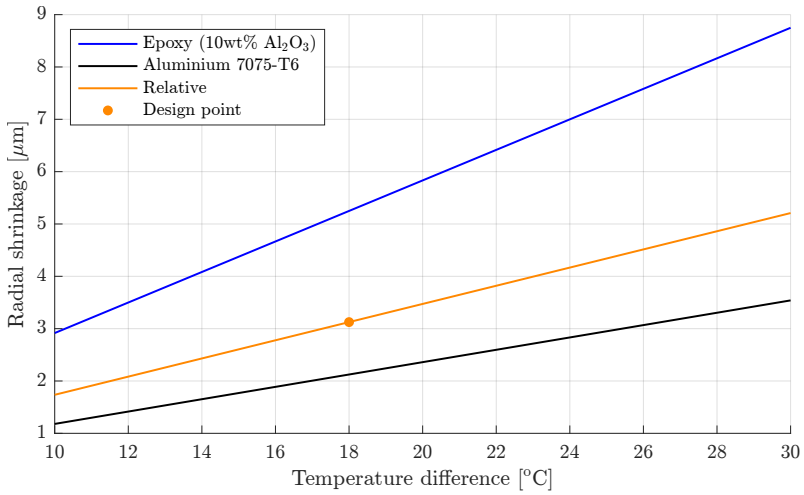

Figure D.59: Radial shrinkage for a given temperature difference.

Glass transition temperature

The glass transition temperature T_g specifies the temperature where the glass transition occurs. This is a reversible process, where a polymer transitions from a hard glassy state, to a rubbery state. This is related to the mobility of the molecular chains in the polymer network [42]. As with other types of materials, the properties of a polymer vary with temperature. However, the mechanical properties of the latter can show extreme changes in mechanical properties. The Young's modulus of an unfilled polymer may decrease by a factor 1000 above the glass transition temperature [42]. Therefore, a polymer should only be used in an environment where the temperature is below the glass transition temperature.

D.4.4 Cure shrinkage

In the curing process, the liquid resin transforms into a viscoelastic solid. During this curing process, cross-links are formed between the polymer chains, which reduces the volume of the resin. This induces stress in the cast part and thus leads to deformation. The curing cycle of epoxy can be visualised as shown figure D.60 [40]. The values for the process and resin used in this research are shown in table D.10.

- Stage 1-2: If the mould is pre-heated, the resin will expand due to an increase in temperature. This basically ordinary thermal expansion of a liquid. If the mould is not pre-heated, the temperature will rise due to the exothermic addition reaction.
- Stage 2-3: The volume of the resin decreases due to the addition reaction. The resin can be kept at or above the curing temperature by adding external heat (e.g. by using an oven or hot-plate). If this is not required, the curing temperature will be achieved by the curing reaction itself. The first part of the curing reaction happens when the majority of the resin is still liquid. This means that the resin can still flow if any cure induce stress occurs. Therefore, only the last part (40-60%) of the cure shrinkage will effectively induce stress and thus deformation.
- Stage 3-5: The volume decreases due to thermal contraction. The change in slope at point 4 can be explained by the fact that the CLTE is different below and above the glass transition temperature T_g. Next to the stress induced due to the polymerization (stage 2-3), there is also the stress that occurs due to thermal contraction.

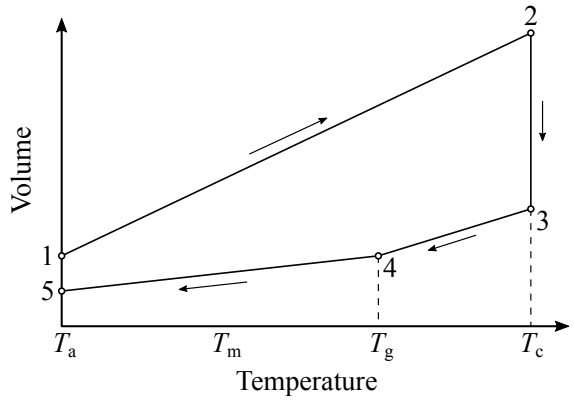

Figure D.60: Schematic volume throughout the curing cycle.

Table D.10: Temperature data used in this research.

Description	Symbol	Temperature [°C]
Ambient	T_a	20
Mould (pre-heat)	T_m	38
Glass transition	T_g	40-45
Curing	T_c	50

The change in radius Δr of an object with nominal radius r due to curing shrinkage can be written as:

$$\Delta r = r \frac{\gamma_c}{3} \tag{D.23}$$

Where γ_c is the linear cure induced shrinkage ratio of the composite material. The factor 1/3 is there due to the fact that it is assumed that only on third of the cure shrinkage actually leads to radial shrinkage of the cast feature. Because the filler material does not shrink during curing, this ratio is dependent on the filler ratio. The shrinkage ratio of the composite γ_c can thus be written as [40]:

$$\gamma_c = (1 - \phi_f)\, \gamma_m \tag{D.24}$$

The linear coefficient of cure induced shrinkage of the composite and the matrix material is indicated by γ_c and γ_m respectively. For epoxies, γ_m is typically 2-4%. The radial shrinkage as a function of the filler fraction is shown in figure D.61.

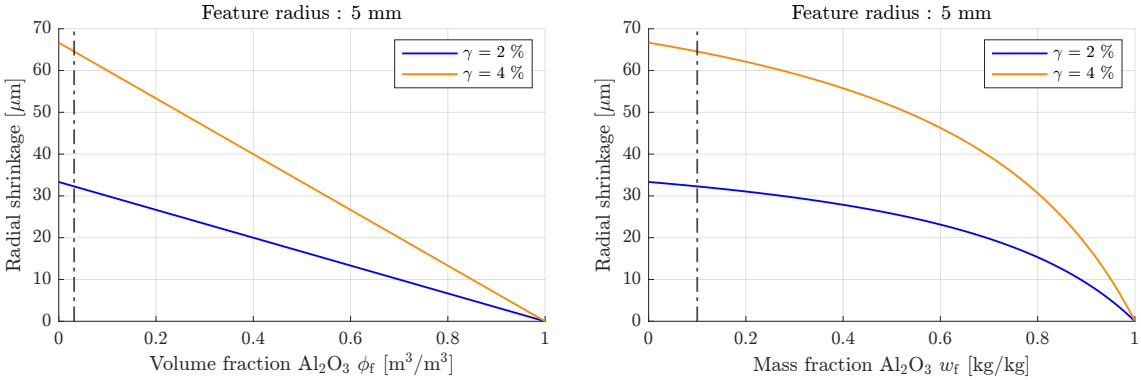

(a) As a function of the volume fraction filler material.

(b) As a function of the mass fraction filler material.

Figure D.61: Radial shrinkage as a function of the filler fraction.

Internal stresses around filler particles

Due to the cure shrinkage internal stresses will arise at the interface between matrix and filler material. These internal stresses can be reduced through the use of coupling agents. By creating covalent bonds between the filler and matrix material, the adhesion is increased. Alternatively, these internal stresses could be removed by "annealing" the composite. The material is heated to slightly above its glass transition temperature T_g.

D.4.5 Hygroscopic swelling

Hygroscopic swelling is the expansion of a material due to the absorption of moisture. This is a reversible process, which means that the material is able to absorb and desorb moisture [43]. The change in radius Δr of an object with nominal radius r due to a change in relative humidity can be written as:

$$\Delta r = r\, \beta_c\, \Delta \mathrm{RH} \tag{D.25}$$

Where β_c represents the Coefficient of linear Moisture Expansion (CME) of the composite material. This coefficient relates the change in relative humidity ΔRH to a change of the length L. Values for the CME will vary with resin type, filler ratio and temperature. Since the filler material will not absorb any moisture, the CME will decrease with increasing filler ratio, as shown in figure D.62. The CME for a composite can be written as:

$$\beta_c = (1 - \phi_f)\, \beta_m \tag{D.26}$$

In [40], values for the CME of *Moulding Compound C* have been reported of 0.33%/(%RH) for $T = 40$°C. Since moulding compound has a high filler fraction in general, this can be seen as a best case value. The radial expansion as a function of the relative humidity are shown in figure D.63. In reality, the rate of swelling will also be dependent on the amount of moisture that is already

absorbed. For typical ambient conditions, the relative humidity varies between 30 and 50%, as indicated by the dashed lines.

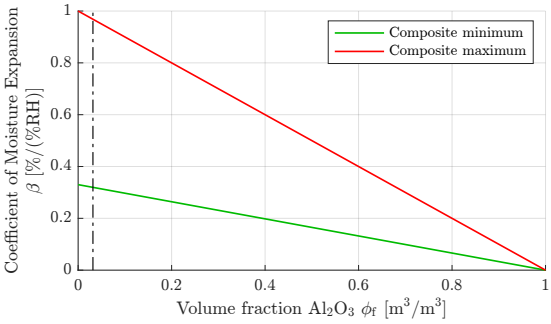

(a) As a function of the volume fraction filler material.

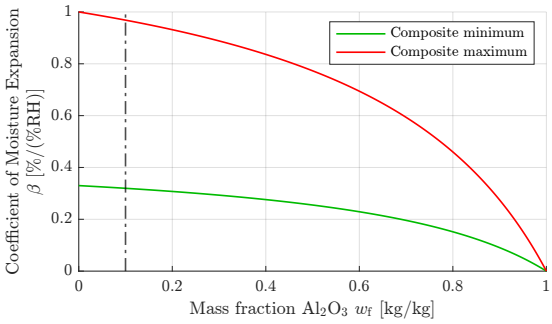

(b) As a function of the mass fraction filler material.

Figure D.62: Coefficient of linear Moisture Expansion as a function of the filler fraction.

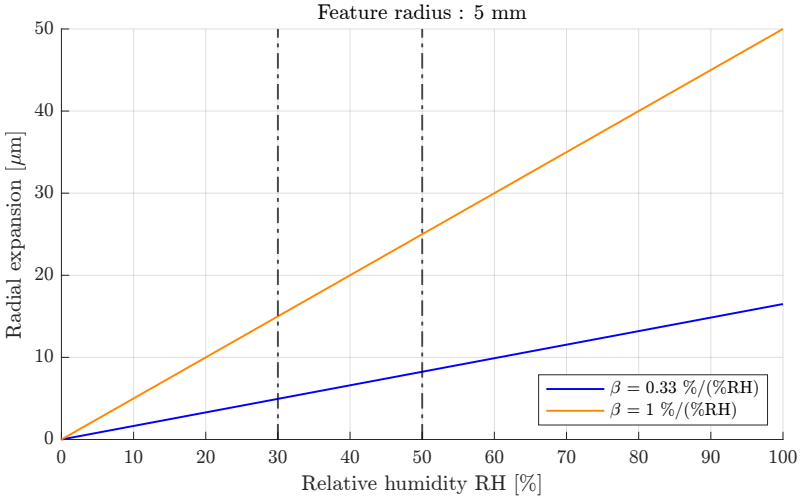

Figure D.63: Radial expansion as a function of the relative humidity.

Initial moisture content

It is unknown what the initial moisture content of the cast resin is. Some moisture will be introduced by adding the aluminium oxide powder. Due to the high relative surface area, moisture will adsorb to the power. In Abdul et. al. [44] the alumina powder is dried in an oven to get rid of the moisture. In this research, the powder has not been dried. If the worst case scenario is assumed, there will be no moisture present in the polymer after casting. The expected swelling then becomes $20 \pm 5\,\mu$m, depending on the relative humidity.

D.4.6 Polymer creep

In contrast to hygroscopic swelling, creep is irreversible [45]. The effects of creep will become increasingly noticeable with higher loads and temperatures. For the intended application in the contactless handling system, the temperature is expected to remain below the glass transition temperature T_g. Due to manufacturing errors, the radial outlet film thickness could be radially uneven in the concentric state. This would generate a net force on the pin in the concentric (i.e. neutral) state. If the system would remain in this neutral state for a long time, creep could occur. Theoretically, this could mean that the pin would effectively re-align itself. No first order estimate for the influence of creep is presented.

D.4.7 Combined influence

An overview of the influence of the three main processes are shown in table D.11. Note that this is a very general, "order of magnitude" type of estimation. The values for the relevant parameters are based on typical values found in the literature. No data could be supplied by the manufacturer, since the epoxy used in this research is general purpose casting resin. For more technical epoxies[21], the technical data-sheet is much more extensive.

Table D.11: First order estimation of the influence on radial outlet film thickness.

	Expression	Relevant parameters			Expected effect
Mechanism	for Δr	Symbol	Value	Unit	on $h_{o,c}$ [μm]
Thermal expansion	$r\,\Delta\alpha\,\Delta T$	$\Delta\alpha$	58	ppm/K	+3
		ΔT	18	K	
Hygroscopic swelling	$r\,\beta_c\,\Delta$RH	β_c	1	%/(%RH)	-20 ± 5
		ΔRH	10	%	
Cure shrinkage	$r\,(\gamma_c/3)$	γ_c	3	%	+50

The stroke of the system was tested using an experimental set-up, as is described in the next section. This will provide some information regarding the combined influence of both the manufacturing errors and the resin behaviour. However, by performing this experiment, no specific claims can be made regarding each individual effect. In order to avoid extensive testing of the resin properties, it is recommended to try and find a commercially available product for which extensive data can be found. This information could be supplied by the manufacturer, or this could be found in the literature.

D.4.8 Stroke test

In order to test the influence of the reaming procedure and the curing temperature on the stroke of the system, four more sample pieces were manufactured, as shown in figure D.64. All relevant design parameters are identical to those used in the final demonstrator. The sample numbers are shown in table D.12, and specify the reaming procedure and curing temperature that was used.

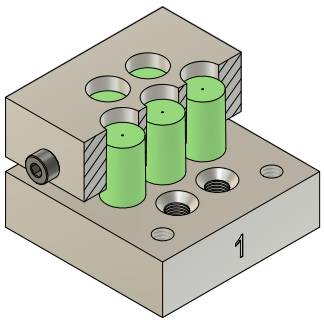

Figure D.64: Partial cross-section of test sample pieces.

Table D.12: Sample number indicated for varying reaming operation and curing temperature

	Machine reaming	Hand reaming
Elevated curing temperature	1	3
Ambient curing temperature	2	4

[21] Masterbond EP30QF, Loctite Stycast series

Mould separation

After curing, each sample piece was separated using a 3D printed adapter, as shown in figure D.65a. In order to ease the separation, the part is cooled in a refrigerator to about −10°C. Due to the difference in thermal expansion coefficient, the cast pins will shrink more than the mating holes. The bearing plate is then supported by socket head cap screws on the side, the plenum lid is free to move. The force is measured using a materials test machine[22]. The result is shown in figure D.65b.

The maximum force for the first sample is the highest (92.4 N). The curing temperature was 50°C. While the drip point for the used mould release agent was specified to be between 42-60°C. Most likely, the curing temperature was too high, which caused the mould release agent to partly disappear. Also, this sample has a high surface waviness compared to samples 3 and 4. For sample 3, the curing temperature was reduced to 38°C, to ensure that the mould release agent would remain on the surface. From the data, it can be concluded that a higher surface waviness and a higher curing temperature both increase the required release force.

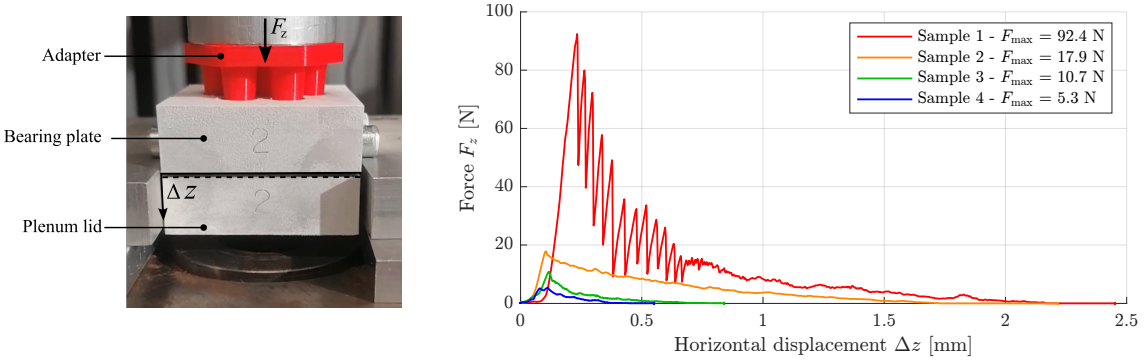

(a) Test set-up for mould separation.

(b) Force measured as a function of displacement.

Figure D.65: Mould separation force measurement.

Sample	Reamer flutes	Curing temperature [°C]	Peak force [N]
1	Spiral	50	92.4
2	Spiral	20	17.9
3	Straight	38	10.7
4	Straight	20	5.3

Test procedure

The stroke of the sample pieces was measured using a new measurement set-up. This is shown in figure D.66. The test sample (5) is held by two toe clamps (4). Two axial probes[23] (3) are held in an adapter block (2) on a breadboard (6). A force is applied by a weight (6 N) that is suspended by a pulley (1). The bearing plate is kept at a fixed distance from the pin plate by ball bearings. Three different sizes of ball bearings ($\varnothing 4, 5, 6$ mm) were used in three different tests. The measurement is repeated three times for each stroke direction and ball diameter combination. The stroke is measured using the probes with an analogue amplifier. The stroke direction is indicated in figure D.66b. Note that the sample has to be rotated in order to measure the stroke in y-direction.

[22] ZwickRoell Z005 materials testing machine
[23] Tesa GT61 probe, ± 5 mm, F = 0.9 N (32.30041)

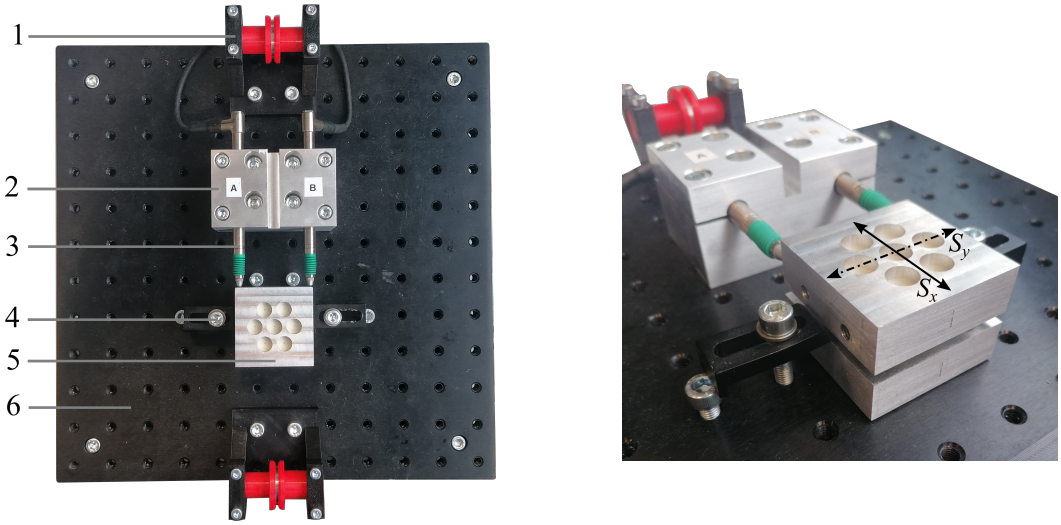

(a) Top view. (b) Close-up view.

Figure D.66: Stroke test set-up.

The averaged results are shown in table D.13, which is derived from the raw data as shown in appendix G.6. The data is graphically shown in figure D.67. The theoretical stroke is equal to:

$$S_\mathrm{t} = 2\,t_\mathrm{v}\,\delta = 2\,d_\mathrm{b}\,\delta \tag{D.27}$$

Where t_v is the height of the vacuum chamber, which is equal to the ball diameter d_b in this case. The conicity δ is equal to $1/100\,\mathrm{rad}$.

For samples 1 and 2, manufactured using only the machine pin reamer, the average stroke is only approximately one third of the theoretical stroke. The stroke of sample 2 in y-direction $\bar{S}_{2,y}$ even decreases for an increasing ball diameter. For samples 3 and 4, which were reamed also with a hand reamer, the stroke increases to approximately half of the theoretical stroke. Also, the difference between the stroke in x- and y-direction decreases. This indicates that the outlet film thickness is more radially symmetric. From this data, it cannot be concluded what the influence of the curing temperature is on the stroke. This is discussed in more detail in appendix D.4.3.

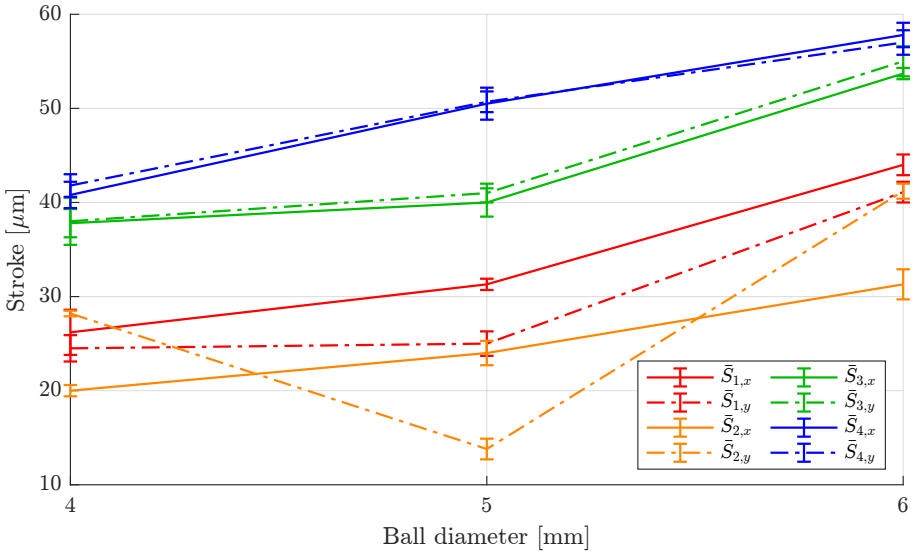

Figure D.67: Measured stoke for different ball diameters.

Table D.13: Stroke test results averaged.

Sample	Reamer flutes	Curing temperature [°C]	Relative stroke x [1]	Relative stroke y [1]
1	Spiral	50	0.34	0.30
2	Spiral	20	0.25	0.28
3	Straight	38	0.44	0.45
4	Straight	20	0.50	0.50

Full scale test

The stroke of the full scale demonstrator has also been tested, though not as rigorously as for the test samples. After the bearing plate had been separated from the plenum lid, the stroke was measured using the set-up shown in figure D.66a. Using $\varnothing 4$ mm balls, there was virtually no stroke. It was then decided to increase the height of the vacuum chamber by adding the spacer plates. The total vacuum height was then increased to 7 mm, which should give a theoretical stroke of $2 \cdot 70\,\mu\text{m} = 140\,\mu\text{m}$. However, the measured stroke was $30\,\mu$m, which translates to a relative stroke of only 0.21.

After the spacer plates had been glued to the bearing plate and plenum lid, the stroke was again virtually 0. This procedure is described in appendix D.1.6. This could be due to the fact that glue seeped into the outlet film. Even though a lot of care was taken to ensure that this could not happen. No clear signs of this could be found upon inspection. Alternatively, the size of the pins could have increased due to swelling.

D.4.9 Tensile test

The Young's modulus of the resin used in this research was analysed according to ASTM638, which defines the standard test method for tensile properties of plastics [46]. The dimensions of the test samples are shown in figure D.68. In order to investigate the influence of the addition of Al_2O_3 on the Young's modulus, a total 10 samples were tested. The samples 1-5 are 100wt% epoxy, and samples 6-10 are 90 wt% epoxy mixed with 10wt% aluminium oxide. According to ASTM638, the force should be increased until the samples fail. However, the maximum force that could be applied with the tensile test bench was 1000 N. Though, this has no influence on the results for the Young's modulus. The distance between the grips is defined as 115 mm.

The stress strain curve is shown in figure D.69. The Young's modulus is found by approximating the gradient at zero strain. The results can be found in tables D.14 and D.15. The Young's modulus of the composite should increase with an increasing filler fraction [39]. This is due to the fact that the filler particles prevent the polymer chains from sliding past each other. In accordance with the theory, an increase in Young's modulus of approximately 13% is achieved.

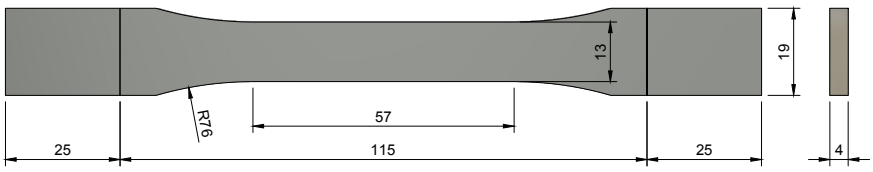

Figure D.68: Dimensions of the test sample (ASTM638-Type 1).

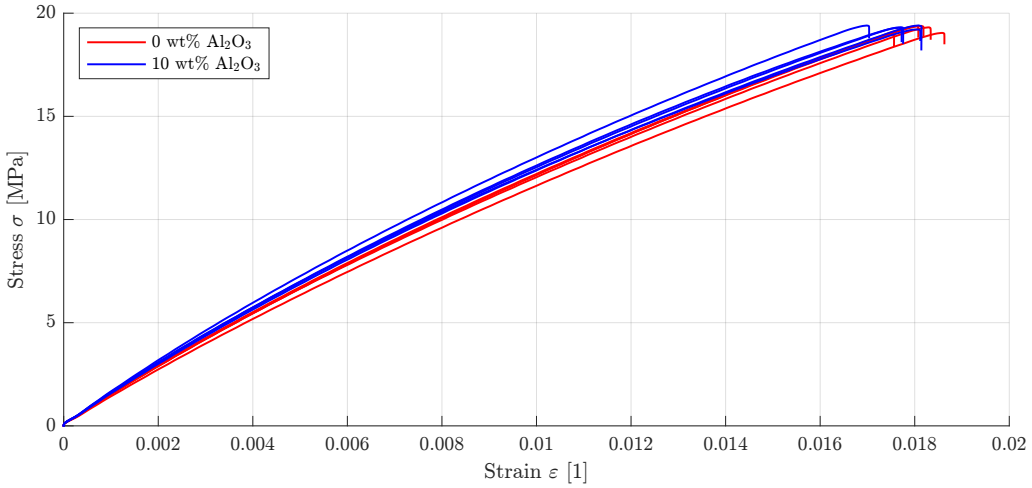

Figure D.69: Stress strain curve for the tensile test according to ASTM638.

Table D.14: 100 wt% epoxy

Sample number	Young's modulus [GPa]
1	1.49
2	1.46
3	1.53
4	1.48
5	1.39
$\mu \pm \sigma$	1.47 ± 0.05

Table D.15: 90wt% epoxy, 10wt% Al_2O_3

Sample number	Young's modulus [GPa]
6	1.64
7	1.68
8	1.65
9	1.67
10	1.65
$\mu \pm \sigma$	1.66 ± 0.02

Additional data

The density of aluminium oxide is taken as $3950\,\mathrm{kg/m^3}$. The density of the epoxy is taken as $1165\,\mathrm{kg/m^3}$. The filled resin with 10wt% aluminium oxide thus gives a density of $1444\,\mathrm{kg/m^3}$.

No data could be provided by the supplier regarding the Poisson's ratio. In the literature, values between 0.34 and 0.46 were found [47, 48]. The Poisson's ratio will depend on the type of resin and the amount of filler material. In this model, the Poisson's ratio is set to 0.39.

D.5 Pocket restriction

A pocket restriction is created by creating a well defined height difference between the top surface of the pin and the top surface of the bearing plate. Typical values for this height difference are 10-20 μm. For the manufacturing procedure of the outlet restriction, not all manufacturing imperfections influence the radial outlet film thickness. Recalling the expression for the concentric outlet film thickness:

$$h_{\mathrm{o,c}} = t_{\mathrm{v}}\,\delta = \frac{t_{\mathrm{v}}}{100} \tag{D.28}$$

It can be seen that any deviation from the specified hole diameter or hole location will not influence the outlet film thickness. Any deviation from the specified vacuum height will be decreased by a factor 100 due to the conicity δ. Such redundancy is not present for the pocket height, which is defined as:

$$h_{\mathrm{p}} = t_{\mathrm{v}} - t_{\mathrm{s}} \tag{D.29}$$

Even the smallest deviation in the height of the vacuum chamber t_{v} or the thickness of the sacrificial material t_{s} will directly influence the outlet film thickness. This means that the pocket height is very sensitive for manufacturing errors as well as the bearing method.

Some redundancy is embedded in the manufacturing procedure, by performing the last manufacturing step on the assembled system. This is explained in more detail at the end of appendix D.1. For now, let us assume that we can take the sacrificial layer thickness out of the equation. This means that the pocket height can then be written as:

$$h_{\mathrm{p}} \propto t_{\mathrm{v}} \tag{D.30}$$

Requirements

From equation (D.30) we can state that in order to meet the requirements of a $< 1\,\mu$m tolerance on the pocket height, the tolerance on the distance between the plates is also $< 1\,\mu$m. The displacement due to the vacuum pressure should be as low as possible. In other words, the vertical stiffness should be as high as possible.

The linear Degree Of Freedom (DOF) in z-direction needs to be constrained. Next to that, the rotational DOFs about the x- and y axis also need to be constrained. Since the bearing plate needs to be able to translate in the x- and y-direction and rotate about the z-axis with respect to the pins, these DOFs should be unconstrained. The practical implication of constraining the required DOFs will be referred to as the bearing method.

The range of motion that is required for the unconstrained DOFs is relatively low: approximately $\pm 50\,\mu$m in x- and y-direction and < 1 mrad about the z-axis. This makes it suitable for a compliant bearing method.

Next to the displacement in z-direction (i.e. rigid body motion) of the bearing plate due to the vacuum pressure, there is also the deformation of the bearing plate due to the vacuum pressure. This deformation also needs to be minimised in order ensure a consistent pocket height in all unit cells. Possible bearing methods are shown in table D.16.

Table D.16: Potential bearing methods.

	Compliant joint	Rigid body joint
Exactly constrained	Wire flexures (3)	Ball bearings (3)
Over-constrained	Wire flexures (>3)	Ball bearings (>3)
	Continuous flexible layer	

D.5.1 Compliant bearing methods

Distributed flexible layer

One option is to create a compliant layer that separates the bearing plate from the plenum lid. In between the pins, there still needs to be space in order to allow for the vacuum flow. Two potential design options are shown in figure D.70. In figure D.70a, there is only a flexible layer on

the outside, whereas in figure D.70b, there are also flexible pillars in between each pin. This could be manufactured by casting silicone in a laser-cut or 3D printed mould for example.

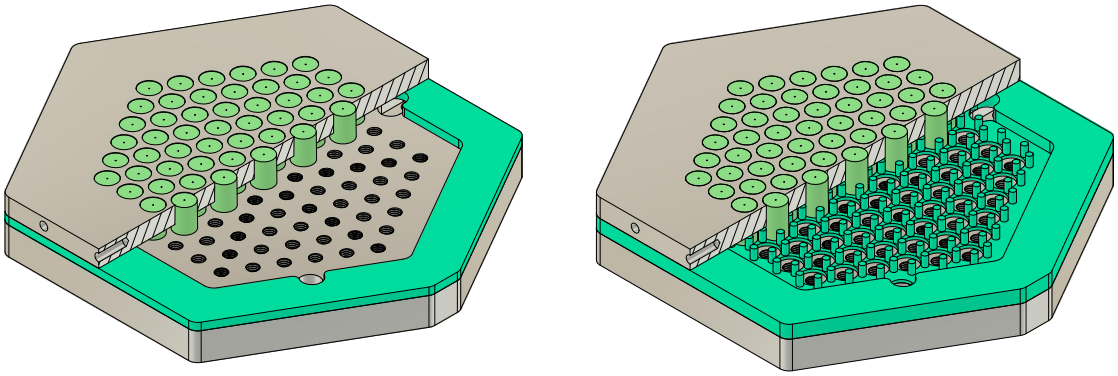

(a) Flexible layer on the side.

(b) Flexible layer on the side with pillars in between the pins.

Figure D.70: Flexible layer support options.

The deformation of such a layers and the deformation of the bearing plate is modelled in COMSOL, using the *Solid Mechanics* physics module. The stiffness of the flexible layer can be approximated by:

$$k = \frac{E\,A}{L} \tag{D.31}$$

Where the length L would be equal to the height of the vacuum chamber t_v, A is the cross-sectional area in the x, y-plane and E is the Young's modulus of the silicone. Using an empirical correlation found by Gent [49], the Young's modulus can be estimated as a function of the Shore A durometer hardness. For the silicone used in this research, the Shore A hardness is 30, which gives a Young's modulus of 1.14 MPa. For a vacuum height of 5 mm, the stiffness in z-direction for each pillar is approximately 1.5 N/m

Shown in figure D.71 are the results of the analysis with a flexible layer and with a flexible layer with pillars. The difference is negligible, since the stiffness of the pillars is negligible compared to the stiffness of the outer layer. The flexible seal is modelled as a *Spring Foundation* where the spring constant is calculated using equation (D.31). The pressure difference across the plate is assumed to be 0.3 bar.

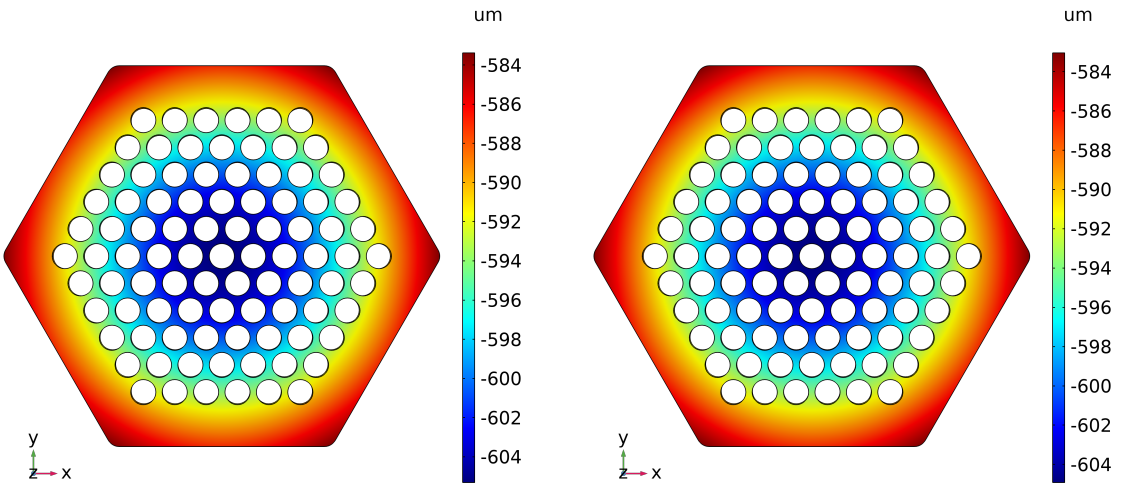

(a) Only on the outside.

(b) On the outside and pillars between each pin.

Figure D.71: Displacement in z-direction using support layer .

A vacuum seal was manufactured from silicone, in order to seal space between the bearing plate and the plenum lid, as shown in figure D.70a. The silicone seal needs to be compressed in order to seal the vacuum chamber. The stiffness of the silicone layer in compression is much higher than in shear mode.

The overall displacement considers the displacement of the bearing plate in z-direction, without considering the deformation. This displacement, is very high ($\sim 580\,\mu$m), due to the relatively low stiffness of the silicone seal. This makes the pocket height highly dependent on the vacuum pressure, which is undesired.

The relative deformation considers the actual deformation of the plate, rather than the rigid body displacement. Since the bearing plate is not supported in the middle, there exists a difference of about $12\,\mu$m between the z-displacement in the centre and the z-displacement on the sides. This is very significant when compared to a pocket height of $19\,\mu$m.

From this analysis, it can be concluded that the bearing method using a flexible layer results in a pocket height that is highly dependent on the vacuum pressure. Next to that, it can be concluded that local support (i.e. between the pins) is required in order to minimise the deformation of the bearing plate. Shown in figure D.72b is the displacement in z-direction, using the same parameters. This time however, local support in the form of ball bearings has been added in between all the pins. This is modelled as a *Spring Foundation*, applied to all 216 points. The ball bearings can be seen as a non-linear spring, i.e. the stiffness increases with increasing deformation.

It becomes clear that both the overall displacement as well as the relative deformation are significantly decreased when compared to the first case (D.71a). Though, in order to constrain 3 DOFs of a rigid body in 3D, 3 constraints are required. One of those constraints should constrain the rigid body in z-direction. That means that the system is now essentially 215 times over-constrained in z-direction. The rotational DOFs about the x- and y- axis are effectively constrained by the vacuum pre-load.

Wire flexures

Three wire flexures in combination with three set-screws were used in [6]. Using the set screws, the pocket height could be adapted. An impression of the situation where the bearing plate is only supported in three locations is shown in figure D.72a. It becomes clear that support using only three wire flexures is insufficient. To decrease the deformation, the stiffness of the bearing plate could be increased by making it thicker, or making it from a material with a higher Young's modulus. Alternatively, the system could be made smaller: i.e. less holes.

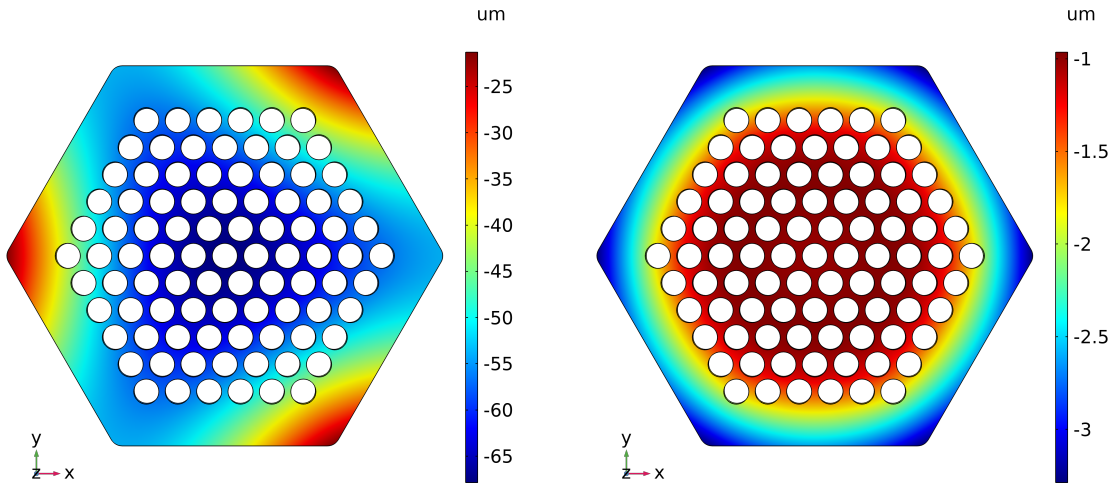

(a) Exactly constrained (3 constraints).

(b) Over-constrained.

Figure D.72: Displacement in z-direction using discrete supports.

D.5.2 Pocket height measurement

The displacement of the bearing plate due to the vacuum pressure was measured. This was done before the spacer plates were glued in place, as explained in appendix D.1.6. The measurements were performed by turning the vacuum pressure ($p_v = 0.6\,\text{bar}$) on and off using a ball valve. The displacement was measured using a Tesa probe[24]. The probe is held by a magnetic base on a cast iron surface plate. The probe tip was placed on the bearing plate, just next to the hole on the corner. This measurement was performed at all six corners. The results as shown in table D.17 are averaged over three measurements for each corner.

Table D.17: Displacement in z-direction due to vacuum pressure.

Corner	Δz [μm]
1	58
2	75
3	50
4	43
5	35
6	40

The displacement is very significant compared to the pocket height. Also, the displacement is different at each corner. This indicated the disc spring-like behaviour of the spacer plates. After this measurement it was decided to glue the spacer plates in place. Curing was performed under vacuum pressure, such that the spacer plates would be fixed in their flat state as much as possible.

The displacement in z-direction after the spacer plates had been glued to the bearing plate and plenum lid were still 10-20 μm for a vacuum pressure of 0.6 bar. This is a significant reduction from the values shown in table D.17, however, this is still far from the displacement expected using only the Hertzian theory ($\sim 1\,\mu$m).

Using this data, a much better comparison can be made between the measured performance of the demonstrator and the theoretical performance predicted by the numerical model. Ideally, this would be done using a white light interferometer. However, this measurement method can only be used if the system can be measured under vacuum. The system does not need to be measured under vacuum pressure if it has been verified in advance that the displacement and deformation due to the vacuum pressure are negligible with respect to the pocket height.

D.5.3 Plenum lid deformation

The plenum lid is used to seal the plenum chamber. The plenum chamber is the central chamber from which all capillary inlet restrictions are fed. The pressure within the plenum chamber is equal to the supply pressure p_s, as shown in figure D.73a.

The distributed load acting on the bearing plate is the difference between the ambient pressure and the vacuum pressure $p_a - p_v$. This force is then supported by the plenum lid, on which the vacuum pressure is also acting. The effective pressure is therefore equal to the ambient pressure p_a, as shown in figure D.73b. The values used for the material properties and pressures are shown in tables D.18 and D.19. Fixed constraints are applied to the holes where the bolts would be located (on the outer ring).

Table D.18: Properties for aluminium 7075-T6.

Property	Symbol	Value	Unit
Young's modulus	E	71.8	GPa
Density	ρ	2800	kg/m^3
Poisson's ratio	ν	0.33	1

Table D.19: Pressure values.

Description	Symbol	Pressure [bar]
Supply	p_s	2.5
Ambient	p_a	1
Vacuum	p_v	0.7

[24] Tesa GT61 probe, ± 5 mm, F = 0.9 N (32.30041)

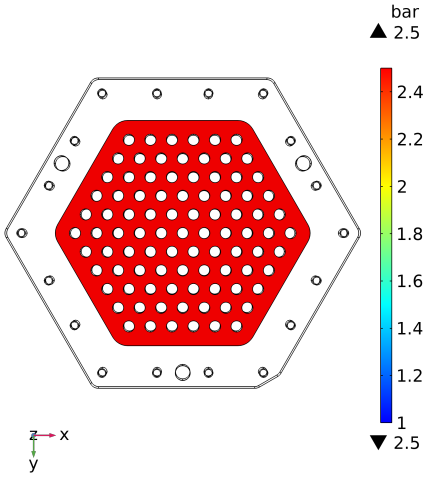

(a) Bottom face, supply pressure p_s.

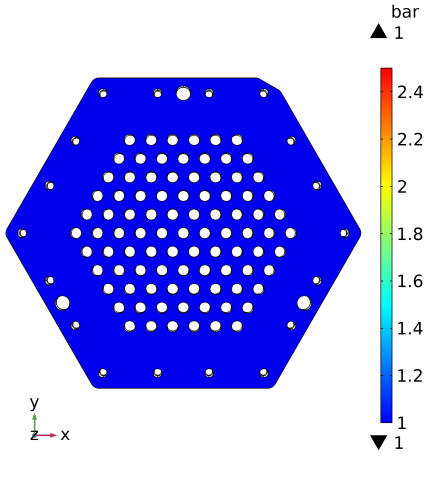

(b) Top face, ambient pressure p_a.

Figure D.73: Load applied to the plenum lid.

The resulting deformation is shown in figure D.74. It can be seen that the resulting deformation is very significant compared to the nominal pocket height of 20 μm. The maximum deformation as a function of the plenum lid thickness is shown in figure D.75a. This analysis is made using the pressures shown in table D.19,

Since at this point in the process, the plenum lid was already machined to a thickness of 15 mm, the pressure needs to be reduced in order to not exceed the maximum allowable deformation. The deformation for a varying supply pressure, given a plenum lid thickness of 15 mm is shown in figure D.75b. For a supply pressure of < 1.2 bar, the maximum deformation will remain below 1 μm.

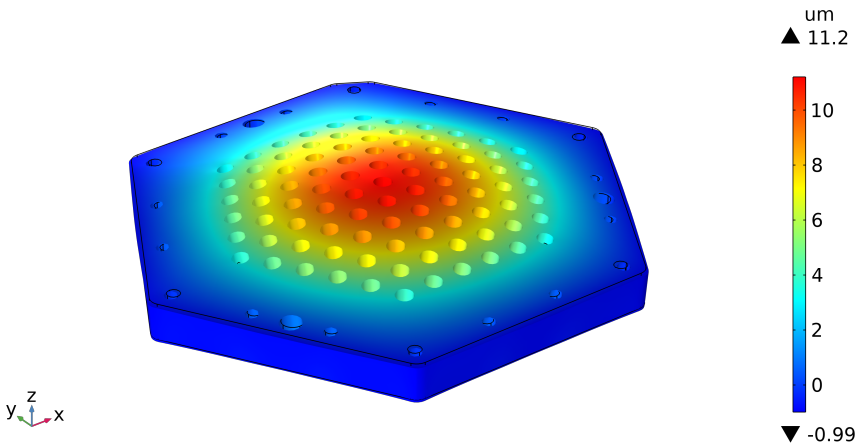

Figure D.74: Deformation of the plenum lid in z-direction.

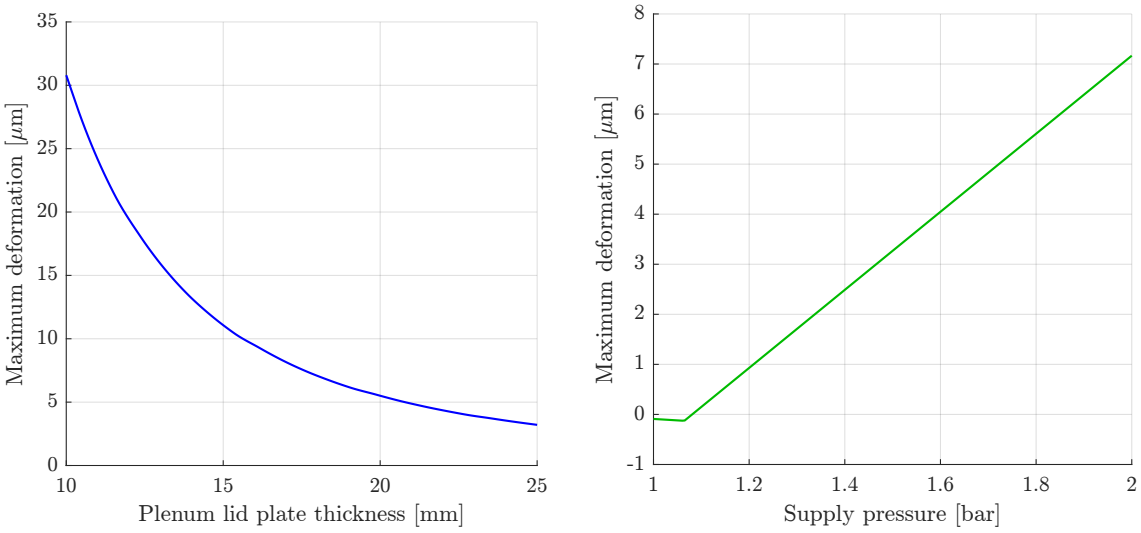

(a) For a varying plenum lid thickness.

(b) For a varying supply pressure p_s.

Figure D.75: Maximum deformation of the plenum lid.

D.5.4 Hertzian theory

Ball bearings are used to maintain a fixed distance between the plenum lid and the bearing plate, while allowing for relative lateral movement. Due to the pressure difference between the top and bottom side of the bearing plate, a distributed load is generated, as shown in figure D.76. This will lead to a deformation both in the ball bearings and the bearing plate/plenum lid. This behaviour is well described by Hertzian contact theory [50]. Using analytical expressions, an estimation can be made about the deformation, stresses and bearing stiffness. A calculator was made using MATLAB. A derivation of the formulas can be found in appendix F.5.

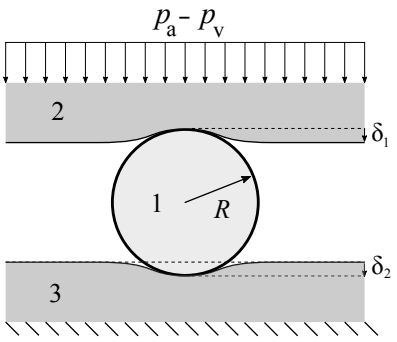

Figure D.76: Schematic Hertzian deformation.

Parameters

The final surface area of the bearing plate is 0.0208 m^2. This means that for a pressure difference of 0.3 bar, a net force of approximately 600 N needs to be supported. If the force would be equally distributed over all 216 balls, the force would be 2.78 N per ball. Shown in figure D.77 is the result of the calculation for a ⌀4 mm hardened steel ball between two aluminium surfaces. The values used for the relevant parameters are shown in table D.20. Figure D.78 shows the result for a 4 mm ball between two steel surfaces. Interestingly, since the steel has a higher Young's modulus, the contact radius is smaller than for the aluminium. Therefore, the stress is higher. In this case, the aluminium (7075-T6) has higher yield strength than the steel (S235), as shown in both figures on the right

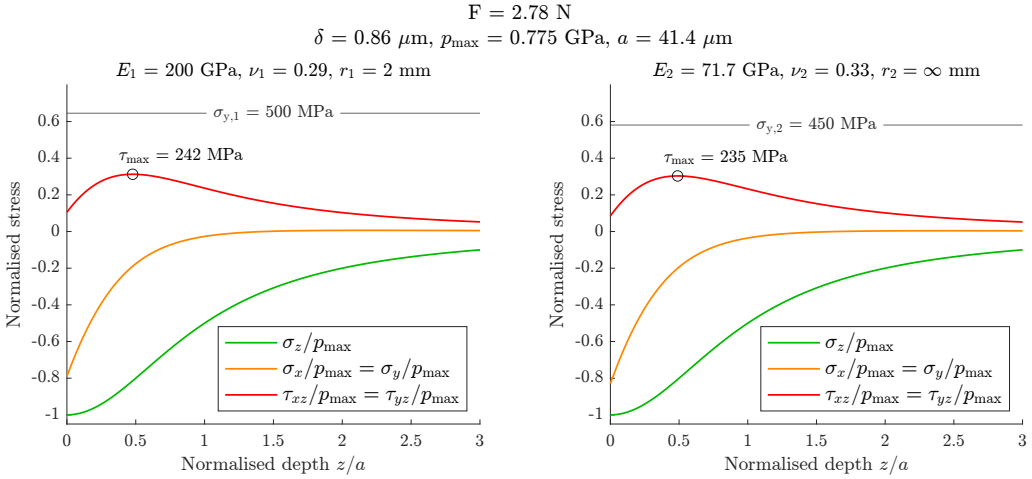

Figure D.77: Hertzian deformation for a steel ball (440C) on an aluminium surface (7075-T6).

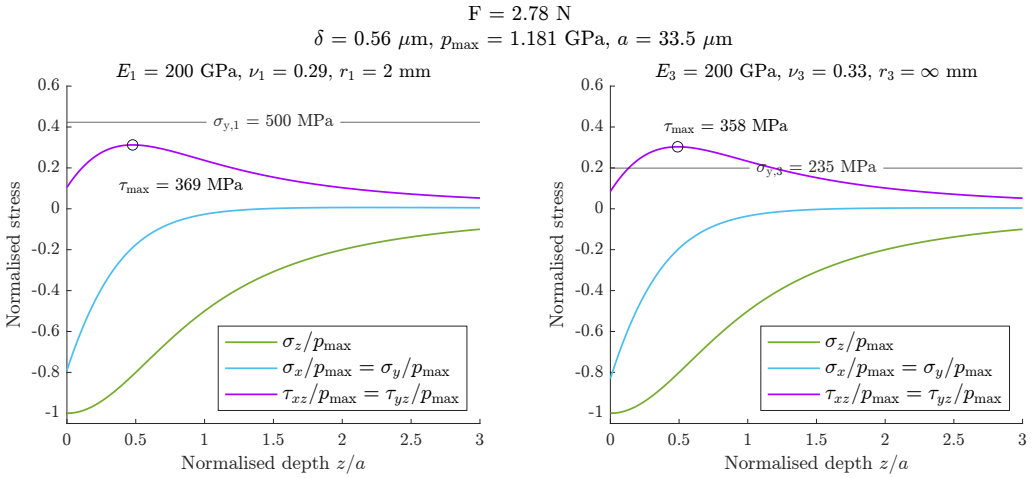

Figure D.78: Hertzian deformation for a steel ball (440C) on a steel surface (S235).

Table D.20: Material parameters used for Hertzian analysis.

Number	Material	Young's modulus E [GPa]	Yield strength σ_y [MPa]
1	Ball (Steel 440C)	210	500
2	Plate (Aluminium 7075-T6)	71	450
3	Plate (Steel S235)	210	235

The unit cells are hexagonal, and are arranged in a centred hexagonal grid. This means that there is one unit cell in the centre, surrounded by concentric rings of unit cells, as shown in figure G.3. The number of unit cells n_u is always equal to some factor of 6, plus 1 (7, 19, 37, 61, 91, 127, ...) and can thus be written as:

$$n_u = 1 + 6\left(\frac{n_r(n_r+1)}{2}\right) \tag{D.32}$$

Where n_r is the number of rings around the central unit cells. Thus, 5 rings gives 91 $(1 + 6 \cdot 15)$ unit cells. Assuming that a ball is placed in each midpoint between three unit cells, and on the outside, the number of balls n_b is given as

$$n_b = 6\,(n_r+1)^2 \tag{D.33}$$

Ball diameter measurement

The ball diameters were measured using a digital micrometer[25], as shown in figure D.79. The micrometer is held in a micrometer stand in order to influence the temperature as little as possible. The spindle faces are made of tungsten carbide, which has a Young's modulus of about 670 GPa. The clamping force of the ratchet mechanism is specified as 5-10 N. The Young's modulus of the balls is assumed to be 210 GPa. For a ball diameter of 4 mm, the Hertzian deformation will be between 0.61 μm and 0.97 μm per contact face. The balls were binned in 1 μm increments according to the value shown on the digital display. The results are shown in figure D.80. The green bars indicate the ball diameters used in the final demonstrator.

Figure D.79: Ball binning measurement set-up.

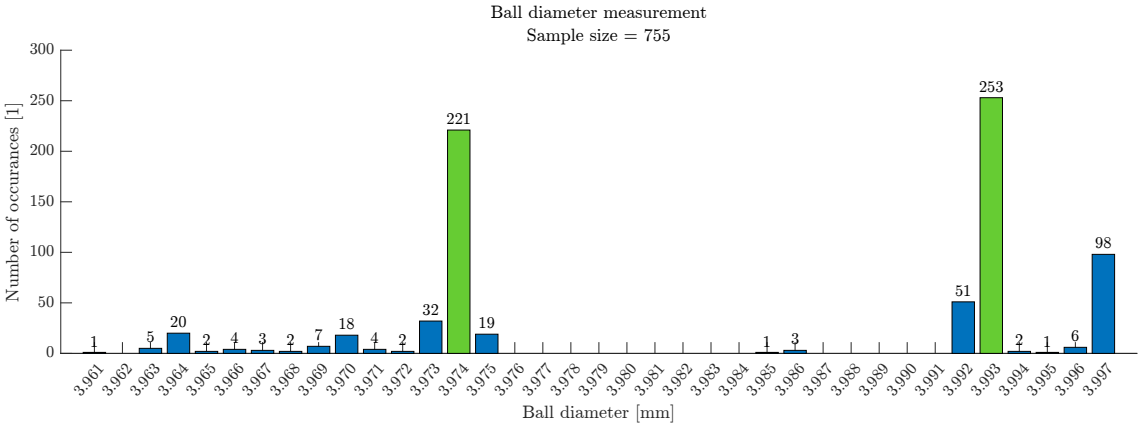

Figure D.80: Ball diameter count.

It was expected that the ball diameter would be more consistent and accurate. The difference in ball diameters might be explained by the fact that the balls came from a drawer in the workshop were several different batches were mixed up.

[25]Mitutoyo digital micrometer (0-25 mm) 293-240-30

D.6 Conclusions

- A demonstrator has been manufactured using epoxy with 10wt% aluminium oxide powder as a filler material. Dispensing needles were used to create capillary inlet restrictions. Vaseline was used as a mould release agent, in order to ensure that the epoxy would not adhere to the bearing plate.
- Using dispensing needles as inlet restrictions is a reliable and accurate way of manufacturing inlet restrictions.
    - The restriction value found using the linear approximation is only valid for very low pressure differences across the restriction. A more accurate model (e.g. Fanno flow) should be used to describe the inlet conductivity.
- The geometry of the outlet film thickness is determined by the mould geometry and the behaviour of the resin. Regarding the geometry of the mould, i.e. the bearing plate it can be concluded that:
    - Waviness of the surface of the conical holes will decrease the stroke of the system. Also, the outlet film thickness will vary along the outlet length, making the behaviour of the system less well defined.
    - Reaming with a machine reamer created a highly profiled surface ($\pm 50\,\mu$m peak to peak.) Post reaming with a hand reamer reduced this value to approximately $\pm 5\,\mu$m peak to peak.
    - The manual reaming procedure will most likely decrease the perpendicularity of the holes with respect to the surface, though this has not been verified.
    - Any deviation from perpendicularity will decrease the stroke of the system and also create radial variations in the outlet restriction. Thereby degrading the performance of the system and introducing parasitic torque.
    - A suitable measurement method the deviation from perpendicularity has not been found yet. This is important in order to correctly match the design parameter of the demonstrator to those used in the numerical model.
    - Since the mould release agent (vaseline) is removed after casting, this effectively increases the radial outlet film thickness. The layer thickness of the mould release agent has not been measured.
- The processes that together make up the behaviour of the resin are identified as thermal expansion, cure shrinkage, hygroscopic swelling and creep. Cure shrinkage and hygroscopic swelling cause the largest variations in the geometry of the pin.
    - The differential thermal expansion coefficient between the mould and the resin should increase the radial film thickness. As a first order approximation this should be around increase the outlet film thickness by approximately $3\,\mu$m.
    - The cure induced shrinkage occurs due to the cross-linking of monomer chains during the polymerization reaction. It is estimated that this will increase the outlet film thickness by $50\,\mu$m.
    - Hygroscopic swelling is a reversible process that causes the cast material to expand due to absorption of moisture. It is estimated that this will decrease the outlet film thickness by $20 \pm 5\,\mu$m, depending on the relative humidity.
    - Creep becomes more noticeable at high temperatures and loads. Since the system will be operating below the glass transition temperature, creep is not considered.
- The influence of these processes in general decreases with an increasing filler fraction. This is due to the fact that filler materials typically do not experience any curing shrinkage nor hygroscopic swelling. Also, their CTE is generally lower than that of polymers.
- Creating a consistent and well defined pocket height proved to be difficult. The vertical stiffness needs to be maximised, while the horizontal stiffness needs to be minimised.

- Local support is required in order to minimise deformation of the bearing plate in z-direction.
- Spacer plates were added to increase the height of the vacuum chamber from 4 to 7 mm. These spacer plates act as two disk springs and thus decrease the vertical stiffness of the system.
- The vertical stiffness is still significantly lower than the Hertzian stiffness, even after glueing the spacer plates to the plenum lid and bearing plate.
- The pressure within the plenum chamber may cause significant deformation of the plenum lid. This will affect the pocket height, and thus needs to be considered in the design process.

Appendix E

Conclusions & recommendations

E.1 Conclusions

E.1.1 General

- In order to reduce the thickness of solar cells below $180\,\mu$m, challenges in many fields of engineering need to be overcome. One of these challenges is the improvement of handling methods. Contactless handling using air bearing technology is a potential candidate.
- In contactless handling, a substrate is levitated on a thin film ($\sim 10\,\mu$m) of air, called the bearing film. The shear stress within the bearing film generates a lateral force that acts on the substrate. In order to control the position of the substrate, the direction of the flow within the bearing film needs to be controlled over time.
- A shear force can be generated through three different concepts:
  1. By directly controlling the supply and vacuum pressure, given a fixed geometry.
  2. By controlling the pocket restriction (i.e controlling the film geometry).
  3. By controlling the outlet restriction (i.e. controlling the outlet geometry).
- For each of the concepts mentioned above, a working demonstrator has been developed in previous researches. Manufacturing these systems is difficult, due to very tight dimensional tolerances ($< 1\,\mu$m).
- The performance ratio for a 2D geometry has been evaluated for each of the concepts. The theoretical performance of the variable outlet restriction concept is identical to that of the variable pocket restriction concept. Both have a higher theoretical performance than the bilateral pressure control concept.

E.1.2 Regarding the conceptual manufacturing method

- The variable outlet restriction consists essentially of only two mating parts. This has been recognised as a potential benefit in terms of manufacturing. If these two mating parts can be created using a method that guarantees the dimensional accuracy, the manufacturing process is greatly simplified.
- The working of the variable outlet restriction concept is dependent on a well defined film thickness in the outlet restriction and pocket restriction.
  - The pocket restriction is created by the thin film between the surface of the pin and the substrate. There needs to be a well defined height difference between the bearing surface and the pin surface ($10 - 20\,\mu$m).
  - The outlet film thickness is created by the radial clearance between a pin in a hole ($\sim 50\,\mu$m). By varying the eccentricity, the film thickness in the outlet will vary radially. This changes the pressure distribution within the outlet film and thereby also the pressure distribution within the bearing film.

- A manufacturing method was developed that is relatively insensitive for manufacturing errors compared to the manufacturing method used by Verbruggen [6].
    - A two-part mould is created by the bearing plate and the plenum lid, that have approximately matching hole patterns. The bearing plate has tapered holes that are used to create tapered pins by means of resin casting. After separating the two-part mould, the pins are fixed to the plenum lid. The geometry of each pin is the exact negative of the tapered hole.
    - By enforcing a distance between the two plates after curing, a radial outlet film is created. Due to the small taper angle, the outlet film thickness is relatively insensitive for variations in the distance enforced between the plates after separating. Alternatively it can be stated that the outlet film thickness can be controlled with high accuracy.
    - The position of each pin with respect to each hole is only determined by the position of the tapered hole. Any discrepancy between the hole locations in both plates will not influence the outlet film thickness.
    - The diameter of the tapered hole does not influence the outlet film thickness.

E.1.3 Regarding the model

- The system has been analysed using a numerical model. The Reynolds equation is defined on the full domain. This means that any inlet or outlet effects are not considered.
- The influence of the pin deformation due to the pressure gradient in the outlet film is negligible compared to the influence of manufacturing tolerances and deformations of the substrate.
- There exists a non-unique set of design parameters for which the fly-height remains relatively constant for a varying eccentricity. In this case, the mass flow also remains relatively constant.
- There exists an optimal ratio for the pocket radius over the inscribed radius of the hexagonal unit cell $\varrho_{\text{opt}} \approx 0.93$.
- There exists an optimal ratio for the fly-height over the pocket height $\beta_{\text{opt}} \approx 3.33$. However, the system might become unstable for large pocket volumes in combination with high eccentricity ratios.

E.1.4 Regarding the demonstrator

- A demonstrator has been developed using a novel manufacturing technique. Unfortunately, the demonstrator did not work as intended. This is due to manufacturing errors in the mould geometry and insufficient dimensional accuracy in the resin.
- The manufacturing process has been designed in such a that manufacturing errors present in the mould geometry should not influence the final outlet film thickness. However, waviness of the surface and a deviation from perpendicularity of the hole will cause variations of the outlet film thickness.
    - The waviness in the surface introduces a variation in the film thickness of approximately $\pm 5\,\mu$m from the nominal value of $70\,\mu$m.
    - Any deviation from perpendicularity will cause radial variations in the outlet film thickness and increases the parasitic force.
    - Since the mould release agent is removed after casting, this will effectively increase the outlet film thickness. The layer thickness has not been measured.
- The behaviour of the resin consists of multiple processes that influence the dimensions of the pin during and after curing. Thermal expansion, cure shrinkage and hygroscopic swelling are the main mechanisms that cause variations in the dimension of the pin. Thereby the outlet film thickness will deviate from the required value.
- A first order estimation of the influence of each process is made. From that it can be concluded that cure shrinkage and swelling have the most significant impact.

- The stroke of various sample pieces has been measured using an experimental set-up. This provides insight of the combined influence of both manufacturing errors in the mould geometry as well as the resin behaviour. Since the stroke of a system of 7 pins is measured, no conclusions can be drawn regarding the individual radial outlet film thickness.
- Using a white light interferometer, the profile of the holes and the cast pins can be inspected. However, this measurement method only provides insight in the height profile, not the effective film thickness.

E.2 Recommendations

E.2.1 Regarding the model

- The behaviour of the numerical model needs to be verified through physical experiments. Currently, the discrepancy between the geometry of the numerical model and the demonstrator is too large. Therefore, the demonstrator cannot be used to verify the findings of the numerical model.
- The inlet conductivity should be modelled more accurately, for example by implementing a Fanno flow model or using empirical data.
- In order to gain insight in the influence of the manufacturing errors, multiple unit cells need to be modelled.
- The dynamic behaviour of the air film upon actuation should be modelled. Currently, only a perturbation of the fly-height is studied. It would be interesting to find out to which actuation frequency the force is proportional to the eccentricity.
- A second numerical model should be made, where the film geometry that has been realised in the demonstrator is implemented. This way, a comparison can be made between the ideal numerical model, the numerical model with manufacturing imperfections and results of physical experiments performed using the demonstrator.

E.2.2 Regarding the demonstrator

- The outlet film thickness should be measured. Currently, only the stroke of a system with multiple pins has been measured. Therefore, no claims can be made regarding the outlet film thickness. Ideally, this should be done using a non-destructive measurement method, such that the data can be implemented in the numerical model.
- Inspecting the system, e.g. measuring the surface profile or pocket height, should ideally be done under operating conditions. Due to the pressure difference, deformations of several μm are easily introduced. These deformations are significant compared to the nominal film dimensions and can therefore not be neglected.
- The reaming procedure using the hand reamer significantly reduces the surface waviness. However, the perpendicularity of the holes will most likely be decreased by this procedure. If possible, the surface waviness of the holes should be further reduced. This could for example be done using a burnishing tool. This will also improve the surface roughness.
- It was attempted to measure the perpendicularity of the holes using a digital microscope and automatic feature recognition. This was however unsuccessful. A solution needs to be found to accurately measure the orientation of the tapered holes. Ideally, this should be done automatically and for the full geometry. This would allow this data to be implemented in the numerical model.
- In order to verify the positioning accuracy, an active system with sensors and actuators should be developed. The manufacturing procedure allows for embedding of active components into the pins. For example:
    - By embedding strain gauges the pressure distribution in the outlet could be implicitly measured.

- Optic fibres could be embedded in the surface in order to measure the position of the wafer [51].
- By embedding actuators within in the pins, no actuators would be required on the side of the system, thereby increasing its effective area.
- Since the required stroke is relatively small ($< 50\,\mu$m) and the required force is relatively high ($\sim 0.6\,$N/pin) piezo-electro actuators could potentially be used.

- The pocket height needs to be better defined and the vertical deflection due to the pressure difference needs to be minimised. Also the deformation of the plenum lid needs to be considered when designing the system.
- The number of unit cells should be reduced. The complete manufacturing process will become easier and less sensitive when the demonstrator is comprised of less unit cells.
- In order to improve the dimensional stability, a resin with a higher filler fraction should be used. A commercial moulding compound could be used. Though, due to the increased viscosity casting may be more difficult.
- In order improve the dimensional stability, the volume of resin used should be reduced. This could be achieved by machining cylinders out of the same material as the plenum lid. This as shown schematically in figure E.1.

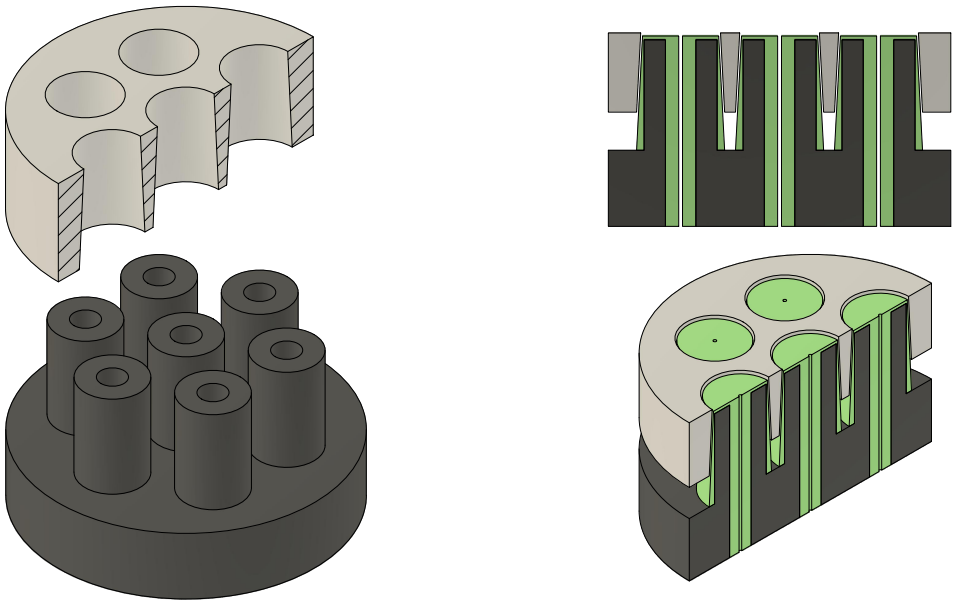

(a) Plenum lid with machined cylinders.

(b) Cross section.

Figure E.1: Potential improved manufacturing method.

- When the system is designed for a high closed loop bandwidth, additional design criteria become important. The mass should be minimised, while the stiffness of system should be maximised. The limiting factor of the bandwidth should be identified.

Appendix F

Derivations

F.1 Reynolds term identification

For we will only show the Reynolds equation in the x direction. However the equation for the y direction can be found by replacing x with y in all equations. The Reynolds equation is given as:

$$\underbrace{\frac{\partial}{\partial x}\left(\frac{\rho h^3}{12\eta}\frac{\partial p}{\partial x}\right)}_{\text{Poiseuille}} = \underbrace{\frac{\partial}{\partial x}\left(\frac{\rho h\left(u_a+u_b\right)}{2}\right)}_{\text{Couette}} + \underbrace{\frac{\partial}{\partial t}\left(\rho h\right)}_{\text{Dynamic}} \tag{F.1}$$

Where the term on the left hand side represents the Poiseuille flow (pressure driven), the first term on the right represents the Couette flow (motion driven) and the second term on the right hand side represents dynamic effects. The physical interpretation of these terms is explained in the sections below.

F.1.1 Poiseuille flow

The Poiseuille flow describes the flow due to a pressure gradient. There is no relative motion between the plates (i.e. $u_\mathrm{a} = u_\mathrm{b}$). Due to the no-slip condition, the velocity of the fluid is equal to the velocity of the body at the interface.

$$\frac{\partial}{\partial x}\left(\frac{\rho h^3}{12\eta}\frac{\partial p}{\partial x}\right) = 0 \tag{F.2}$$

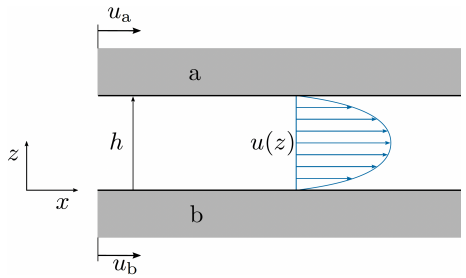

Figure F.1: Velocity profile in a pure Poiseuille flow.

F.1.2 Couette flow

The Couette flow describes a flow due to relative motion of two surfaces. In figure figure F.2, the situation is shown for the flow between two parallel planes where $u_\mathrm{a} > u_\mathrm{b}$. When taking the derivative with respect to x of the density ρ, the film thickness h and the velocity u, three separate terms can be identified.

$$\frac{\partial}{\partial x}\left(\frac{\rho h(u_a+u_b}{2}\right) = \underbrace{\frac{h\left(u_a+u_b\right)}{2}\frac{\partial \rho}{\partial x}}_{\text{Density wedge}} + \underbrace{\frac{\rho h}{2}\frac{\partial}{\partial x}\left(u_a+u_b\right)}_{\text{Stretch}} + \underbrace{\frac{\rho\left(u_a+u_b\right)}{2}\frac{\partial h}{\partial x}}_{\text{Physical wedge}} \tag{F.3}$$

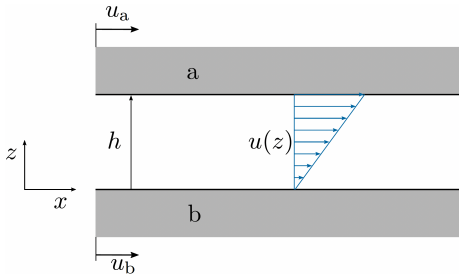

Figure F.2: Velocity profile in a pure Couette flow.

Density wedge

The density wedge describes the flow due to a density gradient $\partial\rho/\partial x$. Since it is not expected that large local temperature differences will occur during operation, the influence of this term is assumed to be negligible.

Stretch

The stretch term describes a flow that is induced due to the elongation the surfaces along the sliding direction. This could be envisioned as if one of the surfaces was an elastic band. The influence of this term is assumed to be negligible.

Physical wedge

The physical wedge term is an important mechanism for pressure generation in aerodynamic bearings. For a positive load capacity, the film thickness must decrease in the sliding direction.

In principle, the substrate should be approximately parallel to the bearing surface. Very small variations in height ($\partial h/\partial x$) might be due to waviness present in the substrate. The pressure distribution within the unit cells will also slightly deform the substrate. It is assumed that these variations in film thickness are very small, and that the velocity of the substrate will be low. Therefore, the influence of this term is deemed to be negligible.

F.1.3 Dynamic effects

The dynamic effects indicated in equation (F.1) can be written as:

$$\frac{\partial}{\partial t}(\rho h) = h\frac{\partial \rho}{\partial t} + \rho\frac{\partial h}{\partial t} \tag{F.4}$$

Where $\partial h/\partial t$ is essentially the velocity in z-direction w. The expression can thus be written as:

$$\frac{\partial}{\partial t}(\rho h) = \underbrace{h\frac{\partial \rho}{\partial t}}_{\text{Expansion}} + \underbrace{\rho(w_a - w_b)}_{\text{Squeeze}} \tag{F.5}$$

Expansion term

Due to a difference in temperature over time $\partial T/\partial t$, the volume of the lubricant will change. If heat is supplied to the lubricant, it will expand. If film thickness h remains the same, this means that part of the lubricant needs to be expelled from the space between the two bearing surfaces. If the bearing surfaces are stationary, the lubricant can only be expelled due to a pressure gradient.

Squeeze term

The squeeze term describes a flow due to a relative motion of the bodies, perpendicular to the bearing surface as:

$$\rho\frac{\partial h}{\partial t} = \rho(w_a - w_b) \tag{F.6}$$

F.2 Velocity profile derivation

From the Navier-Stokes equation we know that [9]:

$$\frac{\partial p}{\partial x} = \frac{\partial \tau_x}{\partial z} \tag{F.7}$$

The shear force in a Newtonian fluid is given as:

$$\tau_x = \eta \frac{\partial u}{\partial z} \tag{F.8}$$

Where η is the kinematic viscosity and u is the velocity profile in x direction. Substituting F.8 in F.7 gives:

$$\frac{\partial p}{\partial x} = \frac{\partial}{\partial z}\left(\eta \frac{\partial u}{\partial z}\right) \tag{F.9}$$

When the kinematic viscosity η is assumed to be constant this simplifies to:

$$\frac{\partial p}{\partial x} = \eta \frac{\partial^2 u}{\partial z^2} \tag{F.10}$$

Integrating with respect to z gives:

$$\begin{aligned} \int \frac{\partial p}{\partial x}\, dz &= \int \eta \frac{\partial^2 u}{\partial z^2}\, dz \\ \frac{\partial p}{\partial x} z &= \eta \frac{\partial u}{\partial z} + C_1 \end{aligned} \tag{F.11}$$

Integrating again with respect to z gives:

$$\begin{aligned} \int \frac{\partial p}{\partial x} z\, dz &= \int \left(\eta \frac{\partial u}{\partial z} + C_1\right) dz \\ \frac{\partial p}{\partial x} \frac{z^2}{2} &= \eta u + C_1 z + C_2 \end{aligned} \tag{F.12}$$

Rewriting F.12 gives:

$$u(z) = \frac{\partial p}{\partial x} \frac{z^2}{2\eta} + C_1 z + C_2 \tag{F.13}$$

Assuming no-slip boundary condition on the bearing surface gives:

$$u\Big|_{z=0} = u_a \rightarrow C_2 = u_a \tag{F.14}$$

Assuming no-slip boundary condition on the substrate surface gives:

$$\begin{aligned} u\Big|_{z=h} = u_b \rightarrow u_b &= \frac{\partial p}{\partial x} \frac{h^2}{2\eta} + C_1 h + u_a \\ C_1 &= \frac{u_b - u_a}{h} - \frac{\partial p}{\partial x} \frac{h}{2\eta} \end{aligned} \tag{F.15}$$

Substituting F.14 and F.15 in F.13 gives:

$$u(x,z) = \underbrace{\frac{1}{2\eta} \frac{\partial p}{\partial x}\left(z^2 - hz\right)}_{\text{Poiseuille flow}} + \underbrace{\frac{u_b - u_a}{h} z + u_a}_{\text{Couette flow}} \tag{F.16}$$

The Poiseuille flow is a pressure driven flow and the Couette flow is caused by relative motion of the two planes. This is explained in more detail in appendices F.1.1 and F.1.2.

F.3 Derivation theoretical analysis

F.3.1 Aerostatic bearing

The geometry for a plain aerostatic bearing unit cell is shown in figure F.3. The dashed blue line indicates the incompressible pressure profile, while the solid line indicates the compressible pressure profile. The restriction scheme is shown on the bottom of the figure, where the film restrictions towards the left and the right are indicated by R_l and R_r respectively.

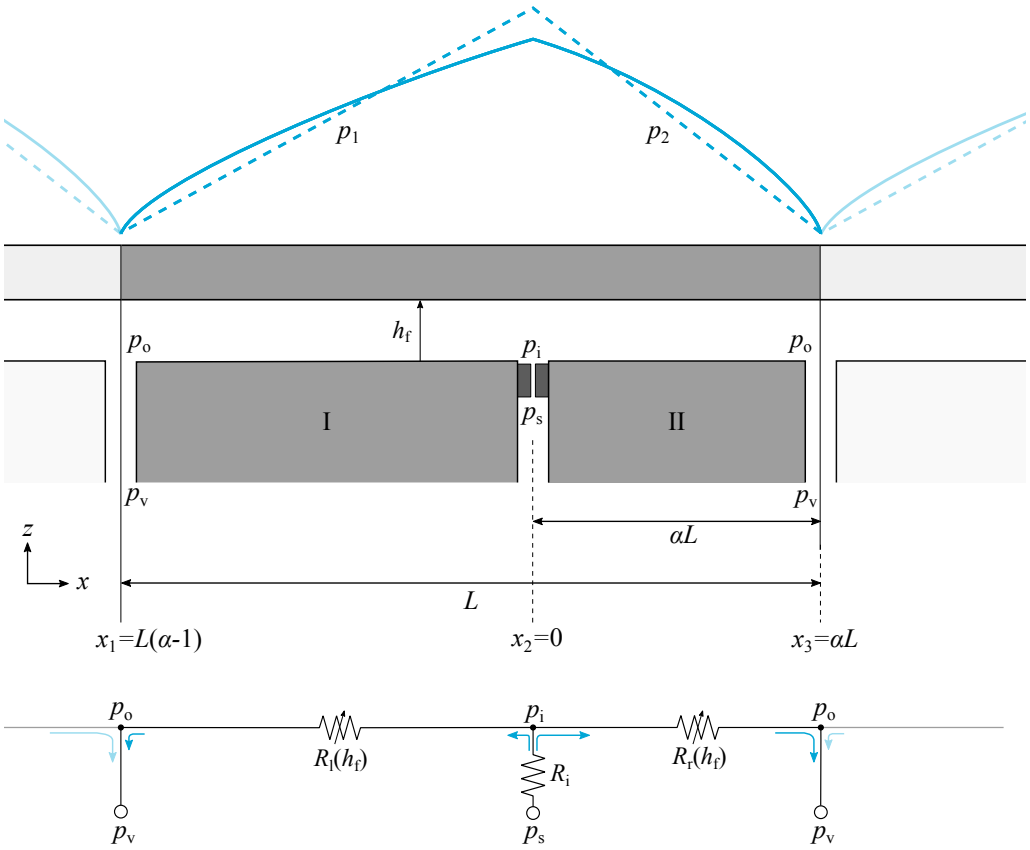

Figure F.3: Geometry of aerostatic bearing unit cell.

Incompressible case

Governing equation

For the incompressible aerostatic bearing case, the governing equation is defined as:

$$\frac{\partial^2 p}{\partial x^2} = 0 \tag{F.17}$$

Integrating once gives:

$$\int \frac{\partial}{\partial x}\left(\frac{\partial p}{\partial x}\right) dx = \frac{\partial p}{\partial x} + A \tag{F.18}$$

Integrating again gives:

$$\int \frac{\partial p}{\partial x} + A\, dx = p(x) + Ax + B \tag{F.19}$$

The solution on the domain L can thus be defined as:

$$p(x) = \begin{cases} p_1 = \dfrac{p_\mathrm{i} - p_\mathrm{o}}{(1-\alpha)L}\, x + p_\mathrm{i} & \text{for } x_1 < x \leq x_2 \\ \\ p_2 = -\dfrac{p_\mathrm{i} - p_\mathrm{o}}{\alpha\, L}\, x + p_\mathrm{i} & \text{for } x_2 < x \leq x_3 \end{cases} \tag{F.20}$$

The incompressible pressure profile for various values of α is shown in figure F.4.

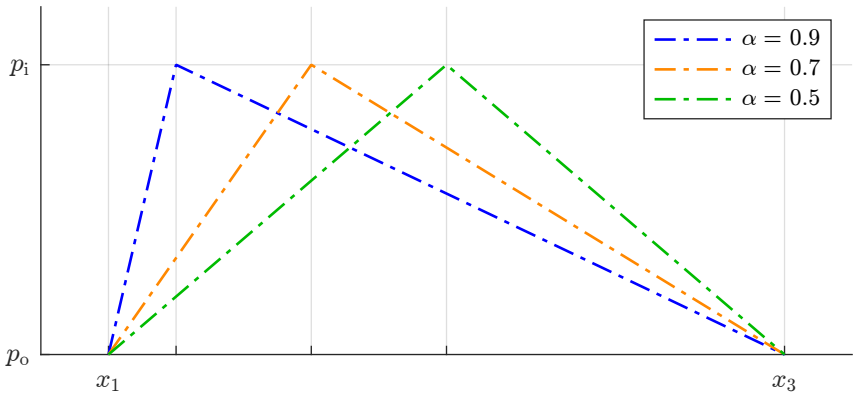

Figure F.4: Incompressible pressure profiles for plain bearing surface.

Load capacity

The load capacity is defined as:

$$\bar{W} = \frac{1}{L}\int_{x_1}^{x_3} \left(p(x) - p_\mathrm{a}\right)\, dx = \frac{p_\mathrm{i} + p_\mathrm{o}}{2} - p_\mathrm{a} \tag{F.21}$$

Combined with the no-load condition $\bar{W} = 0$, the no-load inlet pressure can be defined as:

$$p_{\mathrm{i},0} = 2\,p_\mathrm{a} - p_\mathrm{v} \tag{F.22}$$

It is assumed that the pressure drop across the outlet restriction is negligible, therefore the outlet pressure can be written as:

$$p_\mathrm{o} = p_\mathrm{v} \tag{F.23}$$

Mass flow density

In general, the mass flow is defined as:

$$\dot{m} = \dot{q}\,\rho \tag{F.24}$$

Where the volumetric flow rate is defined as:

$$\dot{q} = \int_0^h u(z)\, dz = -\frac{h^3}{12\,\eta}\frac{\partial p}{\partial x} \tag{F.25}$$

The mass flow density is then defined the sum over the left and right section as:

$$\bar{\dot{m}} = \frac{1}{L}\frac{\rho}{12\,\eta}\left(h^3\frac{\partial p_1}{\partial x} - h^3\frac{\partial p_2}{\partial x}\right) \tag{F.26}$$

The minus sign is inserted since the $\partial p_2/\partial x < 0$, though the mass flow is still positive. This gives an expression for the mass flow density as:

$$\bar{\dot{m}}(p_\mathrm{a}, p_\mathrm{v}, \alpha) = \frac{p_\mathrm{a}}{\mathrm{R_s}T}\frac{h_\mathrm{f}^3}{6\eta L^2}\left(\frac{1}{1-\alpha} + \frac{1}{\alpha}\right)(p_\mathrm{a} - p_\mathrm{v}) \tag{F.27}$$

Alternatively, the mass flow can be determined using the flow restriction schematic. The flow restriction to the left and right side are defined respectively as:

$$\begin{aligned} R_\mathrm{l}(h_\mathrm{f}) &= \frac{12\eta\, L(1-\alpha)}{h_\mathrm{f}^3} \\ R_\mathrm{r}(h_\mathrm{f}) &= \frac{12\eta L\alpha}{h_\mathrm{f}^3} \end{aligned} \tag{F.28}$$

Since both restrictions lead to the same pressure (p_o), they can effectively be seen as two restrictions in parallel. The effective restriction then becomes:

$$R_\mathrm{e}(h_\mathrm{f}) = \left(\frac{1}{R_\mathrm{l}(h_\mathrm{f})} + \frac{1}{R_\mathrm{r}(h_\mathrm{f})}\right)^{-1} = \frac{12\eta L\alpha(1-\alpha)}{h_\mathrm{f}^3} \tag{F.29}$$

Substituting this expression in the volumetric flow through the effective restriction as:

$$\dot{q} = \frac{p_\mathrm{i} - p_\mathrm{o}}{R_\mathrm{e}(h_\mathrm{f})} = (p_\mathrm{i} - p_\mathrm{o})\frac{h_\mathrm{f}^3}{12\,\eta L}\frac{1}{\alpha(1-\alpha)} \tag{F.30}$$

The mass flow density is then defined as:

$$\bar{\dot{m}}(p_\mathrm{i}, p_\mathrm{o}, \alpha) = \frac{1}{L}\rho\dot{q} = \frac{p_\mathrm{i} + p_\mathrm{o}}{2\,\mathrm{R_s}T}\frac{h_\mathrm{f}^3}{12\,\eta L^2}\frac{1}{\alpha(1-\alpha)}(p_\mathrm{i} - p_\mathrm{o}) \tag{F.31}$$

Substituting the no-load inlet pressure (F.22) and neglecting the pressure drop across the outlet restriction (F.23) gives in fact the same result as shown in equation (F.26).

Force density

The force density is defined as:

$$\bar{F}_x = \frac{1}{L}\left(\int_{x_1}^{x_2} -\frac{h}{2}\frac{\partial p_1}{\partial x}\,dx + \int_{x_2}^{x_3} -\frac{h}{2}\frac{\partial p_2}{\partial x}\,dx\right) \tag{F.32}$$

The force towards the left and towards the right are equal and opposite, and also independent of the location of the inlet α.

$$F_\mathrm{r} = -F_\mathrm{l} = \frac{h_\mathrm{f}\,(p_\mathrm{i} - p_\mathrm{o})}{2} \tag{F.33}$$

The net force will therefore always be 0. Since the force density is 0 for all values of α, the performance ratio will also be 0 for all values of α.

Stiffness

In order to determine the stiffness, the variation of the load capacity with respect to a disturbance of the fly-height needs to be defined. Therefore, the load capacity needs to be expressed in terms of the restriction values R_i, $R_\mathrm{e}(h_\mathrm{f})$ and R_o. Then the derivative with respect to the variation in fly-height can calculated. The following system of equations can be set-up:

$$\begin{aligned} p_\mathrm{s} - p_\mathrm{i} &= \dot{q}\,R_\mathrm{i} \\ p_\mathrm{o} - p_\mathrm{v} &= \dot{q}\,R_\mathrm{o} \\ p_\mathrm{s} - p_\mathrm{v} &= \dot{q}\,(R_\mathrm{i} + R_\mathrm{e}(h_\mathrm{f}) + R_\mathrm{o}) \end{aligned} \tag{F.34}$$

From this, the inlet and outlet pressure can be written as:

$$p_\mathrm{i} = \frac{R_\mathrm{i}\,p_\mathrm{v} + p_\mathrm{s}\,(R_\mathrm{o} + R_\mathrm{e}\,(h_\mathrm{f}))}{R_\mathrm{i} + R_\mathrm{o} + R_\mathrm{e}\,(h_\mathrm{f})} \tag{F.35a}$$

$$p_\mathrm{o} = \frac{R_\mathrm{o}\,p_\mathrm{s} + p_\mathrm{v}\,(R_\mathrm{i} + R_\mathrm{e}\,(h_\mathrm{f}))}{R_\mathrm{i} + R_\mathrm{o} + R_\mathrm{e}\,(h_f)} \tag{F.35b}$$

Substituting these expressions in the definition of the load capacity (F.21) gives:

$$\bar{W} = \frac{p_\mathrm{i} + p_\mathrm{o}}{2} - p_\mathrm{a} = \frac{p_\mathrm{s}\,(R_\mathrm{e}(h_\mathrm{f}) + 2R_\mathrm{o}) + p_\mathrm{v}\,(R_\mathrm{e}(h_\mathrm{f}) + 2R_\mathrm{i})}{2\,(R_\mathrm{i} + R_\mathrm{e}(h_\mathrm{f}) + R_\mathrm{o})} - p_\mathrm{a} \tag{F.36}$$

The stiffness can then be found by taking the derivative of the load capacity with respect to the fly-height as:

$$\bar{k} = -\frac{\partial R_\mathrm{e}(h_\mathrm{f})}{\partial h_\mathrm{f}}\frac{R_\mathrm{i} - R_\mathrm{o}}{2\,(R_\mathrm{i} + R_\mathrm{e}(h_\mathrm{f}) + R_\mathrm{o})^2}\,(p_\mathrm{s} - p_\mathrm{v}) \tag{F.37}$$

Compressible case

For the compressible case, the governing equation is defined as:

$$\frac{\partial}{\partial x}\left(p\frac{\partial p}{\partial x}\right) = 0 \tag{F.38}$$

Integrating once gives:

$$\int \frac{\partial}{\partial x}\left(p(x)\frac{\partial p}{\partial x}\right) dx = p(x)\frac{\partial p}{\partial x} + A \tag{F.39}$$

Integrating again, using integration by parts gives:

$$\int p(x)\frac{\partial p}{\partial x} + A\, dx = \frac{p(x)^2}{2} + Ax + B \tag{F.40}$$

The constants A_1, B_1, A_2 and B_2 can be found by enforcing the boundary conditions as shown in figure F.3. The pressure profile can then be written as:

$$p(x, p_\mathrm{i}, p_\mathrm{o}, \alpha, L) = \begin{cases} p_1 = \sqrt{{p_\mathrm{i}}^2 + \dfrac{({p_\mathrm{i}}^2 - {p_\mathrm{o}}^2)}{L\,(1-\alpha)}x} & \text{for } x_1 < x \leq x_2 \\ \\ p_2 = \sqrt{{p_\mathrm{i}}^2 - \dfrac{({p_\mathrm{i}}^2 - {p_\mathrm{o}}^2)}{\alpha\, L}x} & \text{for } x_2 < x \leq x_3 \end{cases} \tag{F.41}$$

The pressure profile in the bearing film for varying values of α is shown in figure F.5.

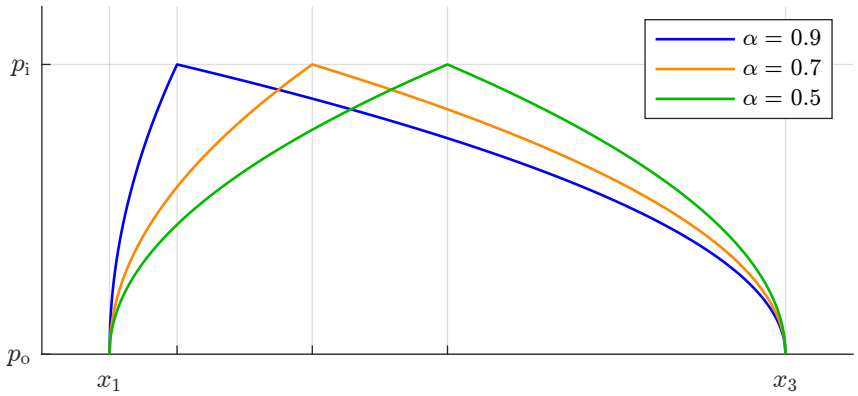

Figure F.5: Compressible pressure profiles for plain bearing surface.

Load capacity

The load capacity is defined as:

$$W = \frac{2}{3}\frac{p_\mathrm{i}^2 + p_\mathrm{i}\,p_\mathrm{o} + p_\mathrm{o}^2}{p_\mathrm{i} + p_\mathrm{o}} - p_\mathrm{a} \tag{F.42}$$

The no-load inlet pressure can therefore be written as:

$$p_{\mathrm{i},0} = \frac{3}{4}p_\mathrm{a} - \frac{1}{2}p_\mathrm{v} + \frac{1}{4}\sqrt{9\,p_\mathrm{a}^2 + 12\,p_\mathrm{a}\,p_\mathrm{v} - 12\,p_\mathrm{v}^2} \tag{F.43}$$

Performance ratio

The force density can be found by substituting the expressions found for the compressible pressure distribution (F.41) in the expression for the force density, shown in equation (F.32). Similarly, the mass flow can be found by using equation (F.31). When evaluating the force density and mass flow density, the expression for the no-load inlet pressure (F.43) needs to be substituted for the inlet pressure p_i. Again, we find that the force density is 0 for all values of α. This means that no net shear force is generated, and thus the performance ratio equals 0.

F.3.2 Variable outlet restriction

The geometry of a variable outlet restriction unit cell is shown in figure F.6. The dashed blue line indicates the incompressible pressure profile, while the solid line indicates the compressible pressure profile. The restriction scheme is shown on the bottom of the figure. The restriction through section I is referred to as the dam restriction R_d. The restriction through the pocket R_p is identical for section II and III.

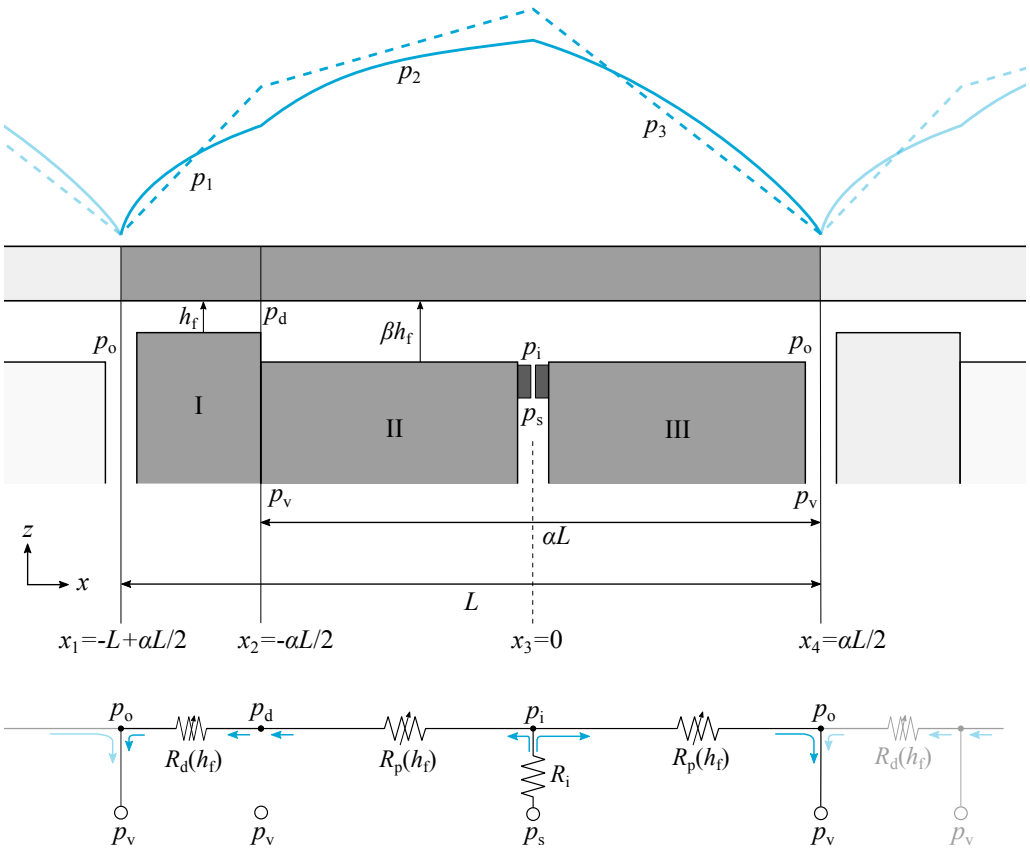

Figure F.6

Incompressible case

By solving the governing equation (F.17) on the domain, the following expressions for the pressure profile can be found:

$$p(x, p_\mathrm{i}, p_\mathrm{d}, p_\mathrm{o}, \alpha, L) = \begin{cases} p_1 = \dfrac{p_\mathrm{d}\,(\alpha-2) + \alpha\, p_\mathrm{o}}{2\,(\alpha-1)} + \dfrac{p_\mathrm{d} - p_\mathrm{o}}{L\,(1-\alpha)}\,x & \text{for } x_1 < x \leq x_2 \\ p_2 = p_\mathrm{i} + \dfrac{2\,(p_\mathrm{i} - p_\mathrm{d})}{\alpha\, L}\,x & \text{for } x_2 < x \leq x_3 \\ p_3 = p_\mathrm{i} - \dfrac{2\,(p_\mathrm{i} - p_\mathrm{o})}{\alpha\, L}\,x & \text{for } x_3 < x \leq x_4 \end{cases} \tag{F.44}$$

The pressure profiles for varying values of β are shown in figure F.7.

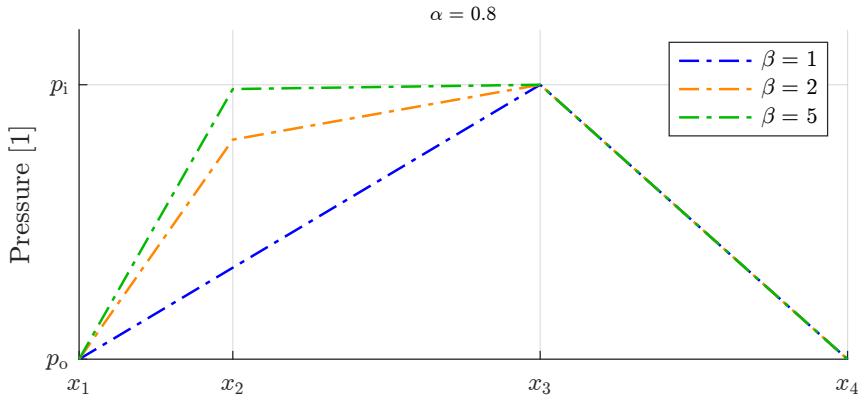

Figure F.7: Incompressible pressure profiles for variable outlet restriction.

Using the restriction scheme, the pressure at the dam p_d can be expressed in terms of p_i, p_o, α and β as:

$$p_\mathrm{d} = \frac{p_\mathrm{i} R_\mathrm{d} + p_\mathrm{o} R_\mathrm{p}}{R_\mathrm{d} + R_\mathrm{p}} \tag{F.45}$$

The values for the dam restriction and pocket restriction are defined as:

$$R_\mathrm{d} = \frac{12\eta L(1-\alpha)}{h_\mathrm{f}^3} \qquad R_\mathrm{p} = \frac{6\eta\alpha L}{(\beta h_\mathrm{f})^3} \tag{F.46}$$

Substituting these expressions in equation (F.45) gives:

$$p_\mathrm{d}(p_\mathrm{i}, p_\mathrm{o}, \alpha, \beta) = \frac{\alpha\, p_\mathrm{o} + 2\,\beta^3\, p_\mathrm{i} - 2\,\alpha\,\beta^3\, p_\mathrm{i}}{\alpha - 2\,\alpha\,\beta^3 + 2\,\beta^3} \tag{F.47}$$

The no-load inlet pressure is thus defined as

$$p_{\mathrm{i},0}(p_\mathrm{a}, p_\mathrm{o}, p_\mathrm{d}., \alpha) = \frac{p_\mathrm{d} + p_\mathrm{o}}{2} - \frac{p_\mathrm{d} + p_\mathrm{o} - 2\,p_\mathrm{a}}{\alpha} \tag{F.48}$$

If the outlet restriction is assumed to be negligible, the outlet pressure is defined as:

$$p_\mathrm{o} = p_\mathrm{v} \tag{F.49}$$

The force density is found by integrating the pressure gradient over the three different sections as:

$$\bar{F}_x = \frac{1}{L}\left(\int_{x_1}^{x_2} -\frac{h}{2}\frac{\partial p_1}{\partial x}\,dx + \int_{x_2}^{x_3} -\frac{h}{2}\frac{\partial p_2}{\partial x}\,dx + \int_{x_3}^{x_4} -\frac{h}{2}\frac{\partial p_3}{\partial x}\,dx\right) \tag{F.50}$$

Which was found to be:

$$\bar{F}(p_\mathrm{d}, p_\mathrm{o}, \beta, h_\mathrm{f}, L) = \frac{h_\mathrm{f}}{2\,L}(\beta - 1)(p_\mathrm{d} - p_\mathrm{o}) \tag{F.51}$$

The restriction scheme is for the variable outlet restriction is essentially identical to the one of the plain bearing case with:

$$R_\mathrm{l} = R_\mathrm{d} + R_\mathrm{p} \qquad R_\mathrm{r} = R_\mathrm{p} \tag{F.52}$$

Thus, equation (F.34) can be used again, where the effective restriction is now defined as:

$$R_\mathrm{e}(h_\mathrm{f}) = \left(\frac{1}{R_\mathrm{d}(h_\mathrm{f}) + R_\mathrm{p}(h_\mathrm{f})} + \frac{1}{R_\mathrm{p}(h_\mathrm{f})}\right)^{-1} = \frac{3\,\alpha\,L\,\eta\left(\alpha - 2\,\alpha\,\beta^3 + 2\,\beta^3\right)}{\beta^3\,{h_\mathrm{f}}^3\left(\alpha - \alpha\,\beta^3 + \beta^3\right)} \tag{F.53}$$

Since the restriction scheme is essentially unchanged, the expressions for the inlet and outlet pressure (F.35a and F.35b) can be re-used. The total mass flow density can then be written as:

$$\bar{\dot{m}}(p_\mathrm{i}, p_\mathrm{o}, \alpha, \beta, h_\mathrm{f}, L, \eta, \mathrm{R_s}, T) = \frac{(p_\mathrm{i} + p_\mathrm{o})}{2\,\mathrm{R_s}\,T}\,\frac{\beta^3\,h_\mathrm{f}^3}{6\,\eta\,L^2}\left(\frac{1}{\alpha} - \frac{1}{\alpha\,(2\,\beta^3 - 1) - 2\,\beta^3}\right)(p_\mathrm{i} - p_\mathrm{o}) \tag{F.54}$$

When substituting the expressions for the dam pressure (F.47), the no-load inlet pressure (F.48) and the vacuum pressure (F.49), the performance ratio can then be defined as an analytical function f as:

$$P = \frac{\bar{F}}{\bar{\dot{m}}} = f(p_\mathrm{a}, p_\mathrm{v}, \alpha, \beta, h_\mathrm{f}, L, \eta, \mathrm{R_s}, T) \tag{F.55}$$

Compressible case

The pressure can be found by solving the governing equation (F.38) on the full domain. Using the boundary conditions as shown in figure F.6, the following expression can be found for the pressure distribution:

$$p(x, p_\mathrm{i}, p_\mathrm{d}, p_\mathrm{o}, \alpha, L) = \begin{cases} p_1 = \sqrt{\dfrac{p_\mathrm{d}^2(\alpha-2)+\alpha p_\mathrm{o}^2}{2\,(\alpha-1)} + \dfrac{p_\mathrm{d}^2 - p_\mathrm{o}^2}{L\,(1-\alpha)}\,x} & \text{for } x_1 < x \leq x_2 \\ p_2 = \sqrt{p_\mathrm{i}^2 + \dfrac{2\,(p_\mathrm{i}^2 - p_\mathrm{d}^2)}{\alpha\,L}\,x} & \text{for } x_2 < x \leq x_3 \\ p_3 = \sqrt{p_\mathrm{i}^2 - \dfrac{2\,(p_\mathrm{i}^2 - p_\mathrm{o}^2)}{\alpha\,L}\,x} & \text{for } x_3 < x \leq x_4 \end{cases} \tag{F.56}$$

The pressure profile for varying values of β is shown in figure F.8.

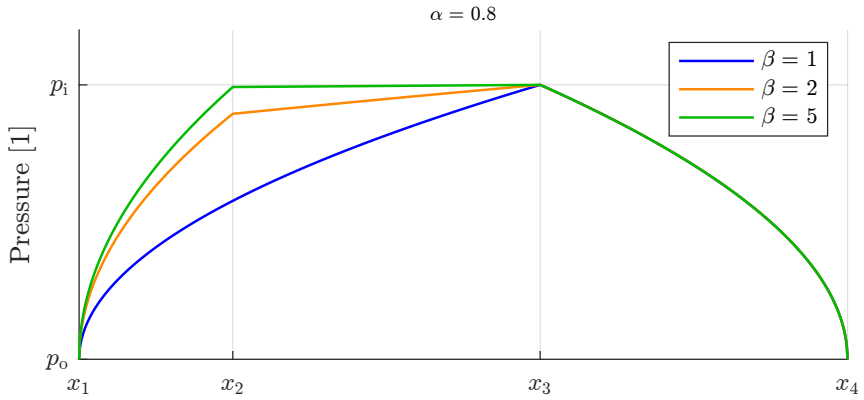

Figure F.8: Compressible pressure profiles for variable outlet restriction.

An analytical expression for the dam pressure can be found by using the mass flow equilibrium:

$$p_\mathrm{d} = \sqrt{\frac{p_\mathrm{o}^2 R_\mathrm{p} + p_\mathrm{i}^2 R_\mathrm{d}}{R_\mathrm{d} + R_\mathrm{p}}} = \sqrt{\frac{\alpha\, p_\mathrm{o}^2 + \beta^3\, p_\mathrm{i}^2 (1-\alpha)}{\alpha + 2\beta^3\,(1-\alpha)}} \tag{F.57}$$

An analytical solution for the no-load inlet pressure $p_{\mathrm{i},0}$ cannot be found. Therefore a numerical solution needs to be found.

F.4 Perturbed Reynolds equation

Let us consider the time-dependent simplified Reynolds equation x-direction:

$$\frac{\partial}{\partial x}\left(\frac{ph^3}{12\eta R_s T}\frac{\partial p}{\partial x}\right) = \frac{\partial}{\partial t}\left(\frac{ph}{R_s T}\right) \tag{F.58}$$

Now let us suppose that the stationary fly-height h_0 is perturbed, which results in a dynamic fly-height, defined as:

$$h(t) = h_0 + \tilde{h}e^{i\omega t} \tag{F.59}$$

Where $\tilde{h}$ is the amplitude of the perturbation, ω is the angular perturbation frequency and t represents time. We assume that this perturbation in the fly-height will lead to a perturbed pressure that can be expressed as:

$$p(t) = p_0 + \tilde{p}e^{i\omega t} \tag{F.60}$$

Substituting equations (F.59) and (F.60) in equation (F.58) gives:

$$\frac{1}{12\eta R_s T}\frac{\partial}{\partial x}\left((p_0+\tilde{p}e^{i\omega t})(h_0+\tilde{h}e^{i\omega t})^3\frac{\partial}{\partial x}(p_0+\tilde{p}e^{i\omega t})\right) = \frac{1}{R_s T}\frac{\partial}{\partial t}\left((p_0+\tilde{p}e^{i\omega t})(h_0+\tilde{h}e^{i\omega t})\right) \tag{F.61}$$

Expanding the second term in the brackets on the left hand side gives:

$$(h_0+\tilde{h}e^{i\omega t})^3 = h_0^3 + 3h_0^2\tilde{h}e^{i\omega t} + 3h_0\tilde{h}^2e^{2i\omega t} + \tilde{h}^3e^{3i\omega t} \tag{F.62}$$

Neglecting higher order terms of $\tilde{h}$ gives:

$$(h_0+\tilde{h}e^{i\omega t})^3 \approx h_0^3 + 3h_0^2\tilde{h}e^{i\omega t} \tag{F.63}$$

Multiplying with the perturbed pressure gives:

$$(p_0+\tilde{p}e^{i\omega t})(h_0^3+3h_0^2\tilde{h}e^{i\omega t}) = p_0h_0^3 + 3p_0h_0^2\tilde{h}e^{i\omega t} + \tilde{p}h_0^3e^{i\omega t} + 3\tilde{p}h_0^2\tilde{h}e^{2i\omega t} \tag{F.64}$$

Neglecting higher order terms of $\tilde{p}\tilde{h}$ gives:

$$(p_0+\tilde{p}e^{i\omega t})(h_0^3+3h_0^2\tilde{h}e^{i\omega t}) \approx p_0h_0^3 + 3p_0h_0^2\tilde{h}e^{i\omega t} + \tilde{p}h_0^3e^{i\omega t} \tag{F.65}$$

Now for the third term within the brackets on the left hand side:

$$\frac{\partial}{\partial x}(p_0+\tilde{p}e^{i\omega t}) = \frac{\partial}{\partial x}p_0 + e^{i\omega t}\frac{\partial}{\partial x}\tilde{p} \tag{F.66}$$

The multiplication of the terms within the brackets on the left hand side can thus be written as:

$$\begin{aligned}\left(p_0h_0^3 + 3p_0h_0^2\tilde{h}e^{i\omega t} + \tilde{p}h_0^3e^{i\omega t}\right)\left(\frac{\partial}{\partial x}p_0 + e^{i\omega t}\frac{\partial}{\partial x}\tilde{p}\right) = \\ p_0h_0^3\frac{\partial}{\partial x}p_0 + p_0h_0^3e^{i\omega t}\frac{\partial}{\partial x}\tilde{p} + 3p_0h_0^2\tilde{h}e^{i\omega t}\frac{\partial}{\partial x}p_0 + \\ 3p_0h_0^2\tilde{h}e^{2i\omega t}\frac{\partial}{\partial x}\tilde{p} + \tilde{p}h_0^3e^{i\omega t}\frac{\partial}{\partial x}p_0 + \tilde{p}h_0^3e^{2i\omega t}\frac{\partial}{\partial x}\tilde{p}\end{aligned} \tag{F.67}$$

Again, the higher order terms ($\tilde{h}\frac{\partial}{\partial x}\tilde{p}$, $\tilde{p}\frac{\partial}{\partial x}\tilde{p}$, $e^{2i\omega t}$) are neglected. The equation then reduces to:

$$\begin{aligned}\left(p_0h_0^3 + 3p_0h_0^2\tilde{h}e^{i\omega t} + \tilde{p}h_0^3e^{i\omega t}\right)\left(\frac{\partial}{\partial x}p_0 + e^{i\omega t}\frac{\partial}{\partial x}\tilde{p}\right) \approx \\ p_0h_0^3\frac{\partial}{\partial x}p_0 + p_0h_0^3e^{i\omega t}\frac{\partial}{\partial x}\tilde{p} + 3p_0h_0^2\tilde{h}e^{i\omega t}\frac{\partial}{\partial x}p_0 + \tilde{p}h_0^3e^{i\omega t}\frac{\partial}{\partial x}p_0\end{aligned} \tag{F.68}$$

Expanding the multiplication within the brackets gives on the right hand side of equation (F.61) gives:

$$(p_0+\tilde{p}e^{i\omega t})(h_0+\tilde{h}e^{i\omega t}) = p_0h_0 + p_0\tilde{h}e^{i\omega t} + \tilde{p}h_0e^{i\omega t} + \tilde{p}\tilde{h}e^{2i\omega t} \tag{F.69}$$

Taking the partial derivative with respect to time gives:

$$\begin{gathered}\frac{\partial}{\partial t}\left(p_0 h_0 + p_0\tilde{h}e^{i\omega t} + \tilde{p}h_0 e^{i\omega t} + \tilde{p}\tilde{h}e^{2i\omega t}\right) = \\ i\omega\left(p_0\tilde{h}e^{i\omega t} + \tilde{p}h_0 e^{i\omega t} + 2\tilde{p}\tilde{h}e^{2i\omega t}\right)\end{gathered} \tag{F.70}$$

Note that p_0 and h_0 represent the stationary solution, thus the derivative with respect to time is 0. Again, neglecting terms of order $\tilde{p}\tilde{h}$ gives:

$$\begin{gathered}\frac{\partial}{\partial t}\left(p_0 h_0 + p_0\tilde{h}e^{i\omega t} + \tilde{p}h_0 e^{i\omega t} + \tilde{p}\tilde{h}e^{2i\omega t}\right) \approx \\ i\omega\left(p_0\tilde{h}e^{i\omega t} + \tilde{p}h_0 e^{i\omega t}\right)\end{gathered} \tag{F.71}$$

Equation (F.61) can thus be written as equation (F.68) on the left hand side and equation (F.71) on the right hand side as:

$$\begin{gathered}\frac{1}{12\eta R_s T}\frac{\partial}{\partial x}\left(p_0 h_0^3\frac{\partial}{\partial x}p_0 + p_0 h_0^3 e^{i\omega t}\frac{\partial}{\partial x}\tilde{p} + 3p_0 h_0^2\tilde{h}e^{i\omega t}\frac{\partial}{\partial x}p_0 + \tilde{p}h_0^3 e^{i\omega t}\frac{\partial}{\partial x}p_0\right) = \\ \frac{1}{R_s T}i\omega\left(p_0\tilde{h}e^{i\omega t} + \tilde{p}h_0 e^{i\omega t}\right)\end{gathered} \tag{F.72}$$

Since we are interested in the perturbed pressure distribution only, the stationary solution can be subtracted, such that a perturbation about 0 remains. The stationary solution is indicated by the first term ($p_0 h_0^3\frac{\partial}{\partial x}p_0$). Subtracting this term and multiplying both sides of the equation by $e^{-i\omega t}$ gives the perturbed Reynolds equation as:

$$\frac{1}{12\eta R_s T}\frac{\partial}{\partial x}\left(p_0 h_0^3\frac{\partial}{\partial x}\tilde{p} + 3p_0 h_0^2\tilde{h}\frac{\partial}{\partial x}p_0 + \tilde{p}h_0^3\frac{\partial}{\partial x}p_0\right) = \frac{1}{R_s T}i\omega\left(p_0\tilde{h} + \tilde{p}h_0\right) \tag{F.73}$$

F.5 Hertzian deformation derivations

A schematic representation of a ball (1) in between two flat plates (2 and 3) is shown in figure F.9.

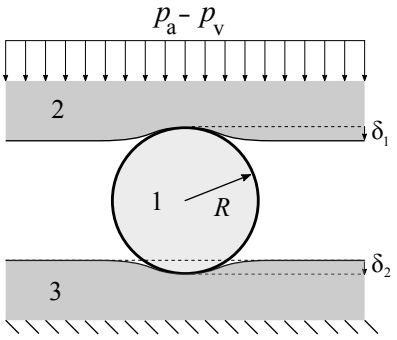

Figure F.9: Schematic Hertzian deformation.

When analysing the contact between body 1 and 2, the effective Young's modulus E' is defined as:

$$\frac{1}{E'} = \frac{1-\nu_1^2}{2E_1} + \frac{1-\nu_2^2}{2E_2} \tag{F.74}$$

The effective radius R' is defined as:

$$\begin{aligned} \frac{1}{R'} &= \frac{1}{R'_x} + \frac{1}{R'_y} \\ \frac{1}{R'_x} &= \frac{1}{r_{1,x}} + \frac{1}{r_{2,x}} \\ \frac{1}{R'_y} &= \frac{1}{r_{1,y}} + \frac{1}{r_{2,y}} \end{aligned} \tag{F.75}$$

Body 1 is a sphere, hence $r_{1,x} = r_{1,y} = R$. Body 2 is a plane, hence $r_{2,x} = r_{2,y} = \infty$. Substituting these results in equation (F.75) gives:

$$R' = R/2 \tag{F.76}$$

The radius of the circular contact that is then formed is given as:

$$r = \left(3F\frac{R'}{E'}\right)^{\frac{1}{3}} \tag{F.77}$$

The force can thus be written explicitly as:

$$F = \frac{r^3}{3}\frac{E'}{R'} \tag{F.78}$$

And the contact area can be written as:

$$A = \pi r^2 = \pi\left(3F\frac{R'}{E'}\right)^{\frac{2}{3}} \tag{F.79}$$

The deformation of the bodies leads to an indentation δ_1, as shown in figure F.9. The relation between the indentation and the contact radius is defined as [52].

$$r = \left(2R'\delta\right)^{\frac{1}{2}} \tag{F.80}$$

Substituting equation (F.80) in equation (F.78) gives:

$$F = \frac{\left(2R'\delta\right)^{\frac{3}{2}}}{3}\frac{E'}{R'} = \frac{2\sqrt{2}}{3}R'^{\frac{1}{2}}\delta^{\frac{3}{2}}E' \tag{F.81}$$

The contact stiffness k_c can be derived by taking the derivative of the force with respect to the displacement, which is the indentation in this case.

$$k_c = \frac{\partial F}{\partial \delta} = \frac{2\sqrt{2}}{3}\frac{3}{2} R'^{\frac{1}{2}} \delta^{\frac{1}{2}} E' = \sqrt{2}\, R'^{\frac{1}{2}} \delta^{\frac{1}{2}} E' \tag{F.82}$$

The mean contact pressure can be found by arranging the terms in equation (F.78) as:

$$p_{\text{mean}} = \frac{F}{A} = \frac{1}{\pi}\left(\frac{1}{3}\frac{E'}{R'}\right)^{\frac{2}{3}} F^{\frac{1}{3}} \tag{F.83}$$

The maximum pressure $p_{\max}$ is $1.5\, p_{\text{mean}}$, and the pressure distribution is half elliptic as [53].

$$p(x) = p_{\max}\left(1 - \frac{x^2}{r^2}\right)^{\frac{1}{2}} \tag{F.84}$$

Appendix G

Additional data

G.1 Dynamic pressure distribution

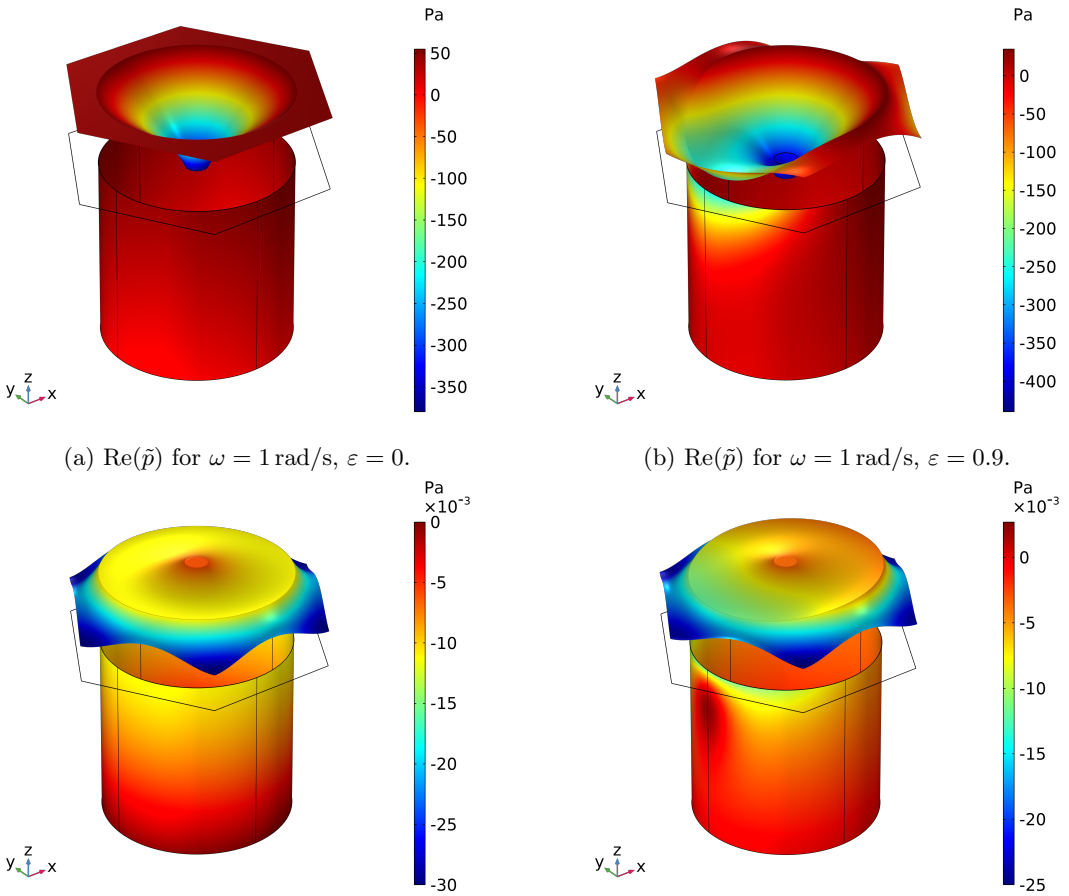

(a) $\mathrm{Re}(\tilde{p})$ for $\omega = 1\,\mathrm{rad/s}$, $\varepsilon = 0$.

(b) $\mathrm{Re}(\tilde{p})$ for $\omega = 1\,\mathrm{rad/s}$, $\varepsilon = 0.9$.

(c) $\mathrm{Im}(\tilde{p})$ for $\omega = 1\,\mathrm{rad/s}$, $\varepsilon = 0$.

(d) $\mathrm{Im}(\tilde{p})$ for $\omega = 1\,\mathrm{rad/s}$, $\varepsilon = 0.9$.

Figure G.1: Perturbed pressure distribution for low perturbation frequency.

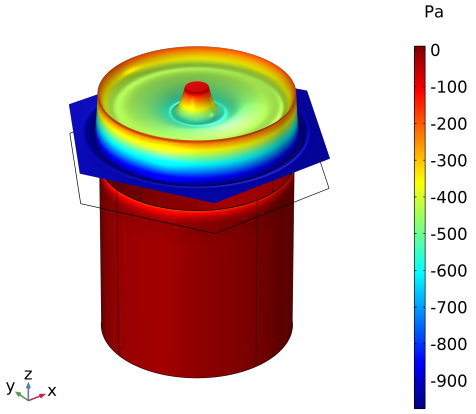

(a) $\mathrm{Re}(\tilde{p})$ for $\omega = 1 \cdot 10^7$ rad/s, $\varepsilon = 0$.

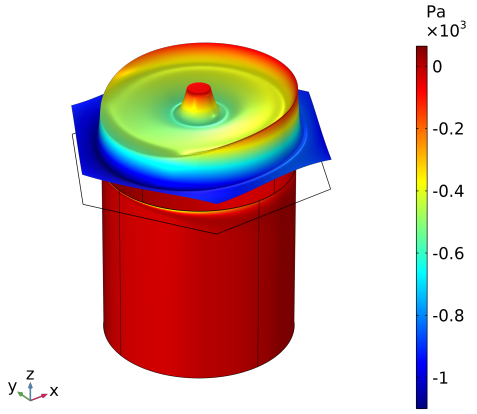

(b) $\mathrm{Re}(\tilde{p})$ for $\omega = 1 \cdot 10^7$ rad/s, $\varepsilon = 0.9$.

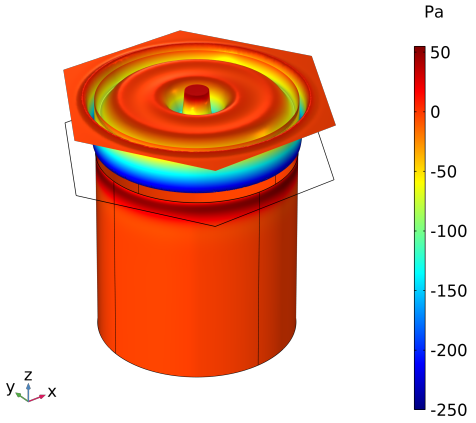

(c) $\mathrm{Im}(\tilde{p})$ for $\omega = 1 \cdot 10^7$ rad/s, $\varepsilon = 0$.

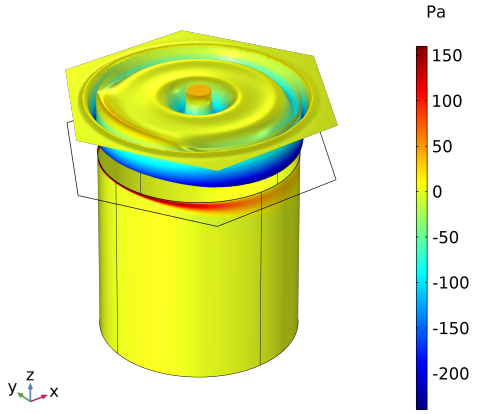

(d) $\mathrm{Im}(\tilde{p})$ for $\omega = 1 \cdot 10^7$ rad/s, $\varepsilon = 0.9$.

Figure G.2: Perturbed pressure distribution for high perturbation frequency.

G.2 Feature numbering

Different inspections are performed on the demonstrator throughout this research. It is important to keep track of the features on which each measurement is performed. Therefore each feature is given a unique ID, according to its ring number, section and row number. This is shown in figure G.3. The vertical line in section 1 refers to the faceted edge that is present on the demonstrator. This numbering assumes that the system is viewed from the bearing side.

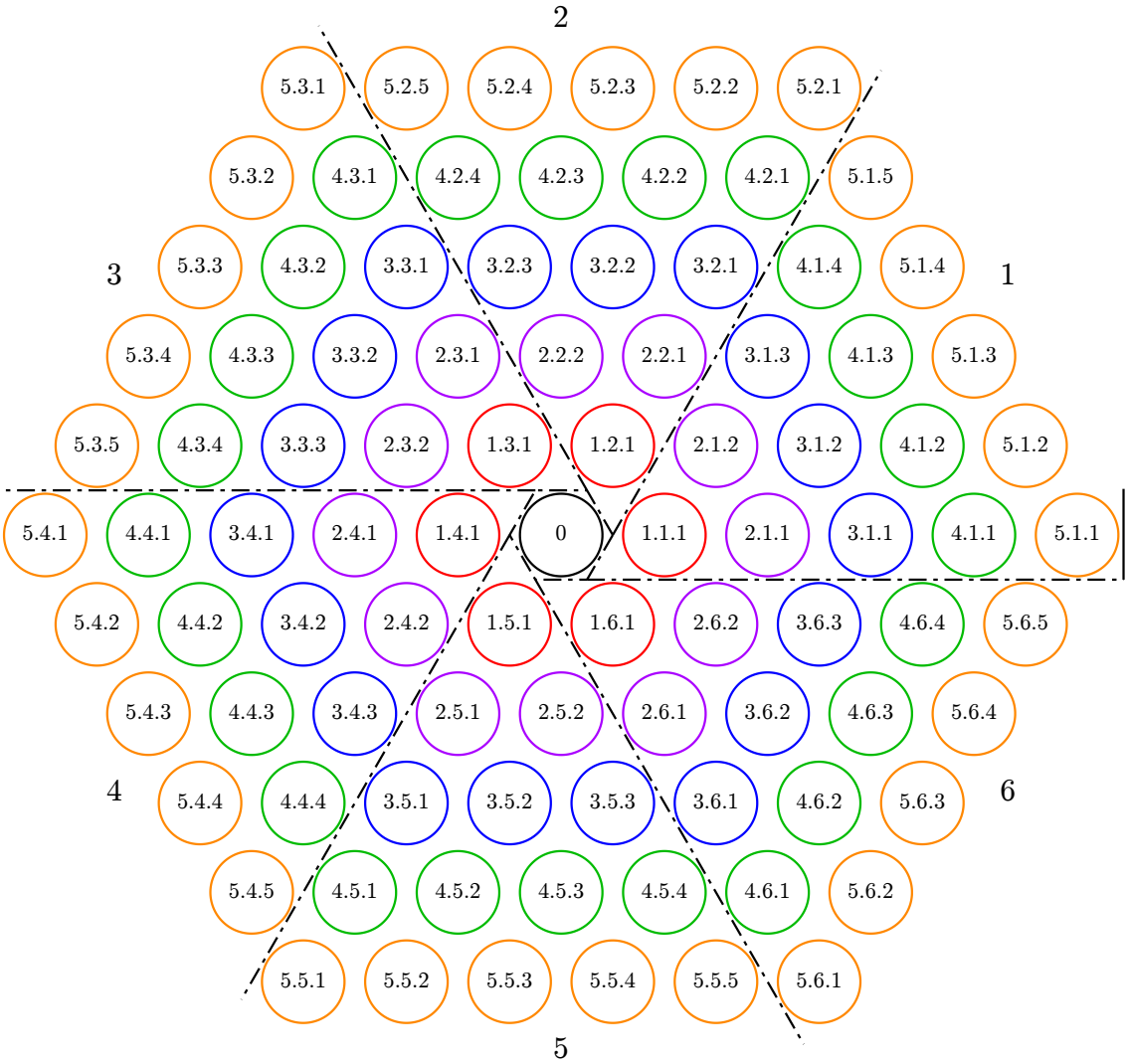

Figure G.3: Feature IDs indicated, viewed from the bearing side.

G.3 Reaming data

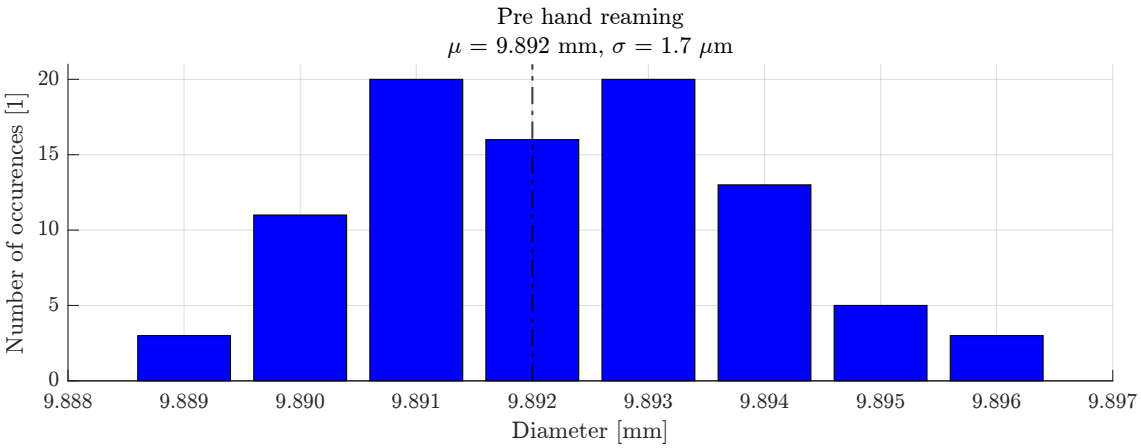

Figure G.4: Hole diameters after CNC machining using the tapered machine reamer.

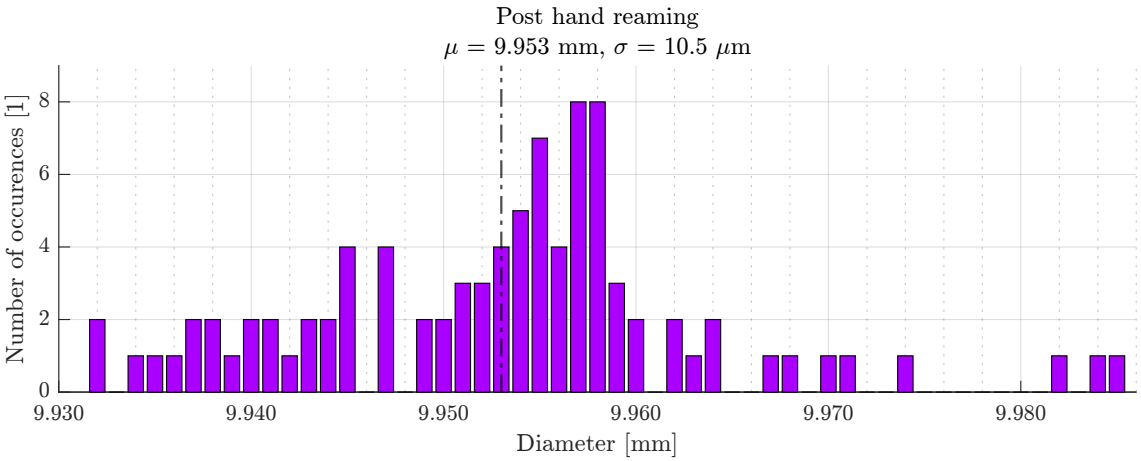

Figure G.5: Hole diameters after handreaming the holes

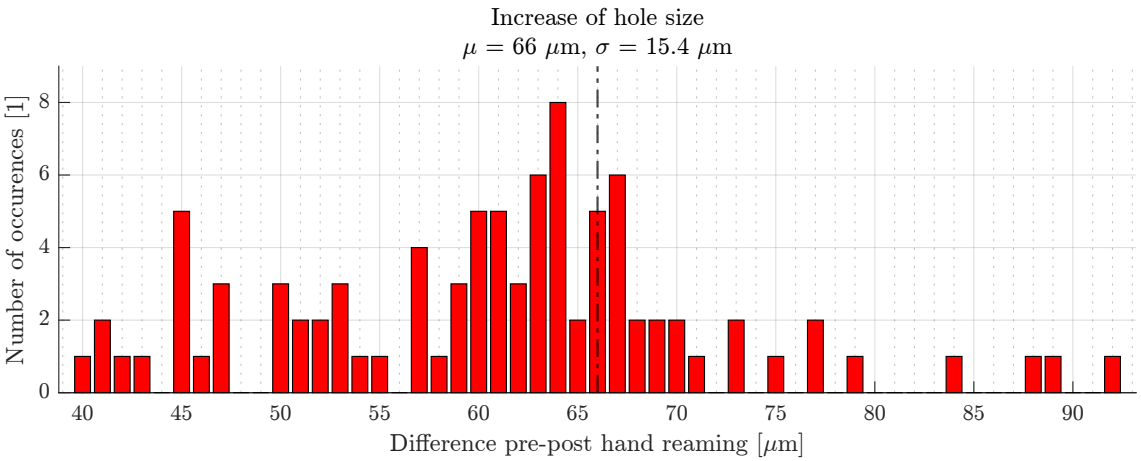

Figure G.6: Increase in diameter after hand reaming.

G.4 Manufacturing images

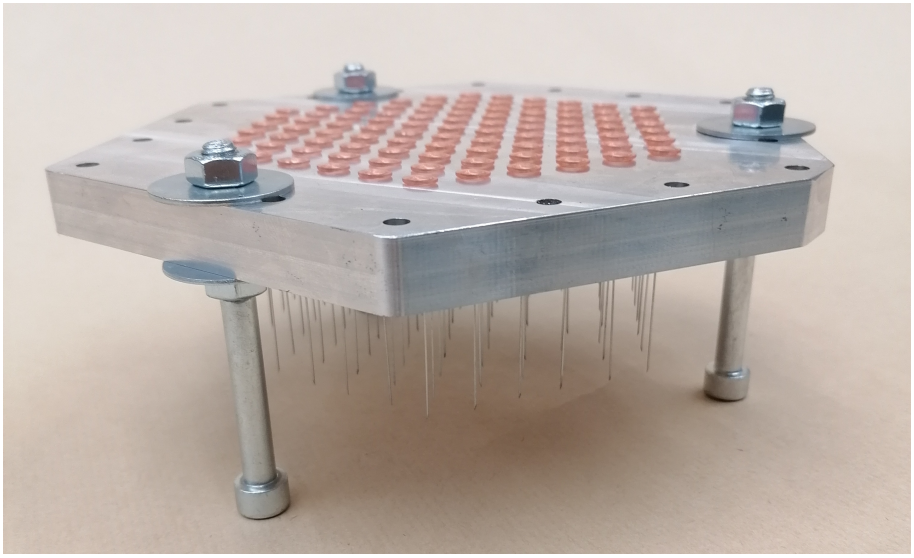

Figure G.7: The needles are pressed in using an arbour press. Long bolts with washers are inserted through the holes that will eventually function as vacuum channels. These bolts are used to support the bearing plate in this process, such that there is clearance between the table and the tips of the needles.

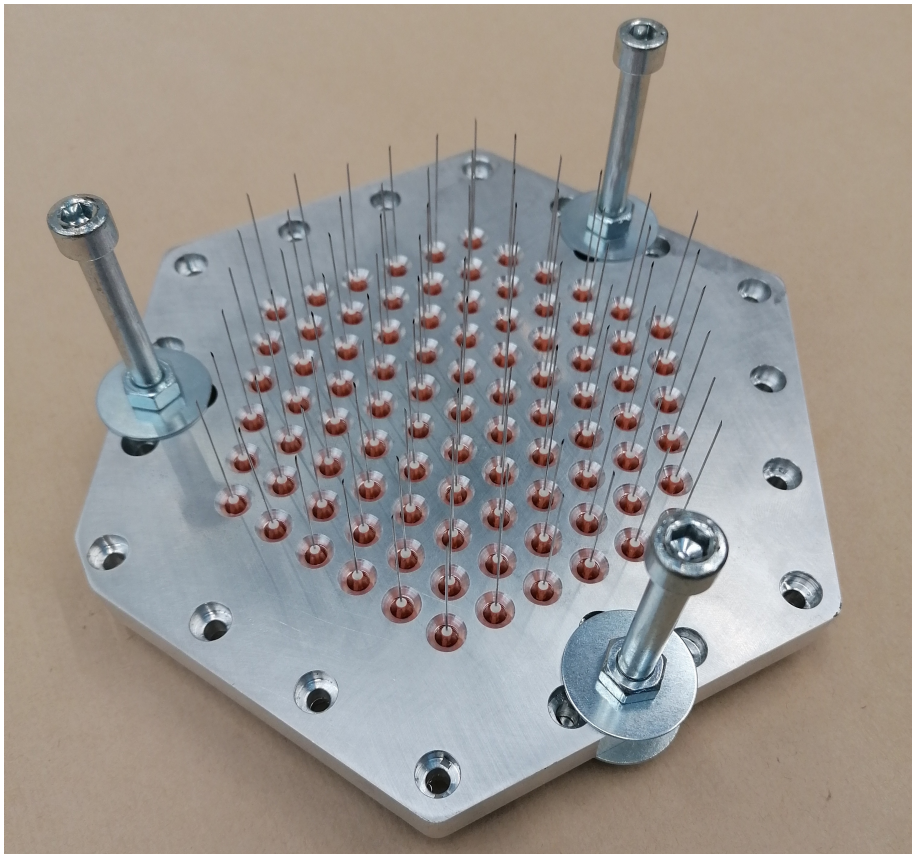

(a) Assembly viewed from the other side.

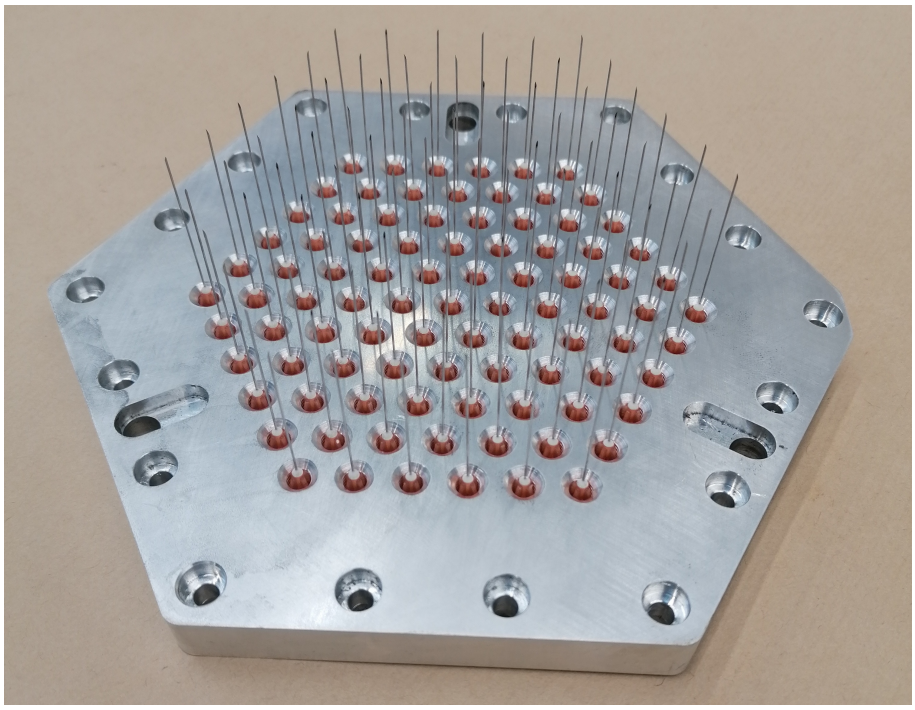

(b) Plenum lid with needles inserted viewed from what will eventually be the vacuum side. The bolts now removed. Note the chamfers, which reduce stress concentrations in the cast pins.

Figure G.8: Needle inserting process.

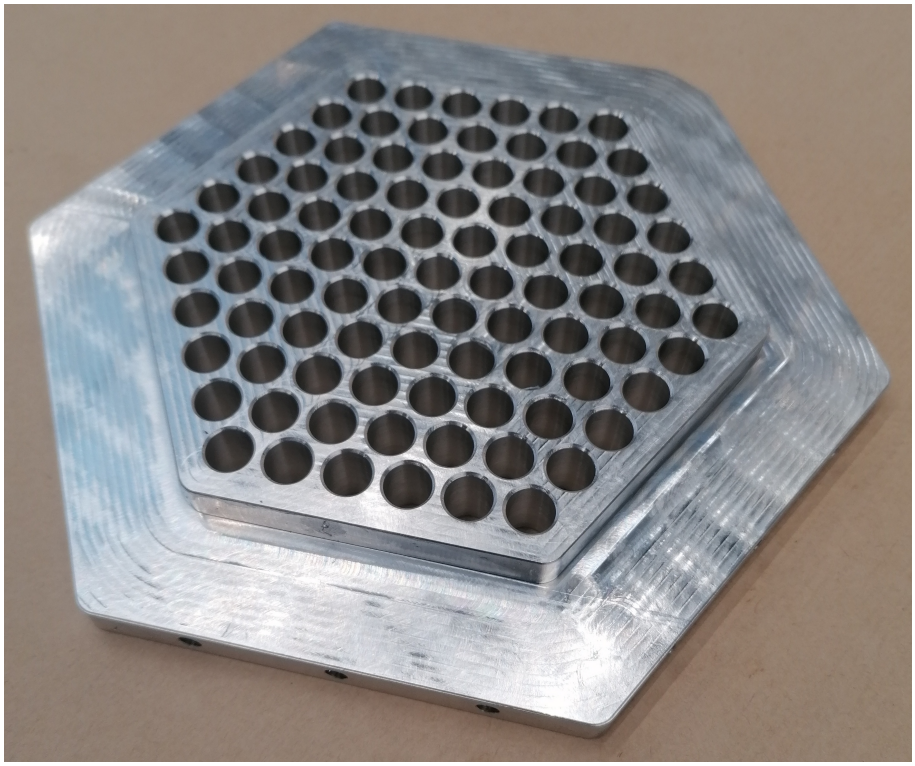

(a) Bearing plate before casting, viewed from what will eventually be the bearing side.

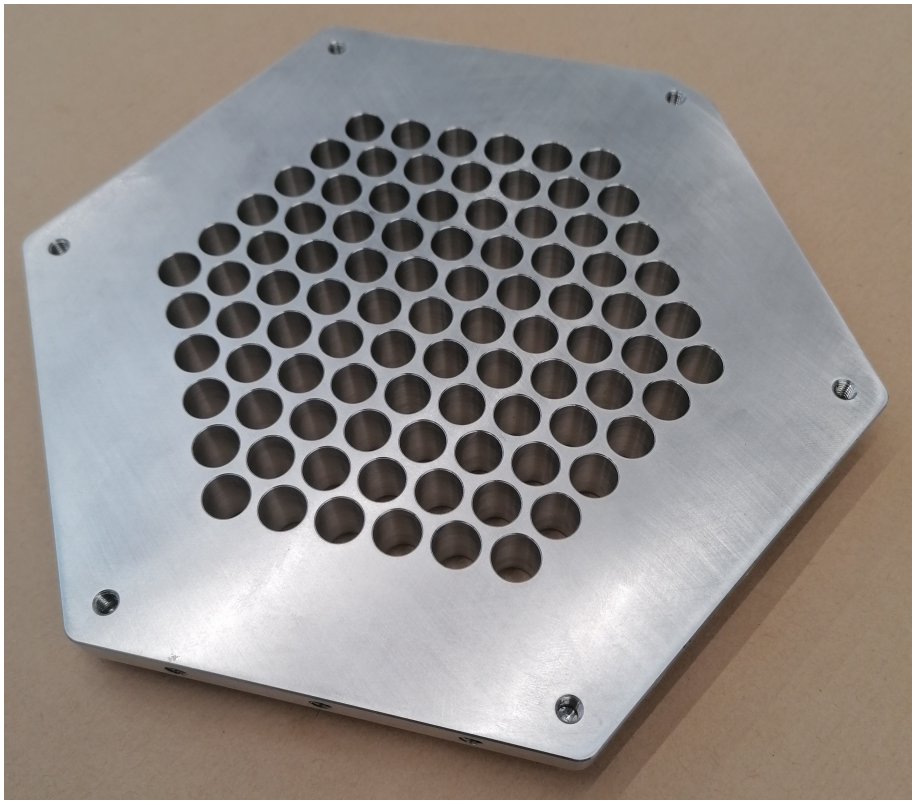

(b) Bearing plate before casting, viewed from what will eventually be the vacuum side. The threaded holes (M5) are used to clamp the assembly during casting.

Figure G.9: Bearing plate.

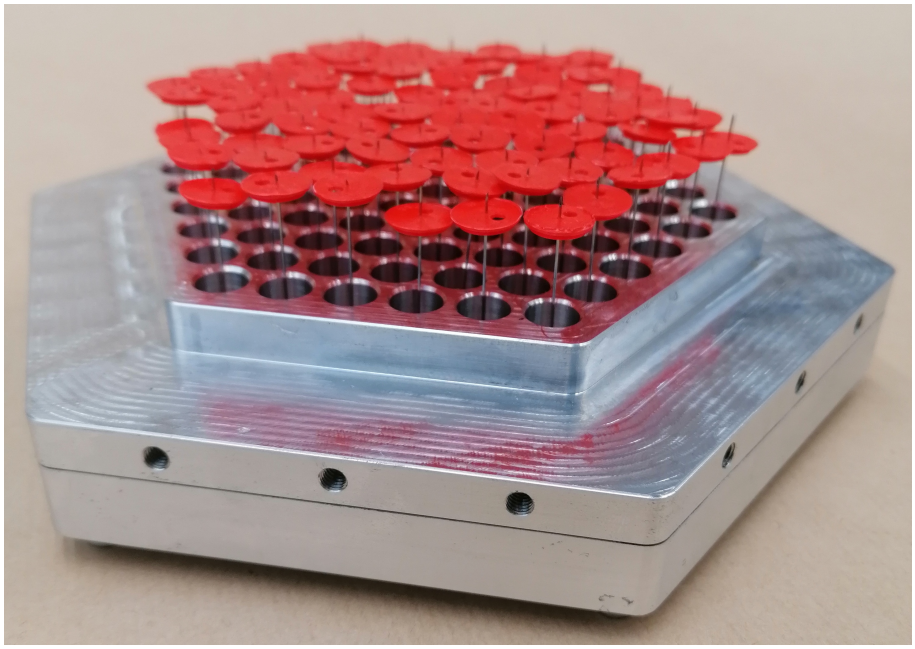

(a) Assembly before the casting process. First, the bearing plate and plenum lid are clamped together using the threaded holes (figure G.9b) in the bearing plate. Then, the needle aligners are slid over the needles.

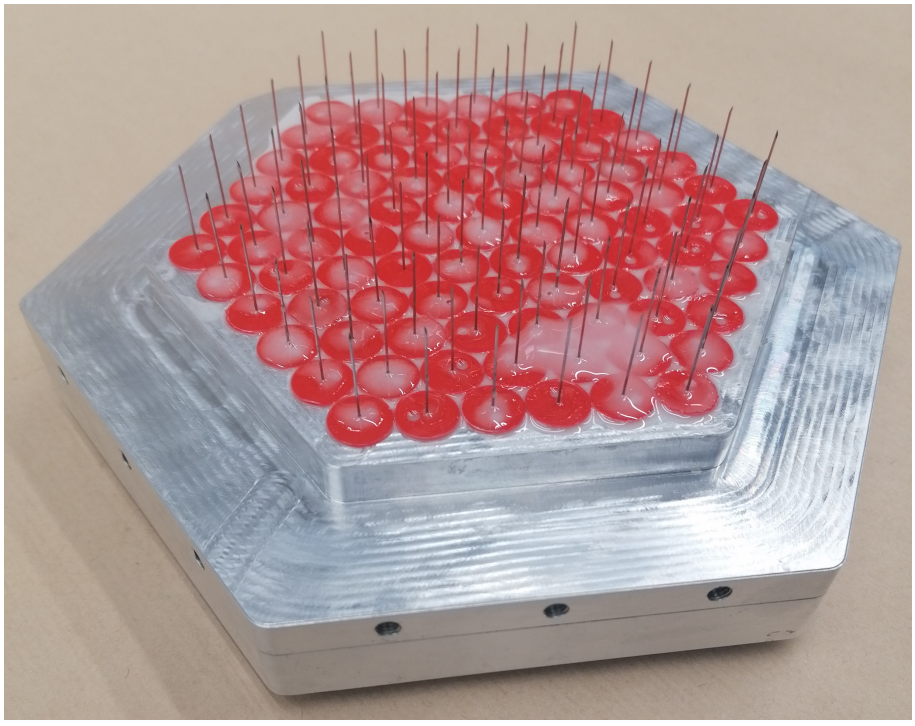

(b) Resin is injected into each hole using a syringe. The needle aligners are then slid down after. The resin is then left to cure on a hot-plate set to a temperature of $T = 38°\text{C}$.

Figure G.10: Assembly before and during casting.

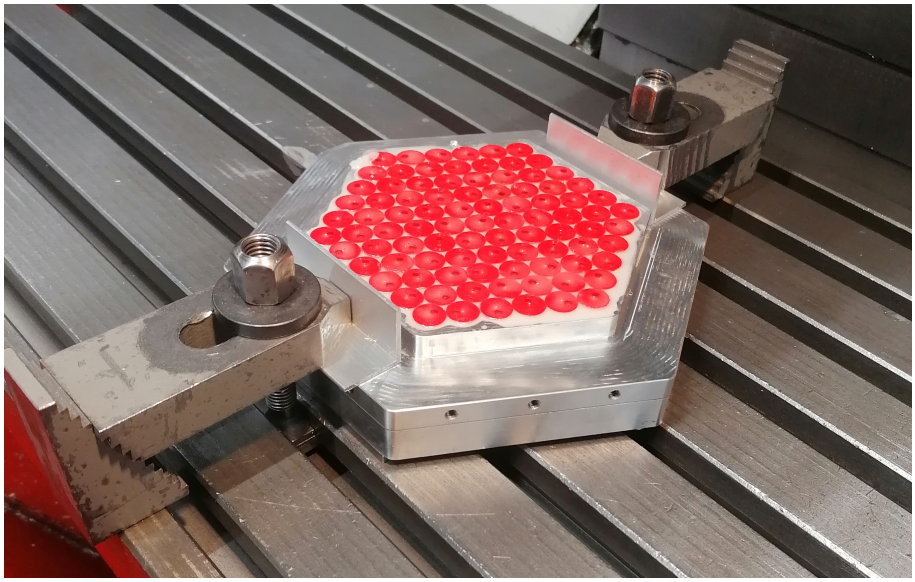

(a) The first machining operation after casting involves removing the top layer of the bearing plate, cast pins and aligners all together. Only then can the two parts be separated.

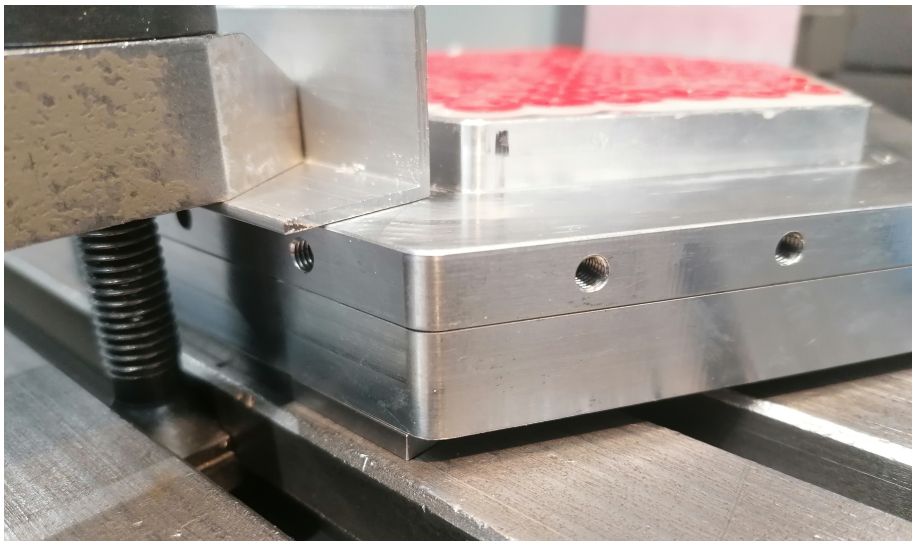

(b) The assembly is supported by parallels, such that it is not resting on the hubs of the needles.

Figure G.11: First machining operation.

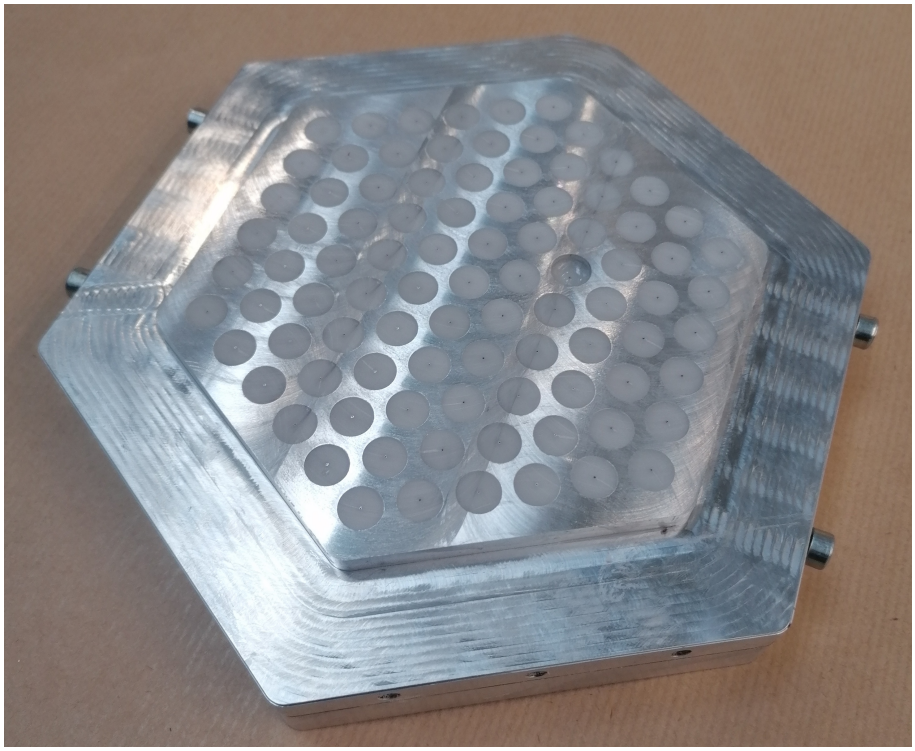

(a) Assembly after first machining step. Socket head cap screws are inserted in order to support the bearing plate when separating the plenum lid from the bearing plate.

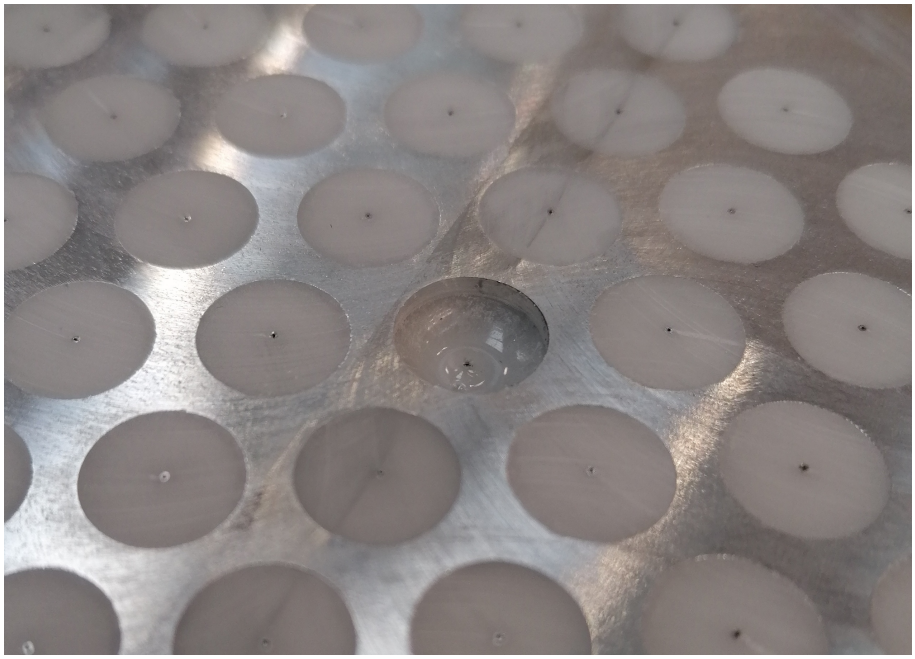

(b) One of the holes was not filled enough. Most likely, an air bubble was trapped during casting the resin.

Figure G.12: Assembly after the first layer of sacrificial material was removed.

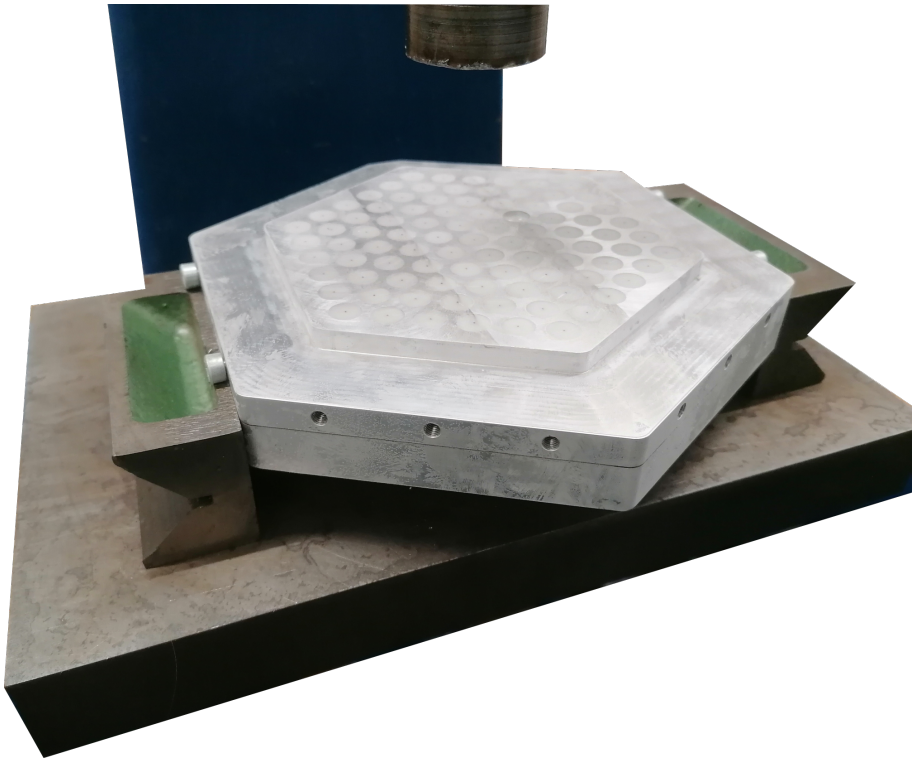

(a) The plenum lid is separated from plenum lid using an arbour press. The sssembly is supported by socket head cap screws, inserted in the tapped holes (M5) in the side of the bearing plate. The frosting is due to the fact that the assembly is refrigerated before separation

.

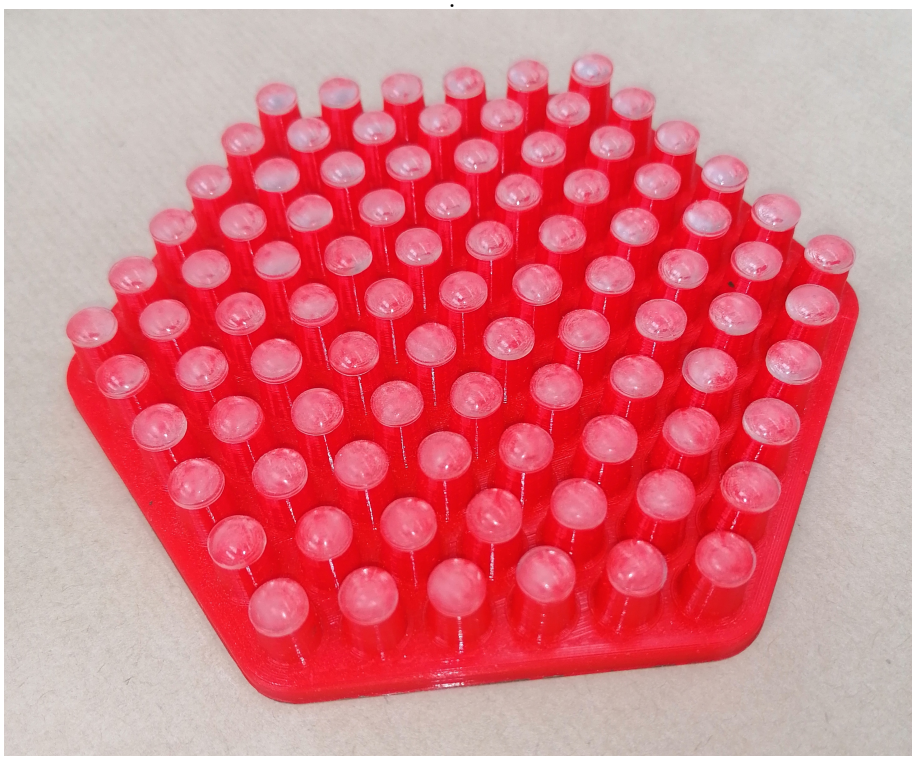

(b) Adapter used to release cast pins from mould.

Figure G.13: Separating the plenum lid from the bearing plate.

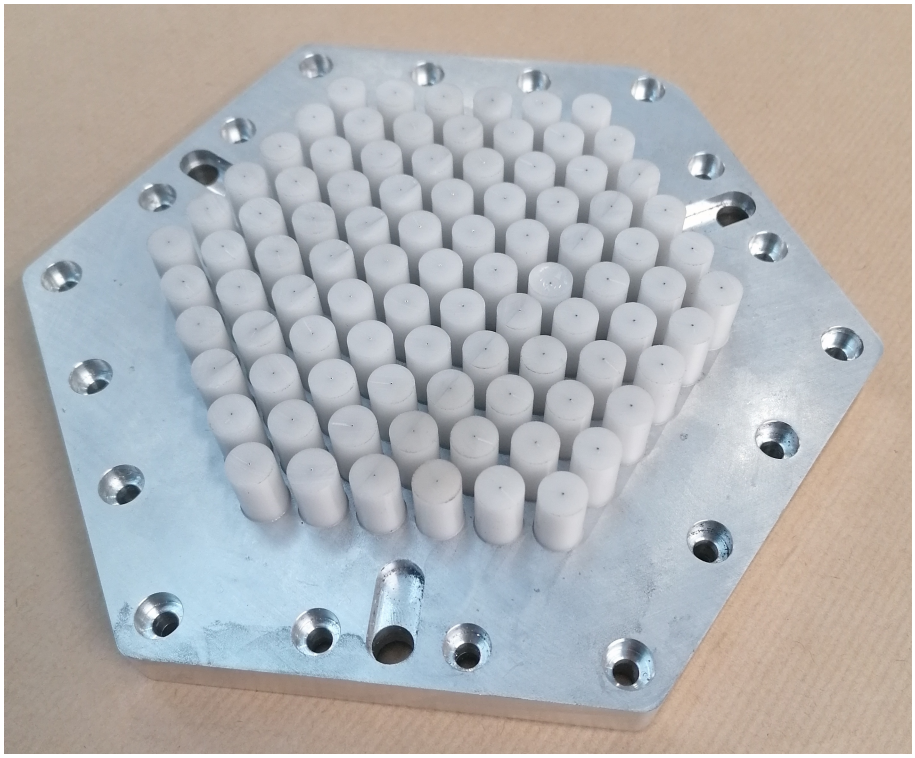

(a) Plenum lid with pins after it has been separated from the bearing plate.

(b) Scratches are still visible in the surface of the pins, however, these will be removed after sanding. Some needles are partly closed due to a burr that is created during the machining operation. This burr is also removed during the sanding process.

Figure G.14: Plenum lid with pins after separating from the bearing plate.

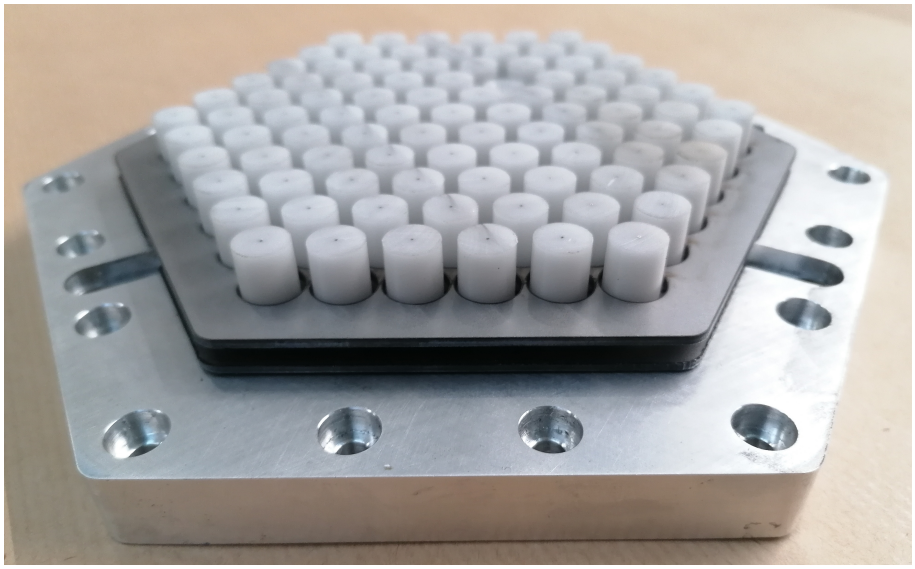

(a) Assembly with two spacer plates ($t = 2 \times 1.5\,\mathrm{mm}$) and 4 mm ball bearings

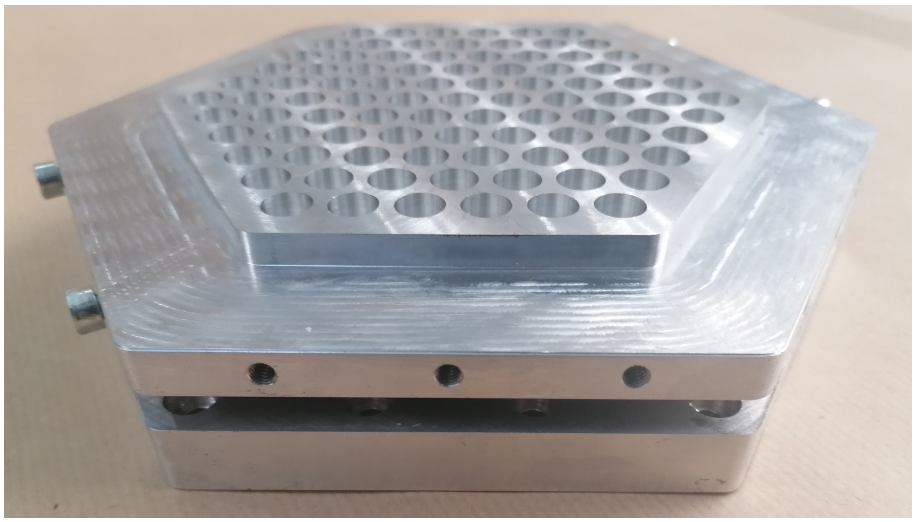

(b) Assembly with the bearing plate added.

Figure G.15: Assembly with the spacer plates, before the second layer of sacrificial material was removed from the bearing plate.

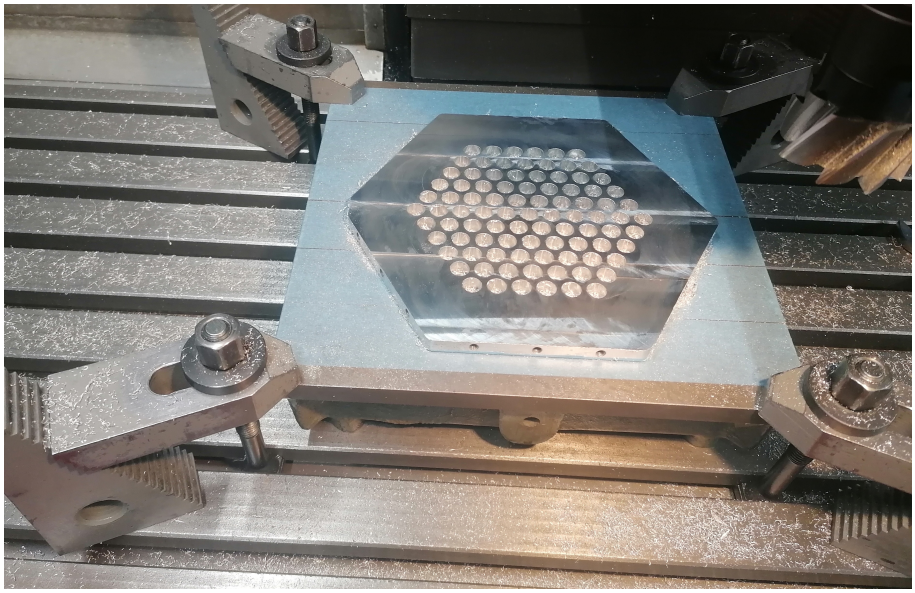

(a) Second machining operation performed on the bearing plate. During machining, the bearing plate is held on a cast iron surface plate, which acts as a flat reference surface. Masking tape is applied both to the surface plate and to the bottom of the bearing plate. They are then glued using Loctite 401.
A dial indicator mounted in the spindle is used to ensure that the surface plate is parallel to the direction of travel (both in x and y direction). By adjusting the toe clamps, the surface plate can be levelled. The holding force is kept as low as possible, to prevent distortion. Very light cuts (0.1 mm per pass) are taken.

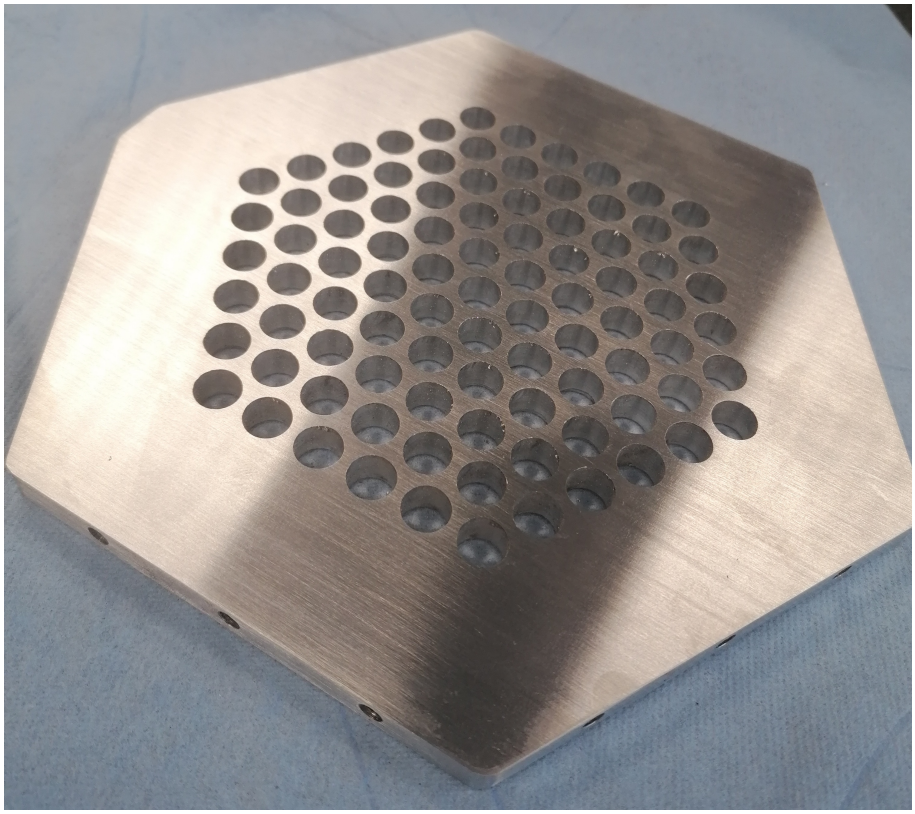

(b) Bearing surface after machining and sanding.

Figure G.16: Second machining operation of the bearing plate.

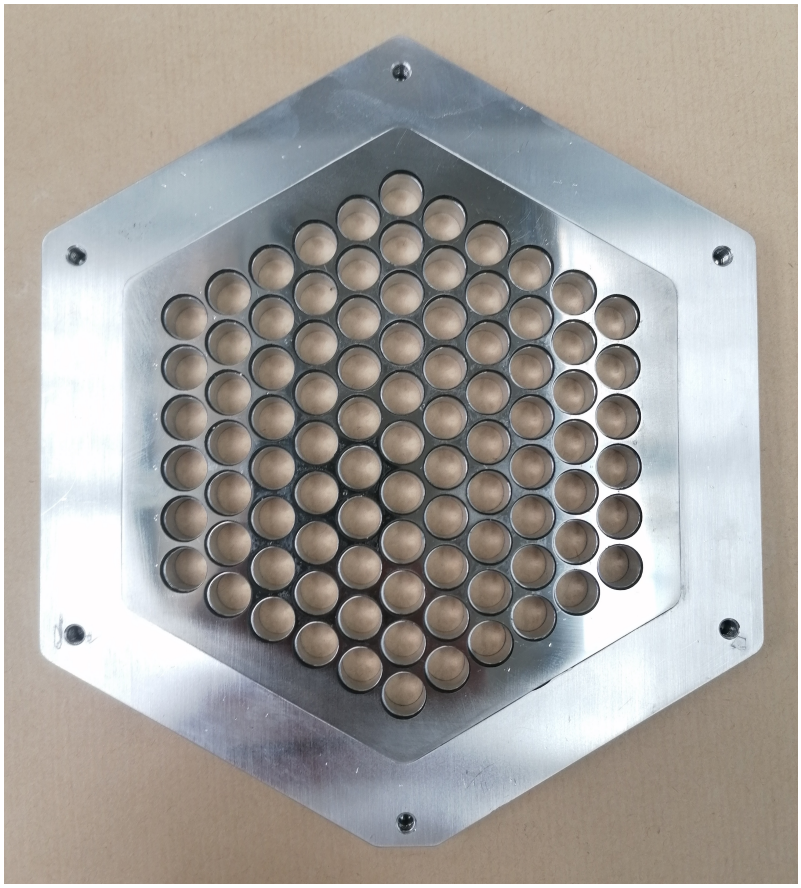

(a) Spacer plate glued to the vacuum side of the bearing plate.

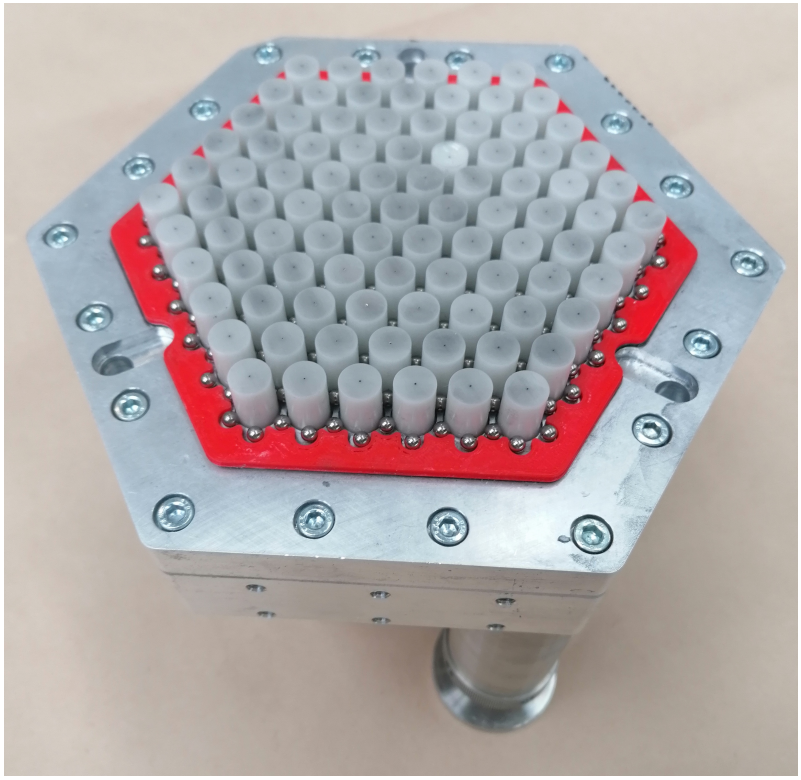

(b) The plenum chamber is sealed by the plenum lid using socket head cap screws (18× M5×25). The outer ring of balls is kept in place using a 3D ball constrainer.

Figure G.17: System partly assembled.

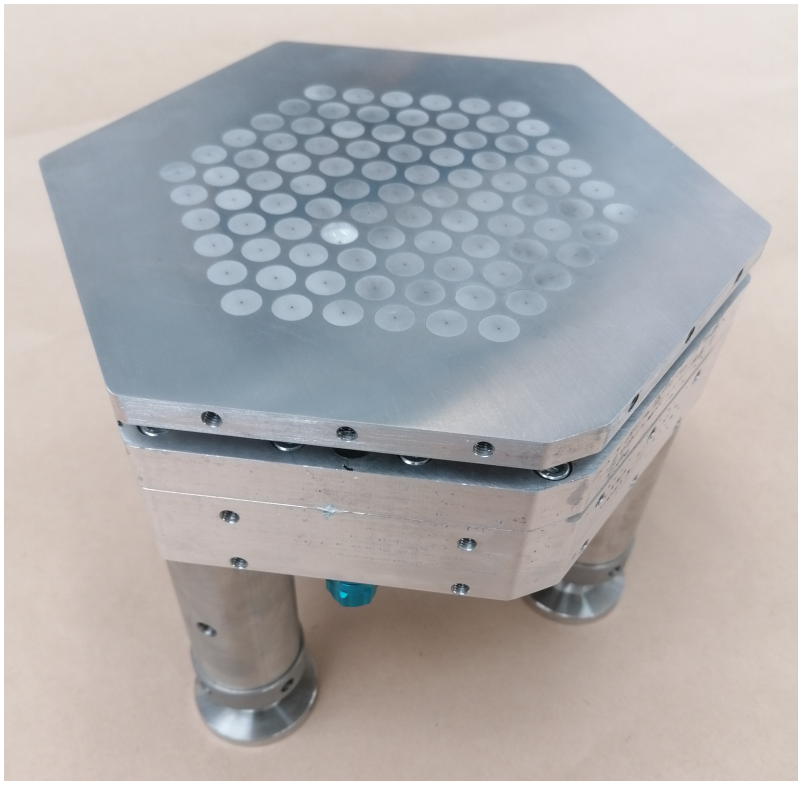

(a) Full system assembled. The bearing plate is suspended on ball bearings.

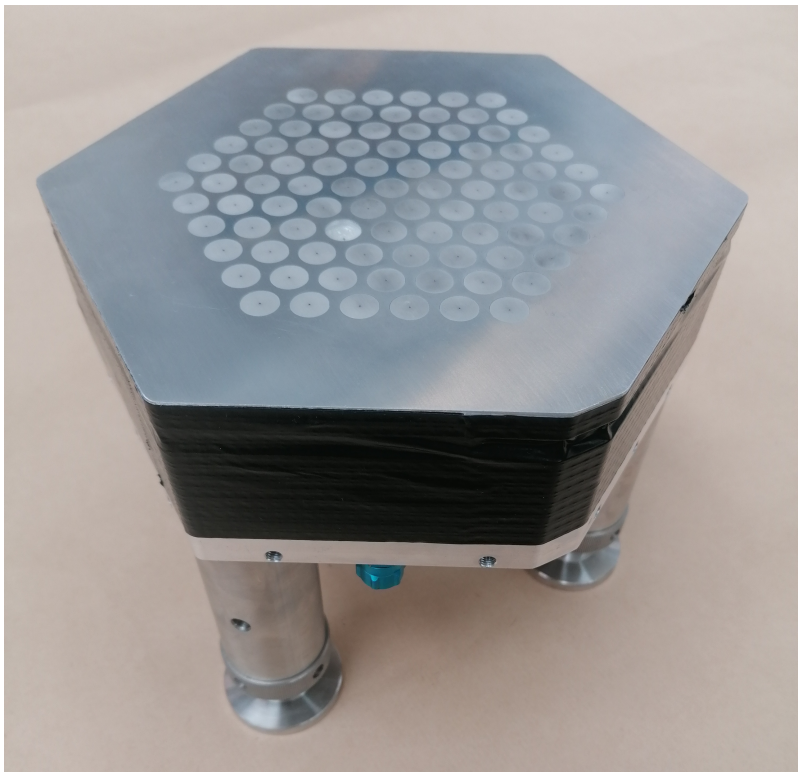

(b) Full system assembled. The space between the bearing plate and the plenum lid is sealed using duct tape, essentially creating the vacuum chamber.

Figure G.18: System fully assembled.

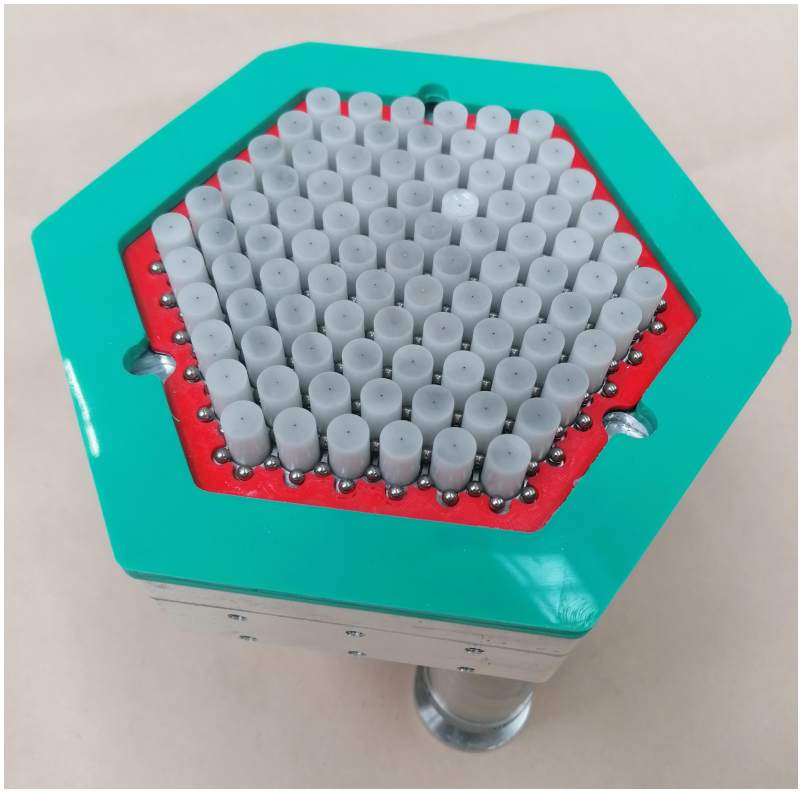

(a) System with silicone vacuum seal, as was originally designed for.

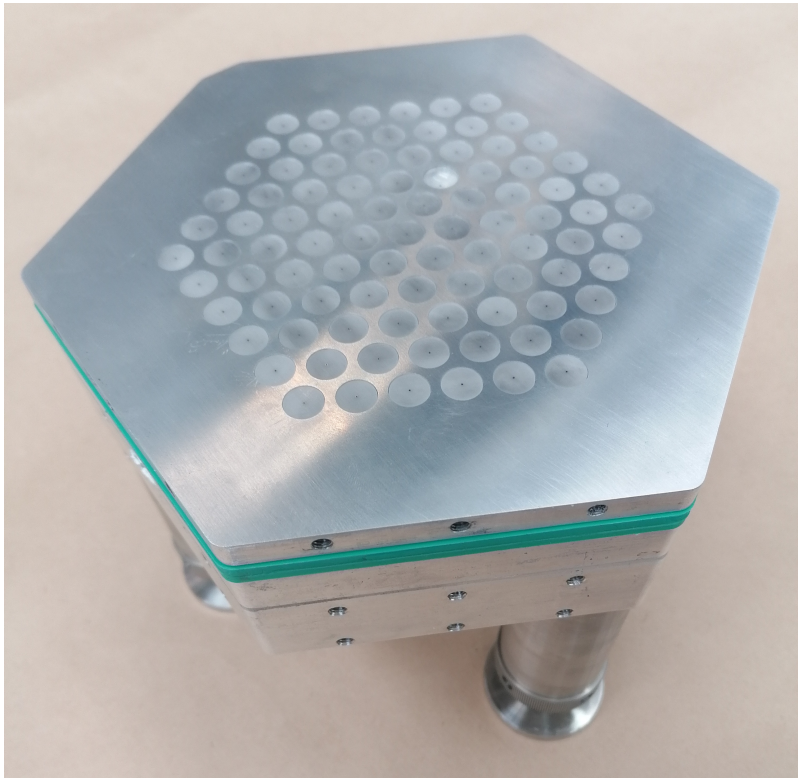

(b) System assembled using silicone vacuum seal. The bearing plate is now supported on the vacuum seal.

Figure G.19: System with a silicone vacuum seal, which has not been used in the end.

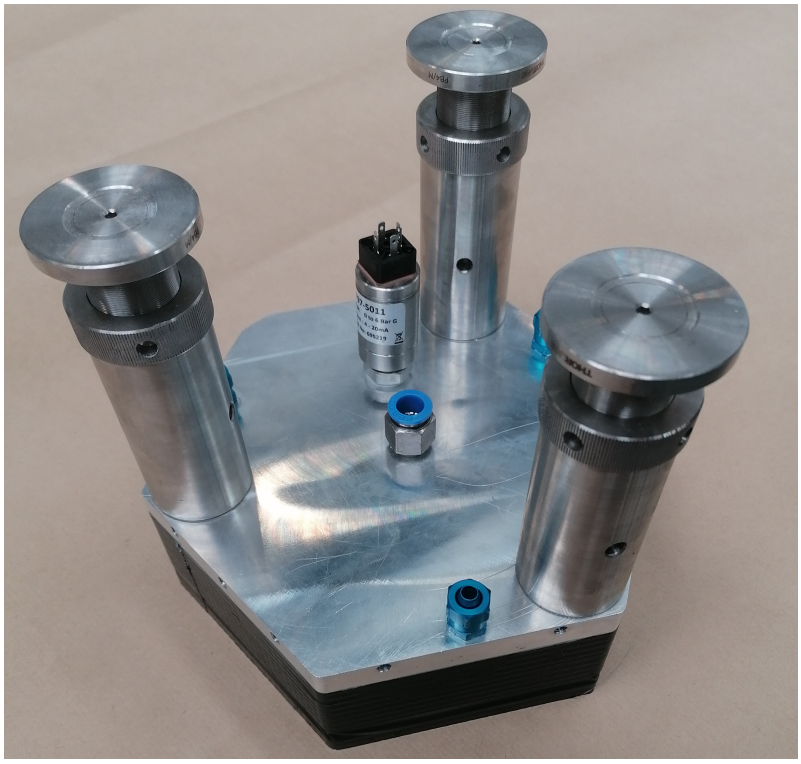

Figure G.20: Assembled system upside down. The pneumatic connector in the centre is used for air supply. The three connectors on the side are used for air evacuation. The sensor can be used to measure the pressure in the plenum chamber.

G.5 Surface inspection

G.5.1 Cast & mould inspection

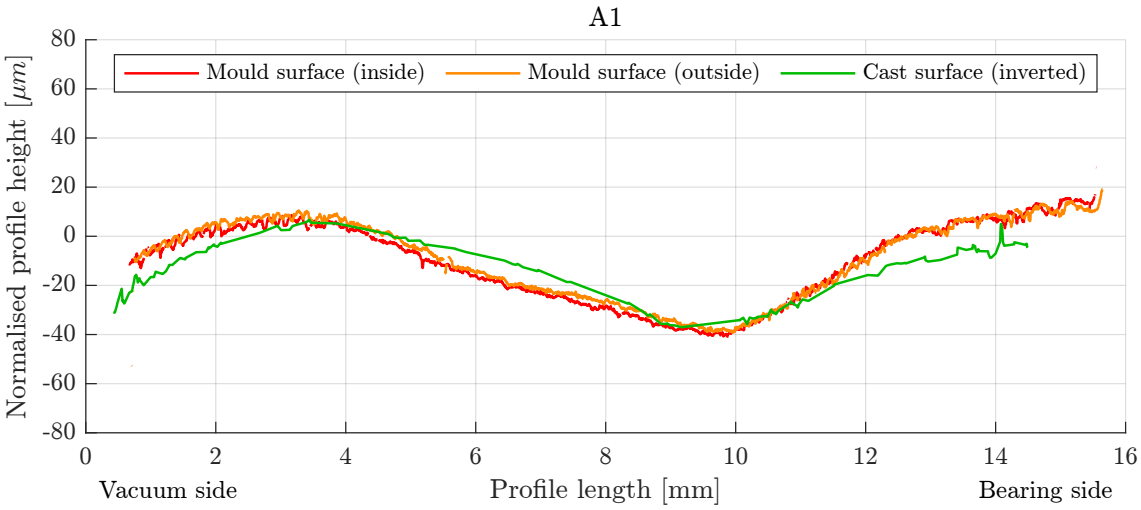

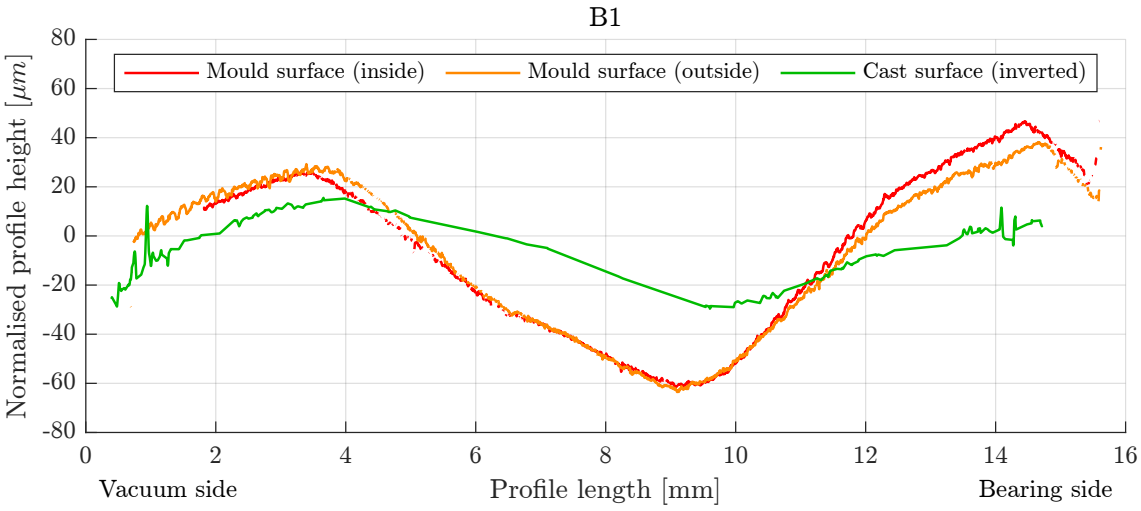

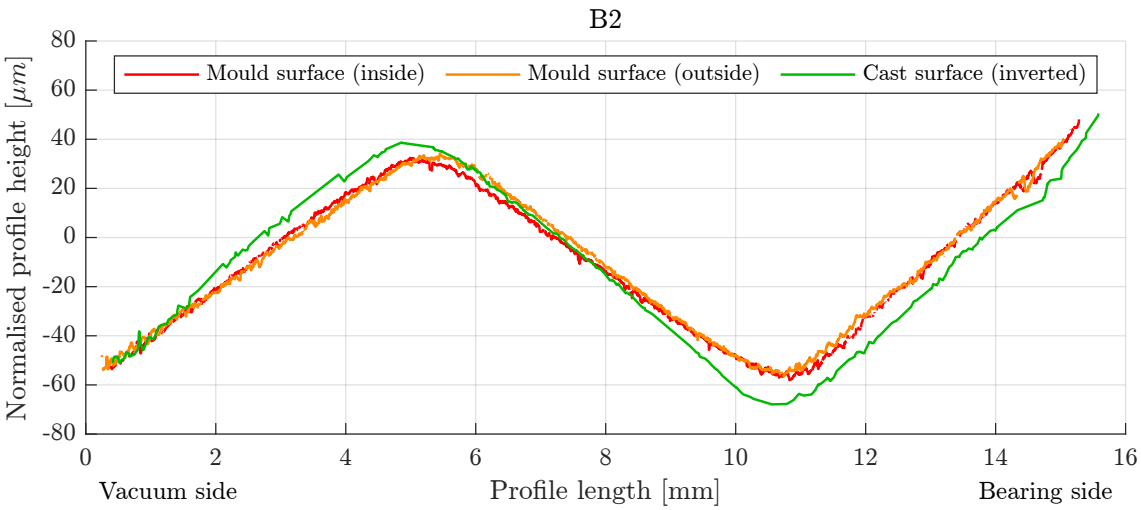

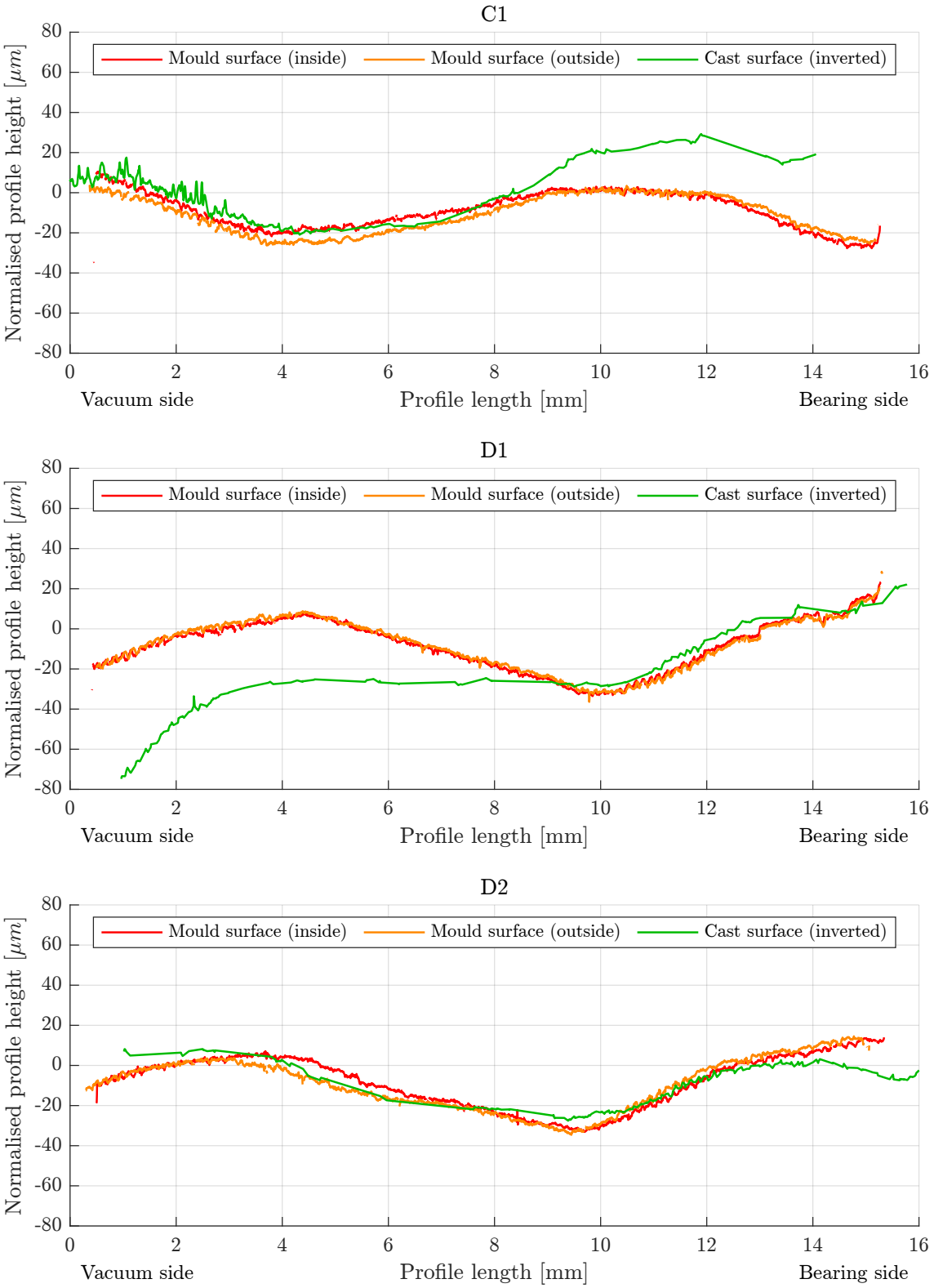
C1
Mould surface (inside)
Mould surface (outside)
Cast surface (inverted)
Normalised profile height [μm]
80
60
40
20
0
-20
-40
-60
-80
0
2
4
6
8
10
12
14
16
Vacuum side
Profile length [mm]
Bearing side
D1
Mould surface (inside)
Mould surface (outside)
Cast surface (inverted)
Normalised profile height [μm]
Vacuum side
Profile length [mm]
Bearing side
D2
Mould surface (inside)
Mould surface (outside)
Cast surface (inverted)
Normalised profile height [μm]
Vacuum side
Profile length [mm]
Bearing side

Figure G.22

G.5.2 Reamer comparison

G.5.3 Machine reamer - spiral flutes

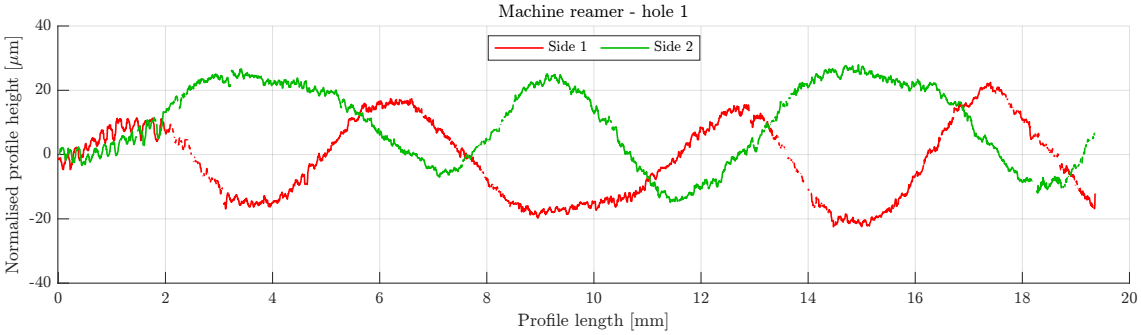

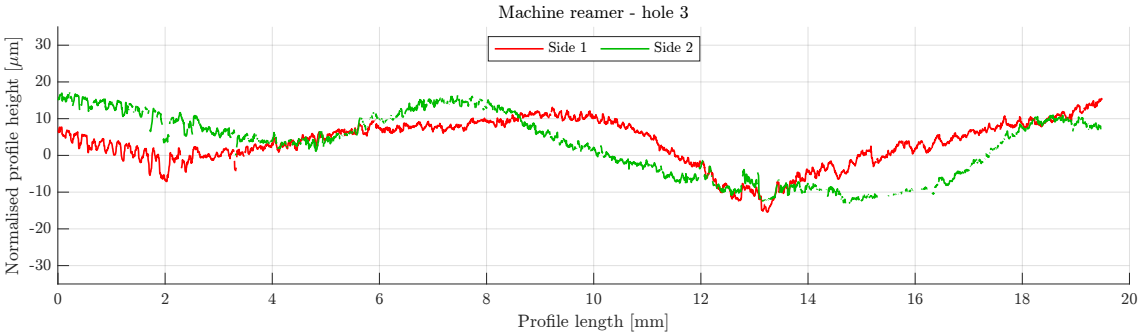

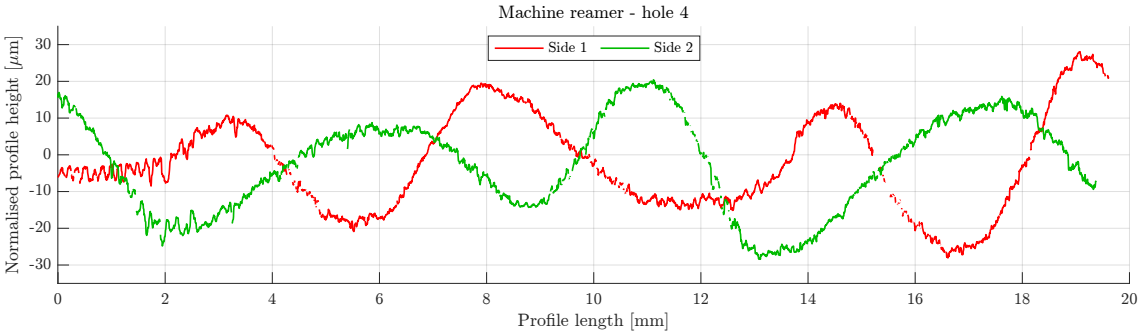

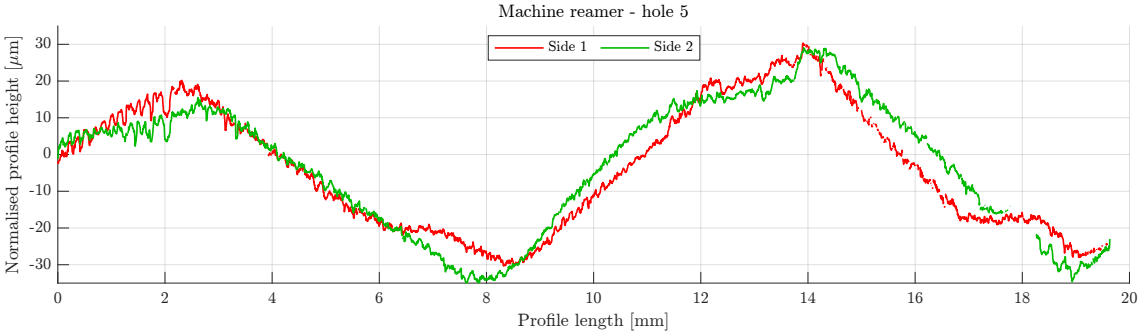

G.5.4 Hand reamer - straight flutes

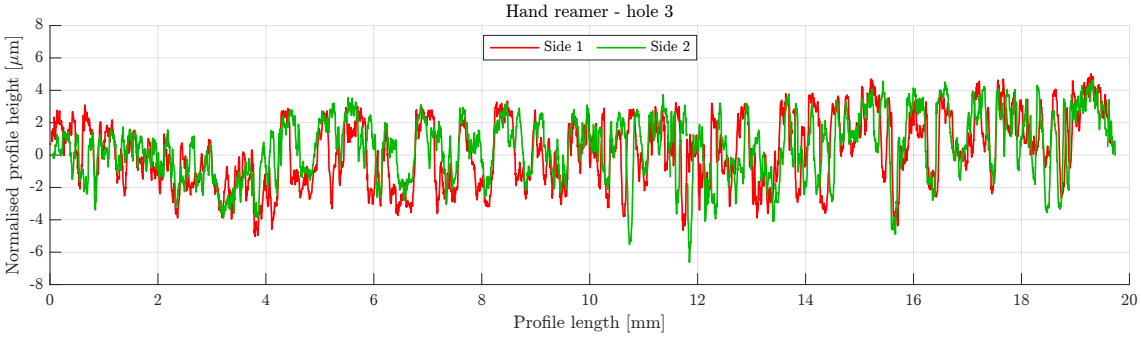


Hand reamer - hole 4
Side 1
Side 2
Normalised profile height [μm]
Profile length [mm]


Hand reamer - hole 5
Side 1
Side 2
Normalised profile height [μm]
Profile length [mm]

G.6 Stroke test data

Data from the stroke test. Each value is averaged over three measurements. The ball diameter is indicated by d_b. The stroke measured by sensor A and B is indicated by S_A and S_B respectively. The relative stroke (i.e. normalised with respect to the theoretical stroke S_t) is indicated by $\bar{S}_\mathrm{A}$ and $\bar{S}_\mathrm{B}$.

Table G.1: Sample 1, $T_\mathrm{cure} = 50°\mathrm{C}$, travel direction parallel with numbered face.

d_b [mm]	S_A $\mu \pm \sigma$ [μm]	S_B $\mu \pm \sigma$ [μm]	S_t [μm]	$\bar{S}_A$ [1]	$\bar{S}_B$ [1]
4	30.0 ± 1.7	22.3 ± 3.1	80	0.38	0.28
5	35.0 ± 0.0	27.7 ± 1.2	100	0.35	0.28
6	46.7 ± 1.5	41.3 ± 0.6	120	0.39	0.34

Table G.2: Sample 1, $T_\mathrm{cure} = 50°\mathrm{C}$, travel direction perpendicular to numbered face.

d_b [mm]	S_A $\mu \pm \sigma$ [μm]	S_B $\mu \pm \sigma$ [μm]	S_t [μm]	$\bar{S}_A$ [1]	$\bar{S}_B$ [1]
4	21.3 ± 2.3	27.7 ± 0.6	80	0.27	0.35
5	23.3 ± 1.5	26.7 ± 1.2	100	0.23	0.27
6	40.3 ± 1.5	41.7 ± 0.6	120	0.34	0.35

Table G.3: Sample 2, $T_\mathrm{cure} = 20°\mathrm{C}$, travel direction parallel with numbered face.

d_b [mm]	S_A $\mu \pm \sigma$ [μm]	S_B $\mu \pm \sigma$ [μm]	S_t [μm]	$\bar{S}_A$ [1]	$\bar{S}_B$ [1]
4	15.3 ± 0.6	24.7 ± 0.6	80	0.19	0.31
5	17.3 ± 1.5	30.7 ± 1.2	100	0.17	0.31
6	26.0 ± 1.7	36.7 ± 1.5	120	0.22	0.31

Table G.4: Sample 2, $T_\mathrm{cure} = 20°\mathrm{C}$, travel direction perpendicular to numbered face.

d_b [mm]	S_A $\mu \pm \sigma$ [μm]	S_B $\mu \pm \sigma$ [μm]	S_t [μm]	$\bar{S}_A$ [1]	$\bar{S}_B$ [1]
4	26.0 ± 0.0	30.3 ± 0.6	80	0.33	0.38
5	21.3 ± 0.6	6.3 ± 1.5	100	0.21	0.06
6	34.3 ± 0.6	48.0 ± 1.0	120	0.29	0.40

Table G.5: Sample 3, $T_\mathrm{cure} = 38°\mathrm{C}$, travel direction parallel with numbered face.

d_b [mm]	S_A $\mu \pm \sigma$ [μm]	S_B $\mu \pm \sigma$ [μm]	S_t [μm]	$\bar{S}_A$ [1]	$\bar{S}_B$ [1]
4	32.7 ± 3.5	43.3 ± 1.5	80	0.41	0.54
5	40.0 ± 1.0	42.0 ± 1.0	100	0.40	0.42
6	53.3 ± 2.1	56.7 ± 1.2	120	0.44	0.47

Table G.6: Sample 3, $T_{\text{cure}} = 38°\text{C}$, travel direction perpendicular to numbered face.

d_{b} [mm]	S_{A} $\mu \pm \sigma$ [μm]	S_{B} $\mu \pm \sigma$ [μm]	S_t [μm]	$\bar{S}_A$ [1]	$\bar{S}_B$ [1]
4	41.0 ± 1.0	34.7 ± 2.1	80	0.51	0.43
5	43.0 ± 2.0	37.0 ± 1.0	100	0.43	0.37
6	54.7 ± 0.6	52.7 ± 0.6	120	0.46	0.44

Table G.7: Sample 4, $T_{\text{cure}} = 20°\text{C}$, travel direction parallel with numbered face.

d_{b} [mm]	S_{A} $\mu \pm \sigma$ [μm]	S_{B} $\mu \pm \sigma$ [μm]	S_t [μm]	$\bar{S}_A$ [1]	$\bar{S}_B$ [1]
4	48.3 ± 1.2	35.3 ± 1.2	80	0.60	0.44
5	59.7 ± 0.6	41.7 ± 1.5	100	0.60	0.42
6	72.7 ± 0.6	41.3 ± 2.1	120	0.61	0.34

Table G.8: Sample 4, $T_{\text{cure}} = 20°\text{C}$, travel direction perpendicular to numbered face.

d_{b} [mm]	S_{A} $\mu \pm \sigma$ [μm]	S_{B} $\mu \pm \sigma$ [μm]	S_t [μm]	$\bar{S}_A$ [1]	$\bar{S}_B$ [1]
4	41.3 ± 0.6	40.3 ± 2.3	80	0.52	0.50
5	52.7 ± 2.3	48.3 ± 1.2	100	0.53	0.48
6	60.0 ± 1.0	55.7 ± 1.5	120	0.50	0.46

Bibliography

[1] Z. Liu, S. E. Sofia, H. S. Laine, M. Woodhouse, S. Wieghold, I. M. Peters, and T. Buonassisi, "Revisiting thin silicon for photovoltaics: A technoeconomic perspective," *Energy and Environmental Science*, vol. 13, no. 1, pp. 12–23, 2020.

[2] Fraunhofer Institute for Solar Energy Systems, "Photovoltaics Report 2020," no. September, 2020.

[3] IEEE, "Internatioal Roadmap for Devices and Systems (2021 Edition)," 2020.

[4] V. Hong Phuc, *Air-based contactless actuation system for thin substrates.* Phd thesis, Delft University of Technology, 2016.

[5] J. Wesselingh, *Contactless positioning using an active air film.* Phd thesis, Delft University of Technology, 2011.

[6] N. Verbruggen, *Air-Based Contactless Positioning of Thin Substrates.* Master thesis, Delft University of Technology, 2017.

[7] R. Jansen, *Actuator System for the Flowerbed.* Master thesis, Delft University of Technology, 2018.

[8] M. E. Krijnen, *Control System Design for a Contactless Actuation System.* Master thesis, Delft University of Technology, 2016.

[9] B. J. Hamrock and S. R. Schmid, *Fundamental of Fluid Film Lubrication.* 1991.

[10] R.P. Hoogeboom, *Design and experimental validation of low stiffness aerostatic thrust bearings.* Master thesis, Delft University of Technology, 2016.

[11] F. Al-Bender, *Air Bearings: Theory, Design and Applications.* Tribology in Practice Series, Wiley, 2021.

[12] W. Brian Rowe, *Hydrostatic, Aerostatic and Hybrid Bearing Design.* Elsevier, first ed., 2012.

[13] F. M. White, *Fluid Mechanics.* McGraw Hill, fourth ed., 2009.

[14] M. J. Moran, H. N. Shapiro, D. D. Boettner, and M. B. Bailey, *Principles of Engineering Thermodynamics.* 8th ed., 2015.

[15] J. Snieder, *Development of an Air-Based Contactless Transport Demonstrator.* Master thesis, Delft University of Technology, 2017.

[16] W. Zhong, X. Li, F. Liu, G. Tao, B. Lu, and T. Kagawa, "Measurement and Correlation of Pressure Drop Characteristics for Air Flow Through Sintered Metal Porous Media," *Transport in Porous Media*, vol. 101, no. 1, pp. 53–67, 2014.

[17] MathWorks Inc., "MATLAB," 2021.

[18] COMSOL Inc., "COMSOL Multiphysics Version 5.6," 2021.

[19] R. Snoeys and F. Al-Bender, "Development of improved externally pressurized gas bearings," *KSME Journal*, vol. 1, no. 1, pp. 81–88, 1987.

[20] C. Hahm, R. Theska, A. Flohr, and O. Hartmann, "Concrete – future material for high precision machines," no. September, pp. 8–12, 2014.

[21] L. W. Morland, "Flow of viscous fluids through a porous deformable matrix," *Surveys in Geophysics*, vol. 13, no. 3, pp. 209–268, 1992.

[22] Z. M. V. Missagia, J. C. dos Santos, L. J. da Silva, T. H. Panzera, J. C. Campos Rubio, and C. Thomas, "Assessment of compacted-cementitious composites as porous restrictors for aerostatic bearings," *Proceedings of the Institution of Mechanical Engineers, Part L: Journal of Materials: Design and Applications*, vol. 234, no. 1, pp. 76–89, 2020.

[23] J. Gaebelein and J. Hribar, "Pushing the envelope of liquid-jet guided laser machining applying modern IR fiber lasers," pp. 1–9, 2019.

[24] G. Singh, A. S. Bhui, Y. Lamichhane, P. Mukhiya, P. Kumar, and B. Thapa, "Machining performance and influence of process parameters on stainless steel 316L using die-sinker EDM with Cu tool," *Materials Today: Proceedings*, vol. 18, pp. 2468–2476, 2019.

[25] R. H. Todd, D. K. Allen, and L. Alting, *Fundamental Principles of Manufacturing Processes*. Industrial Press Inc. New York, 1994.

[26] B. K. Rother, "Micromachining in Exotic Materials," in *Manufacturing Engineering and Materials Handling Engineering*, pp. 549–555, ASMEDC, jan 2004.

[27] M. H. Holmes, *Introduction to Perturbation Methods*. Springer, 2008.

[28] S. Shaw, "Perturbation techniques for nonlinear systems," *Encyclopedia of Vibration*, pp. 1009–1011, 2001.

[29] A. H. Slocum, *Precision Machine Design*. 1992.

[30] F. Al-Bender, "On the modelling of the dynamic characteristics of aerostatic bearing films: From stability analysis to active compensation," *Precision Engineering*, vol. 33, no. 2, pp. 117–126, 2009.

[31] S. H. Song, C. K. Lee, T. J. Kim, I. C. Shin, S. C. Jun, and H. I. Jung, "A rapid and simple fabrication method for 3-dimensional circular microfluidic channel using metal wire removal process," *Microfluidics and Nanofluidics*, vol. 9, no. 2-3, pp. 533–540, 2010.

[32] V. Saggiomo and A. H. Velders, "Simple 3D Printed Scaffold-Removal Method for the Fabrication of Intricate Microfluidic Devices," *Advanced Science*, vol. 2, no. 9, pp. 1–5, 2015.

[33] ASME Standard, "ASME B46.1.2009 - Surface Texture (Surface Roughness, Waviness, and Lay)."

[34] S. Slavov, D. Dimitrov, and M. Konsulova-Bakalova, *Advances in burnishing technology*. Elsevier Inc., 2021.

[35] F. J. Shiou, S. J. Huang, A. J. Shih, J. Zhu, and M. Yoshino, "Fine Surface Finish of a Hardened Stainless Steel Using a New Burnishing Tool," *Procedia Manufacturing*, vol. 10, pp. 208–217, 2017.

[36] C. P. Tan and H. G. Craighead, "Surface engineering and patterning using parylene for biological applications," *Materials*, vol. 3, no. 3, pp. 1803–1832, 2010.

[37] P. Sethu and C. H. Mastrangelo, "Cast epoxy-based microfluidic systems and their application in biotechnology," *Sensors and Actuators, B: Chemical*, vol. 98, no. 2-3, pp. 337–346, 2004.

[38] A. Kinloch, *Adhesion and Adhesives*. Springer, first ed., 1987.

[39] I. Ozsoy, A. Demirkol, A. Mimaroglu, H. Unal, and Z. Demir, "The influence of micro- And nano-filler content on the mechanical properties of epoxy composites," *Strojniski Vestnik/Journal of Mechanical Engineering*, vol. 61, no. 10, pp. 601–609, 2015.

[40] J. de Vreugd, *The Effect of Aging on Moulding Compound Properties*. Phd thesis, Delft University of Technology, 2011.

[41] M. Goosey, *Plastics for Electronics*. Springer Science+Business Media, 1999.

[42] J. Nakka, *Tailoring of Epoxy Material Properties*. Phd thesis, Delft University of Technology, 2010.

[43] Y. He, "Moisture absorption and hygroscopic swelling behavior of an underfill material," *Thermochimica Acta*, vol. 546, pp. 143–152, 2012.

[44] E. S. A. Rashid, H. M. Akil, K. Ariffin, and C. C. Kooi, "The mechanical and thermal properties of alumina filled epoxy," *Proceedings of the IEEE/CPMT International Electronics Manufacturing Technology (IEMT) Symposium*, pp. 282–287, 2006.

[45] C. W. Feng, C. W. Keong, Y. P. Hsueh, Y. Y. Wang, and H. J. Sue, "Modeling of long-term creep behavior of structural epoxy adhesives," *International Journal of Adhesion and Adhesives*, vol. 25, no. 5, pp. 427–436, 2005.

[46] American Society for Testing and Materials, "ASTM D638 Standard Test Method for Tensile Properties of Plastics," *ASTM International*, vol. 82, no. C, pp. 1–15, 2016.

[47] S. Pandini and A. Pegoretti, "Time, Temperature, and Strain Effects on Viscoelastic Poisson's Ratio of Epoxy Resins Stefano," *Society of Plastics Engineers*, pp. 1–10, 2006.

[48] I. Oral, H. Guzel, and G. Ahmetli, "Determining the mechanical properties of epoxy resin (DGEBA) composites by ultrasonic velocity measurement," *Journal of Applied Polymer Science*, vol. 127, no. 3, pp. 1667–1675, 2013.

[49] K. Larson, "Estimating Elastic Modulus from Durometer Hardness for Silicones," *Dow Corning Corporation*, pp. 1–6, 2016.

[50] J. Nisbett and R. D.Budynas, *Shigley's Mechanical Engineering Design*. McGraw Hill, eighth ed.

[51] A. Fritz, *Distributed optical sensor surface concept for planar object detection*. Master thesis, Delft University of Technology, 2021.

[52] K. Johnson, *Contact mechanics*. Cambridge University Press, first ed., 1985.

[53] A. van Beek, *Advanced Engineering Design*. fifth ed., 2012.

Development of a novel manufacturing method for a contactless handling system using a variable outlet restriction

Kees Pijnenburg, Ir. Jelle Snieder, Dr. ir. Ron van Ostayen

April 19th, 2022

Abstract

By using "improved handling methods", the manufacturing cost of solar cells and flat panel display could be decreased. A potential handling method would be to use a contactless handling system based on air bearing technology, where the substrate levitates on a thin film of air. The viscous shear force of the air flow is used to exert a lateral force on the substrate. There are several concepts that can be used to control the magnitude and direction of this lateral force.

In this research, the variable outlet restriction concept is used. The outlet restriction is created by the radial clearance ($\sim 50\,\mu$m) which is formed between a pin in a slightly oversized hole. A novel manufacturing method is developed, where resin casting. This ensures that the fit between the mating parts is guaranteed, regardless of the manufacturing process.

1 Introduction

Solar cells, flat panel displays and silicon wafers are all examples of parts that are thin, fragile and costly. By increasing the size and decreasing the thickness, their cost can be reduced [1, 2]. However, in order to ensure that the manufacturing yield does not decrease, improved handling methods are required [3].

A potential new handling method is contactless handling based on air bearing technology, hereafter referred to as contactless handling. As the name implies, this technology enables the *handling* (i.e. transportation and positioning) of a flat and thin substrate in a *contactless* manner. A thin layer of air ($\sim 10\,\mu$m) is used both to levitate the substrate, as well as to generate a lateral shear force acting on the surface of the substrate. Other physical principles could also be used to achieve contactless handling. An overview is presented in [4, 5].

Contactless handling has multiple advantages over conventional handling methods. First, since there is no physical contact, there is no wear, hence no particle generation. Second, the distributed load allows for the use of thinner substrates without decreasing the product yield. Third, as a result of the fact that the substrate can be carried directly by the air film, a carrier stage is not needed. This reduces the accelerated mass by several orders of magnitude, which in turn leads to lower actuation forces, lower distortion and thus a higher positioning accuracy. Contactless handling using a viscous air film is versatile because of the fact that it does not depend on (electromagnetic) properties of the substrate material.

1.1 State of the art

A schematic representation of a $\varnothing 100\,$mm substrate on a contactless handling system is shown in fig. 1. The substrate is levitating above the bearing surface surface through which a gas (e.g. air) is supplied and evacuated at multiple locations. Most often, a grid of identical unit cells can be identified, where each unit cell has its own supply and evacuation line, referred to as inlet and outlet. The vertical distance between the substrate and the bearing surface is smallest above the dam. The film thickness here is called the fly-height h_f and is typically in the order of $10\,\mu$m. The surface of the pocket is slightly recessed below that of the dam. This distance is referred to as the pocket height h_p, which is also typically in the order of $10\,\mu$m.

In many ways, such a contactless handling system is similar to a vacuum preloaded aerostatic bearing: if properly designed, a substrate will levitate above the bearing surface on a thin film of air, referred to as the *bearing film*. However, in contactless handling, the viscous shear force result-

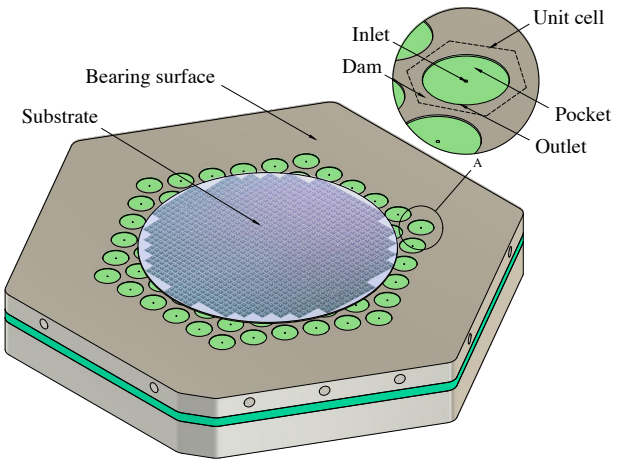

Figure 1: Schematic representation of a contactless handling system.

ing from the flow in the bearing film is used exert a lateral force on the substrate. The lateral forces that can be generated using this method are inherently low (10-100 $\mathrm{N/m^2}$). Though, since the substrates for which these systems are intended have a low distributed weight (20-50 $\mathrm{N/m^2}$), significant accelerations can still be achieved.

In order to control the position of the substrate, the direction and magnitude of the shear force, i.e. the flow, should be controlled over time. The behaviour of the flow is dictated by the geometry of the flow path and the supply and vacuum pressure. If the pressure distribution is symmetric within the unit cell, the shear force is equal and opposite, and thus no net shear force is generated. In general, this is the case in a regular aerostatic bearing, which explains why they are virtually frictionless. In order to generate a net force, an asymmetrical pressure distribution should be created within the unit cell.

We can state that the essence of contactless handling is to be able to control the pressure distribution in the bearing film over time. This can be achieved by either directly controlling the supply and vacuum pressure, or by controlling the geometry of the flow path. Both principles could also be used concurrently. Several demonstrators, using either of these principles, have been developed over the past [4, 5, 6]. These will be discussed in more detail below. First, the lumped restriction model is introduced because it can be used to gain intuitive insight into the qualitative behaviour of contactless handling systems.

1.1.1 Lumped restriction model

A flow restriction can be envisioned as an electrical resistance: like a voltage difference across a resistance will lead to a flow of electrons (i.e. current), a pressure difference across restriction will lead to a flow of air. A restriction in this case is a narrow channel or a thin film.

Using a lumped restriction model, a continuous geometry (i.e. the spatially distributed restriction) can be modelled as a discrete number of restrictions. In general, an inlet, pocket and outlet restriction can be identified.

Note on the figures

Figure 2, fig. 3 and fig. 4 each show a schematic cross-section of a single unit cell, which is part of an infinite grid of identical unit cells. The figures are not to scale: the typical width of a unit cell in x-direction is 10 mm, while the typical fly-height h_f is 10 μm. The the lumped restriction model is shown below the geometry in each figure.

Relevant symbols are indicated in table 1. In all figures, the negative shear stress profile (-τ) is shown, in order to make the figures more intuitive. Each figure shows a different method for generating shear force. In all cases, a net shear force in positive x-direction is exerted on the substrate.

Table 1: Nomenclature for concept comparison.

	Description		Description
R_i	Inlet restriction	p_s	Supply pressure
R_p	Pocket restriction	p_i	Inlet pressure
R_o	Outlet restriction	p_o	Outlet pressure
R_d	Dam restriction	p_v	Vacuum pressure
u	Velocity profile	τ	Shear stress

1.1.2 Pressure control

In this concept, developed by Wesselingh [4] the flow within the pocket is controlled by directly controlling the supply and vacuum pressure. The geometry of the unit cell is fixed, as shown in fig. 2. This means that the direction of the force F is fixed and only the magnitude can be controlled by varying the supply pressure p_s and or the vacuum pressure p_v. In order to achieve actuation in both directions, pairs of unit cells with alternating orientation should be used.

A demonstrator has been developed by Wesselingh, using square cells of $10 \times 10\,\mathrm{mm^2}$, arranged in a grid of 6 by 6. The servo error of this system was $6\,\mathrm{nm}\,(1\sigma)$ in all planar Degrees Of Freedom (DOFs). Acceleration of $600\,\mathrm{mm/s^2}$ has been achieved using a silicon wafer with a thickness of 525 μm. This gives an effective force density of $0.73\,\mathrm{N/m^2}$.

The downside of this concept is that the flow is controlled by valves, which are located far from the bearing surface. The air then has to travel to each inlet and outlet through a complex manifold. Since air is compressible, this introduces a delay in the system. Even for this relatively small demonstrator with an actuator area of $60 \times 60\,\mathrm{mm^2}$, the bandwidth of the system was limited to around 50 Hz. The performance and manufacturability will only decrease further if the size of the system is increased.

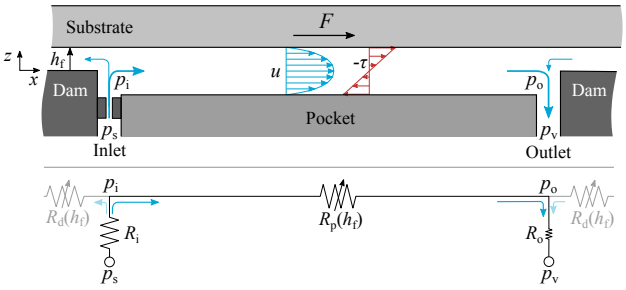

Figure 2: Schematic cross-section of a unit cell using pressure control concept.

1.1.3 Variable pocket restriction

In this concept, developed by Vuong [5], the bearing surface is comprised of separate segments. A net shear force can be generated by tilting the segments, which changes the magnitude of the pocket restriction $R_\mathrm{p}(\alpha)$ left and right.

The variable geometry is schematically shown in fig. 3, where the varying tilting angle is indicated by α.

The demonstrator developed by Vuong was comprised of 61 hexagonal segments that were joined by a leaf spring. The maximum tilt angle was 6 mrad. Using the actuators developed by Jansen [7] and the control system developed by Krijnen [8], an acceleration of $1170\,\mathrm{mm/s^2}$ was achieved using a silicon substrate with a thickness of $750\,\mu\mathrm{m}$. This gives an effective force density of $2.04\,\mathrm{N/m^2}$. The lowest achieved positioning error was $104\,\mathrm{nm}\,(2\sigma)$. For this concept, the bandwidth is no longer limited by the presence of the manifold. A change in tilt angle leads to an instant change of the shear force, at least up to theoretical bandwidth of 1000 Hz. A bandwidth of 300 Hz has been achieved in the experimental set-up [9].

Again, the downside of this concept is in the manufacturing. Each segment is comprised of many parts, which makes the assembly very cumbersome and expensive. Also, this causes the system to degrade over time.

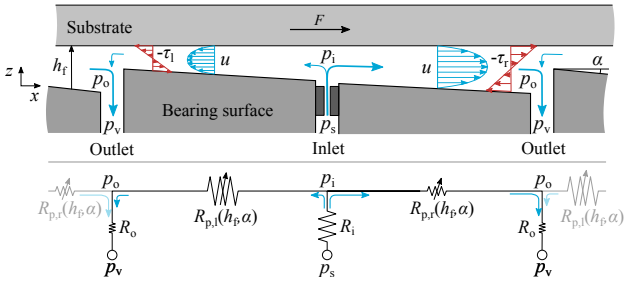

Figure 3: Schematic cross-section of a unit cell using the variable pocket restriction concept.

1.1.4 Variable outlet restriction

Lastly, the flow in the bearing film can be controlled by varying the film thickness in the outlet, i.e. the outlet restriction $R_\mathrm{o}(\varepsilon)$. The variable geometry is shown in fig. 4, where the normalised eccentricity is defined by ε. Since the film thickness is smaller on the left side, the outlet pressure on the left side $p_\mathrm{o,l}$ will be higher than the outlet pressure on the right side $p_\mathrm{o,r}$. The pressure in the bearing film can thus be controlled by controlling the eccentricity of the pocket.

A demonstrator with seven actuator pins was developed by Verbruggen [6], essentially as shown in fig. 7. Each outlet restriction was formed by the radial clearance between a pin ($\varnothing 10.000\,\mathrm{mm}$) and a hole ($\varnothing 10.100\,\mathrm{mm}$). The concentric outlet film thickness is influenced by the size of the pin, the size of the hole, and the relative position of each pin with respect to each hole. No measurements regarding the bandwidth or positioning accuracy were performed.

The demonstrator was manufactured using conventional subtractive manufacturing techniques, i.e. machining. For an increasing number of pins, it becomes increasingly difficult to meet the manufacturing tolerances using conventional subtractive techniques.

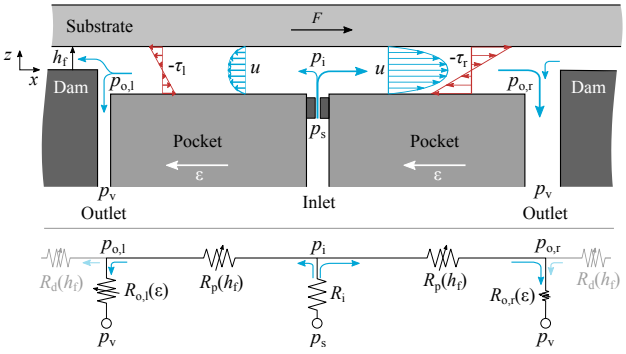

Figure 4: Schematic cross-section of a unit cell using the variable outlet restriction concept

1.2 Concept comparison

The theoretical performance of the different concept can be compared by evaluating their performance ratio P. This is a metric that has been introduced by Vuong, which is defined as [5]:

$$P = \frac{\bar{F}}{\bar{\dot{m}}} \qquad \left[\frac{\mathrm{N/m^2}}{(\mathrm{kg/s})/\mathrm{m^2}}\right] = \left[\frac{\mathrm{m}}{\mathrm{s}}\right] \tag{1}$$

By evaluating the performance ratio for a varying actuator length, the performance curves as shown in fig. 5 are generated. The procedure is described in appendix A.5. The actuator length L decreases along each curve in positive $\bar{\dot{m}}$ direction. The performance of the variable pocket restriction and the variable outlet restriction are virtually identical. Similar results were found by Verbruggen [6].

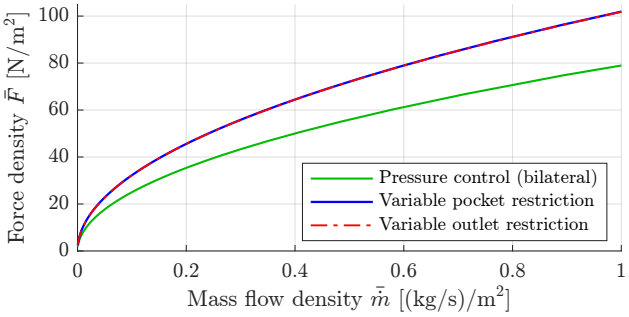

Figure 5: Performance comparison.

1.3 Problem statement

The existing contactless handling systems have shown promising results in the lab, thereby confirming the potential of this technology. The main reason that such systems are not used in the industry yet is the fact that manufacturing them is complicated and thus expensive. This is mainly due to very tight manufacturing tolerances.

1.4 Research objective

The aim of this research is to develop a contactless handling system that can be more easily manufactured than previously developed concepts. A redundancy for manufacturing errors should be created, such that very tight tolerances are no longer required.

The variable pocket restriction and variable outlet restriction have an identical theoretical performance, as shown in fig. 5. A potential improvement in terms of manufacturability is identified for the variable outlet restriction concept, since it essentially consists out of only two mating parts.

1.5 Reader's guide

This paper can be seen as an extended summary of the report. Throughout the paper, references will be made to the appendices, where additional and more extensive information is presented.

In this paper, the conceptual design and numerical model are presented in section 2. The manufacturing procedure is explained in section 3. The results are shown in section 4. Finally, the discussion and conclusion are shown in sections 5 and 6 respectively.

2 Design & modelling

The behaviour of any contactless handling system is to a large extent determined the geometry of the flow path. In general, an inlet, pocket and outlet restriction can be identified within this flow path. In case of the variable outlet restriction concept, the outlet restriction is formed by the clearance between a hole and a pin, as indicated in fig. 6b. The pocket restriction is formed by the thin film between the pocket surface and the substrate, which is not shown in this figure. The inlet restriction is created by a narrow channel in the centre of the pin.

Since the manufacturability of the system has a high priority, the conceptual manufacturing procedure is introduced first, in section 2.1. Here, an ideal case is presented where resin behaviour and manufacturing errors are not considered. However, these will be discussed in section 3.

2.1 Conceptual design

The proposed manufacturing method uses resin casting in order to create a system as shown in fig. 7. Casting methods have been used before to produce counter surfaces for aerostatic bearings [10, 11]. However, it has not been used in the proposed configuration, which requires extremely high dimensional accuracy and stability on the cast parts.

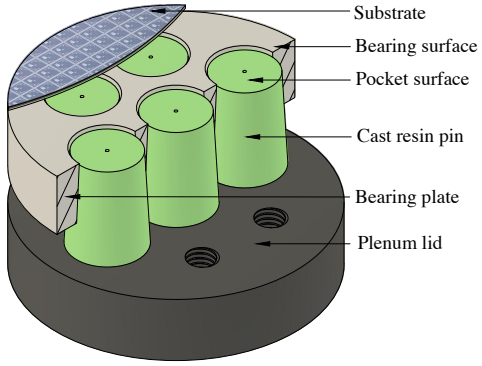

Figure 7: Schematic representation of proposed system.

The pins are created by means of resin casting in a two-part mould, formed by the plenum lid and bearing plate, as shown in fig. 6a. After curing, the two parts will be separated. The pins will be fixed to the plenum lid, as shown in fig. 6b. Since the geometry of the pin will be the exact negative the hole, the fit between the two parts is guaranteed. Next to that, the location of each pins on the plenum lid with respect to the bearing plate will only be determined by the geometry of the bearing plate itself. The tolerance on the position of the holes thus becomes obsolete.

There are two reasons why the holes are tapered. First, the taper helps to release the pins after curing. Second, by enforcing a distance t_v between the two plates after the resin has cured, a thin radial film is created as:

$$h_{o,c} = t_v \tan\delta \cos\delta \approx t_v \, \delta \tag{2}$$

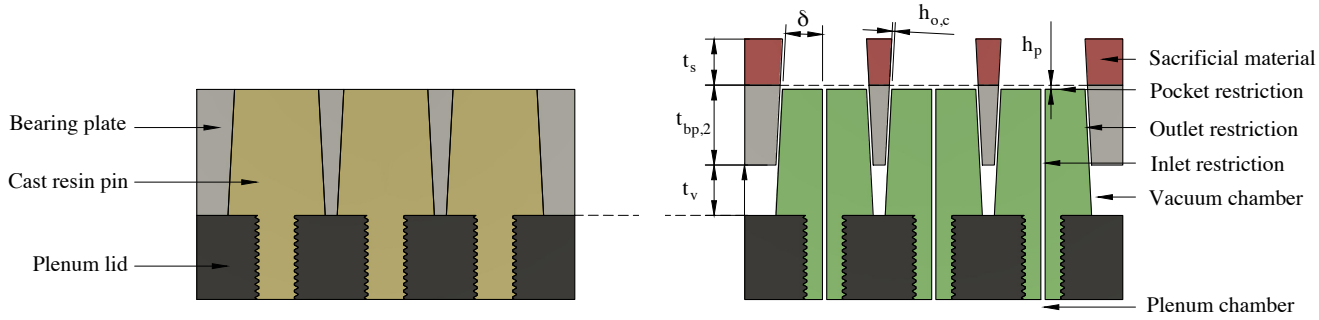

(a) System during casting

(b) System after curing and separating.

Figure 6: Cross section of the system shown in fig. 7.

The cavity that is created between the plates will serve as the vacuum chamber to which all outlet restrictions flow. High pressure air is supplied through the inlet restrictions, which are fed from a central plenum chamber, located below the pins.

In order to create the required pocket height h_p, the sacrificial material t_s is removed from the bearing plate after casting. The height of the pocket is defined as:

$$h_\mathrm{p} = t_\mathrm{v} - t_\mathrm{s} \tag{3}$$

This means that both the thickness of the sacrificial material, as well as the distance enforced between the two plates needs to be controlled with high accuracy.

2.2 Modelling

A numerical model was made in COMSOL, using the *General Form Boundary PDE* physics [12]. The model is used as a tool to find a suitable set of design parameters for the demonstrator. More information regarding the modelling method is presented in appendix C.

2.2.1 Governing equations

The behaviour of a fluid in a thin film is described by the simplified compressible Reynolds equation [13]:

$$\nabla\left(\frac{ph^3}{12\eta R_\mathrm{s} T}\nabla p\right) = 0 \tag{4}$$

Where p is the pressure, h is the local film thickness, η is the dynamic viscosity of the fluid, R_s is the specific gas constant and T the temperature.

The Reynolds equation is used to model both the flow in the bearing film, as well as the flow in the radial outlet film. Only the flow due to a pressure gradient (i.e. Poiseuille flow) is considered. The flow due to relative motion of the substrate (i.e. Couette flow) is neglected. Since the film height is much smaller than the film length, the pressure is assumed constant across the film height (i.e. perpendicular to the surface). A no-slip condition is assumed at all interface surfaces.

2.2.2 Shear force

A net shear force can be generated by establishing an asymmetric pressure distribution in the bearing film. The force density in x-direction $\bar{F}_x$ is found by integrating the shear stress over the total area (eq. 5a). If the gas is assumed to be a Newtonian fluid, the shear stress is directly proportional to the velocity gradient (eq. 5b). The shear force is then found by evaluating the velocity profile at the surface of the substrate, i.e. $z = h$ (eq. 5c).

$$\bar{F}_x = \frac{1}{A}\int_A -\tau_x \, dA \tag{5a}$$

$$= \frac{1}{A}\int_A -\eta\frac{\partial u}{\partial z} \, dA \tag{5b}$$

$$= \frac{1}{A}\int_A -\frac{h}{2}\frac{\partial p}{\partial x} \, dA \tag{5c}$$

Note that the shear force is dependent on the film thickness and the pressure gradient, however these are not independent. An increase in film thickness will drastically decrease the pressure gradient. Minimising the film thickness (i.e. fly-height) is therefore desired.

2.2.3 Stiffness

When in operation, the substrate should levitate at a fixed fly-height. In order for the system to be stable, it should be able to restore this fly-height in case of a disturbance. Note that in a physical system, disturbances will always be present. Stiffness is achieved if the load capacity of the system is dependent on the fly-height.

The load capacity of a system is defined as the integral of all pressures over the area of the substrate A. For a system with a fixed geometry, the pressure distribution in the bearing film $p(x,y)$ is dependent on three operating conditions: the supply pressure p_s, vacuum pressure p_v, and the fly-height h_f. The load-capacity is thus defined as:

$$W = \int_A \Big(p(p_\mathrm{s}, p_\mathrm{v}, h_\mathrm{f}) - p_\mathrm{a} - p_\mathrm{sub}\Big)\, dA \tag{6}$$

Where p_a is the ambient pressure and p_sub is the distributed weight of the substrate. Assuming quasi-static behaviour, levitation is achieved if $W = 0$. This is referred to as the no-load condition.

If the load capacity increases upon a decreasing fly-height and vice versa, a positive stiffness is achieved. This can be written as:

$$k = -\frac{\partial W}{\partial h_\mathrm{f}} > 0 \tag{7}$$

A commonly used method to generate a positive stiffness in the bearing film is through the use of an inlet restriction. This could be a capillary tube, an orifice, or a porous restriction [14]. In this research, capillary tubes are used, since they can be easily integrated in the casting procedure. An inlet restriction introduces positive stiffness, while an outlet restriction introduces negative stiffness. This is explained in more detail in appendix A.3.3. For the system developed in this research, a variable outlet restriction is used to control the flow direction. As a result, the stiffness of the bearing is reduced.

Manual perturbation

From the stationary solution, a perturbation of the fly-height δh_f can be manually prescribed. Since the supply and vacuum pressure are fixed, perturbing the fly-height (i.e. altering the bearing film geometry) will lead to a different pressure distribution and thus a different load capacity. The stationary stiffness k_s (for low frequencies) can be approximated by:

$$k_s = -\frac{\Delta W}{\Delta h_f} = -\frac{W|_{h=h_{f,0}+\delta h_f} - W|_{h=h_{f,0}-\delta h_f}}{2\,\delta h_f} \tag{8}$$

Where $W|_{h=h_{f,0}}$ is the load capacity at the fly-height for which the no-load condition is satisfied (i.e. $W=0$). The perturbation amplitude is defined as $\delta h_f = 0.01 \cdot h_f$.

Perturbed Reynolds equation

For the perturbation method, the stationary film thickness h_0 is replaced by a dynamic film thickness (eq. 9a). Solving the Reynolds equation for this dynamic fly-height will lead to a dynamic pressure distribution (eq. 9b).

$$h(t) = h_0 + \delta h(t), \qquad \delta h = \tilde{h} e^{i\omega t} \tag{9a}$$

$$p(t) = p_0 + \delta p(t), \qquad \delta p = \tilde{p} e^{i\omega t} \tag{9b}$$

Here, h_0 and p_0 represent the stationary solution, $\tilde{h}$ represent the amplitude of the fly-height perturbation and $\tilde{p}(x,y,z)$ represents the perturbed pressure distribution. Substituting eq. (9a) and (9b) in eq. (4) gives the perturbed Reynolds equation as [15]:

$$\begin{aligned} \nabla\left(p_0 h_0^3 \nabla\tilde{p} + 3p_0 h_0^2 \tilde{h} \nabla p_0 + \tilde{p} h_0^3 \nabla p_0\right) = \\ 12\eta i\omega\left(p_0\tilde{h} + \tilde{p} h_0\right) \end{aligned} \tag{10}$$

Where ω represents the perturbation frequency. In order to observe the influence of the perturbation only, the stationary solution (eq. 4) is subtracted. A derivation can be found in appendix F.4. The dynamic stiffness is then defined as:

$$\begin{aligned} k = -\frac{\partial W}{\partial h} \approx -\frac{W_0 - W(t)}{h_0 - h(t)} = -\frac{\int \delta p\, dA}{\delta h} \\ = -\frac{\int_A \mathrm{Re}(\tilde{p})\, dA}{\tilde{h}} \end{aligned} \tag{11}$$

And the damping is defined as:

$$\begin{aligned} c = -\frac{\partial W}{\partial \dot{h}} \approx -\frac{W_0 - W(t)}{\dot{h}_0 - \dot{h}(t)} = -\frac{\int \delta p\, dA}{\delta \dot{h}} \\ = -\frac{\int_A \mathrm{Im}(\tilde{p})\, dA}{\omega\tilde{h}} \end{aligned} \tag{12}$$

2.2.4 Geometry

The final prototype consists of 91 unit cells in hexagonal close packing, as shown in fig. 1. For simplicity, only one unit cell is modelled. The geometry of this unit cell is shown in fig. 8. The dashed line indicates the cross-section shown in fig. 9. The nominal values for the design parameters are shown in table 2. The taper angle δ is equal to $1/100$ rad. Note that the figure is not to scale, and the film thickness has been exaggerated for clarity.

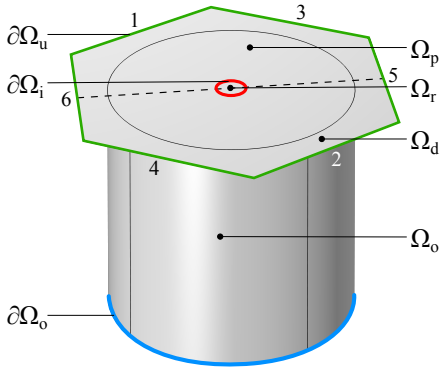

Figure 8: Unit cell geometry as used in COMSOL.

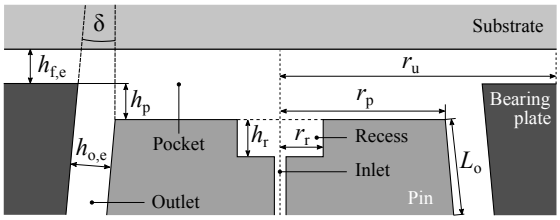

Figure 9: Schematic cross-section of unit cell for $\varepsilon = 0$.

The substrate is not modelled as a separate body, but is implemented through the definition of the film thickness of the top surfaces as shown in table 3. The eccentric outlet film thickness is defined as:

$$h_{o,e}(\varepsilon) = h_{o,c}\,(1 + \varepsilon\cos\varphi) \tag{13}$$

Where ε is the normalised eccentricity, which varies between -1 and 1. The concentric outlet film thickness $h_{o,c}$ has a sinusoidal profile, where φ indicates the local angle in the x,y plane. By definition $h_{o,c} = h_{o,e}|_{(\varepsilon=0)}$.

Table 2: Nominal values for design parameters.

Symbol	Value [mm]	Symbol	Value [μm]
r_r	0.6	h_r	200
r_p	5	h_p	20
r_u	6.25	$h_{f,c}$	15
L_o	10	$h_{o,c}$	50

Table 3: Film thicknesses for stationary study.

Boundary	Section	Expression for h	Value [μm]
Ω_d	Dam	$h_{f,e}$	15
Ω_p	Pocket	$h_{f,e} + h_p$	35
Ω_r	Recess	$h_{f,e} + h_p + h_r$	235
Ω_o	Outlet	$h_{o,e}$	50

2.3 Expected behaviour

The concentric fly-height $h_{f,c}$ and the vacuum pressure p_v are prescribed by the user. The supply pressure p_s for which the no-load condition is satisfied is found using a *Global Equation* in the concentric state.

In the eccentric state, the outlet film thickness will vary locally, while the supply and vacuum pressure remain fixed. Therefore, it is expected that the no-load condition will be satisfied for a different fly-height. This will be referred to as the eccentric fly-height $h_{f,e}$. By definition: $h_{f,c} = h_{f,e}|_{\varepsilon=0}$.

The total magnitude of the outlet restriction decreases in the eccentric state. Since an outlet restriction introduces negative stiffness, it is expected that the total stiffness will increase with the eccentricity.

2.3.1 Stationary boundary conditions

On the inlet edge a flux is defined as:

$$g = G_i \left(p_s^2 - p_i^2\right) \frac{1}{2\pi r_r} \qquad \text{on } \partial\Omega_i \tag{14}$$

Where G_i is the inlet conductivity of the capillary restriction, which is assumed to be independent of the flow through the capillary. In reality, the inlet conductivity is dependent on the flow: the higher the flow through the restriction, the lower the conductivity.

This behaviour could be more accurately modelled, using a Fanno flow model [16], or by implementing the empirical data. In this model, the inlet conductivity was set to $1 \cdot 10^{-15}\,[\mathrm{m^2\,s^3/kg}]$, which is the restriction value that was experimentally found for a pressure drop of 1 bar across the restriction ($\Delta p = p_s - p_i$). This is explained in appendix D.2.1.

On the unit cell edge a periodic continuity is defined. Since the cell is assumed to be part of an infinite grid of unit cells, no net flux should pass the unit cell boundary. In other words, everything that leaves on one side should enter at the opposing side and vice versa. This can be written as:

$$\begin{array}{ccc} p_1 = p_2 & p_3 = p_4 & p_5 = p_6 \\ \nabla p_1 = -\nabla p_2 & \nabla p_4 = -\nabla p_3 & \nabla p_6 = -\nabla p_5 \end{array} \quad \text{on } \partial\Omega_u \tag{15}$$

Where the subscripts refer to the sides of the hexagon, as indicated in fig. 8. In reality, the cells in the centre of the grid will have slightly different boundary condition compared to those on the outside.

On the outlet edge a pressure is prescribed using a Dirichlet boundary condition as:

$$p = p_v \qquad \text{on } \partial\Omega_o \tag{16}$$

The outlet restriction flows into the vacuum chamber, of which the flow restriction is negligible compared to that of the outlet restriction. Hence, a constant vacuum pressure can be assumed. The vacuum pressure p_v was set to 0.7 bar gauge, i.e. 0.3 bar below the ambient pressure p_a of 1 bar.

2.3.2 Perturbed boundary conditions

The perturbation of the fly-height only influences film thickness of the top boundaries. Expressions for the perturbed film thickness $\tilde{h}$ are shown in table 4.

Since the stationary solution is subtracted from the perturbed solution, the stationary boundary conditions are subtracted from the perturbed boundary conditions as well. The perturbed inlet flux can thus be defined as:

$$g = \left(-2\,G_i\,p_0\tilde{p} - \frac{V_r \tilde{p} i\omega}{R_s T}\right) \frac{1}{2\pi r_r} \qquad \text{on } \partial\Omega_i \tag{17}$$

Where V_r represents the volume of the recess ($\pi r_r^2 h_r$). The derivation of this expression is shown in appendix C.3.3.

On the unit cell edge, the boundary condition is essentially identical, except now applied to the perturbed pressure $\tilde{p}$ as:

$$\begin{array}{ccc} \tilde{p}_1 = \tilde{p}_2 & \tilde{p}_3 = \tilde{p}_4 & \tilde{p}_5 = \tilde{p}_6 \\ \nabla\tilde{p}_1 = -\nabla\tilde{p}_2 & \nabla\tilde{p}_4 = -\nabla\tilde{p}_3 & \nabla\tilde{p}_6 = -\nabla\tilde{p}_5 \end{array} \quad \text{on } \partial\Omega_u \tag{18}$$

For the outlet, the perturbed pressure on the outlet is defined as:

$$\tilde{p} = 0 \qquad \text{on } \partial\Omega_o \tag{19}$$

Table 4: Film thicknesses for perturbation study.

Boundary	Section	Expression for $\tilde{h}$
Ω_d	Dam	$0.01 \cdot h_{f,e}$
Ω_p	Pocket	$0.01 \cdot h_{f,e}$
Ω_r	Recess	$0.01 \cdot h_{f,e}$
Ω_o	Outlet	0

3 Manufacturing

3.1 Proposed manufacturing process

The manufacturing method used to manufacture the demonstrator is explained in this section. For more detailed information, the reader is referred to appendix D. Photos of the actual manufacturing process are shown in appendix G.3.

The finished system is shown in fig. 10. Air flows into the plenum chamber through the inlet. From there the air

flows through the dispensing needles into the pockets. The bearing surface would normally be covered by the substrate, which is not shown in the figure. The vacuum chamber is created by the cavity between the bearing plate and the plenum lid. The air is evacuated from the vacuum chamber through three outlets, spaced 120° apart. In order to allow for relative movement of the bearing plate with respect to the pins, the bearing plate is supported on 216 ball bearings placed in between the pins.

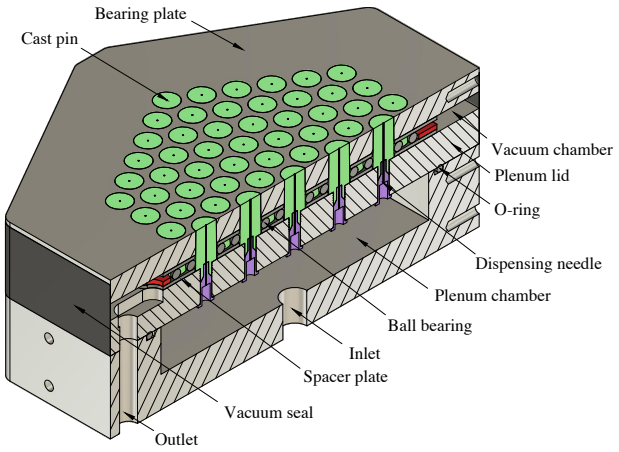

Figure 10: Cross section of the full system.

3.1.1 Machining

The manufacturing process starts by machining the bearing plate ($t_{bp,0} = 20\,\text{mm}$) and plenum lid ($t_{pl,0} = 15\,\text{mm}$). Both were machined from aluminium 7075-T6 on a DMG Mori Milltap 700. The tapered holes in the bearing plate were made using a machine pin reamer[1] with a conicity (i.e. included angle) of 1:50 (i.e. $\delta = 1/100$ rad). In order to reduce the waviness of the surface, each hole was post-reamed using a hand pin reamer[2] with the same conicity.

3.1.2 Casting

A cross-section of the system in the casting set-up is shown in fig. 11. Before casting, both the plenum lid and the bearing plate are thoroughly cleaned using isopropyl alcohol. In order to ensure that the resin will only adhere to the plenum lid, the surface of the bearing plate is covered in a very thin layer of vaseline[3]. The needle hubs are pressed into the holes of the plenum lid, thereby sealing them from the bottom. By clamping the bearing plate and plenum lid together, a two-part mould is created. During casting and curing, temperature of the mould is maintained at $T_c = 38°\text{C}$.

[1] Dormer Pramet D9538.0
[2] Dormer Pramet D9038.0
[3] Kroon White Vaseline

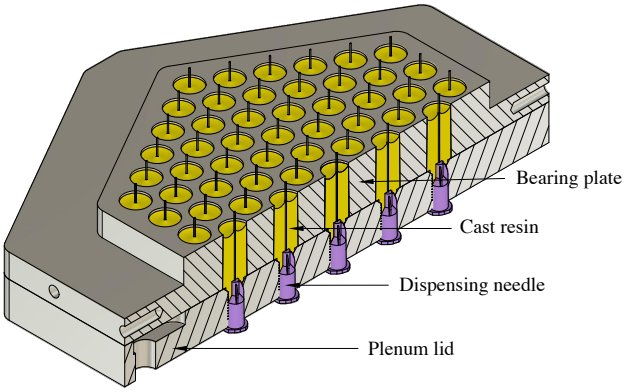

Figure 11: System during casting.

3.1.3 Post-processing

After curing, the first sacrificial layer ($t_{s,1} = 3.5\,\text{mm}$) is removed using a face mill. This is indicated in orange and red in fig. 12. After this step, the situation is essentially as shown fig. 6a.

The two parts can then be separated using a press brake and a 3D printed adapter. Since the pins have a higher Coefficient of Thermal Expansion (CTE) than the bearing plate, cooling the system will cause the pins to shrink more than the bearing plate. Therefore, the system is cooled to $-10°\text{C}$ before separating, in order to ease the separation step.

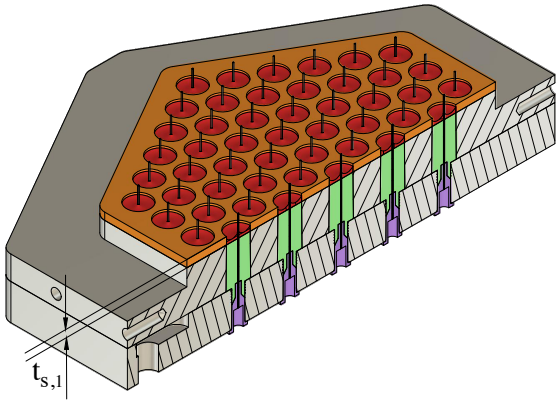

Figure 12: First sacrificial layer indicated.

After separating the parts, the bearing plate is machined to final size, by removing the second layer sacrificial material from the top of the bearing plate ($t_{s,2} = 7.3\,\text{mm}$). This is indicated in orange in fig. 13. The final thickness of the bearing plate $t_{bp,2}$ is 9.2 mm. This is effectively also the length L of the outlet restriction film.

$$t_{bp,2} = t_{bp,0} - t_{s,1} - t_{s,2} \tag{20}$$

In order to increase the nominal outlet film thickness and in order to improve the contact (steel on steel), two spacer plates (S235 steel, lasercut, $t_{sp} = 1.5\,\text{mm}$) have been placed

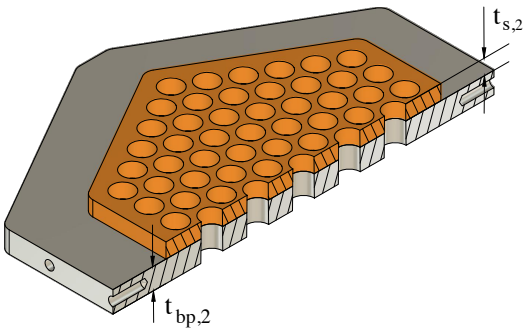

Figure 13: Bearing plate before second post-casting machining operation.

between the plates as shown in fig. 14. The final height of the vacuum chamber t_v can thus be defined as:

$$t_v = 2 \cdot t_{sp} + d_b \tag{21}$$

If the system is assembled using undersized balls ($d_{b^-} = 3.974\,\text{mm}$), the pins are slightly protruding from the surface. The whole assembly is then abraded on a flat granite reference surface until the pin surfaces are flush with the top surface of the bearing plate. The system is then assembled using the slightly larger balls ($d_{b+} = 3.993\,\text{mm}$). The pocket height h_p will then be equal to the difference in ball diameter $\Delta d = 19\,\mu\text{m}$.

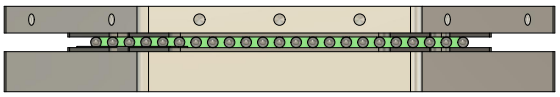

Figure 14: Side view of the system with spacer plates.

3.2 Inlet restriction

A capillary inlet restriction is created by using dispensing needles[4]. They are affordable, yet have a very well defined diameter and thus a predictable restriction value. Next to that, they are very suited to be implemented in the casting process, in contrast to orifice or porous restrictions.

The needles were aligned in the centre of the tapered holes using 3D printed adapters. The misalignment from the centre using this method was verified using a digital microscope[5] to be $73 \pm 30\,\mu\text{m}$. More information regarding the inlet restriction can be found in appendix D.2.

3.3 Outlet restriction

In this research, the main mechanism used to create a thin outlet film is conical spacing as shown in eq. (2). Despite the fact that the current manufacturing method should be relatively insensitive for manufacturing errors, there are still various factors that influence the final geometry of the system. The main factors are:

I. Mould geometry (appendix D.3)
   - ○ Deviation from perpendicularity
   - ○ Surface waviness
   - ○ Mould release agent layer thickness

II. Resin behaviour (appendix D.4)
   - ○ Thermal expansion
   - ○ Hygroscopic swelling
   - ○ Cure shrinkage
   - ○ Polymer creep

3.3.1 Mould geometry

The geometry of the mould will determine the geometry of the cast pins. Due to the design, the geometry of the mould is relatively insensitive for manufacturing errors. However, there are still three factors that will influence the final outlet film thickness.

Deviation from perpendicularity of the hole with respect the surface of the bearing plate, will cause the pins to also be non-perpendicular to that surface. The radial outlet film thickness then becomes asymmetric if the pin is concentric.

The theoretical stroke is defined as twice the concentric outlet film thickness. For a single pin, the stroke will become asymmetric for a misoriented hole, but it will not be reduced in total magnitude. However, for an increasing number of pins, the stroke of the full system in each direction will be bounded by most misoriented pin in that direction. No effective method to measure the misorientation of the holes has been found during this research.

Surface waviness of hole will be transferred to the surface of the cast pin. If the bearing plate is then shifted with respect to the casting arrangement, local variations in the outlet film thickness are created. The waviness of the pin surface was measured using a white light interferometer[6]. It is expected that the variations in film thickness due to the waviness are approximately $\pm 5\,\mu\text{m}$.

A mould release agent is used to ensure that the resin will not adhere to the bearing plate. This effectively changes the mould geometry. In this research, vaseline is used. Since the vaseline is removed from the mould surface after the resin has cured it will effectively increase the outlet film thickness. The thickness of the mould release agent has not been measured in this research.

3.3.2 Resin behaviour

The behaviour of the resin is to a large extent determined by the type of resin and the filler fraction. The resin used

[4] Miraject Luer 17/42
[5] Keyence VHX-6000
[6] Bruker Contour GT-K1

Table 5: First order approximation of influence on outlet filmthickness.

		Relevant parameters			
Mechanism	Expression for Δr	Symbol	Value	Unit	Expected effect on $h_{o,c}$ [μm]
Thermal expansion	$r\Delta\alpha\Delta T$	$\Delta\alpha$	58	ppm/K	$+3$
		ΔT	18	K	
Hygroscopic swelling	$r\beta_c\Delta$RH	β_c	1	%/(%RH)	-20 ± 5
		ΔRH	10	%	
Cure shrinkage	$r(\gamma_c/3)$	γ_c	3	%	$+50$

in this research is a bisphenol A/F type epoxy[7], in combination with an amine hardener[8]. In order to improve the mechanical properties of the resin, filler materials in the form of powders or fibres can be added. In this research, 10 wt% aluminium oxide powder[9] (Al_2O_3, D50 < 3.5 μm) is added.

The main mechanisms that influence the geometry of the cast pins are thermal expansion, hygroscopic swelling and cure shrinkage. The significance of these mechanisms decreases with an increasing filler ratio. This is due to the fact that the CTE of commonly used filler materials is much lower than that of the resin. Also, a filler material does not shrink during curing, nor does it absorb any moisture. A first order estimation of the influence of each mechanism on the radial outlet film thickness is shown in table 5.

Thermal expansion refers to the phenomena that a material will change its shape upon a change in temperature. The mould material (aluminium) has a lower CTE than the cast material (epoxy). This means that if the temperature during casting T_c differs from the temperature in operation T_o, the outlet film thickness will change.

The difference in radius Δr between the external radius of the pin and the internal radius of the hole can be written as:

$$\Delta r = r\Delta\alpha\Delta T \tag{22}$$

Where $\Delta\alpha$ represents the difference in CTE between the pin material and the mould material. ΔT represents the difference between the temperature during curing and in operation, i.e. $T_c - T_o$.

Hygroscopic swelling is the expansion of a material due to the absorption of moisture. The bearing plate is not susceptible to swelling, while the pins will expand due to swelling. This process will therefore decrease the radial outlet film thickness. Swelling is a reversible process, which means that the material can absorb and desorb moisture [17].

[7] Resion EP101
[8] Resion EP115
[9] Aluminium oxide powder

The difference in radius can then be written as [18]:

$$\Delta r = r\beta_c\Delta\text{RH} \tag{23}$$

Where β_c represents the linear Coefficient of Moisture Expansion (CME) of the composite material and ΔRH refers to the change in relative humidity.

Cure shrinkage refers to the phenomena that a thermosetting resin, such as an epoxy will undergo an increase in density and thus a decrease in volume during the polymerization reaction. This is due to the cross-links that are formed between the monomer chains. The linear cure induced shrinkage can be written as:

$$\Delta r = r\frac{\gamma_c}{3} \tag{24}$$

Where γ_c is the linear coefficient of cure shrinkage of the composite material. For unfilled epoxy, γ is typically 2-4%. The first 40-60% of the curing reaction occurs when the resin is still in the liquid state, and therefore does cause any shrinkage of the cast feature [18]. The epoxy used in this research cures very slowly, and thus stays in the liquid state longer. Therefore, the effective linear coefficient of cure shrinkage is taken as $\gamma_c/3$.

4 Results

The demonstrator did not perform as intended, due to a combination of reasons as presented in section 3.3. Hence, no experimental data can be presented to validate the numerical results. The results section therefore contains only results from the numerical analysis.

4.1 3D pressure distribution

The 3D pressure distribution is shown in fig. 15. Because of the asymmetric pressure distribution for $\varepsilon = 0.9$, a net shear force is generated in positive x-direction. Note that the pressure profiles on each of the opposing edges of the unit cell are identical.

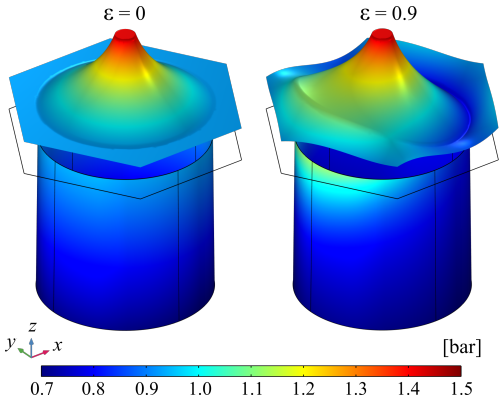

Figure 15: Three dimensional pressure distribution.

4.2 Dynamic behaviour

The dynamic behaviour of the system is shown in fig. 16. Since the magnitude of the outlet restriction decreases for the eccentric case, the stiffness $\bar{k}$ increases, while the damping $\bar{c}$ decreases. The cross-over point is around 10^4 Hz. The stiffness and damping are both positive for low frequencies, which means that the system is stable.

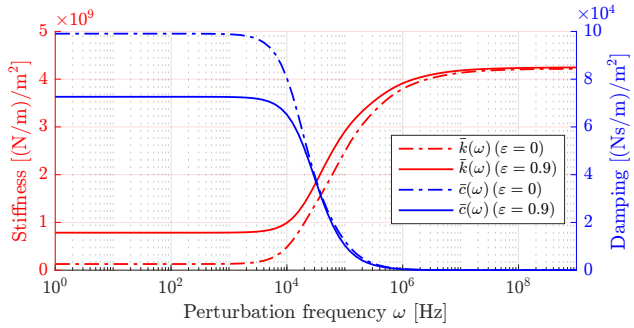

Figure 16: Dynamic behaviour of the system.

4.3 Performance

The force density for a varying mass flow density is shown in fig. 17. This plot was created by varying the vacuum pressure from $p_v = 1$ to 0.5 bar for $\varepsilon = 0.9$. The nominal operating point is indicated. The theoretical force density $\bar{F}$ is 19.5 N/m^2 for a vacuum pressure of 0.7 bar. For a silicon substrate (e.g. solar cell) with a thickness of 200 μm, the distributed weight is approximately 5 N/m^2. That means an acceleration of 4 m/s^2 could be achieved.

Table 6: Normalisation parameters.

Parameter	Value	Unit
$\bar{k}_{max}$	$78.5 \cdot 10^7$	$(N/m)/m^2$
$\bar{c}_{max}$	$99.1 \cdot 10^3$	$(Ns/m)/m^2$
P_{max}	66.0	m/s
$h_{f,c}$	15.0	μm

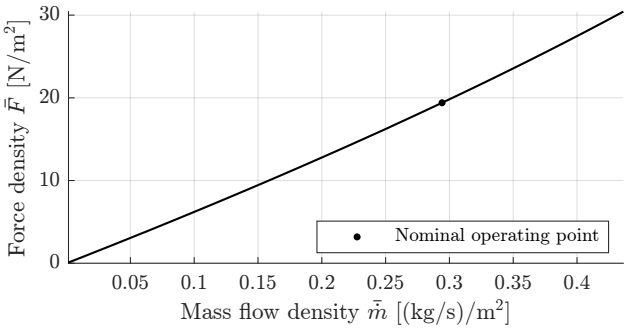

Figure 17: Force density as a function of the mass flow.

Relevant performance parameters for varying eccentricity are shown in fig. 18. They are normalised as:

$$\kappa = \frac{\bar{k}}{\bar{k}_{max}} \qquad \zeta = \frac{\bar{c}}{\bar{c}_{max}} \qquad \Pi = \frac{P}{P_{max}} \qquad H = \frac{h_{f,e}}{h_{f,c}}$$

Where the maximum value for each parameter can be found in table 6.

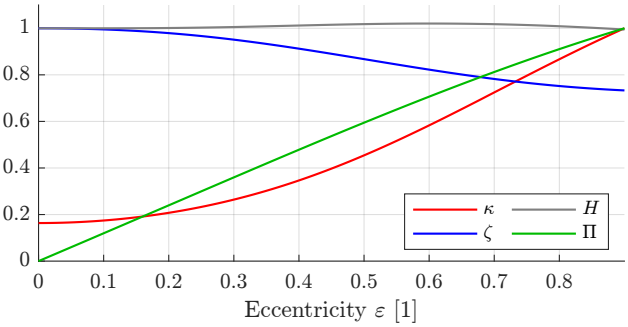

Figure 18: Relevant system parameters as a function of eccentricity.

4.4 Constant fly-height

From fig. 18, it can be seen that the normalised eccentric fly-height H is relatively constant. However, this is in general not the case. This is illustrated by analysing the system for three different values for the pocket height h_p as shown in fig. 19. Apart from a varying pocket height, the nominal design parameters as shown in table 2 are used.

For a pocket height of 17 μm, the fly-height increases with increasing eccentricity. This causes the magnitude of the pocket restriction to decrease and thus the mass flow increases. For a pocket height of 25 μm, the opposite behaviour is observed. The eccentric fly-height decreases and so does the mass flow. For a fly-height of 21 μm, the fly-height is relatively constant. Therefore, the mass flow is also relatively constant, which is desirable in an experimental set-up.

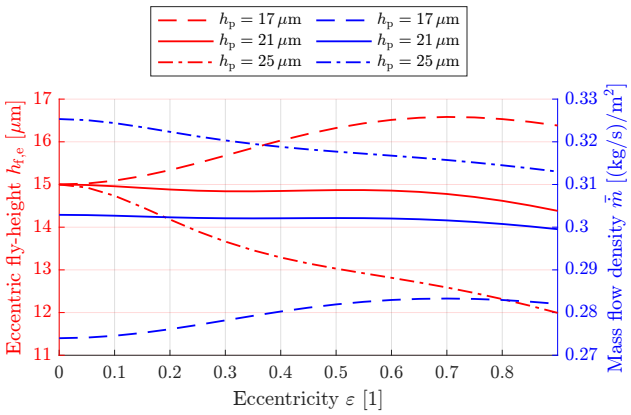

Figure 19: Eccentric fly-height and mass flow as a function of eccentricity.

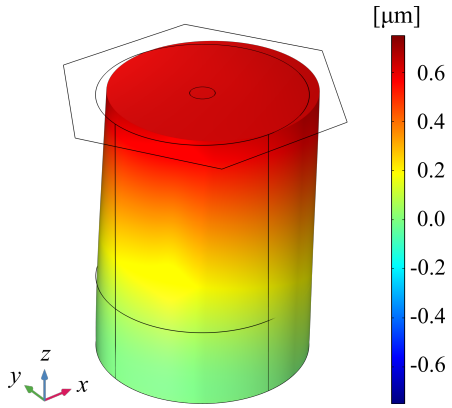

Figure 20: Pin deformation in x-direction.

4.5 Asymmetric pressure distribution

For the eccentric case, there exists an asymmetric pressure distribution in the outlet film, as shown in fig. 15. This means that in the quasi-static, frictionless case, an actuation force F_{act} of 0.67 N per unit cell is required to create an eccentricity of $\varepsilon = 0.9$. The friction of the bearing between plenum lid and bearing plate is not considered in this case.

The resulting deformation of the pin due to this pressure distribution is shown in fig. 20. This has little effect on the performance of the system as is shown in appendix C.7.

5 Discussion

5.1 Numerical model

The Reynolds equation is commonly used to describe the behaviour of aerostatic bearings and contactless handling systems. Therefore, it is assumed that the numerical model used in this research predicts the behaviour of the system with reasonable accuracy. Even though inlet and outlet effects and deformations of the geometry are not taken into account.

The following elementary conditions were satisfied:

1. Mass flow in equals mass flow out.
2. Net mass flow across unit cell edge equals zero.
3. Stiffness found using manual perturbation equals stiffness found using perturbed Reynolds for low frequencies

Currently, the discrepancy between the geometry used in the numerical model and the geometry of the demonstrator is too large. Therefore, the demonstrator cannot be used to verify the results found using the numerical model.

The first step towards achieving this is to create a demonstrator that forms a better resemblance of the geometry used in the numerical model. Where possible, manufacturing errors should be measured such that they can be implemented in a *true* numerical model. If possible, using non-destructive measurement techniques. The true numerical model should show results similar to those found in physical experiments.

5.1.1 Constant fly-height

Using the numerical model it was found that there exists a non-unique set of design parameters for which the eccentric fly-height remains relatively constant for a varying eccentricity (see fig. 19). Creating a system that maintains a constant fly-height while actuating can be very useful, for example during inspection of a substrate using a microscope.

In the numerical model, the supply and vacuum pressure are assumed to be constant, i.e. they are ideal pressure sources. In reality, for non-ideal pressure sources, the pressure will depend on the flow. If the fly-height remains relatively constant, the mass flow also remains relatively constant, which makes it easier to maintain a constant pressure. As an alternative of designing a system for a maximum performance ratio P, it could also be decided to design a system for a minimum variation in fly-height.

5.1.2 Pin deformation

As shown in fig. 20, the pin deforms due to the pressure gradient. Both the geometry of the outlet film as well as that of the pocket deform. The influence of this deformation on the performance of the system is minimal. and it is likely, the influence of deformation of the substrate is more significant. Wesselingh found that these deformations are in the order of 1 μm [4]. This will obviously depend on the type of substrate, operating conditions and unit cell dimensions.

5.2 Manufacturing

It has been difficult to manufacture a system with the required dimensional tolerances. Despite the redundancy inherent to the manufacturing method and all the care that has been taken.

The final geometry of the flow path is determined by the geometry of the mould and the geometry of the cast pin. The latter is to a large extent determined by the behaviour of the resin. The influence of the resin behaviour needs to be minimised, in order to obtain a higher dimensional accuracy and stability of the pins. To improve the manufacturing method, the mould geometry needs to be better defined.

5.2.1 Mould geometry

Any misorientation (i.e. deviation from perpendicularity) of the hole leads to an asymmetrical outlet film and thus also an uneven stroke. The stroke of the system has been measured, as is described in appendix D.4.8. However, this does not provide any information regarding the geometry of each individual outlet film. It does provide some information regarding the combined influence of both the mould geometry and resin behaviour combined.

Ideally, the influence of each mechanism can be measured separately. Obviously, the goal should always be to minimise the influence of these mechanisms. That way, the outlet film thickness will approach the theoretical outlet film thickness defined in eq. (2).

Any waviness present in the mould surface will be transferred to the surface of the cast pin. This causes the outlet film thickness to be uneven along the flow path and therefore not well defined. The waviness could be further reduced by additional manufacturing steps, e.g. burnishing or grinding. The waviness has been measured, however only using a destructive measurement technique.

The mould release agent is added in order to ensure that the resin does not adhere to the mould (i.e. the bearing plate). In this research, vaseline is used. After curing, it is removed, and thus it effectively increases the size of the outlet film thickness. The thickness of this layer has not been measured and thus its influence is unknown. If the thickness is consistent and can be well predicted, this can be taken into account during the manufacturing process. Alternatively, a solid release agent coating, e.g. parylene C, could be used [19]. In that case, this will not influence the outlet film thickness.

5.2.2 Resin behaviour

The behaviour of the resin determines the dimensions of the pin to a large extent in the current demonstrator. Thermal contraction and cure shrinkage will both decrease the size of the pin with respect to the bearing plate, thereby increasing the radial outlet film thickness. Hygroscopic swelling will cause the pins to expand, while the bearing plate is not susceptible to swelling, and thus decreases the radial outlet film thickness.

Exactly predicting the influence of these phenomena is complicated and would be a research on its own. Ideally, an extensive technical data sheet should be provided by the manufacturer. Alternatively, information regarding a certain type of resin could be found in the literature.

The dimensional stability will also increase by decreasing the volume of resin that is required. This could be achieved by machining a plenum lid that has solid cylinders in the centre of each pin, as shown in fig. 21. The resin will then only be used to fill in the gap, rather than to form the complete pin. By using a resin with a higher filler fraction, the dimensional stability will be further increased.

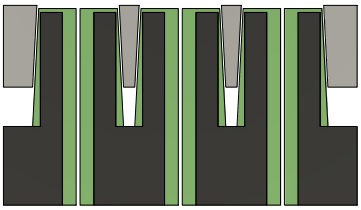

Figure 21: Plenum lid with solid core cylinders.

5.2.3 Inlet restriction

Using the dispensing needles as capillary flow restrictions worked well. The inlet conductivity was consistent and predictable. During the research of Hoogeboom [20] and Verbruggen [6], capillary flow restrictions were also used. They experienced difficulty minimising the recess volume, which increased the chance of pneumatic hammer. Due to the casting process, there is effectively no recess. An additional manufacturing step is required to create a recess.

5.2.4 Pocket restriction

As explained, the pocket restriction is created between the substrate and the surface of each pin. The pocket height is defined by the height of the pin, the thickness of the bearing plate and the distance enforced between the two plates. Alternatively it can thus be stated that the pocket height is equal to (see fig. 6):

$$h_{\mathrm{p}} = t_{\mathrm{bp},2} + t_{\mathrm{v}} - h_{\mathrm{pin}} \tag{25}$$

The pins are levelled with respect to the bearing surface when the system is assembled using undersized ball bearings. This effectively ensures that the exact dimensions are not relevant and that the pocket height is only determined by the difference in ball diameter (i.e. $h_{\mathrm{p}} = \Delta t_{\mathrm{v}} = \Delta d_{\mathrm{b}}$).

Ball bearings were used since their diameter is well defined, and they allowed for local support of the bearing plate. This is required, since otherwise, the deformation due to the pressure gradient across the plate would be too high. In theory, the stiffness achieved using ball bearings should be equal to the Hertzian stiffness. This would result in a deformation in z-direction of $< 1\,\mu$m.

In reality however, the deformation due to the vacuum pressure was 10-20 μm. This is a very significant deformation compared to the nominal pocket height of 19 μm. The

reason is most likely due to the disk spring action of the spacer plates and the non-flatness of both plates in general.

For a future demonstrator, pocket height needs to be more accurately defined. This means that the vertical stiffness needs to be higher and the deformation needs to be minimised. Performing the final manufacturing step on the system in its assembled state is also cumbersome and could therefore be improved.

Reduced stroke

The system was initially designed for an outlet film thickness of $40\,\mu m$, for a distance between the two plates of 4 mm. By adding the spacer plates, this distance was increased to 7 mm. In theory, the outlet film thickness should then be equal to $70\,\mu m$, and thus the total stroke should be equal to $140\,\mu$m. However, the total stroke was only $29\,\mu$m before glueing the spacer plates. After glueing the spacer plates, the stroke essentially reduced to 0. This could be due to glue that seeped into the outlet restriction during curing, however, no sign of this was found upon inspection. Alternatively, it could be due to hygroscopic swelling of the pins.

6 Conclusion

Contactless handling based on air bearing technology is a technology that can be used to handle substrates in a fully contactless manner. Promising results have been shown in a lab environment, however, manufacturing such systems is in general complicated and expensive, due to very tight tolerances.

A system using the variable outlet restriction concept was developed. It was shown that this system has a performance ratio identical to that of the variable pocket restriction concept. The variable outlet restriction concept was selected for further development since the manufacturing process could potentially be simplified.

A novel manufacturing method has been developed. In theory, the system developed using method should be less sensitive for manufacturing errors than previously developed concepts. In practice however, the required manufacturing tolerances have not been met. This is partly due to geometrical errors present in the mould and partly due to insufficient dimensional stability of the cast pins.

The system has been modelled using COMSOL. It was discovered that there exists a set of design parameters for which the fly-height, and therefore the mass flow, remain relatively constant. However, this claim still needs to be confirmed by experimental data.

Additional research into the manufacturing method is required. By using non-destructive measurement techniques, relevant dimensions should be measured and implemented into a numerical model that forms a better resemblance of the geometry of the demonstrator.

References

[1] B. Hoefflinger, *Chips 2020: A Guide To the Future of Nanoelectronics*. 2012.

[2] G. M. Wilson, M. Al-Jassim, W. K. Metzger, S. W. Glunz, P. Verlinden, G. Xiong, L. M. Mansfield, B. J. Stanbery, K. Zhu, Y. Yan, J. J. Berry, A. J. Ptak, F. Dimroth, B. M. Kayes, A. C. Tamboli, R. Peibst, K. Catchpole, M. O. Reese, C. S. Klinga, P. Denholm, M. Morjaria, M. G. Deceglie, J. M. Freeman, M. A. Mikofski, D. C. Jordan, G. Tamizhmani, and D. B. Sulas-Kern, "The 2020 photovoltaic technologies roadmap," *Journal of Physics D: Applied Physics*, vol. 53, no. 49, 2020.

[3] Z. Liu, S. E. Sofia, H. S. Laine, M. Woodhouse, S. Wieghold, I. M. Peters, and T. Buonassisi, "Revisiting thin silicon for photovoltaics: A technoeconomic perspective," *Energy and Environmental Science*, vol. 13, no. 1, pp. 12–23, 2020.

[4] J. Wesselingh, *Contactless positioning using an active air film*. Phd thesis, Delft University of Technology, 2011.

[5] V. Hong Phuc, *Air-based contactless actuation system for thin substrates*. Phd thesis, Delft University of Technology, 2016.

[6] N. Verbruggen, *Air-Based Contactless Positioning of Thin Substrates*. Master thesis, Delft University of Technology, 2017.

[7] R. Jansen, *Actuator System for the Flowerbed*. Master thesis, Delft University of Technology, 2018.

[8] M. E. Krijnen, *Control System Design for a Contactless Actuation System*. Master thesis, Delft University of Technology, 2016.

[9] R. Hooijschuur, N. Saikumar, S. H. Hosseinnia, and R. A. van Ostayen, "Air-based contactless wafer precision positioning system," *Applied Sciences (Switzerland)*, vol. 11, no. 16, 2021.

[10] R. Snoeys and F. Al-Bender, "Development of improved externally pressurized gas bearings," *KSME Journal*, vol. 1, no. 1, pp. 81–88, 1987.

[11] C. Hahm, R. Theska, A. Flohr, and O. Hartmann, "Concrete – future material for high precision machines," no. September, pp. 8–12, 2014.

[12] COMSOL Inc., "COMSOL Multiphysics Version 5.6," 2021.

[13] B. J. Hamrock and S. R. Schmid, *Fundamental of Fluid Film Lubrication*. 1991.

[14] W. Brian Rowe, *Hydrostatic, Aerostatic and Hybrid Bearing Design*. Elsevier, first ed., 2012.

[15] F. Al-Bender, *Air Bearings: Theory, Design and Applications*. Tribology in Practice Series, Wiley, 2021.

[16] E. Urata, "A flow rate equation for subsonic Fanno flow," *Proceedings of the Institution of Mechanical Engineers, Part C: Journal of Mechanical Engineering Science*, vol. 227, no. 12, pp. 2724–2729, 2013.

[17] Y. He, "Moisture absorption and hygroscopic swelling behavior of an underfill material," *Thermochimica Acta*, vol. 546, pp. 143–152, 2012.

[18] J. de Vreugd, *The Effect of Aging on Moulding Compound Properties*. Phd thesis, Delft University of Technology, 2011.

[19] P. Sethu and C. H. Mastrangelo, "Cast epoxy-based microfluidic systems and their application in biotechnology," *Sensors and Actuators, B: Chemical*, vol. 98, no. 2-3, pp. 337–346, 2004.

[20] R.P. Hoogeboom, *Design and experimental validation of low stiffness aerostatic thrust bearings*. Master thesis, Delft University of Technology, 2016.